



National Library  
of Canada

Bibliothèque nationale  
du Canada

Canadian Theses Service

Service des thèses canadiennes

Ottawa, Canada  
K1A 0N4

## NOTICE

The quality of this microform is heavily dependent upon the quality of the original thesis submitted for microfilming. Every effort has been made to ensure the highest quality of reproduction possible.

If pages are missing, contact the university which granted the degree.

Some pages may have indistinct print especially if the original pages were typed with a poor typewriter ribbon or if the university sent us an inferior photocopy.

Reproduction in full or in part of this microform is governed by the Canadian Copyright Act, R.S.C. 1970, c. C-30, and subsequent amendments.

## AVIS

La qualité de cette microforme dépend grandement de la qualité de la thèse soumise au microfilmage. Nous avons tout fait pour assurer une qualité supérieure de reproduction.

S'il manque des pages, veuillez communiquer avec l'université qui a conféré le grade.

La qualité d'impression de certaines pages peut laisser à désirer, surtout si les pages originales ont été dactylographiées à l'aide d'un ruban usé ou si l'université nous a fait parvenir une photocopie de qualité inférieure.

La reproduction, même partielle, de cette microforme est soumise à la Loi canadienne sur le droit d'auteur, SRC 1970, c. C-30, et ses amendements subséquents.

UNIVERSITY OF ALBERTA

Nonlinear Finite Element Analysis of Axisymmetric Solids with Asymmetric  
Deformations

by

Trent Michael Victor Kaiser

A THESIS

SUBMITTED TO THE FACULTY OF GRADUATE STUDIES AND RESEARCH  
IN PARTIAL FULFILMENT OF THE REQUIREMENTS FOR THE DEGREE  
OF DOCTOR OF PHILOSOPHY

IN

DEPARTMENT OF MECHANICAL ENGINEERING

EDMONTON, ALBERTA

FALL 1991



National Library  
of Canada

Bibliothèque nationale  
du Canada

Canadian Theses Service    Service des thèses canadiennes

Ottawa, Canada  
K1A 0N4

The author has granted an irrevocable non-exclusive licence allowing the National Library of Canada to reproduce, loan, distribute or sell copies of his/her thesis by any means and in any form or format, making this thesis available to interested persons.

The author retains ownership of the copyright in his/her thesis. Neither the thesis nor substantial extracts from it may be printed or otherwise reproduced without his/her permission.

L'auteur a accordé une licence irrévocable et non exclusive permettant à la Bibliothèque nationale du Canada de reproduire, prêter, distribuer ou vendre des copies de sa thèse de quelque manière et sous quelque forme que ce soit pour mettre des exemplaires de cette thèse à la disposition des personnes intéressées.

L'auteur conserve la propriété du droit d'auteur qui protège sa thèse. Ni la thèse ni des extraits substantiels de celle-ci ne doivent être imprimés ou autrement reproduits sans son autorisation.

ISBN 0-315-70031-9

University of Alberta

**RELEASE FORM**

NAME OF AUTHOR: Trent Michael Victor Kaiser  
TITLE OF THESIS: Nonlinear Finite Element Analysis of Axisymmetric Solids  
with Asymmetric Deformations  
DEGREE: Doctor of Philosophy  
YEAR THIS DEGREE GRANTED: FALL 1991

Permission is hereby granted to THE UNIVERSITY OF ALBERTA  
LIBRARY to reproduce single copies of this thesis and to lend or sell such copies  
for private, scholarly or scientific research purposes only.

The author reserves other publication rights, and neither the thesis nor  
extensive extracts from it may be printed or otherwise reproduced without the  
author's written permission.

(SIGNED)  .....

PERMANENT ADDRESS:

7039 32 Avenue

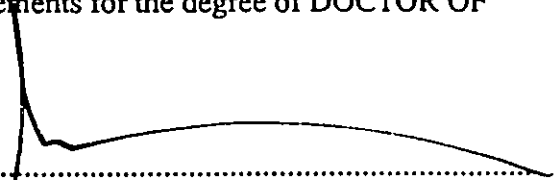
Edmonton, Alberta

T6K 2K9

DATE: May 31, 1991

THE UNIVERSITY OF ALBERTA  
FACULTY OF GRADUATE STUDIES AND RESEARCH

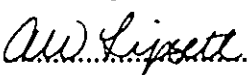
The undersigned certify that they have read, and recommend to the  
Faculty of Graduate Studies and Research, for acceptance, a thesis entitled NONLINEAR  
FINITE ELEMENT ANALYSIS OF AXISYMMETRIC SOLIDS WITH  
ASYMMETRIC DEFORMATIONS submitted by TRENT MICHAEL VICTOR  
KAISER in partial fulfillment of the requirements for the degree of DOCTOR OF  
PHILOSOPHY.

  
.....  
A.E. Elwi (Supervisor)

  
.....  
A. Mioduchowski (Supervisor)

  
.....  
D. Budney

  
.....  
M.G. Faulkner

  
.....  
A.W. Lipsett

  
.....  
S. Lukasiewicz

Date: May 31, 1991

To my wife Lucille

## **Abstract**

Axisymmetric finite element models are useful for modelling many axisymmetric or nearly axisymmetric structures. However, if three dimensional behaviour must be modelled, either due to non-axisymmetric loads or buckling behaviour, a full three dimensional mesh is usually required. One approach to utilizing axisymmetric elements for three dimensional behaviour is to use Fourier decomposition to model the circumferential variation in the displacement field. This is very effective for linear problems because the harmonics become decoupled, and the finite element equations are represented as a series of equation sets, each half again as large as the axisymmetric case. This technique has not previously been extended to general large displacement formulations, because the nonlinear terms couple the harmonics, and the size of the system of equations increases significantly. However, for problems where only a few harmonics are required, Fourier decomposition can be much more efficient than conventional three dimensional elements.

In this thesis, a nonlinear finite element formulation for an axisymmetric solid element is developed which models asymmetric behaviour. The element is based on a Total Lagrangian formulation and uses Fourier decomposition to model the displacement field in the circumferential direction. The formulation is developed in terms of two displacement types; Cartesian and cylindrical displacement components. Verification is performed by comparison with results from the literature and general purpose analysis programs. Problem types include linear and nonlinear axisymmetric problems, linear tube - beam (asymmetric) analyses, asymmetric thin shell analyses, and a thick wall tube loaded as a beam - column, exhibiting combined Euler and Brazier buckling behaviour.

## **Acknowledgements**

This research was developed out of the core research program at The Centre for Frontier Engineering Research (C-FER) in Edmonton, Alberta, Canada. The author wishes to thank C-FER and its funding members for their support and technical assistance in the development of this project, and for their permission to release the results to fulfill the requirements of this degree.

The author would also like to thank his project supervisors, Dr. Alaa Elwi and Dr. Andrew Mioduchowski for their guidance in this research project.



## Table of Contents

1.	Introduction.....	1
2.	Incremental Finite Element Formulation in General Curvilinear Coordinates .....	7
2.1.	Lagrangian Strains in Curvilinear Coordinates.....	7
2.1.1.	Strain .....	8
2.1.2.	The Strain Increments .....	13
2.1.3.	Strain Increment Variation .....	15
2.1.4.	Total Strain Increment.....	16
2.2.	The Principle of Incremental Virtual Work.....	16
2.2.1.	Virtual Work Expression.....	16
2.2.2.	Total Lagrangian Formulation of Virtual Work Equation .....	17
2.2.3.	Incremental Form of Virtual Work Equation .....	19
2.3.	Finite Element Equations.....	20
2.3.1.	Linear Stiffness Matrix.....	20
2.3.2.	Geometric or Nonlinear Stiffness Matrix .....	21
2.3.3.	Loads .....	22
2.3.4.	Finite Element Form of Incremental Virtual Work .....	23
2.4.	Chapter Summary .....	24
3.	Cylindrical Formulation .....	29
3.1.	Overview .....	29
3.2.	Displacement Field .....	29
3.2.1.	Fourier Decomposition of Circumferential (Out-of-Plane) Displacement.....	30
3.2.2.	Polynomial In-Plane Interpolation with Parametric Transformation.....	31

3.2.3.	Combined Interpolation.....	32
3.2.4.	Vector Notation for the Interpolation Functions .....	34
3.3.	In Plane Isoparametric Coordinate Transformation .....	37
3.4.	The Strain Representation.....	39
3.4.1.	The Small Strain Increment.....	40
3.4.2.	The Nonlinear Strain Component Increment .....	42
3.5.	The Linear Stiffness Matrix .....	44
3.6.	The Geometric or Nonlinear Stiffness Matrix .....	45
3.6.1.	The Displacement Gradient Part.....	45
3.6.2.	The Scale Function Part .....	46
3.6.3.	The Mixed Part .....	48
3.7.	Integration .....	50
3.7.1.	Integration of the Conventional Axisymmetric Element .....	50
3.7.2.	Integration of the Linear Elastic Non-Axisymmetric Element.....	51
3.7.3.	Nonlinear Non-Axisymmetric Integration .....	53
3.8.	Boundary Conditions .....	60
3.9.	Cylindrical Formulation Summary.....	62
4.	Cartesian Formulation .....	66
4.1.	Overview .....	66
4.2.	Displacement Field .....	66
4.2.1.	Displacement Components .....	66
4.2.2.	Fourier Decomposition of Circumferential (Out-of-Plane) Displacement.....	67
4.2.3.	Polynomial In-Plane Interpolation with Parametric Transformation.....	68

4.2.4.	Combined Interpolation.....	68
4.2.5.	Displacement Gradients.....	69
4.2.6.	Vector Notation for Interpolation Functions .....	72
4.3.	The Strain Representation.....	75
4.3.1.	Small Strain Increment - Matrix Representation .....	76
4.3.2.	Nonlinear Strain Increment Component .....	78
4.3.3.	Linear Stiffness Matrix.....	79
4.3.4.	Geometric or Nonlinear Stiffness Matrix .....	79
4.4.	Integration .....	81
4.4.1.	Nonlinear Non-Axisymmetric Integration .....	82
4.5.	Boundary Conditions .....	84
4.6.	Transformation to Cylindrical Degrees of Freedom .....	87
4.7.	Cartesian Formulation Summary.....	91
5.	Program "Static Lagrangian Analysis of Tubular Structures (SLATS)" .....	95
5.1.	The Harmonic Lagrangian Tubular (HLT) Finite Element.....	95
5.1.1.	General Description.....	95
5.1.2.	Geometric Properties.....	95
5.1.3.	Nodal Degrees of Freedom.....	96
5.1.4.	Integration Requirements .....	97
5.2.	Element Generation .....	98
5.3.	Stiffness Matrix Storage .....	99
5.4.	Load Vector Calculation .....	100
5.5.	Boundary Conditions .....	101
5.6.	Solution Strategies .....	102
5.7.	Summary .....	104

6.	Discussion and Verification of Formulation .....	109
6.1.	Introduction .....	109
6.2.	Linear Formulation in Pure Bending .....	110
6.3.	Nonlinear Analyses .....	115
6.3.1.	Torus .....	116
6.3.2.	Spherical Cap .....	117
6.3.3.	Cylinder Collapse .....	123
6.3.4.	Hyperbolic Cooling Tower .....	125
6.3.5.	Cylindrical Shell under Wind Load .....	127
6.4.	Large Displacement Analysis: Beam Bending .....	129
6.5.	Large Displacement Analysis: Beam-Column Collapse .....	131
6.5.1.	Problem Overview .....	131
6.5.2.	Model Descriptions .....	132
6.5.3.	General Behaviour .....	132
6.5.4.	Numerical Verification .....	135
6.6.	Element Parameters .....	137
6.6.1.	Polynomial Displacement Field .....	137
6.6.2.	Harmonic Displacement Field .....	138
6.6.3.	Gaussian Integration Order .....	140
6.6.4.	Fourier Integration Order .....	141
6.6.5.	Element Geometry .....	143
6.7.	Solution Efficiency .....	144
6.8.	Chapter Summary .....	146
7.	Summary and Conclusions .....	212
7.1.	Overview of Formulation .....	212

7.2.	Solution Efficiency .....	213
7.3.	Future Directions .....	213
7.3.1.	Nonlinear Material Models.....	213
7.3.2.	Contact Model.....	214
7.3.3.	Antisymmetric Capability.....	214
7.3.4.	Curved Axis of Symmetry.....	214
7.3.5.	Additional Symmetric and Selective Harmonic Capabilities. ....	214
7.3.6.	Improved Integration Techniques .....	215
7.3.7.	Resolve Cylindrical Formulation Rigid Body Motion.....	215
7.4.	Closure .....	216
8.	References.....	217

## 9. List of Tables

Table 2.1	Coordinates and Scale Factors for Common Reference Systems .....	25
Table 6.1	Cylinder Critical Pressures, Basic Mesh Results.....	148
Table 6.2	Cylinder Critical Pressures, 30 inch Cylinder.....	149
Table 6.3	Cylinder Critical Pressures, 600 inch Cylinder, Basic Mesh.....	150

## List of Figures

Figure 1.1	Threaded connection for Oil Country Tubular Goods (OCTG) .....	5
Figure 1.2	Well model at formation interface zone .....	6
Figure 2.1	Common orthogonal coordinate systems.....	26
Figure 2.2	Displacement increments in cylindrical coordinates .....	27
Figure 2.3	Path dependence of physical displacements in cylindrical coordinates .....	28
Figure 3.1	Axisymmetric three dimensional solid element .....	64
Figure 3.2	Isoparametric geometry transformation.....	65
Figure 4.1	Decomposition of radial pressure into Cartesian components .....	93
Figure 4.2	Transformation between Cartesian and cylindrical displacements .....	94
Figure 5.1	Main program flow chart .....	105
Figure 5.2	Flow chart for stiffness matrix or equilibrating force vector generation - full element matrix form .....	106
Figure 5.3	Flow chart for stiffness matrix or equilibrating force vector generation - partial element matrix form, inside loops (see Figure 5.2 for outside loops) .....	107
Figure 5.4	Strain - displacement matrix generation flow chart .....	108
Figure 6.1	Tube - beam bending problem .....	151
Figure 6.2	Tube - beam bending model.....	152
Figure 6.3	Formulation comparison in pure bending, small displacement and quadratic element displacement field .....	153
Figure 6.4	Cylindrical formulation with coordinate displacements: pure bending, small displacement, quadratic element displacement field .....	154
Figure 6.5	Radial mesh refinement performance of the cylindrical formulation with coordinate displacements .....	155
Figure 6.6	Radial mesh refinement performance of the cartesian formulation four node element, three point quadrature, pure bending, small displacement.....	156

Figure 6.7	Torus model.....	157
Figure 6.8	Normal displacement distribution in a toroidal shell under external pressure .....	158
Figure 6.9	Hoop stress distribution in toroidal shell under external pressure - nonlinear results - 40 quadratic elements.....	159
Figure 6.10	Bending moment distribution in toroidal shell under external pressure - nonlinear results.....	160
Figure 6.11	Spherical cap models .....	161
Figure 6.12	Pressure displacement relationship for Cap 1. Full displacement range.....	162
Figure 6.13	Pressure - displacement relationship for Cap 2.....	163
Figure 6.14	Pressure - displacement relationship for Cap 2, Full displacement range.....	164
Figure 6.15	Equilibrium curves at secondary points on Cap 2.....	165
Figure 6.16	Bending stress distribution in Cap 1 during pressure loading sequence .....	166
Figure 6.17	Bending stress distribution in Cap 2 during pressure loading sequence .....	167
Figure 6.18	Cap 2 displacement distribution at first four critical points, a, b, c, and d in figure 6.14.....	168
Figure 6.19	Cap 2 displacement distribution comparison for critical points d and h in load displacement curve (refer to Figure 6.14).....	169
Figure 6.20	Radial displacement distribution during snap back of Cap 2.....	170
Figure 6.21	Displacement distribution for Cap 2 from snap back to snap through .....	171
Figure 6.22	Load - displacement relationship for asymmetrically loaded spherical cap (Cap 3) .....	172
Figure 6.23	Load - displacement for asymmetrically loaded cap. Harmonic displacement components, Cartesian formulation.....	173
Figure 6.24	Harmonic displacement components at maximum displacement location for asymmetrically loaded cap .....	174



Figure 6.25	Buckling modes for various cylinders under external pressure .....	175
Figure 6.26	Cylindrical shell model under uniform external pressure.....	176
Figure 6.27	Full size cooling tower model, two load cases.....	177
Figure 6.28	Load - radial displacement amplitude response for the cooling tower under external pressure measured 150 ft below throat .....	178
Figure 6.29	Load - radial displacement amplitude at top of hyperbolic tower under wind loading using 10 harmonics .....	179
Figure 6.30	Total radial displacements at two vertical locations at the stagnation point of the cooling tower using 10 harmonics .....	180
Figure 6.31	Deformed shapes for cooling tower: a) initial deformation magnified 500x; b) advanced deformation magnified 6x.....	181
Figure 6.32	Radial displacement at top of cylindrical shell subject to wind load.....	182
Figure 6.33	Load - Harmonic displacement relationship for cylinder under wind loading - lower Fourier numbers .....	183
Figure 6.34	Higher order harmonic displacement amplitudes at top of cylinder under wind loads.....	184
Figure 6.35	Displacement patterns at top of cylinder subjected to wind load. (10 harmonics, 4 elements) .....	185
Figure 6.36	Large displacement bending model (not shown to scale).....	186
Figure 6.37	Pinching effect of deformation independent nodal harmonic loads.....	187
Figure 6.38	Deformed beam geometry, pure bending .....	188
Figure 6.39	Deformation dependence of bending load with deformation independent nodal harmonic forces .....	189
Figure 6.40	Load vs. displacement at neutral axis for the slender beam .....	190
Figure 6.41	Large displacement tube - column models .....	191
Figure 6.42	Initial load - displacement comparison between SLATS and secant formula for column.....	192
Figure 6.43	Load vs. displacement at end of tube for the tube - column problem .....	193

Figure 6.44	Bending moment at plane of symmetry vs. displacement at middle for the tube - column problem.....	194
Figure 6.45	Overall tube shape at various stages of buckling .....	195
Figure 6.46	Enlarged view of collapsed cross section at middle of tube .....	196
Figure 6.47	Load - displacement comparison between SLATS and ADINA .....	197
Figure 6.48	Cylindrical formulation results (load eccentricity = 0.0004 inches) .....	198
Figure 6.49	Polynomial displacement field comparison, Eight node vs. nine node elements, 8 harmonics .....	199
Figure 6.50	Load - displacement variation with harmonic refinement .....	200
Figure 6.51	Load - ovalization relationship at middle of tube .....	201
Figure 6.52	Load - third harmonic displacement at middle of tube.....	202
Figure 6.53	Load - fourth harmonic displacement at middle of tube .....	203
Figure 6.54	Deformed shape of tube cross section at middle.....	204
Figure 6.55	Load vs. lateral displacement with additional harmonic refinement.....	205
Figure 6.56	Influence of circumferential integration order on results .....	206
Figure 6.57	Effect of axial mesh refinement on the nonlinear solution.....	207
Figure 6.58	Normalized axial distribution of harmonic radial displacement at point b on equilibrium curve (Figure 6.43) .....	208
Figure 6.59	Effect of radial mesh refinement on nonlinear solution .....	209
Figure 6.60	Solution time comparison for thin shell type problems.....	210
Figure 6.61	Solution time comparison for solid type problems .....	211

## 1. Introduction

Most general purpose finite element analysis codes include a solid element for analysing axisymmetric problems. These problems are modelled by a two dimensional mesh in a plane of symmetry and the element volumes are produced by a revolution about the axis of symmetry. In these problems, the loads are axisymmetric and the deformation field description is also restricted to modelling axisymmetric behaviour.

When the restrictions on the load and/or the deformation field description are removed the behaviour varies in the circumferential direction (non-axisymmetric behaviour) and three dimensional elements must usually be used to construct a model. No benefit of the geometric symmetry is thus gained. The complexity of the model increases, and the problem becomes much larger computationally. Even relatively simple problems are beyond the capability of available computing systems when modelled in three dimensions.

Because it is often important to determine the response to non-axisymmetric loads with limited computing resources, efforts have been made to develop axisymmetric elements which can model such behaviour. These elements are now becoming available in some general purpose finite element programs such as ABAQUS, ANSYS, and Cosmos. The most basic application of an axisymmetric element for non-axisymmetric behaviour was presented by Zienkiewicz and Cheung(1967). They discussed an element for modelling the torsional response of shafts by using the circumferential, or out of plane, displacement component as degrees of freedom for the nodal points. A more general discussion of non-axisymmetric modelling was put forth by Wilson(1965) in which he discusses the technique of decomposing the displacement field in the circumferential direction into a Fourier series. His focus was on linear problems, and he recognized that for such formulations the harmonic stiffnesses are decoupled because of the orthogonal properties of the Fourier functions. This characteristic made it practical to extend an axisymmetric analysis to model three dimensional responses using the same mesh and required only a modest increase in computing time over the axisymmetric case.

As the technique of Fourier decomposition became a recognized, effective means of modelling three dimensional behaviour in axisymmetric structures, some authors explored avenues for extending the capabilities of these "harmonic elements." Several shell elements were developed, including the SABA element of Chan and Firmin(1970).

Interesting applications of mixed formulations for shells were put forth by Chan and Trbojevic(1976). Spilker and Daugirda(1981) discussed a hybrid-stress formulation for a solid element. All of the above were based on linear formulations in which the Fourier terms were decoupled.

Some of these authors pursued the development of these models further to accommodate material and geometric nonlinearities. Winnicki and Zienkiewicz(1979) and Singh and Spilker(1984) demonstrated applications of Fourier decomposition to elastic-plastic problems, incorporating nonlinear behaviour in the evaluation of the nodal stress-equivalent equilibrating vector, which required numerical integration in the circumferential direction. In both of these discussions, the initial stiffness matrix was retained, avoiding the increased burden of coupled harmonics, and equilibrium iterations were used to achieve equilibrium. Chan and Firmin(1970a), and Chan and Trbojevic(1976) extended the shell elements referred to above to model "large" displacements, however, their models were restricted to non-axisymmetric deformations which were in the order of the shell thickness, and the geometry of the structure was assumed to remain essentially axisymmetric. These elements permitted an estimate of the buckling loads, but could not model deformations near the point of total collapse, nor in the post buckling regime. Although Chan recognized that the harmonics are coupled by the geometric nonlinearities, the deformations were small enough that the coupling matrices were relatively small and could be ignored. He did, however, update the geometric stiffness matrix for each harmonic, and used an iterative solution strategy to achieve equilibrium.

More recently, Wunderlich, Cramer and Obrecht, 1985, and Wunderlich et al., 1989 presented shell formulations which are more general in terms of their displacement capabilities. Their approach is to model the nonlinearities as pseudo-load vectors so as to retain an uncoupled system of equations. While this reduces the time required to solve the system of equations, it does not reduce the amount of time required to evaluate the harmonic coupling matrices. It also requires an iterative conjugate gradient method solution technique to avoid convergence problems which requires significantly more equilibrium iterations than does a Newton-Raphson type of solution using a coupled stiffness matrix. Wunderlich et al., 1989, also employed a numerical integration technique in the circumferential direction for improved solution accuracy.

Although these models are effective for modelling the problems for which they were developed, most are limited to small or relatively small displacements. Also, the

techniques which do model geometric nonlinearities are shell formulations which can only model simple stress and deformation patterns in the thickness dimension of the element. Many problems require solid elements to model more general three dimensional behaviour and demand a truly large displacement capability, which is best provided by an incremental Lagrangian formulation. One example is a threaded connection problem with asymmetric loads such as bending, Figure 1.1. The performance of the connection can be evaluated by determining the behaviour in the threaded and (where applicable) seal regions. Another example is a three dimensional model of a well subject to general three dimensional loads, Figure 1.2. Currently, three dimensional elements would be necessary to construct the problem geometry and model the asymmetric deformations, but the number of elements and degrees of freedom become enormous. Using an axisymmetric element with an asymmetric displacement field is potentially many times more efficient than the three dimensional element because of the reduction in the number of degrees of freedom required in the model.

Other authors have pointed out that the harmonic equations become coupled in a general nonlinear formulation. While this makes the Fourier decomposition technique less efficient for nonlinear problems than it is for linear problems, little effort has been made to formulate and solve the coupled nonlinear equations and compare the effectiveness of the resulting formulation with existing general purpose three dimensional models.

The topic of this thesis is to formulate the Fourier decomposition technique in terms of an incremental Total Lagrangian formulation to provide a general large displacement, non-axisymmetric modelling capability for axisymmetric structures. The result is a model which takes advantage of the geometric symmetry of the structure and also includes all kinematic nonlinearities. While the material properties used in this study or discussed in the publications cited above are limited, the proposed incremental formulation used can accommodate a much wider variety of material properties than the models.

The Total Lagrangian formulation is developed in terms of orthogonal curvilinear coordinate systems. This general formulation is used to develop two axisymmetric solid elements; one in a cylindrical coordinate system, the other using a Cartesian coordinate system. Both elements use the Fourier decomposition technique to model circumferential variation in the response of the structure to non-axisymmetric loads, and both are capable of modelling large displacements. The harmonics in the

system of equations that these elements produce are coupled, making the solution time significantly greater relative to the uncoupled formulations in the literature. However the results show that for many problems, solution efficiency is much greater than that of general purpose three dimensional elements. The elements are used to model a variety of problems and comparisons are made with solutions from general purpose finite element programs executed to verify the formulation and to compare solution efficiency. Comparisons are also made with some analytical and experimental solutions from the literature. Problem types include linear axisymmetric and asymmetric problems, large displacement thin shell problems such as the torus subject to external pressure, and spherical caps with symmetric and asymmetric loading. Considerable attention is also paid to a thick shell tube subjected to axial loading, which is the primary vehicle for evaluating the influence of various element properties and parameters.

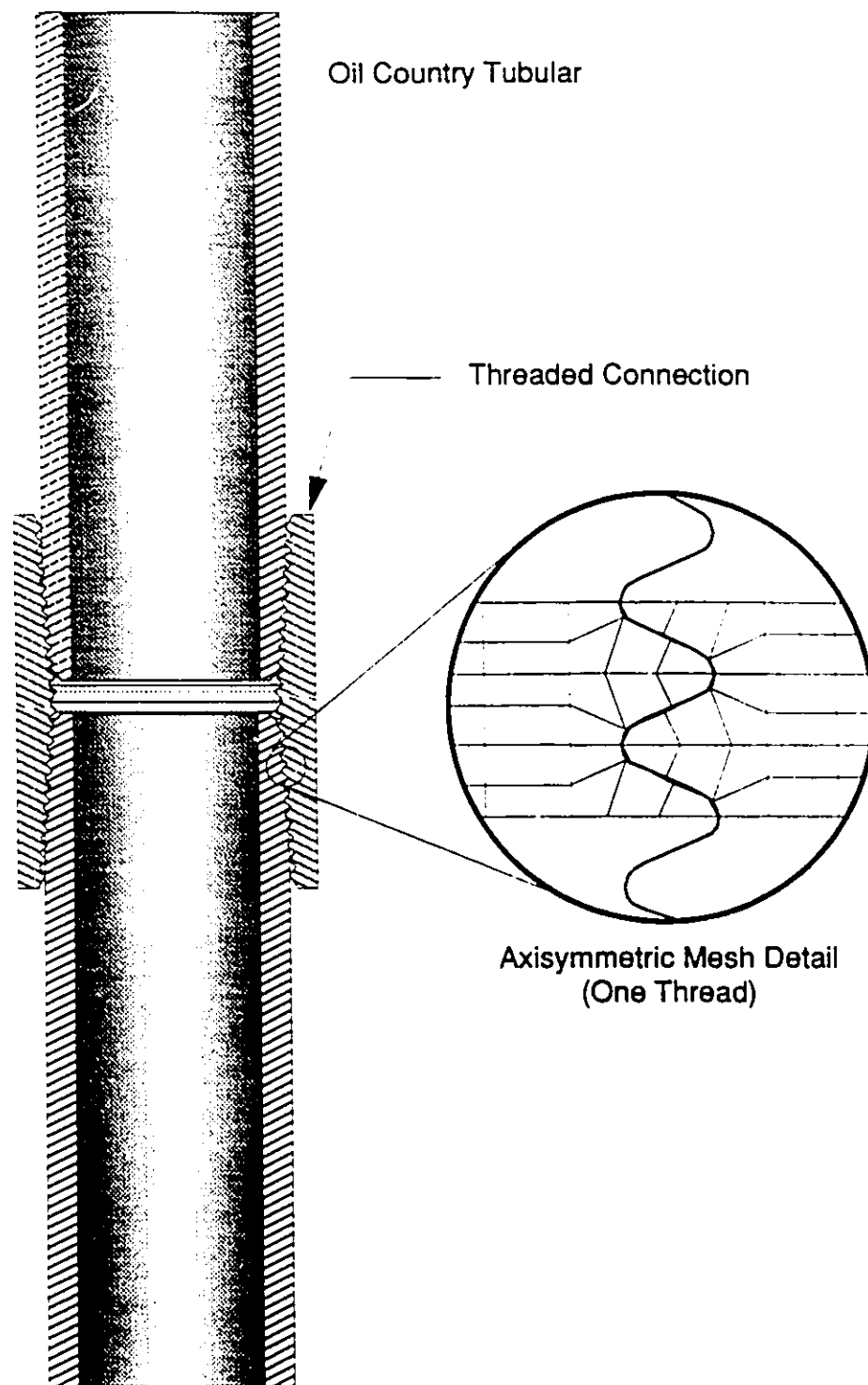


Figure 1.1 Threaded connection for Oil Country Tubular Goods (OCTG)

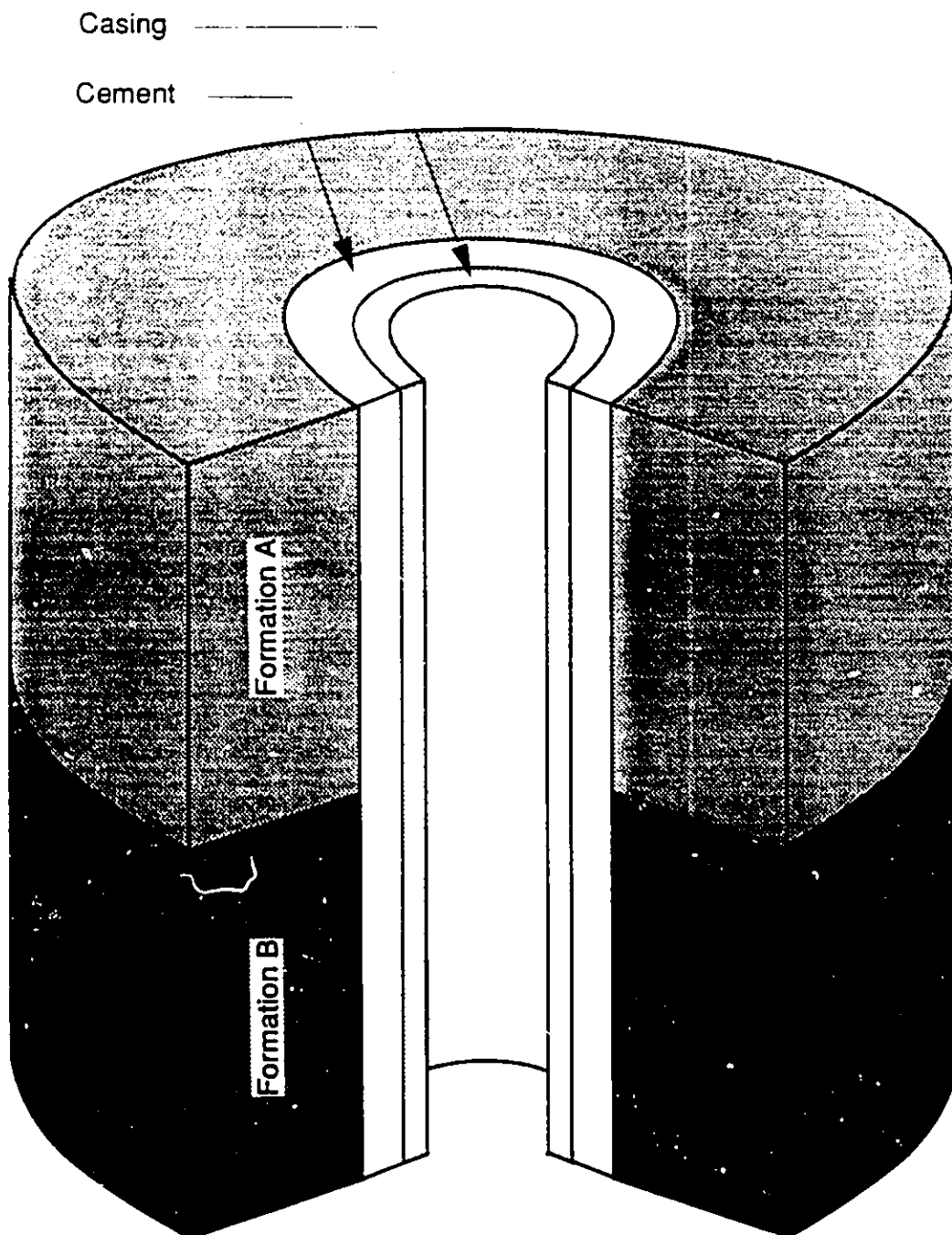


Figure 1.2 Well model at formation interface zone



## **2. Incremental Finite Element Formulation in General Curvilinear Coordinates**

This chapter discusses a basic Lagrangian finite element formulation in a general orthogonal curvilinear coordinate system. It includes the basic elements for describing Lagrangian strains and strain increments using coordinates and displacement components in orthogonal curvilinear coordinate systems, and the procedure for incorporating these components into the integral virtual work equation which forms the basis of most structural finite element applications. This generalized formulation is applied to a large displacement cylindrical formulation in Chapter 3, which is an extension of the small displacement Fourier decomposition formulations commonly available. In Chapter 4, a Cartesian version of the formulation is developed. This version departs from the conventional approach by using Cartesian displacement components in the core formulation. Transformations between cylindrical and Cartesian degrees of freedom are developed for this version, however, to maintain an interpretive reference frame which is consistent with conventional Fourier decomposition finite element techniques.

### **2.1. Lagrangian Strains in Curvilinear Coordinates**

Incremental formulations for finite element programs have been largely based on Cartesian reference systems (for example Bathe, 1982, and Zienkiewicz, 1977]. Many programs use cylindrical, spherical, or local coordinate systems for input convenience, then transform the values to global Cartesian coordinates for the underlying finite element formulation.

These approaches then use Cartesian coordinate systems for geometry, displacements, stresses and strains. However, for some problems it may be advantageous to formulate the problem in terms of some other coordinate system, for example cylindrical or spherical coordinates. Significant efforts have been devoted to cylindrical formulations (Wilson, 1965; Winnicki and Zienkiewicz, 1979; Spilker and Daugirda, 1981; Kleiber and Hien, 1983), however, these have typically been small displacement formulations.

Lagrangian formulations are able to model nonlinear behaviour arising out of large displacements, rotations, and strains. The Green-Lagrange strains on which these formulations are based have the desirable characteristic of remaining invariant under rigid body rotation. In this section, the Green - Lagrange strains, strain increments and

strain increment variations are developed in terms of general orthogonal curvilinear coordinate systems.

### 2.1.1. Strain

#### Lagrangian Strains Based on the Deformation Gradient Tensor

Many authors (Malvern, 1969; Fung, 1965; Truesdell and Toupin, 1960) developed expressions for Green-Lagrange strains in terms of the deformation gradient tensor in general curvilinear or orthogonal curvilinear coordinate systems. The following development of the strain tensor in terms of the deformation gradient is based largely on Malvern's discussion.

The Lagrangian strain tensor is defined to give the change in the squared length of the material vector in terms of the material (or reference) coordinates,  $X_i$ :

$$(ds)^2 - (dS)^2 = 2dX_i E_{ij} dX_j \quad (2.1)$$

where  $dS$  is the original material vector,  $ds$  is the deformed or strained material vector,  $X_i$  are the material (original) coordinates, and  $E_{ij}$  is the Green-Lagrange strain tensor.

The deformation tensor,  $C_{ij}$ , gives the new squared length of the material vector in terms of material coordinates,

$$(ds)^2 = dX_i C_{ij} dX_j. \quad (2.2)$$

The Green-Lagrange strain tensor may then be written in terms of the deformation tensor and the Kronecker delta,  $\delta_{ij}$ :

$$E_{ij} = \frac{1}{2} (C_{ij} - \delta_{ij}). \quad (2.3)$$

In general orthogonal curvilinear coordinates, the material vector components are functions of position:

$$dS_i = H^i dX_i \quad (\text{no sum}), \text{ and} \quad (2.4a)$$

$$ds_i = h^i dx_i \quad (\text{no sum}), \quad (2.4b)$$

where  $H^i$  are the material (original) scale functions, and  $h^i$  are the spatial (deformed) scale functions.

Many authors use subscript and superscript indices to denote, respectively, covariant and contravariant components of tensors, and sum over repeated indices on different levels. Others use a convention that sums any repeated index. In orthogonal coordinate systems, the covariant and contravariant components are coincident, therefore, only one set of components is considered, and a convention which distinguishes between the two is not required. Instead, the convention introduced in Eq. (2.4) is employed where summation occurs only for repeated subscript indices.

The most common orthogonal coordinate systems are the Cartesian, cylindrical and spherical systems. The following treatment is concerned with the first two, although, some interesting applications to spherical systems are certainly possible. Figure 2.1 illustrates these three coordinate systems, and Table 2.1 lists the scale factor functions for each system.

The spatial material vector,  $ds$ , may be expressed in terms of the original material vector through the deformation gradient tensor,  $F_{km}$ :

$$ds_k = F_{km} dS_m. \quad (2.5)$$

Using Eq. (2.4b) it can be shown that

$$ds_k = \frac{h^k}{H^m} \frac{\partial x_k}{\partial X_m} dS_m, \quad (2.6)$$

and thus

$$F_{km} = \frac{h^k}{H^m} \frac{\partial x_k}{\partial X_m}. \quad (2.7)$$

Substituting Eq. (2.6) into Eq. (2.2), the deformation tensor  $C_{ij}$  is now recovered as

$$C_{ij} = F_{ki} F_{kj}. \quad (2.8)$$

When this is substituted into the Green-Lagrange strain tensor Eq. (2.3) and expanded, the expression becomes

$$E_{ij} = \frac{1}{2} \left[ \frac{(h^k)^2}{H^i H^j} \frac{\partial x_k}{\partial X_i} \frac{\partial x_k}{\partial X_j} - \delta_{ij} \right]. \quad (2.9)$$

These are the equations for the Green-Lagrange strain tensor in terms of general curvilinear spatial coordinates, which are not field variables suitable for numerical solution. For this purpose, the spatial coordinates, and consequently the strain tensor, can be expressed in terms of the displacement field.

### Displacement Based Strain

In keeping with common displacement based finite element formulations, the strains are expressed as functions of the displacement field. To do so, appropriate displacement measures must be incorporated. In Cartesian formulations, this is straight forward since the scale factors are unity and are independent of location, and displacement. Within other coordinate systems, however, location dependent scale functions introduce some complexity, and it is at this point that most authors restrict their discussions to infinitesimal strain formulations. In this section a novel but simple definition of displacement is introduced which accommodates the nonlinear scale functions. However, the rationale for digressing from the traditional displacement definition is first presented.

Small displacement formulations in cylindrical coordinates (Zienkiewicz, 1977; Wilson, 1965; Spilker and Daugirda, 1981; Winnicki and Zienkiewicz, 1979) typically use physical<sup>1</sup> displacements as degrees of freedom. Assuming that the displacements are infinitesimally small relative to the size of the body suggests that the scale functions are independent of displacements, and a simple relationship between physical displacements and coordinate changes can be stated:

$$u_i = H^i(X_i - x_i) . \quad (2.10)$$

Appropriate substitution of these physical displacements into the small strain component of the strain tensor produces the relatively simple expressions for infinitesimal strains used in most cylindrical finite element formulations.

---

<sup>1</sup> Physical displacements are the actual or physical distances travelled by a particle of material initially located at the material coordinates such as  $\Delta r$ ,  $r\Delta\theta$  and  $\Delta z$  in cylindrical coordinates, assuming small displacements.

Incorporation of physical displacements into the complete Green-Lagrange strains is less obvious because it cannot be assumed that the scale functions are independent of the motion of the body. Consider, for example, displacement increments in the  $r$ - $\theta$  plane in a cylindrical coordinate system (Figure 2.2). The definition of displacement used in the small displacement formulation is retained, specifically

$$\Delta u_\theta = R\Delta\theta, \quad (2.11)$$

where  $R$  is the radial coordinate.

If the first increment is in the  $R$  direction, the physical displacement would simply be the distance moved in that direction. If this were followed by motion in the  $\theta$  direction, the displacement would be defined by Eq. (2.11), but clearly, the actual distance travelled by the position vector would be

$$\Delta u_\theta^{\text{physical}} = (R + u_r)\Delta\theta. \quad (2.12)$$

Thus, such a definition does not actually achieve its goal of describing a physical displacement. It might be possible to define a more meaningful physical displacement increment where the coordinate change is linear with some other variable such as time:

$$\Delta u_\theta = \int_{t_1}^{t_2 = t_1 + \Delta t} r(t)\theta(t)dt \quad (2.13)$$

$$r(t) = \frac{r_1(t_2 - t) + r_2(t - t_1)}{t_2 - t_1}$$

$$\theta(t) = \frac{\theta_1(t_2 - t) + \theta_2(t - t_1)}{t_2 - t_1}$$

This, however, makes substitution into the strain expressions quite onerous, not to mention development of the finite element matrix expressions. Furthermore, a physical displacement definition would make the spatial position vector path dependent. In other words, if the same displacement increments were made in a different order, the final location would also be different (for an example, see Figure 2.3). Other, less complicated approaches which approximate physical displacements are possible, but inconsistencies between total displacements and displacement increments remain, and such definitions introduce considerable complexity into the strain expressions.

The solution presented here to overcome these difficulties is to abandon the use of physical displacements, and instead use coordinate displacements as the field variables. Truesdell and Toupin(1960) used this approach to describe Lagrangian strains in general curvilinear coordinate systems, but it has not been extended to an incremental form suitable for implementation in a finite element. This definition eliminates the ambiguities in the relationships between physical displacements, defined displacements and displacement increments. It also enables sufficient simplification of the Green-Lagrange strains, expressed in terms of displacements, to develop a generalized incremental finite element formulation in orthogonal curvilinear coordinate systems. The displacements are defined simply as

$$u_i = x_i - X_i. \quad (2.14)$$

The deformation gradient tensor may now be expressed in terms of the displacement field as

$$\frac{\partial x_i}{\partial X_j} = \frac{\partial X_j}{\partial X_j} + \frac{\partial u_i}{\partial X_j}, \quad (2.15)$$

or

$$F_{ij} = \frac{h^i}{H^j} (\delta_{ij} + u_{i,j}). \quad (2.16)$$

Substituting for  $F_{ij}$  into Eq. (2.9), the Green-Lagrange strains can then be expressed strictly in terms of the displacement field and scale functions<sup>2</sup>:

$$E_{ij} = \frac{1}{2} \left\{ \left[ \frac{(h^k)^2}{H^i H^j} \delta_{ki} \delta_{kj} - \delta_{ij} \right] + \left[ \frac{(h^j)^2}{H^i H^j} u_{j,i} + \frac{(h^i)^2}{H^i H^j} u_{i,j} \right] + \left[ \frac{(h^k)^2}{H^i H^j} u_{k,j} u_{k,i} \right] \right\}, \quad (2.17)$$

or

---

<sup>2</sup> The spatial scale functions depend only on the displacement field, thus this expression for strain ultimately is a function of the displacement field alone.

$$E_{ij} = \frac{1}{2} \left\{ \left[ \frac{(h^j)^2}{H^i H^j} u_{j,i} + \frac{(h^i)^2}{H^i H^j} u_{i,j} + \frac{(h^k)^2}{H^i H^j} u_{k,i} u_{k,j} \right] + \left[ \frac{(h^k)^2}{H^i H^j} \delta_{kj} \delta_{ki} - \delta_{ij} \right] \right\}. \quad (2.18)$$

The terms are rearranged in the latter equation to group the displacement gradient components in the first term, and the pure scale factor components in the second term. The displacement gradient terms are similar to the usual expressions developed for Cartesian systems, however the pure scale function terms are less familiar. In a cylindrical coordinate system, for example, it is the scale function components which describe the  $\theta$  or hoop strains that develop when a cylinder experiences a pure radial displacement.

### 2.1.2. The Strain Increments

Since this study aims to develop an incremental formulation, it is required that the incremental strains be expressed in terms of the incremental displacement field. To accomplish this, the strains, displacements, and scale functions after an increment are written in terms of the values before the increment and the incremental values as

$$E_{ij,t+\Delta t} = E_{ij} + \Delta E_{ij}, \quad (2.19a)$$

$$u_{i,t+\Delta t} = u_i + \Delta u_i, \text{ and} \quad (2.19b)$$

$$h_{i,t+\Delta t}^i = h^i + \Delta h^i, \quad (2.19c)$$

where  $E_{ij}$ ,  $u_i$ , and  $h^i$  are, respectively, the strains, displacements and scale functions at time  $t$ , and the subscript  $t+\Delta t$  denotes the same quantity after the time increment. Using these expressions to write the Green - Lagrange strain tensor after the increment yields

$$E_{ij} + \Delta E_{ij} = \frac{1}{2H^i H^j} \left\{ (h^j + \Delta h^j)^2 (u_j + \Delta u_j)_{,i} + (h^i + \Delta h^i)^2 (u_i + \Delta u_i)_{,j} \right. \\ \left. + (h^k + \Delta h^k)^2 (u_k + \Delta u_k)_{,i} (u_k + \Delta u_k)_{,j} \right\} \\ + \frac{1}{2} \left\{ \frac{(h^k + \Delta h^k)^2}{H^i H^j} \delta_{kj} \delta_{ki} - \delta_{ij} \right\}. \quad (2.20)$$

Subtracting expression (2.18) from Eq. (2.20), the strain increment tensor,  $\Delta E_{ij}$ , is recovered. For convenience, it is split into parts corresponding to the order of displacement gradient increment:

$$\Delta E_{ij} = \Delta \varepsilon_{ij} + \Delta \varepsilon'_{ij} + \Delta \varepsilon''_{ij} + \Delta \varepsilon'''_{ij} + \Delta \varepsilon''''_{ij}, \quad (2.21)$$

in which

$$2H^iH^j\Delta\epsilon_{ij} = \{ (h^j)^2\Delta u_{j,i} + (h^i)^2\Delta u_{i,j} \} + (2h^k\Delta h^k\delta_{ki}\delta_{kj}), \quad (2.22a)$$

$$2H^iH^j\Delta\epsilon'_{ij} = \left\{ \begin{aligned} & (h^k)^2(u_{k,j}\Delta u_{k,i} + u_{k,i}\Delta u_{k,j}) \\ & + 2(h^j\Delta h^i u_{j,i} + h^i\Delta h^i u_{i,j} + h^k\Delta h^k u_{k,j} u_{k,i}) \end{aligned} \right\}, \quad (2.22b)$$

$$2H^iH^j\Delta\epsilon''_{ij} = \left\{ \begin{aligned} & (h^k)^2\Delta u_{k,j}\Delta u_{k,i} \\ & + (\Delta h^j)^2 u_{j,i} + (\Delta h^i)^2 u_{i,j} + (\Delta h^k)^2(u_{k,j}u_{k,i} + \delta_{kj}\delta_{ki}) \\ & + 2 \left[ \begin{aligned} & h^j\Delta h^j\Delta u_{j,i} + h^i\Delta h^i\Delta u_{i,j} \\ & + h^k\Delta h^k(u_{k,j}\Delta u_{k,i} + u_{k,i}\Delta u_{k,j}) \end{aligned} \right] \end{aligned} \right\}, \quad (2.22c)$$

$$2H^iH^j\Delta\epsilon'''_{ij} = \left\{ \begin{aligned} & 2h^k\Delta h^k\Delta u_{k,i}\Delta u_{k,j} \\ & + (\Delta h^i)^2\Delta u_{i,j} + (\Delta h^j)^2\Delta u_{j,i} \\ & + (\Delta h^k)^2(\Delta u_{k,i} + \Delta u_{k,j}) \end{aligned} \right\}, \text{ and} \quad (2.22d)$$

$$2H^iH^j\Delta\epsilon''''_{ij} = (\Delta h^k)^2\Delta u_{k,i}\Delta u_{k,j}. \quad (2.22e)$$

Note that  $\Delta\epsilon_{ij}$  is a first order strain component which does not depend on the displacement gradient,  $u_{i,j}$ , and corresponds to the infinitesimal strain. The second term,  $\Delta\epsilon'$ , is also a first order strain increment component, but is nonlinear because it depends on the displacement gradients at time  $t$ . The second order strain increment component,  $\Delta\epsilon''$ , is given in three parts; second order displacement gradient increments on the first line, second order scale function increments on second line, and mixed terms containing displacement gradient increments and scale function increments grouped together at the end of Eq. (2.22c). The remaining two terms,  $\Delta\epsilon'''$ , and  $\Delta\epsilon''''$ , are respectively third and fourth order strain increment components. The first and second order terms are used in the finite element formulations which follow in subsequent chapters. The higher order terms are ignored in the linearization of the equations, and in fact,  $\epsilon'''$  and  $\epsilon''''$  reduce to zero in Cartesian formulations.

It should be noted that  $\Delta\epsilon_{ij}$  is dependent on the displacement field because of the presence of  $h^i$ , and is thus not truly "infinitesimal". The terms are consistent, however, because the separation is done according to the order of the **displacement gradient** increment, not the displacement increment. The terms could have been separated according to the order of the displacement increment, however, the expressions would have been complicated unnecessarily by the separation of the spatial scale functions into



material scale functions and scale function displacements, producing many more terms. The only advantage to such an approach would be a complete separation of the true infinitesimal strain increment required for small displacement formulations. It can be shown, however, that Eq. (2.22a) also reduces to the usual infinitesimal form when the spatial scale functions are replaced by material scale functions, i.e.,  $h^i = H^i$ , providing a small displacement formulation when required.

### 2.1.3. Strain Increment Variation

Expressions for the differential strain increment variation are required in the virtual work expression that is used to develop the finite element equations, and which will be shown in Section 2.2. Although there are five components in the strain increment, linearizing assumptions are made which remove the highest order terms from consideration in the virtual work expression. The terms of the strain increment variation that will be required are limited to the first and second order terms of Eq. (2.21),  $\delta\Delta\epsilon$ ,  $\delta\Delta\epsilon'$ , and  $\delta\Delta\epsilon''$ . In the following, quantities prefixed with  $\delta$  denote variations.

Applying a differential variation to the displacement field, the first and second order strain component variations become

$$2H^iH^j\delta\Delta\epsilon_{ij} = (h^j)^2\delta\Delta u_{i,j} + (h^i)^2\delta\Delta u_{i,j} + 2h^k\delta\Delta h^k\delta_{kj}\delta_{ki}, \quad (2.23a)$$

$$2H^iH^j\delta\Delta\epsilon'_{ij} = \left\{ \begin{aligned} &(h^k)^2(u_{k,j}\delta\Delta u_{k,i} + u_{k,i}\delta\Delta u_{k,j}) \\ &+ 2(h^j\delta\Delta h^i u_{j,i} + h^i\delta\Delta h^i u_{i,j} + h^k\delta\Delta h^k u_{k,i}u_{k,j}) \end{aligned} \right\}, \text{ and} \quad (2.23b)$$

$$2H^iH^j\delta\Delta\epsilon''_{ij} = \left[ \begin{aligned} &(h^k)^2(\delta\Delta u_{k,j}\Delta u_{k,i} + \Delta u_{k,j}\delta\Delta u_{k,i}) \\ &+ 2\left\{ \begin{aligned} &\delta\Delta h^j\Delta h^i u_{j,i} + \delta\Delta h^i\Delta h^i u_{i,j} \\ &+ \delta\Delta h^k\Delta h^k(u_{k,j}u_{k,i} + \delta_{kj}\delta_{ki}) \end{aligned} \right\} \\ &+ 2\left\{ \begin{aligned} &h^j\Delta h^j\delta\Delta u_{j,i} + h^i\Delta h^i\delta\Delta u_{i,j} \\ &+ h^j\delta\Delta h^j\Delta u_{j,i} + h^i\delta\Delta h^i\Delta u_{i,j} \\ &+ h^k\Delta h^k(u_{k,j}\delta\Delta u_{k,i} + u_{k,i}\delta\Delta u_{k,j}) \\ &+ h^k\delta\Delta h^k(u_{k,j}\Delta u_{k,i} + u_{k,i}\Delta u_{k,j}) \end{aligned} \right\} \end{aligned} \right]. \quad (2.23c)$$

Each of the strain increment variations are presented in the same way as the strain increments were in Eq. (2.22), with deformation gradient increments first, scale function increments second, and in the second order expressions, mixed terms containing scale function increments and deformation gradient increments grouped together at the end.

#### 2.1.4. Total Strain Increment

The exact strain increment in terms of the displacement field increment would require the evaluation of all five strain increment components in Eq. (2.22). The number of terms makes this evaluation time consuming, and matrix forms of the higher order terms are difficult to produce. Instead, the total strains can be expressed in terms of the total displacements from Eq. (2.18), which may be expressed in matrix form relatively easily. Thus, the strain increment is more effectively evaluated by saving the strains at the start of the increment and subtracting them from strains calculated after the increment.

### 2.2. The Principle of Incremental Virtual Work

#### 2.2.1. Virtual Work Expression

The basic formulation for most structural finite element programs is based on the principle of virtual work:

$$\int_V \sigma_{ij} \delta \epsilon_{ij} dV = \int_\Gamma T_i \delta u_i d\Gamma + \int_V \rho F_i \delta u_i dV, \quad (2.24)$$

where  $\sigma_{ij}$  are the Cauchy stresses,  $\rho$  is the mass density,  $T_i$  are the surface tractions per unit area, and  $F$  is the body force per unit volume. All quantities are referred to the current (deformed) configuration.  $\delta \epsilon_{ij}$  and  $\delta u_i$  are respectively variations of the strains and displacements referred to spatial coordinates. Both terms must also be kinematically admissible.

The term on the left represents the variation in the strain energy integrated over the volume of the body in its deformed configuration. The first term on the right is the virtual work of the surface tractions integrated over the surface of the body, and the second term is the virtual work of body forces integrated over its volume.

The integral expression in Eq. (2.24) must be satisfied for equilibrium at each point in time during the incremental solution process. Thus, it is assumed that at time  $t$ , a solution exists which satisfies this condition within some desired degree of accuracy. Such a configuration is called the current converged configuration. The problem is to satisfy this equilibrium equation after an increment at time  $t + \Delta t$ , at which point the configuration is unknown. The approach taken is to use a known configuration for reference and transform the values in Eq. (2.24) to the reference configuration. This is

known as a Lagrangian (or material) formulation, because the original material points are used for reference. This is in contrast to an Eulerian formulation, which uses a stationary control volume. The choice of reference configurations is limited only by the number of converged solutions in the incremental solution process. However, in practice the reference configuration is taken to be either the initial or the latest converged configuration, and the respective formulations are referred to as **Total Lagrangian** and **Updated Lagrangian**. Kinematically, these formulations are identical, however, considerations such as constitutive modelling or the unique coordinate system formulation discussed here, may suggest one or the other as being more efficient for a particular modelling problem.

### 2.2.2. Total Lagrangian Formulation of Virtual Work Equation

The purpose of this work is to develop a formulation which models complex three dimensional behaviour, while taking advantage of the structure's geometric symmetry, relative to the particular coordinate system. This symmetry usually exists at the start of the solution, and is lost as the body undergoes three dimensional deformation. To utilize this symmetry suggests that the formulation should be referred to the initial configuration, and therefore a Total Lagrangian formulation would be most effective.

Expressing Eq. (2.24) in terms of the original configuration requires the use of appropriate stress and strain measures, and the transformation of the mass density to the original geometry. The second Piola-Kirchhoff stress tensor,  $S_{ij}$ , is used as the stress measure, and is defined<sup>3</sup> in terms of the Cauchy stress tensor,  $\sigma_{mn}$  as

$$S_{ij} = \frac{\rho_0}{\rho} \frac{\partial X_i}{\partial x_m} \sigma_{mn} \frac{\partial X_n}{\partial x_j}, \quad (2.25)$$

where  $\rho_0$  is the original mass density and  $\rho$  is the current mass density.

It can be shown (Bathe, 1982) that a variation in the small strain tensor is related to a variation in the Lagrange strain tensor by

---

<sup>3</sup> For simplicity, derivation of the Total Lagrangian formulation of the virtual work equation is done in a Cartesian coordinate system.

$$\delta E_{ij} = \frac{\partial x_m}{\partial X_i} \frac{\partial x_n}{\partial X_j} \delta \epsilon_{ij} . \quad (2.26)$$

The mass in the differential volume is conserved during the deformation, therefore,

$$\rho_0 dV_0 = \rho dV . \quad (2.27)$$

Combining Eqs. (2.25) and (2.26), it can be seen that:

$$\int_{V_0} S_{ij} \delta E_{ij} dV_0 = \int_{V_0} \frac{\rho_0}{\rho} \frac{\partial X_i}{\partial x_m} \frac{\partial X_j}{\partial x_n} \tau_{mn} \frac{\partial x_k}{\partial X_i} \frac{\partial x_l}{\partial X_j} \delta \epsilon_{kl} dV_0 . \quad (2.28)$$

Using Eq. (2.27) and the identity

$$\frac{\partial x_k}{\partial X_i} \frac{\partial X_l}{\partial x_m} = \delta_{km} ,$$

Eq. (2.28) reduces to

$$\int_{V_0} S_{ij} \delta E_{ij} dV_0 = \int_V \tau_{mn} \delta \epsilon_{mn} dV . \quad (2.29)$$

This shows conjugation of the second Piola - Kirchhoff stresses and Green - Lagrange strains because the volume integrated is arbitrary. Equation (2.29) can also be substituted directly into Eq. (2.24) to produce the Total Lagrangian formulation for the virtual work expression<sup>4</sup>:

$$\int_{V_0} S_{ij} \delta E_{ij} dV_0 = \int_{\Gamma} T_i \delta u_i d\Gamma + \int_{V_0} \rho_0 F_i \delta u_i dV_0 . \quad (2.30)$$

---

<sup>4</sup> In this form, the traction loads are assumed to be deformation dependent. If deformation independent loading can be assumed,  $\Gamma_0$  can be used in place of  $\Gamma$ . It is also assumed that the mass-body forces,  $F_i$  are not deformation dependent, which is adequate for most structural analysis.

The above development is of course well known, but is included for completeness.

### 2.2.3. Incremental Form of Virtual Work Equation

Equation (2.30) must be true for equilibrium to be satisfied at time  $t$ , and, with appropriate substitutions for  $E$ ,  $S$ ,  $T$ ,  $F$ , and  $u$ , after a time increment,  $\Delta t$ . In Eq. (2.19), the strains at time  $t + \Delta t$  are expressed in terms of the strains at time  $t$  and the incremental strain,  $\Delta E$ . Similar decompositions can be performed for  $S$ ,  $T$ ,  $F$ , and  $u$  and substituted into the virtual work equation producing

$$\begin{aligned} \int_{V_0} (S_{ij} + \Delta S_{ij}) \delta(E_{ij} + \Delta E_{ij}) dV_0 = & \int_{\Gamma} (T_i + \Delta T_i) \delta(u_i + \Delta u_i) d\Gamma \\ & + \int_{V_0} \rho_0 (F_i + \Delta F_i) \delta(u_i + \Delta u_i) dV_0. \end{aligned} \quad (2.31)$$

It is assumed that at time  $t$  the strain,  $E_{ij}$  and the displacement,  $u_i$  are known quantities. Hence, the variation in these quantities vanishes. Thus Eq. (2.31) reduces to

$$\int_{V_0} (S_{ij} + \Delta S_{ij}) \delta \Delta E_{ij} dV_0 = \int_{\Gamma} (T_i + \Delta T_i) \delta \Delta u_i d\Gamma + \int_{V_0} \rho_0 (F_i + \Delta F_i) \delta \Delta u_i dV_0. \quad (2.32)$$

The constitutive tensor,  $C_{ijkl}$ , defining the relationship between the stress and strain tensors is linearized for the increment. However, nonlinear material response during a load step can be accommodated by equilibrium iterations:

$$\Delta S_{ij} = C_{ijkl} \Delta E_{kl}. \quad (2.33)$$

Substituting Eq. (2.33) into Eq. (2.32), the incremental virtual work equation becomes

$$\begin{aligned} \int_{V_0} \Delta E_{kl} C_{ijkl} \delta \Delta E_{ij} dV_0 + \int_{V_0} S_{ij} \delta \Delta E_{ij} dV_0 = & \int_{\Gamma} (T_i + \Delta T_i) \delta \Delta u_i d\Gamma \\ & + \int_{V_0} \rho_0 (F_i + \Delta F_i) \delta \Delta u_i dV_0. \end{aligned} \quad (2.34)$$

Now, the expressions for the strain increments (2.22) and the strain increment variations (2.23) can be substituted for  $\Delta E$  and  $\delta \Delta E$ . The virtual work expression is next

linearized by neglecting the terms involving products of  $\delta\Delta u$ . Rearranging and placing the stiffness terms on the left and load terms on the right gives

$$\begin{aligned} \int_{V_0} \delta(\Delta\epsilon_{ij} + \Delta\epsilon'_{ij}) C_{ijkl} (\Delta\epsilon_{kl} + \Delta\epsilon'_{kl}) dV_0 + \int_{V_0} S_{ij} \delta \Delta\epsilon''_{ij} dV_0 = \\ \int_{\Gamma} (T_i + \Delta T_i) \delta\Delta u_i d\Gamma + \int_{V_0} \rho_0 (F_i + \Delta F_i) \delta\Delta u_i dV_0 - \int_{V_0} S_{ij} \delta(\Delta\epsilon_{ij} + \Delta\epsilon'_{ij}) dV_0 . \end{aligned} \quad (2.35)$$

Equation (2.35) is the same as that presented for a Total Lagrangian formulation by Bathe et al., 1975. Expressing the strain increments and variations in matrix form as functions of the displacement field is, however, considerably more involved because of the additional terms introduced by the nonlinear scale functions.

## 2.3. Finite Element Equations

### 2.3.1. Linear Stiffness Matrix

The first term in Eq. (2.35) will produce the incremental linear stiffness matrix when the set of linearized incremental equilibrium equations is recovered. The first order strain increments can be expressed in terms of the displacement increments in matrix form as

$$\{\Delta\epsilon\} = [b]\{\Delta u\} , \text{ and} \quad (2.36a)$$

$$\{\Delta\epsilon'\} = [b']\{\Delta u\} , \quad (2.36b)$$

where  $[b]$  is the linear differential operator matrix,  $[b']$  is the differential operator matrix for large rotations,  $\{\Delta\epsilon\}$  is a vector of small strain components,  $\{\Delta\epsilon'\}$  is a vector of large rotation strain components, and  $\{\Delta u\}$  is a vector of displacement field component functions.

The differential operator matrices,  $[b]$  and  $[b']$ , each have a component which is simply a scaled version of those in the description by Bathe, 1982, and represents the first terms of Eqs. (2.22a) and (2.22b). The second terms in those equations are scale function increments that are not seen in other Total Lagrangian formulations because they resolve to zero in a Cartesian formulation. The differential operator matrices can be symbolically rewritten to show these components separately:

$$[b] = [d] + [h] , \text{ and} \quad (2.37a)$$

$$[b'] = [d'] + [h'] , \quad (2.37b)$$

where  $[d]$  is the small displacement gradient component of  $[b]$ ,  $[h]$  is the small displacement scale function component of  $[b]$ ,  $[d']$  is the large rotation displacement gradient component of  $[b']$ , and  $[h']$  is the large rotation scale function component of  $[b']$ .

Substituting Eqs. (2.36) into the first term of Eq. (2.35),

$$\int_{V_0} \delta(\Delta \varepsilon_{ij} + \Delta \varepsilon'_{ij}) C_{ijkl} (\Delta \varepsilon_{kl} + \Delta \varepsilon'_{kl}) dV_0 = \int_{V_0} \{\delta \Delta u\}^t [b + b']^t [C] [b + b'] \{\Delta u\} dV_0 . \quad (2.38)$$

When interpolation functions are introduced in subsequent sections, this integral equation becomes the linear stiffness matrix for the element.

### 2.3.2. Geometric or Nonlinear Stiffness Matrix

The second term in Eq. (2.35) represents the second order strain stiffness, usually referred to as the geometric or nonlinear stiffness matrix. The second order component of the strain increment, Eq. (2.22c), can be decomposed further into subcomponents, in the same manner that  $\Delta \varepsilon$  and  $\Delta \varepsilon'$  were decomposed in the previous section, however, because second order terms are involved, three subcomponents are involved; second order displacement gradient components, second order scale function components, and cross terms including products of first order displacement gradient and first order scale function components. These three sets of strain increment variation can be seen in the grouping of terms in Eq. (2.23c). Again, the first subcomponent is simply a scaled version of a conventional Cartesian formulation. The other terms are quite complex. However, in a specific coordinate system, only one or two scale functions depend on the displacement field, and many of the terms drop out.

A similar approach to that taken for the linear stiffness matrix is adopted here so that those components similar to conventional formulations can be illustrated distinctly. The usual approach is to express the second term on the left side of Eq. (2.35) in matrix form in terms of the displacement field:

$$\int_{V_0} S_{ij} \delta \Delta \varepsilon''_{ij} dV_0 = \int_{V_0} \{\delta \Delta u\}^t [b_G]^t [S] [b_G] \{\Delta u\} dV_0 . \quad (2.39)$$

In conventional Cartesian formulations, the matrix  $[S]$  is simply a matrix containing the stress tensor components, and  $[b_G]$  is a matrix of differential operators, both arranged in such a way that a product equivalent to the tensor form on the left side of the equation is produced (for example see Bathe, 1982). In the general formulation, the same  $[S]$  matrix can be used, however, because there are three groups of components in the second order strain variation, the geometric stiffness matrix function must be decomposed into three parts:

$$\begin{aligned} \int_{V_0} S_{ij} \delta \Delta \epsilon_{ij}'' dV_0 = & \int_{V_0} \{\delta \Delta u\}^T [b_G^D]^T [S] [b_G^D] \{\Delta u\} dV_0 \\ & + \int_{V_0} \{\delta \Delta u\}^T [b_G^H]^T [S] [b_G^H] \{\Delta u\} dV_0 \\ & + \int_{V_0} \{\delta \Delta u\}^T [b_G^{DH}]^T [S] [b_G^{DH}] \{\Delta u\} dV_0, \end{aligned} \quad (2.40)$$

where  $[b_G^D]$  is a matrix of differential operators arranged to produce the dot product of  $S_{ij}$  with the displacement gradient components of Eq. (2.23c). Similarly,  $[b_G^H]$  produces the dot product with the pure scale function components which are expressed in terms of the displacement increments, and  $[b_G^{DH}]$  gives the dot product with the cross-term components.

### 2.3.3. Loads

The terms on the right hand side of Eq. (2.35) represent the load terms of the virtual work equation. The surface traction and body force components can be expressed directly in terms of the incremental displacement field. Using Eq. (2.36), the equivalent internal stress loads can also be expressed in terms of the displacement increment field. In matrix form, the load terms are then

$$\int_{\Gamma} (T_i + \Delta T_i) \delta \Delta u_i d\Gamma = \int_{\Gamma} \langle \delta \Delta u \rangle^T (T + \Delta T) d\Gamma, \quad (2.41a)$$

$$\int_{V_0} \rho_0 (F_i + \Delta F_i) \delta \Delta u_i dV_0 = \int_{V_0} \langle \delta \Delta u \rangle^T (F + \Delta F) \rho_0 dV_0, \text{ and} \quad (2.41b)$$

$$\int_{V_0} S_{ij} \delta (\Delta \epsilon_{ij} + \Delta \epsilon_{ij}') dV_0 = \int_{V_0} \langle \delta \Delta u \rangle^T [b + b']^T [S] dV_0. \quad (2.41c)$$



### 2.3.4. Finite Element Form of Incremental Virtual Work

All of the terms in Eq. (2.35) have been expressed in matrix form in terms of the displacement field increment. The usual finite element procedure of discretizing the body is now applied, whereby the body is divided into elemental volumes. The virtual work equation is integrated on an element by element basis and summed to give the total virtual work on the body. The displacement field within an element is interpolated using displacement degrees of freedom at nodal locations on the body:

$$\{u\} = [N]\{u\}^N, \quad (2.42a)$$

$$\{\Delta u\} = [N]\{\Delta u\}^N, \text{ and} \quad (2.42b)$$

$$\{\delta \Delta u\} = [N]\{\delta \Delta u\}^N. \quad (2.42c)$$

where  $[N]$  is a matrix of interpolation functions, and  $\{u\}^N$ ,  $\{\Delta u\}^N$  are vectors containing nodal displacements and nodal displacement increments for the element.

When Eqs. (2.38), (2.40), and (2.41) are substituted into (2.35), and noting that the variation in the nodal displacement increments is arbitrary, the final system of incremental finite element equations is produced:

$$\begin{aligned} \sum_{n=1}^{nel} \left[ \int_{V_0} [N]^t [b + b'] [C] [b + b'] [N] dV_0 + \int_{V_0} [N]^t [b_G]' [S] [b_G] [N] dV_0 \right] \{\Delta u\}^N = \\ \sum_{n=1}^{nel} \left\{ \int_{\Gamma} (T_i + \Delta T_i)' [N] d\Gamma \right\} + \sum_{n=1}^{nel} \left\{ \int_{V_0} \rho_0 (F_i + \Delta F_i) [N] dV_0 \right\} \\ - \sum_{n=1}^{nel} \left\{ \int_{V_0} \{S\}' [b + b'] [N] dV_0 \right\}. \end{aligned} \quad (2.43)$$

The differential operator matrices are combined with the interpolation function matrix for efficiency:

$$[B] = [b][N], \quad (2.44a)$$

$$[B'] = [b'] [N] , \quad (2.44b)$$

$$[B_G] = [b_G] [N] . \quad (2.44c)$$

and so on. The system of equations is then expressed as

$$[[K_L] + [K_G]] \{\Delta u\}^N = \{\Delta R\} , \quad (2.45)$$

where  $[K_L]$  is the linear stiffness matrix.  $[K_G]$  is the geometric stiffness matrix which was shown as one term in Eq. (2.43), but is actually integrated in three parts;  $[B_G^D]^T [S] [B_G^D]$ ,  $[B_G^H]^T [S] [B_G^H]$ , and  $[B_G^{DH}]^T [S] [B_G^{DH}]$ . The three parts of  $[K_G]$  correspond respectively to the displacement gradient, pure scale function, and mixed term components of the second order strain variation found in Eq. (2.23c). Finally  $\{\Delta R\}$  is a vector of the total incremental unbalanced loads for the element.

The element stiffness and incremental unbalanced loads are assembled in the manner of the direct stiffness technique to produce the system of equations for the entire structure, which must be solved iteratively for the displacements using a nonlinear solution strategy.

## 2.4. Chapter Summary

The general Total Lagrangian formulation of the virtual work equation was developed for general orthogonal curvilinear coordinate systems. The equations are used in the following two chapters to produce cylindrical isoparametric elements using both cylindrical and Cartesian formulations, including detailed descriptions of the matrices which were introduced symbolically in this chapter. Although any of the common solution techniques for nonlinear systems of equations may be employed to solve the finite element equations which are generated, subsequent chapters demonstrate the power of the formulation when it is combined with the constant arc-length solution strategy (Crisfield, 1980 and Ramm, 1981).

**Table 2.1      Coordinates and Scale Factors for Common Reference Systems**

Cartesian Coordinates		Cylindrical Coordinates		Spherical Coordinates	
$X_i$	$H^i$	$X_i$	$H^i$	$X_i$	$H^i$
X	1	R	1	R	1
Y	1	$\theta$	R	$\theta$	$R \cos(\phi)$
Z	1	Z	1	$\phi$	R

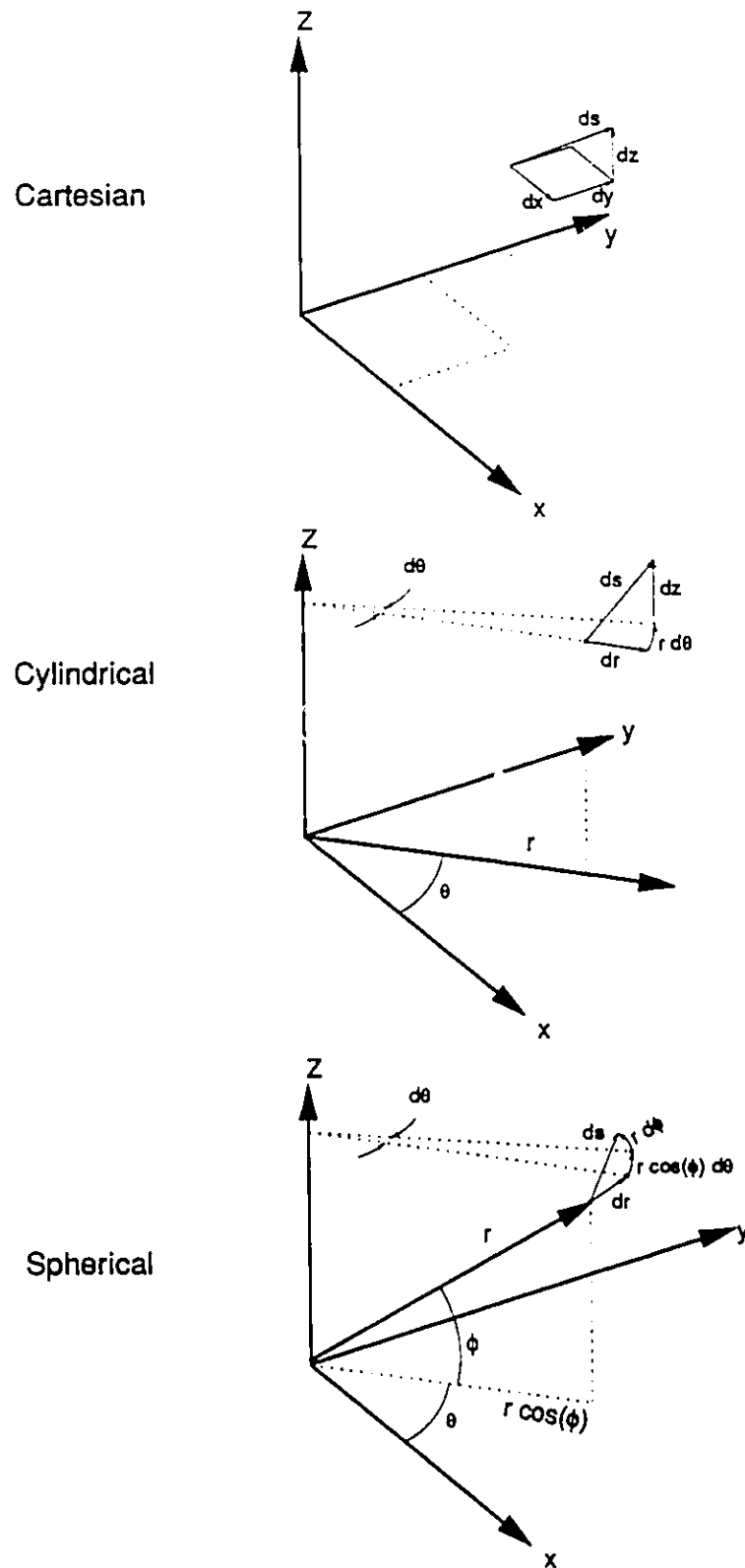


Figure 2.1 Common orthogonal coordinate systems

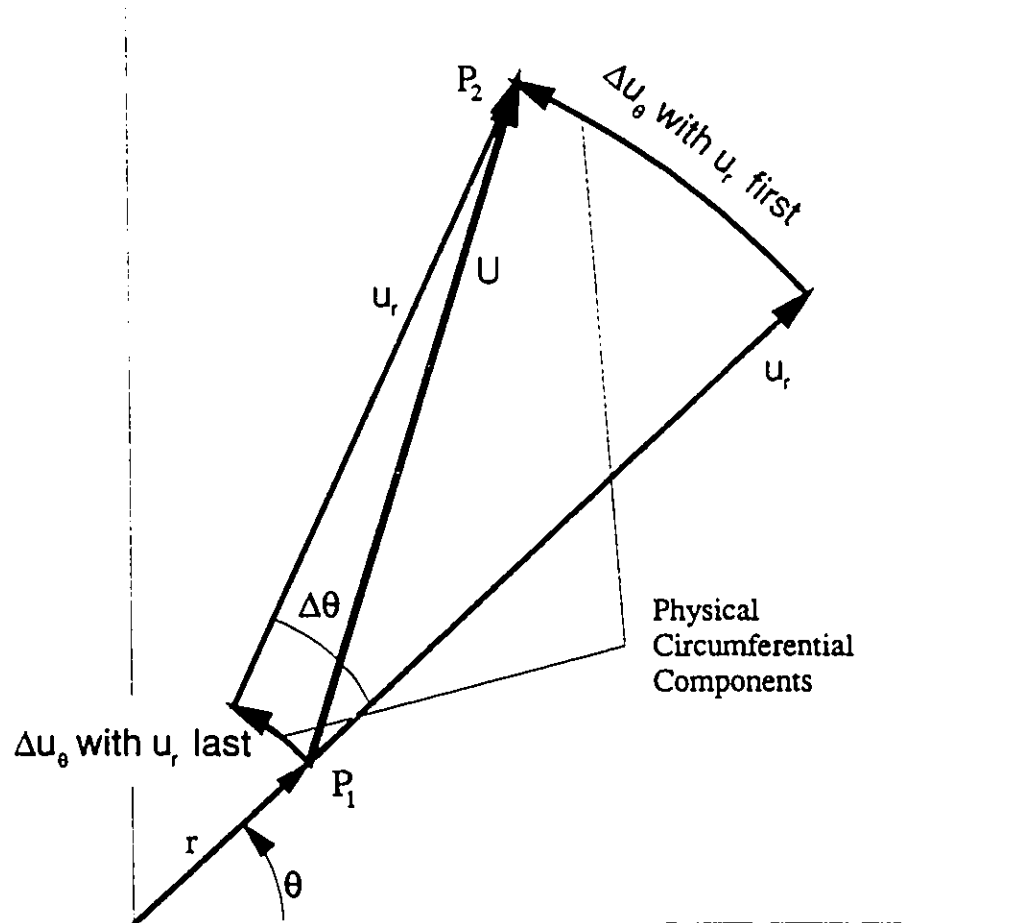


Figure 2.2 Displacement increments in cylindrical coordinates

	Path A		Path B	
	$u_r$	$u_\theta$	$u_r$	$u_\theta$
Increment 1	0	1	1	0
Increment 2	2	0	0	2

Two paths with identical displacement increments, executed in reverse order. The final position depends on the order in which the increments are executed.

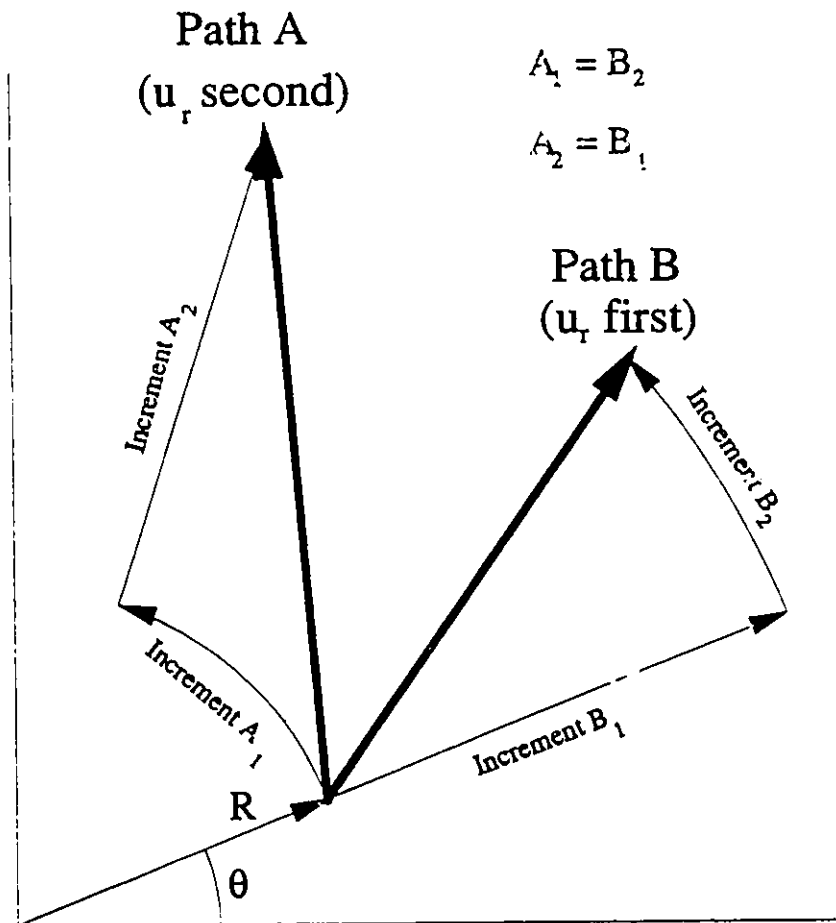


Figure 2.3 Path dependence of physical displacements in cylindrical coordinates

### 3. Cylindrical Formulation

#### 3.1. Overview

In the preceding chapter, a basic Lagrangian formulation in general orthogonal curvilinear coordinates was developed. The geometry of an initially axisymmetric element is best described in terms of an axisymmetric coordinate system (Figure 3.1). In this chapter, the incremental Total Lagrangian formulation of the finite element equations are developed for such an element in terms of the cylindrical coordinate system. All components of the equations are referenced in terms of this coordinate system including geometry, displacements, strains and stresses. The displacement field is described using the usual polynomial interpolation functions in the axisymmetric plane, and Fourier decomposition is used to represent the circumferential variation in the displacement field. Additionally, integration techniques for the finite element equations are developed, and the implications of boundary conditions in the framework of Fourier decomposition are discussed.

Problems with this cylindrical formulation arise because the element displacement field in cylindrical coordinates cannot exactly model all rigid body modes with a finite number of harmonics. Consequently, only a modest amount of motion can be accurately modelled with this formulation. Because of this deficiency, the Cartesian formulation which is discussed in the subsequent chapter was developed so that arbitrarily large displacements could be modelled. It may be possible to define an element displacement field in cylindrical coordinates which can model rigid body modes with one or two harmonics, but such pursuits will be left for future studies. The cylindrical formulation is therefore given here to show how the general curvilinear formulation presented in the preceding chapter is applied in a cylindrical coordinate system.

#### 3.2. Displacement Field

The cylindrical system uses coordinates defined by the radius,  $r$ , the angle about the longitudinal axis,  $\theta$ , and the location along the longitudinal axis,  $z$ . The scale factors for these coordinates are respectively 1,  $r$ , and 1 (Table 2.1). Coordinate displacements were shown to be more appropriate for large displacement formulations (Chapter 2). Thus, the displacements are defined to be

$$u_r = r - R, \quad (3.1a)$$

$$u_\theta = \theta - \Theta, \text{ and} \quad (3.1b)$$

$$u_z = z - Z, \quad (3.1c)$$

in which  $R$ ,  $\Theta$ , and  $Z$  are the undeformed (original) position vector component values for the cylindrical coordinate system.

The incremental displacements are required, and since the scale functions depend on the displacement field, incremental scale functions are also required. In the cylindrical reference system, only the  $\theta$  scale function varies, thus the incremental values required are  $\Delta u_r$ ,  $\Delta u_\theta$ ,  $\Delta u_z$  and  $\Delta h^\theta$ , in which  $\Delta h^\theta = \Delta u_r$  and  $\Delta h^r = \Delta h^z = 0$ . Note that the circumferential scale function is a linear function of the displacement field<sup>5</sup>. Thus the incremental equations can be expressed in terms of displacement field increment using displacement increment components as the degrees of freedom; additional degrees of freedom are not required for the scale functions.

### 3.2.1. Fourier Decomposition of Circumferential (Out-of-Plane) Displacement

The three dimensional displacement field is decomposed into a Fourier series of two dimensional functions. Using indicial notation

$$u_i = \sum_{f=1}^{\infty} u_{ic}^f(R,Z) \cos(f\Theta) + \sum_{f=1}^{\infty} u_{is}^f(R,Z) \sin(f\Theta), \quad i = r, \theta, z, \quad (3.2)$$

where  $u_{ic}^f$  and  $u_{is}^f$  are respectively the amplitude functions for the cosine and sine Fourier terms. These harmonic amplitude functions are field variables, and while there are an infinite number in the general displacement field description, for some (usually linear) problems all but a few Fourier amplitudes reduce to zero. Many other displacement fields are accurately described by the first several harmonic terms, reducing the problem to the solution of a few Fourier terms.

---

<sup>5</sup> This is a special case for cylindrical reference systems, and does not apply to spherical reference systems. In such circumstances, it would be necessary to linearize the scale function increment in terms of the incremental displacement field to formulate the finite element equations.



Spatial derivatives of the displacement field are required, and follow easily from the series expansion. The harmonic amplitude functions are independent of  $\Theta$ , thus differentiating term by term with respect to  $\Theta$ , the derivative becomes

$$\frac{\partial u_i}{\partial \Theta} = \sum_{f=0}^{\infty} -f u_{ic}^f(R,Z) \sin(f\Theta) + \sum_{f=1}^{\infty} f u_{ia}^f(R,Z) \cos(f\Theta), \quad i = r, \theta, z. \quad (3.3)$$

### 3.2.2. Polynomial In-Plane Interpolation with Parametric Transformation

Each of the harmonic amplitudes are functions in the two dimensional Cartesian R-Z plane. The usual approach to interpolating field variables in Cartesian space is to assume a polynomial distribution. Classically, the field variables (usually displacement components) at discrete (nodal) locations in the element are defined as the degrees of freedom for the element and the field in the element interior is defined in terms of the nodal values using polynomial interpolation functions. For example, the field variable  $\Phi$  is interpolated in terms of the nodal values  $\Phi^p$  as

$$\Phi(\xi, \mu, \zeta) = \sum_{p=1}^{NP} P_p(\xi, \mu, \zeta) \Phi^p, \quad (3.4)$$

where NP is the number of interpolation functions (and thus the number of nodes),  $P_p$  are the interpolation functions, and  $\xi, \mu$ , and  $\zeta$  are coordinates in a local system which can be transformed to global Cartesian coordinates by a transformation function. Zienkiewicz(1977), provides a good discussion of field variable and spatial derivative transformations from local to global coordinate systems, and a more detailed discussion is also included later in this section.

Since the displacement in the circumferential direction is handled by Fourier decomposition, the displacement amplitudes only require two dimensional interpolation:

$$u_{ic}^f = \sum_{p=1}^{NP} P_p(\xi, \mu) u_{ic}^{pf}, \text{ and} \quad (3.5a)$$

$$u_{ia}^f = \sum_{p=1}^{NP} P_p(\xi, \mu) u_{ia}^{pf}. \quad (3.5b)$$

The variables  $u_{ic}^{pf}$  and  $u_{is}^{pf}$  are the nodal values of displacement field amplitudes for cosine and sine harmonics respectively.

Spatial derivatives of the displacement field with respect to R and Z depend directly upon the spatial derivatives of the harmonic displacement field variables. The nodal values are discrete values, thus the spatial derivatives are easily produced:

$$\frac{\partial u_{ic}^f}{\partial R} = \sum_{p=1}^{NP} \frac{\partial P_p}{\partial R} u_{ic}^{pf} \quad (3.6)$$

The derivative of  $u_{ic}^f$  with respect to Z has the same form, as do the derivatives of  $u_{is}^f$ . In the parametric formulation, the interpolation functions are in terms of the local coordinates  $\xi$  and  $\mu$ . However, transformation of the derivatives from local  $\xi$ - $\mu$  to global R-Z coordinates will be shown subsequently.

### 3.2.3. Combined Interpolation

The element displacement field has now been decomposed into nodal harmonic degrees of freedom,  $u_{ic}^{pf}$  and  $u_{is}^{pf}$ . To summarize, the subscript (i) represents the displacement component r,  $\theta$ , or z ; subscripts (c) and (s) respectively denote cosine and sine terms of the Fourier series; superscript (p) represents the polynomial interpolation number, or node number; and superscript (f) denotes the harmonic number. The complexity of the element is evident in the number of nodal degrees of freedom. Where traditional three dimensional formulations for solid elements use three degrees of freedom per node, the Fourier element has six degrees of freedom per harmonic at each node. However, an axisymmetric model requires far fewer nodal points than a full three dimensional model, and in most cases, conditions of symmetry will reduce the number of degrees of freedom to three per harmonic.

Combining Eq. (3.2) and Eq. (3.5), and expanding for each displacement component produces the following expressions for the element displacement field:

$$u_i = \sum_{p=1}^{NP} \sum_{f=0}^{NF} (N_c^{pf} u_{ic}^{pf} + N_s^{pf} u_{is}^{pf}) , \quad (3.7)$$

in which

$$N_c^{pf} = P_p(r,s) \cos(f\Theta) , \text{ and} \quad (3.8a)$$

$$N_s^{pf} = P_p(r,s) \sin(f\Theta) . \quad (3.8b)$$

The functions  $N_c^{pf}$  and  $N_s^{pf}$  are interpolation functions for node p, harmonic f, with subscripts c and s representing cosine and sine functions respectively.

Equations (3.3) and (3.6) are used to produce the unscaled displacement gradients. The derivatives of the interpolation functions are

$$\frac{\partial N_c^{pf}}{\partial R} = \frac{\partial P_p}{\partial R} \cos(f\Theta) , \quad (3.9a)$$

$$\frac{\partial N_s^{pf}}{\partial R} = \frac{\partial P_p}{\partial R} \sin(f\Theta) , \quad (3.9b)$$

$$\frac{\partial N_c^{pf}}{\partial Z} = \frac{\partial P_p}{\partial Z} \cos(f\Theta) , \quad (3.9c)$$

$$\frac{\partial N_s^{pf}}{\partial Z} = \frac{\partial P_p}{\partial Z} \sin(f\Theta) , \quad (3.9d)$$

$$\frac{\partial N_c^{pf}}{\partial \Theta} = -f P_p \sin(f\Theta) , \text{ and} \quad (3.9e)$$

$$\frac{\partial N_s^{pf}}{\partial \Theta} = f P_p \cos(f\Theta) . \quad (3.9f)$$

The interpolation function derivatives are used in the unscaled displacement gradients, which are produced by differentiating Eq. (3.7):

$$\frac{\partial u_i}{\partial X_j} = \sum_{p=1}^{NP} \sum_{f=0}^{NF} \left[ \frac{\partial N_c^{pf}}{\partial X_j} u_{ic}^{pf} + \frac{\partial N_s^{pf}}{\partial X_j} u_{is}^{pf} \right] . \quad (3.10)$$

The unscaled displacement gradient increments are produced simply by replacing  $u_{ic}^{pf}$  with  $\Delta u_{ic}^{pf}$ , and  $u_{is}^{pf}$  with  $\Delta u_{is}^{pf}$ .

### 3.2.4. Vector Notation for the Interpolation Functions

With the displacement field defined in terms of nodal degrees of freedom, it is necessary to arrange the degrees of freedom in a consistent manner so that the displacement field and displacement gradients can be expressed in matrix form. The usual approach is to define a nodal numbering sequence and assign the degrees of freedom accordingly. The Fourier decomposition approach to defining the displacement field imposes an additional level of complexity due to the number of degrees of freedom which are assigned to each node.

In linear formulations such as that by Wilson(1965) the orthogonal properties of the Fourier functions decouple the harmonic stiffnesses, and it is most efficient to group together the degrees of freedom for each harmonic to produce sets of uncoupled equations which may be solved separately:

$$\begin{bmatrix} [K^0] & & 0 \\ & [K^1] & \\ 0 & & \ddots \\ & & [K^{NF}] \end{bmatrix} \begin{Bmatrix} \{U^0\} \\ \{U^1\} \\ \vdots \\ \{U^{NF}\} \end{Bmatrix} = \begin{Bmatrix} \{F^0\} \\ \{F^1\} \\ \vdots \\ \{F^{NF}\} \end{Bmatrix}. \quad (3.11)$$

In this system of equations,  $[K^f]$ ,  $\{U^f\}$  and  $\{F^f\}$  represent the element stiffness, displacements amplitudes and loads for the  $f$ th harmonic. Both element and global matrices are partitioned this way to minimize computer storage requirement.

The harmonics become coupled in the nonlinear incremental formulation because the strain-displacement relationship includes higher order harmonic products. However, to remain notationally consistent with other authors, the element stiffness matrix will be arranged into harmonic parts.

The displacement amplitudes are arranged first by Fourier number, then according to node number, and the six degrees of freedom are arranged for each node with symmetric degrees of freedom first, antisymmetric degrees of freedom last. In this application, symmetric degrees of freedom are defined as those which model behaviour which is symmetric about the plane  $\Theta = 0$ , which include the cosine terms for  $u_r$  and  $u_z$ , and sine terms for  $u_\theta$ . The remaining degrees of freedom describe behaviour which is antisymmetric about the same plane. The element displacement vector is then

$$\{U\} = \left\{ \begin{array}{c} \{U^1\} \\ \{U^2\} \\ \vdots \\ \{U^f\} \\ \vdots \\ \{U^{NF}\} \end{array} \right\}, \text{ where} \quad (3.12a)$$

$$\{U^f\} = \left\{ \begin{array}{c} \{U^{1f}\} \\ \{U^{2f}\} \\ \vdots \\ \{U^{pf}\} \\ \vdots \\ \{U^{Npf}\} \end{array} \right\}, \text{ and} \quad (3.12b)$$

$$\{U^{pf}\} = \left\{ \begin{array}{c} u_{rc}^{pf} \\ u_{\theta s}^{pf} \\ u_{zc}^{pf} \\ u_{rs}^{pf} \\ u_{\theta c}^{pf} \\ u_{zs}^{pf} \end{array} \right\}. \quad (3.12c)$$

The arrangement of nodal degrees of freedom is thus defined. The displacement field is next interpolated in terms of the nodal values as

$$\{u_i(R, \Theta, Z)\} = [N(R, \Theta, Z)] \{U\}, \quad (3.13)$$

in which the interpolation functions are defined in matrix form, and partitioned into nodal harmonic parts:

$$[N(R, \Theta, Z)] = \left[ [N^0] \ [N^2] \ \dots \ [N^f] \ \dots \ [N^{NF}] \right], \text{ where} \quad (3.14a)$$

$$[N^f] = \left[ [N^{1f}] \ [N^{2f}] \ \dots \ [N^{pf}] \ \dots \ [N^{Npf}] \right], \text{ and} \quad (3.14b)$$

$$[N^{pf}] = \begin{bmatrix} N_c^{pf} & 0 & 0 & N_s^{pf} & 0 & 0 \\ 0 & N_s^{pf} & 0 & 0 & N_c^{pf} & 0 \\ 0 & 0 & N_c^{pf} & 0 & 0 & N_s^{pf} \end{bmatrix}. \quad (3.14c)$$

Thus, the first three columns of  $[N^p]$  contain the symmetric interpolation functions, while the antisymmetric interpolation functions are in the last three columns.

The spatial derivatives of the displacement fields are written as

$$\langle D_u \rangle = \left\langle \frac{\partial u_r}{\partial R} \frac{\partial u_r}{\partial \Theta} \frac{\partial u_r}{\partial Z} \frac{\partial u_\theta}{\partial R} \frac{\partial u_\theta}{\partial \Theta} \frac{\partial u_\theta}{\partial Z} \frac{\partial u_z}{\partial R} \frac{\partial u_z}{\partial \Theta} \frac{\partial u_z}{\partial Z} \right\rangle. \quad (3.15)$$

The derivatives vector may also be written in terms of nodal displacement amplitudes and interpolation function derivatives as indicated by Eq. (3.10) as

$$\{D_u\} = [N'_u] \{u\}, \quad (3.16)$$

in which the matrix of interpolation function derivatives,  $[N'_u]$ , is partitioned into nodal harmonics:

$$[N'_u(R, \Theta, Z)] = [N'_u{}^{0f}] [N'_u{}^{2f}] \dots [N'_u{}^{pf}] \dots [N'_u{}^{NFf}], \text{ where} \quad (3.17a)$$

$$[N'_u{}^{pf}] = [N'_u{}^{1pf}] [N'_u{}^{2pf}] \dots [N'_u{}^{ppf}] \dots [N'_u{}^{Nppf}], \text{ and} \quad (3.17b)$$

$$[N_u^{pf}] = \begin{bmatrix} \frac{\partial N_c^{pf}}{\partial R} & 0 & 0 & \frac{\partial N_s^{pf}}{\partial R} & 0 & 0 \\ \frac{\partial N_c^{pf}}{\partial \Theta} & 0 & 0 & \frac{\partial N_s^{pf}}{\partial \Theta} & 0 & 0 \\ \frac{\partial N_c^{pf}}{\partial Z} & 0 & 0 & \frac{\partial N_s^{pf}}{\partial Z} & 0 & 0 \\ 0 & \frac{\partial N_s^{pf}}{\partial R} & 0 & 0 & \frac{\partial N_c^{pf}}{\partial R} & 0 \\ 0 & \frac{\partial N_s^{pf}}{\partial \Theta} & 0 & 0 & \frac{\partial N_c^{pf}}{\partial \Theta} & 0 \\ 0 & \frac{\partial N_s^{pf}}{\partial Z} & 0 & 0 & \frac{\partial N_c^{pf}}{\partial Z} & 0 \\ 0 & 0 & \frac{\partial N_c^{pf}}{\partial R} & 0 & 0 & \frac{\partial N_s^{pf}}{\partial R} \\ 0 & 0 & \frac{\partial N_c^{pf}}{\partial \Theta} & 0 & 0 & \frac{\partial N_s^{pf}}{\partial \Theta} \\ 0 & 0 & \frac{\partial N_c^{pf}}{\partial Z} & 0 & 0 & \frac{\partial N_s^{pf}}{\partial Z} \end{bmatrix}. \quad (3.18)$$

The displacement and displacement gradients have now been expressed in terms of the interpolation functions and nodal harmonic displacement amplitudes. These expressions are used in the following sections to develop matrix forms of the strain equations, but first a more detailed discussion of the transformation functions for the parametric formulation is presented.

### 3.3. In Plane Isoparametric Coordinate Transformation

The geometry of the element is described in exactly the same way as conventional axisymmetric elements, and although the nodal degrees of freedom are harmonic displacement amplitudes, the same interpolation functions are used to interpolate these amplitudes in the axisymmetric plane. In the usual parametric transformations, the element geometry in global space is transformed to a simple geometry in some local space, a square for example (Figure 3.2). The transformation function between local and global space is performed by a polynomial function. Usually, the order of the polynomial function is the same as the displacement field function, utilizing the same interpolation functions, and the transformation is referred to as an isoparametric function.

Occasionally, the spatial transformation uses a lower order polynomial, producing a subparametric transformation. Conversely, a higher order spatial transformation would be used to produce superparametric elements.

Transforming the element geometry to a simpler geometry in a local coordinate system may appear to be an unnecessary complication. It does, however, provide two important advantages: it greatly simplifies the numerical integration of the element properties because the integration occurs over a simple geometric region; and since the geometry of the local element does not change, the interpolation functions need be evaluated only once, rather than for each element.

Isoparametric elements are usually the most convenient to implement, because separate interpolation functions are not required for displacements and geometry, and the structure of the system of equations is easier to manage since additional book-keeping is not required to assure correct assembly of the element stiffnesses. Because of these simplifications, this discussion will focus on isoparametric formulations. Although the geometric transformation will be of the same order as the displacement field, the order of the element will not be fixed.

In Eq. (3.4), the polynomial interpolation functions were introduced to describe the harmonic displacement amplitude field in terms of the nodal values. The same interpolation functions are used to transform the coordinates within the isoparametric element:

$$R(\xi, \mu) = \sum_{p=1}^{NP} P_p(\xi, \mu) R^p, \text{ and} \quad (3.19a)$$

$$Z(\xi, \mu) = \sum_{p=1}^{NP} P_p(\xi, \mu) Z^p, \quad (3.19b)$$

where  $R^p$  and  $Z^p$  are the coordinates of the element nodes. The matrix of derivatives of the global coordinate functions with respect to the local coordinates is referred to as the Jacobian matrix:



$$[J] = \begin{bmatrix} \frac{\partial R}{\partial \xi} & \frac{\partial Z}{\partial \xi} \\ \frac{\partial R}{\partial \mu} & \frac{\partial Z}{\partial \mu} \end{bmatrix} = \begin{bmatrix} \sum_{p=1}^{NP} \frac{\partial P_p}{\partial \xi} R^p & \sum_{p=1}^{NP} \frac{\partial P_p}{\partial \xi} Z^p \\ \sum_{p=1}^{NP} \frac{\partial P_p}{\partial \mu} R^p & \sum_{p=1}^{NP} \frac{\partial P_p}{\partial \mu} Z^p \end{bmatrix} \quad (3.20)$$

The Jacobian matrix represents the transformation of a differential operation from one coordinate system to another:

$$\begin{Bmatrix} \frac{\partial}{\partial \xi} \\ \frac{\partial}{\partial \mu} \end{Bmatrix} = [J] \begin{Bmatrix} \frac{\partial}{\partial R} \\ \frac{\partial}{\partial Z} \end{Bmatrix} \quad (3.21)$$

Conversely, the inverse of the Jacobian matrix will perform the reverse transformation:

$$\begin{Bmatrix} \frac{\partial}{\partial R} \\ \frac{\partial}{\partial Z} \end{Bmatrix} = [J]^{-1} \begin{Bmatrix} \frac{\partial}{\partial \xi} \\ \frac{\partial}{\partial \mu} \end{Bmatrix} \quad (3.22)$$

When Eqs. (3.6) and (3.10) were presented, it was noted that, although the interpolation functions were not functions of  $R$  and  $Z$ , derivatives with respect to these global coordinates were required to produce the displacement gradients. The Jacobian matrix provides the required transformation to the global system:

$$\begin{Bmatrix} \frac{\partial P^p}{\partial R} \\ \frac{\partial P^p}{\partial Z} \end{Bmatrix} = [J]^{-1} \begin{Bmatrix} \frac{\partial P^p}{\partial \xi} \\ \frac{\partial P^p}{\partial \mu} \end{Bmatrix} \quad (3.23)$$

### 3.4. The Strain Representation

In Chapter 2 the finite element form of the virtual work equation was developed in general terms. Differential operator matrices were defined symbolically in Eqs. (2.36) and (2.40) which, combined with the interpolation matrix  $[N]$ , form the basic

components of the stiffness matrix. In this section, the symbolic components of Eq. (2.43) are developed for the cylindrical coordinate system into a matrix form suitable for computer implementation.

### 3.4.1. The Small Strain Increment

The small strain increments were defined in Eq. (2.22a), which in matrix form became, according to Eqs. (2.36) and (2.37)

$$\{\Delta \epsilon\} = [b]\{\Delta u\} = [[d] + [h]]\{\Delta u\},$$

in which  $[d]$  is a differential operator matrix for the displacement gradient based component of  $\{\epsilon\}$ , and  $[h]$  is the scale factor based component. The complete matrix form of the small strain increments in cylindrical coordinates is

$$\begin{Bmatrix} \Delta \epsilon_r \\ \Delta \epsilon_\theta \\ \Delta \epsilon_z \\ 2\Delta \epsilon_{r\theta} \\ 2\Delta \epsilon_{\theta z} \\ 2\Delta \epsilon_{rz} \end{Bmatrix} = \begin{bmatrix} \frac{\partial}{\partial R} & 0 & 0 \\ 0 & \left(\frac{R+u_r}{R}\right)^2 \frac{\partial}{\partial \Theta} & 0 \\ 0 & 0 & \frac{\partial}{\partial Z} \\ \frac{1}{R} \frac{\partial}{\partial \Theta} & \frac{(R+u_r)^2}{R} \frac{\partial}{\partial R} & 0 \\ 0 & \frac{(R+u_r)^2}{R} \frac{\partial}{\partial Z} & \frac{1}{R} \frac{\partial}{\partial \Theta} \\ \frac{\partial}{\partial Z} & 0 & \frac{\partial}{\partial R} \end{bmatrix} + \begin{bmatrix} 0 & 0 & 0 \\ \frac{(R+u_r)}{R^2} & 0 & 0 \\ 0 & 0 & 0 \\ 0 & 0 & 0 \\ 0 & 0 & 0 \\ 0 & 0 & 0 \end{bmatrix} \begin{Bmatrix} \Delta u_r \\ \Delta u_\theta \\ \Delta u_z \end{Bmatrix} \quad (3.24)$$

where the first submatrix on the right hand side is the deformation gradient operator, and the second matrix represents the scale function component. Only six strain terms need be considered, since the strain tensor is symmetric. However, to include all of the strain energy of the shear strain components, the shear strains must be doubled as shown on the left hand side so that the matrix form of the virtual work equation is energetically equivalent to the tensor form.

Eq. (3.13) gives the displacement field in terms of the nodal degrees of freedom using the interpolation matrix. Substituting this into the equation above, and combining the differential operator matrix with the interpolation matrix, the strain vector is

expressed in terms of an element strain-displacement matrix,  $[B]$ , and the element displacement increment vector:

$$\{\Delta \epsilon\} = [B]\{\Delta U\}, \quad (3.25)$$

in which  $[B] = [b][N]$ .

Recalling from Eq. (3.14) that the interpolation matrix is partitioned into parts associated with nodal harmonic parts of the element displacement vector, it follows that the strain-displacement matrix can be partitioned in a similar manner:

$$[B] = [B^0][B^1] \dots [B^f] \dots [B^{N^f}], \quad (3.26a)$$

$$[B^f] = [B^{0f}][B^{1f}] \dots [B^{pf}] \dots [B^{N^pf}], \text{ and} \quad (3.26b)$$

$$[B^{pf}] = [B_s^{pf}][B_a^{pf}], \text{ where} \quad (3.26c)$$

$$[B_s^{pf}] = \begin{bmatrix} \frac{\partial N_c^{pf}}{\partial R} & 0 & 0 \\ \left(\frac{R+u_r}{R^2}\right) N_s^{pf} & \left(\frac{R+u_r}{R}\right)^2 \frac{\partial N_s^{pf}}{\partial \Theta} & 0 \\ 0 & 0 & \frac{\partial N_c^{pf}}{\partial Z} \\ \frac{1}{R} \frac{\partial N_c^{pf}}{\partial \Theta} & \frac{(R+u_r)^2}{R} \frac{\partial N_s^{pf}}{\partial R} & 0 \\ 0 & \frac{(R+u_r)^2}{R} \frac{\partial N_s^{pf}}{\partial Z} & \frac{\partial N_c^{pf}}{\partial \Theta} \\ \frac{1}{R} \frac{\partial N_c^{pf}}{\partial \Theta} & 0 & \frac{\partial N_c^{pf}}{\partial R} \end{bmatrix}. \quad (3.27)$$

The matrix  $[B^{pf}]$  is the strain-displacement matrix associated with node  $p$  and harmonic  $f$ , and is partitioned into symmetric and antisymmetric parts<sup>6</sup>. The symmetric part,  $[B_s^{pf}]$  is

---

<sup>6</sup> The terms symmetric and antisymmetric parts of the strain - displacement matrices refer to the parts which operate on the symmetric and antisymmetric degrees of freedom described in

shown in full, and the antisymmetric part,  $[B_s^{pf}]$  is the same, except that  $N_c^{pf}$  is replaced by  $N_s^{pf}$ , and vice versa. Thus the infinitesimal strains are essentially expressed as a sum of nodal harmonic components:

$$\{\Delta\epsilon\} = \sum_{f=1}^{NF} \sum_{p=1}^{NP} \{\delta\epsilon^{pf}\}, \text{ where} \quad (3.28a)$$

$$\{\delta\epsilon^{pf}\} = [B^{pf}]\{u^{pf}\} \quad (3.28b)$$

The vector  $\{\delta\epsilon^{pf}\}$  is the component of the linear strain tensor associated with the  $f$ th harmonic displacement amplitude at node  $p$  and  $\{u^{pf}\}$  is the nodal harmonic displacement vector.

### 3.4.2. The Nonlinear Strain Component Increment

The strain increment components that depend on the displacement gradients where defined in Eq. (2.22b), and include components of the displacement gradient tensor,  $D_{ij}$ . The displacement gradient tensor in cylindrical coordinates can be produced from the unscaled displacement gradients, given in vector form in Eq. (3.15), by including the scale factor components in the appropriate elements which is written in vector form as

---

Section 3.2.4. This should not be confused with the decomposition of square matrices into symmetric and antisymmetric components.

$$\{D\} = \begin{Bmatrix} D_{11} \\ D_{12} \\ D_{13} \\ D_{21} \\ D_{22} \\ D_{23} \\ D_{31} \\ D_{32} \\ D_{33} \end{Bmatrix} = \begin{Bmatrix} \frac{\partial u_r}{\partial R} \\ \frac{1}{R} \frac{\partial u_r}{\partial \Theta} \\ \frac{\partial u_r}{\partial Z} \\ (R+u_r) \frac{\partial u_\theta}{\partial R} \\ \frac{R+u_r}{R} \frac{\partial u_\theta}{\partial \Theta} \\ (R+u_r) \frac{\partial u_\theta}{\partial Z} \\ \frac{\partial u_z}{\partial R} \\ \frac{1}{R} \frac{\partial u_z}{\partial \Theta} \\ \frac{\partial u_z}{\partial Z} \end{Bmatrix} . \quad (3.29)$$

The displacement gradient matrix, expressed in terms of the nodal displacements and a scaled interpolation gradient matrix is

$$\{D\} = [N'] \{U\} . \quad (3.30)$$

where  $[N']$  is formed by scaling the rows of  $[N'_0]$  in Eq. (3.14) in the same manner that  $\{D_0\}$  is scaled to produce  $\{D\}$ .

The procedure to develop the small strain-displacement matrix also applies to the nonlinear strain-displacement matrix,  $[B']$ . The nodal harmonic part of  $[B]$  was shown to be similar in form to the small strain differential operator matrix, and the same is true for  $[B']$ , therefore, the intermediate steps to arriving at the nodal harmonic part are not shown, and the symmetric part,  $[B_i^{pf}]$ , is presented directly:

$$[B_i^{pf}] = [D_i^{pf}] + [H_i^{pf}] , \text{ where} \quad (3.31)$$

$$[D_s^{pf}] = \begin{bmatrix} D_{11} \frac{\partial N_c^{pf}}{\partial R} & D_{21}(R+u_r) \frac{\partial N_s^{pf}}{\partial R} & D_{31} \frac{\partial N_c^{pf}}{\partial R} \\ \frac{D_{12}}{R} \frac{\partial N_c^{pf}}{\partial \Theta} & D_{22} \frac{R+u_r}{R} \frac{\partial N_s^{pf}}{\partial \Theta} & \frac{D_{32}}{R} \frac{\partial N_c^{pf}}{\partial \Theta} \\ D_{13} \frac{\partial N_c^{pf}}{\partial Z} & D_{23}(R+u_r) \frac{\partial N_s^{pf}}{\partial Z} & D_{33} \frac{\partial N_c^{pf}}{\partial Z} \\ \left( D_{12} \frac{\partial N_c^{pf}}{\partial R} + D_{11} \frac{1}{R} \frac{\partial N_c^{pf}}{\partial \Theta} \right) & (R+u_r) \left( D_{22} \frac{\partial N_s^{pf}}{\partial R} + D_{21} \frac{1}{R} \frac{\partial N_s^{pf}}{\partial \Theta} \right) & \left( D_{32} \frac{\partial N_c^{pf}}{\partial R} + D_{31} \frac{1}{R} \frac{\partial N_c^{pf}}{\partial \Theta} \right) \\ \left( D_{13} \frac{1}{R} \frac{\partial N_c^{pf}}{\partial \Theta} + D_{12} \frac{\partial N_c^{pf}}{\partial Z} \right) & (R+u_r) \left( D_{23} \frac{1}{R} \frac{\partial N_s^{pf}}{\partial \Theta} + D_{22} \frac{\partial N_s^{pf}}{\partial Z} \right) & \left( D_{33} \frac{1}{R} \frac{\partial N_c^{pf}}{\partial \Theta} + D_{32} \frac{\partial N_c^{pf}}{\partial Z} \right) \\ \left( D_{11} \frac{\partial N_c^{pf}}{\partial Z} + D_{13} \frac{\partial N_c^{pf}}{\partial R} \right) & (R+u_r) \left( D_{21} \frac{\partial N_s^{pf}}{\partial Z} + D_{23} \frac{\partial N_s^{pf}}{\partial R} \right) & \left( D_{31} \frac{\partial N_c^{pf}}{\partial Z} + D_{33} \frac{\partial N_c^{pf}}{\partial R} \right) \end{bmatrix}, \quad (3.31a)$$

$$[H_s^{pf}] = \begin{bmatrix} \frac{(D_{21})^2}{(R+u_r)} N_c^{pf} & 0 & 0 \\ D_{22} \left( \frac{2}{R} + \frac{D_{22}}{(R+u_r)} \right) N_c^{pf} & 0 & 0 \\ \frac{(D_{23})^2}{(R+u_r)} N_c^{pf} & 0 & 0 \\ 2D_{21} \left( \frac{1}{R} + \frac{D_{22}}{(R+u_r)} \right) N_c^{pf} & 0 & 0 \\ 2D_{23} \left( \frac{1}{R} + \frac{D_{22}}{(R+u_r)} \right) N_c^{pf} & 0 & 0 \\ 2 \frac{D_{21} D_{23}}{(R+u_r)} N_c^{pf} & 0 & 0 \end{bmatrix}. \quad (3.31b)$$

### 3.5. The Linear Stiffness Matrix

The linear stiffness matrix is the integral over the element volume of the matrix expression  $[B_L]^T [C] [B_L]$ . The matrix  $[B_L]$  is the sum of  $[B]$  and  $[B']$  which were developed above. With the infinitesimal and deformation gradient strains defined in

terms of element nodal degrees of freedom, the element linear stiffness matrix can be evaluated and integrated using an appropriate numerical integration technique. Because the geometric stiffness matrix, which is discussed in the next section, must also be integrated numerically, the integration strategy will be addressed in a subsequent section of this chapter.

### 3.6. The Geometric or Nonlinear Stiffness Matrix

In Chapter 2 the geometric stiffness matrix was shown in Eq. (2.40) to be composed of three parts corresponding to the parts of the second order strain increment variation in Eqs. (2.23). All three parts include the stress matrix, arranged to produce a product equivalent to the tensor form of the virtual work equation:

$$[S] = \begin{bmatrix} [s] & [0] & [0] \\ [0] & [s] & [0] \\ [0] & [0] & [s] \end{bmatrix}, \quad [s] = \begin{bmatrix} S_{rr} & S_{r\theta} & S_{rz} \\ S_{\theta r} & S_{\theta\theta} & S_{\theta z} \\ S_{zr} & S_{z\theta} & S_{zz} \end{bmatrix} \quad (3.32)$$

The three displacement operator matrices which form the basis of the geometric stiffness matrix are also formulated in terms of the Fourier functions, just as the small strain differential operator matrix was, and the intermediate steps to arrive at the nonlinear strain-displacement matrix are again omitted. The nodal harmonic parts of each matrix are presented directly.

#### 3.6.1. The Displacement Gradient Part

The displacement gradient part of Eq. (2.23c) is the same as the geometric stiffness matrix for a three dimensional solid element (Bathe, 1982), except that the terms of the nonlinear strain-displacement matrix are replaced by equivalent scaled terms, in a fashion similar to that used for the interpolation gradient matrix in Eq. (3.29):

$$[B_{G_s}^{Dpf}] = \begin{bmatrix} \frac{\partial N_c^{pf}}{\partial R} & 0 & 0 \\ \frac{1}{R} \frac{\partial N_c^{pf}}{\partial \Theta} & 0 & 0 \\ \frac{\partial N_c^{pf}}{\partial Z} & 0 & 0 \\ 0 & (R+u_r) \frac{\partial N_s^{pf}}{\partial R} & 0 \\ 0 & \frac{(R+u_r)}{R} \frac{\partial N_s^{pf}}{\partial \Theta} & 0 \\ 0 & (R+u_r) \frac{\partial N_s^{pf}}{\partial Z} & 0 \\ 0 & 0 & \frac{\partial N_c^{pf}}{\partial R} \\ 0 & 0 & \frac{1}{R} \frac{\partial N_c^{pf}}{\partial \Theta} \\ 0 & 0 & \frac{\partial N_c^{pf}}{\partial Z} \end{bmatrix}. \quad (3.33)$$

As before,  $[B_{G_s}^{Dpf}]$  contains the terms for the symmetric harmonic displacement amplitudes, and the antisymmetric terms,  $[B_{G_s}^{Dpf}]$ , are formed by replacing  $N_c^{pf}$  with  $N_s^{pf}$ , and vice versa. The complete element matrix is assembled from these nodal harmonic parts just as the linear strain-displacement matrix was assembled in Eq. (3.26).

### 3.6.2. The Scale Function Part

The pure scale function terms of the second order strain variation were shown in Eq. (2.23c) to be

$$(\delta \Delta \varepsilon_{ij}'')^H = \frac{1}{H^i H^j} \left\{ \delta \Delta h^j \Delta h^i u_{j,i} + \delta \Delta h^i \Delta h^j u_{i,j} \right. \\ \left. + \delta \Delta h^k \Delta h^k (u_{k,j} u_{k,j} + \delta_{k,j} \delta_{k,j}) \right\}. \quad (3.34)$$

Because there is only one non-constant scale function in the cylindrical reference system, the pure scale function part contains far fewer non-zero terms than the displacement gradient part. Expanding each of the pure scale function terms, and substituting the displacement gradient terms ( $D_{ij}$ ) wherever possible produces



$$(\delta\Delta\varepsilon''_{rr})^H = \delta\Delta u_r \left[ \frac{D_{21}}{(R+u_r)} \right]^2 \Delta u_r, \quad (3.35a)$$

$$(\delta\Delta\varepsilon''_{\theta\theta})^H = \delta\Delta u_r \left[ \frac{D_{22}}{(R+u_r)} + \frac{1}{R} \right]^2 \Delta u_r, \quad (3.35b)$$

$$(\delta\Delta\varepsilon''_{zz})^H = \delta\Delta u_r \left[ \frac{D_{23}}{(R+u_r)} \right]^2 \Delta u_r, \quad (3.35c)$$

$$(2\delta\Delta\varepsilon''_{r\theta})^H = \delta\Delta u_r \left[ \frac{2D_{21}}{(R+u_r)} \left[ \frac{D_{22}}{(R+u_r)} + \frac{1}{R} \right] \right] \Delta u_r, \quad (3.35d)$$

$$(2\delta\Delta\varepsilon''_{\theta z})^H = \delta\Delta u_r \left[ \frac{2D_{23}}{(R+u_r)} \left[ \frac{D_{22}}{(R+u_r)} + \frac{1}{R} \right] \right] \Delta u_r, \text{ and} \quad (3.35e)$$

$$(2\delta\Delta\varepsilon''_{rz})^H = \delta\Delta u_r \left[ \frac{2D_{21}D_{23}}{(R+u_r)^2} \right] \Delta u_r. \quad (3.35f)$$

The tensor product,  $S_{ij}\delta\Delta\varepsilon''_{ij}$ , is then expressed in matrix form. However, because only one scale function is incremented, the number of terms is reduced, and the matrix equivalent expression is formed using the smaller form of the stress matrix:

$$[K_G^H] = [B_G^H]^T [s] [B_G^H], \quad (3.36)$$

in which

$$[B_{G_s}^{Hpf}] = \begin{bmatrix} \left[ \frac{D_{21}}{(R+u_r)} \right] N_c^{pf} & 0 & 0 \\ \left[ \frac{D_{22}}{(R+u_r)} + \frac{1}{R} \right] N_c^{pf} & 0 & 0 \\ \left[ \frac{D_{23}}{(R+u_r)} \right] N_c^{pf} & 0 & 0 \end{bmatrix}. \quad (3.37)$$

The nodal harmonic matrix,  $[B_{G_s}^{Hpf}]$ , is associated with the symmetric part of the nodal harmonic degrees of freedom, and the antisymmetric part is formed by replacing the cosine interpolation functions with sine functions. Again, the complete matrix is formed by assembling these nodal harmonic parts together.

### 3.6.3. The Mixed Part

The mixed term part of the second order strain variation was shown in Eq. (2.23c) to be

$$(\delta\Delta\epsilon''_{ij})^{DH} = \frac{1}{H^i H^j} \left\{ \begin{aligned} &h^j \Delta h^j \delta\Delta u_{j,i} + h^i \Delta h^i \delta\Delta u_{i,j} \\ &+ h^j \delta\Delta h^j \Delta u_{j,i} + h^i \delta\Delta h^i \Delta u_{i,j} \\ &+ h^k \Delta h^k (u_{kj} \delta\Delta u_{ki} + u_{ki} \delta\Delta u_{kj}) \\ &+ h^k \delta\Delta h^k (u_{kj} \Delta u_{ki} + u_{ki} \Delta u_{kj}) \end{aligned} \right\}. \quad (3.38)$$

Expanding this for each strain component in cylindrical coordinates, and using the scaled displacement gradient terms gives

$$(\delta\Delta\epsilon''_{rr})^{DH} = 2D_{21} \left[ \Delta u_r \frac{\partial(\delta\Delta u_\theta)}{\partial R} + \delta\Delta u_r \frac{\partial(\Delta u_\theta)}{\partial R} \right], \quad (3.39a)$$

$$(\delta\Delta\epsilon''_{\theta\theta})^{DH} = 2 \left[ \frac{(R+u_r)}{R^2} + \frac{D_{22}}{R} \right] \left[ \Delta u_r \frac{\partial(\delta\Delta u_\theta)}{\partial \Theta} + \delta\Delta u_r \frac{\partial(\Delta u_\theta)}{\partial \Theta} \right], \quad (3.39b)$$

$$(\delta\Delta\epsilon''_{zz})^{DH} = 2D_{23} \left[ \Delta u_r \frac{\partial(\delta\Delta u_\theta)}{\partial Z} + \delta\Delta u_r \frac{\partial(\Delta u_\theta)}{\partial Z} \right], \quad (3.39c)$$

$$2(\delta\Delta\epsilon''_{r\theta})^{DH} = 2 \left\{ \begin{aligned} &\Delta u_r \left[ \left[ \frac{(R+u_r)}{R} + D_{22} \right] \frac{\partial(\delta\Delta u_\theta)}{\partial R} + \frac{D_{21}}{R} \frac{\partial(\delta\Delta u_\theta)}{\partial \Theta} \right] \\ &+ \delta\Delta u_r \left[ \left[ \frac{(R+u_r)}{R} + D_{22} \right] \frac{\partial(\Delta u_\theta)}{\partial R} + \frac{D_{21}}{R} \frac{\partial(\Delta u_\theta)}{\partial \Theta} \right] \end{aligned} \right\}, \quad (3.39d)$$

$$\delta\Delta\epsilon''_{\theta z})^{DH} = 2 \left\{ \begin{aligned} &\Delta u_r \left[ \left[ \frac{(R+u_r)}{R} + D_{22} \right] \frac{\partial(\delta\Delta u_\theta)}{\partial Z} + \frac{D_{23}}{R} \frac{\partial(\delta\Delta u_\theta)}{\partial \Theta} \right] \\ &+ \delta\Delta u_r \left[ \left[ \frac{(R+u_r)}{R} + D_{22} \right] \frac{\partial(\Delta u_\theta)}{\partial R} + \frac{D_{23}}{R} \frac{\partial(\Delta u_\theta)}{\partial \Theta} \right] \end{aligned} \right\}, \text{ and} \quad (3.39e)$$

$$2(\delta\Delta\epsilon''_{rz})^{DH} = 2 \left\{ \begin{aligned} &\Delta u_r \left[ D_{21} \frac{\partial(\delta\Delta u_\theta)}{\partial Z} + D_{23} \frac{\partial(\delta\Delta u_\theta)}{\partial R} \right] \\ &+ \delta\Delta u_r \left[ D_{21} \frac{\partial(\Delta u_\theta)}{\partial Z} + D_{23} \frac{\partial(\Delta u_\theta)}{\partial R} \right] \end{aligned} \right\}. \quad (3.39f)$$

As with the pure deformation gradient and scale function parts, the product of the mixed second order strain variation part with the Piola - Kirchoff stress tensor is expressed in matrix form. However, because these are mixed terms, this part of the geometric stiffness matrix can be formed as the sum of two matrices, each the transpose of the other, using the smaller form of the stress matrix,  $[s]$  as shown in Eq. (3.32)

$$S_{ij} \delta \Delta \epsilon_{ij}'' = \{\delta \Delta U\}^T \left[ [B1_G^{DH}]^T [s] [B2_G^{DH}] + [B2_G^{DH}]^T [s] [B1_G^{DH}] \right] \{\delta \Delta U\} , \quad (3.40)$$

in which

$$[B1_{G_s}^{DHpf}] = \begin{bmatrix} 2D_{21}N_c^{pf} & 0 & 0 \\ 2\left(\frac{(R+u_r)}{R} + D_{22}\right)N_c^{pf} & 0 & 0 \\ 2D_{23}N_c^{pf} & 0 & 0 \end{bmatrix}, \text{ and} \quad (3.41)$$

$$[B2_{G_s}^{DHpf}] = \begin{bmatrix} 0 & \frac{\partial N_s^{pf}}{\partial R} & 0 \\ 0 & \frac{1}{R} \frac{\partial N_s^{pf}}{\partial \Theta} & 0 \\ 0 & \frac{\partial N_s^{pf}}{\partial Z} & 0 \end{bmatrix}. \quad (3.42)$$

The matrices  $[B1_{G_s}^{DHpf}]$  and  $[B2_{G_s}^{DHpf}]$  are the nodal harmonic parts of  $[B1]$  and  $[B2]$  corresponding to the symmetric degrees of freedom for harmonic  $f$  of node  $p$ . The antisymmetric parts are produced by replacing  $N_c^{pf}$  with  $N_s^{pf}$ , and vice-versa, and the complete element matrices are assembled from the nodal harmonic components in the same manner as the linear strain-displacement matrix.

The first order components of the geometric stiffness matrix have now been defined in matrix form. Because of the sparse structure of the  $[B_G]$  matrices, however, the geometric stiffness matrix components should be implemented in computer code by direct evaluation, bypassing matrix operations involving a zero.

### 3.7. Integration

The stiffness functions defined above must be integrated into the linear and geometric stiffness matrices for the element. These functions are based on the polynomial interpolation functions in the local  $\xi$ - $\mu$  space and harmonic interpolation in the  $\Theta$  dimension of the element. In matrix form the process is defined as

$$\int_{V_{el}} ([K_L] + [K_G]) dV = \int_{V_{el}} ([K_L(\xi, \mu, \Theta)] + [K_G(\xi, \mu, \Theta)]) dV .$$

Integration procedures for the simple axisymmetric element and the linear axisymmetric element for nonaxisymmetric behaviour are shown first to illustrate the development of an integration strategy for the nonlinear equations for the nonlinear cylindrical formulation.

#### 3.7.1. Integration of the Conventional Axisymmetric Element

With most conventional axisymmetric solid elements, Gauss quadrature is employed in the R-Z plane. Since no variation in the  $\Theta$  direction is modelled, extending the integration from this plane around the element circumference is straight forward. The two dimensional quadrature is applied over the simple local region, and extended to the global element space using the usual parametric transformation for the differential area:

$$dA = dRdZ = |J|d\xi d\mu , \quad (3.43)$$

where the Jacobian,  $|J|$ , is the determinant of the Jacobian matrix in Eq. (3.20), and is only a function of local coordinates  $\xi$  and  $\mu$ . The differential volume in the ring produced by revolving  $dA$  about the centre of rotation is then

$$dV = 2\pi R |J| d\xi d\mu . \quad (3.44)$$

The usual axisymmetric element, is then integrated thus:

$$[K_{el}] = 2\pi \int_{\xi=-1}^1 \int_{\mu=-1}^1 [K(\xi, \mu)] R |J| d\xi d\mu . \quad (3.45)$$

### 3.7.2. Integration of the Linear Elastic Non-Axisymmetric Element

The Fourier decomposition element has been developed to model a circumferential variation in behaviour, and therefore requires a more general integration strategy in the  $\Theta$  direction. Consider the differential volume described by Eq. (3.44) which is infinitesimally small in the circumferential direction, as well as in the axisymmetric plane. When the Fourier decomposition technique was introduced by Wilson(1965) and applied to a small displacement, linear elastic formulation, it was shown that the harmonic components were decoupled because of the orthogonal properties of the Fourier functions. This can be shown in matrix form by partitioning the stiffness function according to the order of the Fourier functions in each term:

$$[K_{el}] = \begin{bmatrix} [K_{00}] & [K_{01}] & \dots & [K_{0NF}] \\ [K_{10}] & [K_{11}] & \dots & [K_{1NF}] \\ \vdots & \vdots & \ddots & \vdots \\ [K_{NF0}] & [K_{NF1}] & \dots & [K_{NFPF}] \end{bmatrix}, \quad (3.46)$$

in which

$$[K_{nm}] = \int_{V_{el}} [B^n]^T [C] [B^m] R I J d r d s d \Theta, \quad n, m = 0, 1, \dots, NF \quad (3.47)$$

Each harmonic strain-displacement matrix can be separated into its sine and cosine parts. The corresponding stiffness matrix is thus separated into second order sine and cosine components,

$$[B^f] = [B_f^c] + [B_f^s]. \quad (3.48)$$

Equation (3.47) can therefore be written in the form

$$[K_{nm}] = [K_{nm}^{cc}] + [K_{nm}^{cs}] + [K_{nm}^{sc}] + [K_{nm}^{ss}], \quad (3.49)$$

in which

$$[K_{nm}^{cc}] = \int_{\Theta} \int_s \int_r [B_n^c]^T [C] [B_m^c] \cos(n\Theta) \cos(m\Theta) R I J d r d s d \Theta, \quad (3.50)$$

where  $[B_f^c]\cos(f\Theta)$  and  $[B_f^s]\sin(f\Theta)$  are the cosine and sine components of the harmonic strain-displacement matrix for the  $f$ th Fourier term, and  $[K_{nm}^{cc}]$  contains the cosine terms of the harmonic stiffness matrix which couples the  $n$ 'th load harmonics to the  $m$ 'th displacement harmonics. The sine terms and mixed cosine-sine terms in  $[K_{nm}^{ss}]$ ,  $[K_{nm}^{cs}]$ , and  $[K_{nm}^{sc}]$  are produced using  $\sin()$  in place of  $\cos()$  corresponding to where  $s$  replaces  $c$  in Eq. (3.50).

Since the Jacobian matrix is independent of  $\Theta$ , and all dependence on  $\Theta$  has been moved outside of  $[B_n^c]$ , Eq. (3.50) is first integrated with respect to the local coordinates  $\xi$  and  $\mu$  leaving:

$$[K_{nm}^{cc}] = [k_{nm}^{cc}] \int_{-\pi}^{\pi} \cos(m\Theta)\cos(n\Theta)d\Theta, \quad (3.51a)$$

where  $[k_{nm}^{cc}]$  is the inner integral of Eq. (3.50). Similarly for the sine and mixed parts of the harmonic stiffness:

$$[K_{nm}^{ss}] = [k_{nm}^{ss}] \int_{-\pi}^{\pi} \sin(m\Theta)\sin(n\Theta)d\Theta, \quad (3.51b)$$

$$[K_{nm}^{sc}] = [k_{nm}^{sc}] \int_{-\pi}^{\pi} \sin(m\Theta)\cos(n\Theta)d\Theta, \text{ and} \quad (3.51c)$$

$$[K_{nm}^{cs}] = [k_{nm}^{cs}] \int_{-\pi}^{\pi} \cos(m\Theta)\sin(n\Theta)d\Theta. \quad (3.51d)$$

The integrals with respect to  $\Theta$  are the well known Fourier integrals which manifest the orthogonality of the Fourier functions:

$$\int_{-\pi}^{\pi} \cos(a\Theta)\cos(b\Theta) d\Theta = \begin{cases} 0 & \text{for } a \neq b \\ 2\pi & \text{for } a = b = 0 \\ \pi & \text{for } a = b \text{ and } a, b > 0 \end{cases}, \quad (3.52a)$$

$$\int_{-\pi}^{\pi} \sin(a\Theta)\sin(b\Theta) d\Theta = \begin{cases} 0 & \text{for } a \neq b \\ 0 & \text{for } a = b = 0 \\ \pi & \text{for } a = b \text{ and } a, b > 0 \end{cases}, \text{ and} \quad (3.52b)$$

$$\int_{-\pi}^{\pi} \cos(a\Theta)\sin(b\Theta) d\Theta = 0. \quad (3.52c)$$

Thus, when the harmonic stiffness matrices are integrated with respect to  $\Theta$ , the harmonics become decoupled in linear formulations because the coupled harmonic stiffness matrices,  $[K_{nm}]$ ,  $n \neq m$ , vanish. The Fourier decomposition technique is very effective for linear problems because of the simplified stiffness matrix structure produced by the harmonic decoupling, and because the circumferential integration can be performed analytically.

### 3.7.3. Nonlinear Non-Axisymmetric Integration

With the nonlinear formulation, the orthogonality advantage is lost, because the harmonic stiffnesses remain coupled. Many of the virtual work equation components which are constant in linear elastic formulations will vary in three dimensional  $r, z, \theta$  space in more general nonlinear formulations. This produces higher order Fourier products which couple the harmonic stiffnesses. These nonlinear components include the constitutive matrix,  $[C]$ , and the deformation gradient terms of the strain increment components,  $\Delta\epsilon'$ , and  $\Delta\epsilon''$ . Integration of the virtual work equation in nonlinear applications is thus most effectively achieved using numerical integration in the  $\Theta$  direction, as well as in the  $R - Z$  plane. However, to understand the best means of performing this integration, it is necessary to consider analytical integration of the equations in the  $\Theta$  dimension.

Firstly, the constitutive matrix  $[C]$  is not constant, and will vary with  $\Theta$ . This variation could be considered in terms of a Fourier series using the same approach applied to the displacement field:

$$[C(r,s,\Theta)] = \sum_{f=1}^{NF} [C_c^f(r,s)] \cos(f\Theta) + [C_s^f(r,s)] \sin(f\Theta). \quad (3.53)$$

Secondly, the deformation gradient strain - displacement matrix includes the deformation gradient components, which also vary circumferentially. This too is a Fourier series, because the displacement field is expressed in terms of a Fourier series:

$$[B + B']_c^f = \cos(f\Theta) \sum_{a=0}^{NF} [B + B']_c^{fc} \cos(a\Theta) + [B + B']_c^{fs} \sin(a\Theta) . \quad (3.54)$$

If these expressions were used to evaluate the harmonic coupling stiffness matrices, the higher order Fourier decompositions would require a large summation be performed:

$$\begin{aligned} [K_{nm}] = \sum_{a=0}^{NF} \sum_{b=0}^{NF} \sum_{c=0}^{NF} & \left( [k_{nmabc}^{cccc}] \cos(n\Theta) \cos(m\Theta) \cos(a\Theta) \cos(b\Theta) \cos(c\Theta) + \right. \\ & [k_{nmabc}^{cccs}] \cos(n\Theta) \cos(m\Theta) \cos(a\Theta) \cos(b\Theta) \sin(c\Theta) + \\ & \dots + \\ & \left. [k_{nmabc}^{sssss}] \sin(n\Theta) \sin(m\Theta) \sin(a\Theta) \sin(b\Theta) \sin(c\Theta) \right) \end{aligned} \quad (3.55)$$

Clearly, analytical integration of the harmonic coupling stiffness matrices is impractical, by virtue of the sheer number of terms which must be evaluated. The number of matrix evaluations required is in the order of the number of sampling points required for numerical integration. Furthermore, a large amount of overhead would be required to separate the harmonic terms. The strain - displacement matrices are more easily evaluated at sample points than the decomposition shown in Eq. (3.54), and the decomposition expressed in Eq. (3.53) requires knowledge of the constitutive properties at sample points around the circumference. Since this information is easier to obtain, numerical integration of the stiffness and load terms is much more efficient than attempting to carry out analytical integrations.

Gauss integration was developed to integrate polynomial functions. The Fourier functions can be approximated by higher order polynomial functions, but this is not the most effective approach to integrating the Fourier functions. First order Newton-Cotes integration (trapezoidal rule) was investigated as a numerical means of integrating Fourier equations such as Eq. (3.55) with some interesting results. It was discovered that applying the trapezoidal rule to the Fourier functions produces exact results with relatively few integration points in the  $\Theta$  direction. To understand the sampling period that provides adequate integration, and that which provides exact integration of the



Fourier integrals requires that exact results be available for comparison with the numerical result. Analytical integration of the product of two Fourier functions is relatively simple, using the trigonometric identities

$$\cos(ax) \cos(bx) = \frac{\cos(a-b)x}{2} + \frac{\cos(a+b)x}{2}, \quad (3.56a)$$

$$\sin(ax) \sin(bx) = \frac{\cos(a-b)x}{2} - \frac{\cos(a+b)x}{2}, \text{ and} \quad (3.56b)$$

$$\sin(ax) \cos(bx) = \frac{\sin(a-b)x}{2} + \frac{\sin(a+b)x}{2}. \quad (3.56c)$$

The product of three or more Fourier functions can be expressed as sums of trigonometric functions by recursively applying these identities. For example, three function products would be

$$\begin{aligned} \sin(ax) \sin(bx) \sin(cx) = & \frac{\sin(a-b+c)x}{4} + \frac{\sin(a+b-c)x}{4} - \frac{\sin(a-b-c)x}{4} \\ & - \frac{\sin(a+b+c)x}{4}, \end{aligned} \quad (3.57a)$$

$$\begin{aligned} \sin(ax) \sin(bx) \cos(cx) = & \frac{\cos(a-b+c)x}{4} + \frac{\cos(a-b-c)x}{4} - \frac{\cos(a+b-c)x}{4} \\ & - \frac{\cos(a+b+c)x}{4}, \end{aligned} \quad (3.57b)$$

$$\begin{aligned} \sin(ax) \cos(bx) \cos(cx) = & \frac{\sin(a-b+c)x}{4} + \frac{\sin(a-b-c)x}{4} + \frac{\sin(a+b-c)x}{4} \\ & + \frac{\sin(a+b+c)x}{4}, \text{ and} \end{aligned} \quad (3.57c)$$

$$\begin{aligned} \cos(ax) \cos(bx) \cos(cx) = & \frac{\cos(a-b-c)x}{4} + \frac{\cos(a-b+c)x}{4} + \frac{\cos(a+b-c)x}{4} \\ & + \frac{\cos(a+b+c)x}{4}. \end{aligned} \quad (3.57d)$$

In general form, then, a product of  $n$  Fourier functions can be expressed as a sum of  $2^{n-1}$  cosine or sine functions (but not both) with each term a unique combination of

$$w_i \frac{\cos(a \pm b \pm c \pm \dots \pm \alpha_n)}{2^{n-1}} \quad \text{or} \quad w_i \frac{\sin(a \pm b \pm c \pm \dots \pm \alpha_n)}{2^{n-1}},$$

where  $w_i$  is a function of value 1 or -1, and  $\alpha_n$  is the  $n$ 'th character of the alphabet. It is important to note that if the number of sine terms in the Fourier product is even, the equivalent Fourier sum will consist of cosine terms, otherwise, all terms will be sine functions.

The Fourier product integration for an even number of sine functions can therefore be considered as a summation of several terms in the form of

$$\int_{-\pi}^{\pi} \prod_{j=1}^n (\cos | \sin)(\alpha_j \theta) d\theta = \sum_{i=1}^{2^{n-1}} \frac{w_i}{2^{n-1}} \int_{-\pi}^{\pi} \cos(\gamma_i \theta) d\theta \quad (\text{even sines}), \quad (3.58)$$

where  $\Pi$  is the product symbol,  $(\cos | \sin)$  signifies cosine or sine Fourier functions, and  $\gamma_i$  is a unique combination of the Fourier numbers in  $(a \pm b \pm \dots \pm \alpha_n)$ .

The Fourier product integration for an odd number of sine functions is the same, with the cosine functions replaced with sine functions in the integrand. Because the sine functions are odd functions about the origin, the integration from  $-\pi$  to  $\pi$  will be zero, thus eliminating Fourier products with an odd number of sine functions.

Integrating the cosine functions produces

$$\int_{-\pi}^{\pi} \prod_{j=1}^n (\cos | \sin)(\alpha_j \theta) d\theta = \sum_{i=1}^{2^{n-1}} \frac{w_i}{2^{n-1}} \left[ \frac{\sin(\gamma_i \theta)}{\gamma_i} \right]_{-\pi}^{\pi}. \quad (3.59)$$

Because the Fourier numbers are integer values,  $\gamma_i$  must also be an integer value. Evaluating the integral at the limits of the interval produces a zero result for all nonzero values of  $\gamma_i$ . The result for  $\gamma_i = 0$  is undefined, but can be determined by considering the limit

$$\lim_{x \rightarrow 0} \frac{\sin(x)}{x} = 1$$

Substituting  $x = \gamma\pi$

$$\lim_{\gamma \rightarrow 0} \frac{\pi \sin(\gamma\pi)}{\gamma\pi} = \pi$$

Thus substituting for the limits of the integration interval, the integration is complete:

$$\frac{w_i}{2^{n-1}} \left[ \frac{\sin(\gamma_i \theta)}{\gamma_i} \right]_{-\pi}^{\pi} = \begin{cases} w_i \frac{\pi}{2^{n-2}} & \text{for } \gamma_i = 0 \\ 0 & \text{for } \gamma_i \neq 0 \end{cases} \quad (3.60)$$

These results are consistent with those reported by Chan and Trbojevic(1975) for a three Fourier function product, but higher order results have not been reported in the literature for comparison. An interesting point to note is that the denominator increases in magnitude by a factor of two with each additional Fourier function in the product, showing that the most significant terms in the integral are the lowest order, or linear, terms. This has important implications for the minimum integration order required for the Fourier element.

Numerical integration of the Fourier products, then, must produce zero for all sine functions and for all cosine functions with  $a \pm b \pm \dots \pm \alpha_n \neq 0$ . For cosine functions with  $a \pm b \pm \dots \pm \alpha_n = 0$ ,  $\pm \frac{\pi}{2^{n-2}}$  must result. The numerical approach should consistently handle both cases so that all of the terms can be evaluated and summed simultaneously. It should also be general in the sense that if the highest order Fourier product is integrated exactly, lower order Fourier products will also be integrated exactly and simultaneously.

First, consider the case of non-zero  $\gamma$ . If one cycle of the harmonic is considered, it can be proven by application of a trigonometric identity that evaluating the harmonic function at two or more evenly spaced sample points and summing the results will produce zero. This suggests that if the number of sampling points over the total range  $-\pi < \theta \leq \pi$  is greater than or equal to  $2\gamma$ , the integration will be exact. Giving the problem further consideration, however, one can show that only  $\gamma+1$  sample points evenly spaced over the total range are required to generate the zero result, because the sampling will occur at uniform interval points in each cycle. Using fewer sample points will produce a nonzero result; more sample points require more computation, but generate the zero result. Thus the optimal number of sample points required to evaluate the zero terms

exactly is  $\gamma_{\max} + 1$ , where  $\gamma_{\max}$  is the largest integral Fourier number that can be produced from all the combinations of the Fourier terms.

If, in nonlinear analyses, fewer than  $\gamma_{\max} + 1$  sample points are used, a valid result can be produced, because only the higher order components are not evaluated exactly. The linear components are still integrated exactly, as long as at least  $2NF + 1$  sample points are used. Because the denominator is largest for these terms, and because the deformation gradient terms are usually small relative to unity, integration with this number of sample points is often adequate. However, if the stiffness matrix is ill conditioned or the deformation gradients are large, it is important that full integration be used. This is analogous to integration rules discussed by Bathe, 1982 for Gauss quadrature of polynomial based elements. For example, two point quadrature provides reliable integration of a quadratic element, however three point quadrature is required to integrate the stiffness of the element in its deformed configuration when large displacements are modelled.

A series of numerical integrations using the trapezoidal rule were carried out with a large number of sample points to verify the analytical results presented above. The tests proved that integration of two Fourier functions is exact when  $2n+1$  or more sampling points are used, where  $n$  is the larger of the Fourier numbers. Integrating three Fourier functions, the result converged at  $3n+1$  sampling points, where  $n$  is the largest of the three Fourier numbers. Integrating four Fourier terms required  $4n+1$  sampling points, and finally, five Fourier functions could be integrated with  $5n+1$  sampling points. These results show that the trapezoidal rule will produce an exact result if the number of sampling points is one greater than the sum of Fourier numbers in the product to be integrated.

The circumferential integration rules may then be summarized as follows:

**Small displacement, linear material:** Product of two Fourier functions may be integrated analytically, or numerically using  $2*NF+1$  circumferential integration points, where  $NF$  is the number of harmonics to be modelled.

**Small displacement, nonlinear material:** Product of three Fourier functions are integrated.  $3*NF+1$  integration points will model a material variation of the same order as the displacement variation. More circumferential points will improve the

circumferential representation of the material by increasing the effective number of Fourier terms in the material model.

**Large displacement, linear material:** Deformation gradient strain-displacement matrix includes products of two Fourier functions, thus the stiffness matrix must integrate four Fourier functions. Therefore,  $4*NF+1$  integration points will exactly integrate the stiffness matrix in the circumferential direction.

**Large displacement, nonlinear material:** Two Fourier functions from the strain - displacement matrix and one from the constitutive matrix produce a total of five Fourier functions which must be integrated. This requires  $5*NF+1$  integration points to model material variation equivalent to displacement variation in the circumferential direction.

The element uses the usual polynomial serendipity functions in the axisymmetric plane, for which Gauss quadrature provides the most effective integration. Thus, the integration formula is expressed as

$$[K_{el}] = \int_{V_{el}} [K] dV = w_T R \sum_{i=1}^{NG_\xi} \sum_{j=1}^{NG_\mu} w_i w_j |J| \sum_{k=1}^{NT} [K_{ijk}] , \quad (3.61)$$

where  $NG_\xi$  and  $NG_\mu$  are the number of Gauss points in the  $\xi$  and  $\mu$  directions of the element in local coordinate space,  $NT$  is the number of circumferential sampling points,  $w_i$  and  $w_j$  are the usual Gauss quadrature weighting factors, and  $w_T$  is the weighting factor for trapezoidal integration, which is simply  $2\pi/NT$ . The matrix  $[K_{ijk}]$  is the stiffness matrix function evaluated at the integration point:

$$\begin{aligned} [K_{ijk}] = & [B(\xi_i, \mu_j, \Theta_k)]^T [C] [B(\xi_i, \mu_j, \Theta_k)] + [B_G^D(\xi_i, \mu_j, \Theta_k)]^T [S] [B_G^D(\xi_i, \mu_j, \Theta_k)] \\ & + [B_G^H(\xi_i, \mu_j, \Theta_k)]^T [s] [B_G^H(\xi_i, \mu_j, \Theta_k)] + [B_1^{DH}(\xi_i, \mu_j, \Theta_k)]^T [s] [B_2^{DH}(\xi_i, \mu_j, \Theta_k)] \\ & + [B_2^{DH}(\xi_i, \mu_j, \Theta_k)]^T [s] [B_1^{DH}(\xi_i, \mu_j, \Theta_k)] \end{aligned} \quad (3.62)$$

The coordinate values of  $\xi_i$  and  $\mu_j$  are the Gauss integration point coordinates, and  $\Theta_k$  are the circumferential integration locations,  $(k-1)(2\pi/NT)$ .

This completes the formulation of the Fourier decomposition element in cylindrical coordinates. All of the matrix equations required to generate the element stiffness matrix have been defined and can be implemented in computer code for a finite

element program. All of the usual procedures for assembling and solving the complete system of equations may be applied. Some additional consideration must be given to accommodate the large number of degrees of freedom per node, but this is not a large problem to address. A description of a finite element computer program which implements this element, and results produced by the program are given in subsequent chapters.

### **3.8. Boundary Conditions**

The implications of boundary conditions require some additional discussion in the context of Fourier displacement field decomposition. It is interesting to note that boundary conditions which are difficult to impose on axisymmetric models composed of conventional elements are often simple to apply to models based on Fourier decomposition elements. For example, shear stresses may be applied to one end of a pipe using the circumferential ( $\theta$ ) degrees of freedom of the first harmonic, and reacted at the other end by constraining the circumferential degrees of freedom of the first harmonic. If no other constraints are applied (other than those needed to remove rigid body modes), the pipe cross section is as free to deform at the boundary as it is in the middle. This is equivalent to the idealized boundary conditions used to evaluate a section of pipe with internal stress equivalent boundary conditions. Modelling such boundary conditions is difficult, if not impossible, with conventional elements.

The rigid body axial displacement mode and rigid body rotation about the axisymmetric axis are all modelled by the zero'th harmonic. This harmonic also includes the usual axisymmetric deformation modes, and uses boundary conditions associated with axisymmetric analyses. Rigid body motion normal to the axisymmetric axis, and rigid body rotation about any axis normal to the axisymmetric axis is primarily modelled by the first displacement harmonic. However, because of the curvilinear nature of the cylindrical coordinate system, the interpolation functions will not exactly model rigid body motions with one harmonic. Constraining these degrees of freedom will, however, remove the rigid body modes.

Common load applications are also relatively easy to impose on a Fourier element based model. As illustrated earlier, pure shear on a thin wall is modelled exactly by the circumferential degrees of freedom of the first harmonic. Similarly, pure bending is modelled in the first harmonic using the axial degrees of freedom, as shown in Chapter 6. Torsional loads are applied using the  $\Theta$  degree of freedom of the zero'th harmonic, while

the R and Z degrees of freedom in the zero'th harmonic are used to apply the usual axisymmetric load cases.

Often, more complex load cases are required, such as concentrated axial loads applied to an axisymmetric shell. Such load cases must be separated into radial, axial and circumferential component functions, and the functions decomposed into Fourier components:

$$T_i(R, \Theta, Z) = \sum_{f=0}^{\infty} (T_{ic}^f(R, Z) \cos(f\Theta) + T_{is}^f(R, Z) \sin(f\Theta)) , \quad (3.63)$$

where  $T_i(R, \Theta, Z)$  are the traction component functions and  $T_{ic}^f(R, Z)$  and  $T_{is}^f(R, Z)$  are the harmonic traction function amplitudes. Once this decomposition is achieved, the orthogonal properties of the Fourier functions are utilized to integrate the harmonic nodal equivalent loads for assembly into the global load vector in the same way used in conventional formulations:

$$\{F_{el}\} = \int_{S_{el}} [N]^T \{T\} dS . \quad (3.64)$$

Separating the interpolation matrix and tractions into harmonic components, the load vector can also be expressed in terms of harmonic components:

$$\{F_{cc}^{pf}\} = \int_{S_{el}} [N^p]^T \{T_c^{pf}\} \cos^2(f\Theta) R dl d\Theta , \text{ and} \quad (3.65a)$$

$$\{F_{ss}^{pf}\} = \int_{S_{el}} [N^p]^T \{T_s^{pf}\} \sin^2(f\Theta) R dl d\Theta , \quad (3.65b)$$

where  $\{F_{el}\}$  is the vector of nodal equivalent traction loads for the element boundary,  $\{F_{cc}^{pf}\}$  and  $\{F_{ss}^{pf}\}$  are the cosine and sine portions of the load vector associated with node p and harmonic f,  $[N]$  is the full interpolation function matrix,  $[N^p]$  is the matrix of polynomial functions,  $dl$  is the two dimensional, axisymmetric differential surface of the element, and  $dS$  is the three dimensional surface generated by rotating  $dl$  about the axis of axisymmetry. Other terms are, of course, generated in the expansion from Eq. (3.64)

to the Fourier form in Eq. (3.65). However, those extra terms vanish because of the orthogonal properties of the Fourier functions. The integration with respect to  $\Theta$  was presented in Eqs. (3.52), so the nodal harmonic load vector becomes

$$\{F^{pf}\} = \pi \int_{l_{el}} [N^p]^T \{T^{pf}(R,Z)\} R dl \quad \text{for } f > 0. \quad (3.66)$$

The interpolation matrix must include two polynomial interpolation submatrices so that both sine and cosine parts of the harmonic are included. The axisymmetric load function (that is, the harmonic load vector associated with  $f=0$ ) uses the usual multiplier of  $2\pi$  rather than  $\pi$  because of its unique integration with respect to  $\Theta$ .

Development of these nodal harmonic load components have all assumed that the loading tractions are independent of deformation. While many analysis cases are accommodated by such assumptions, those that require deformation dependent loading must include nonlinear terms which couple the harmonics of the load function integration. The additional complexity is comparable to that introduced into the stiffness functions by large displacements which is not unachievable, but is significant. Since such a capability is not required to prove the large displacement formulation, its development is not included here.

### 3.9. Cylindrical Formulation Summary

The formulation for a Fourier decomposition element in a cylindrical reference system is complete. The basic formulation in general curvilinear coordinate systems has been specialized to the cylindrical coordinate system and expanded into the full finite element matrix form. Integration procedures have been developed to handle the unique requirements of the Fourier decomposition, and boundary conditions for the Fourier formulation have been discussed.

A discussion of the element displacement field has also been presented, specifically with regard to rigid body motion requirements. In a subsequent chapter, results produced using this formulation are presented and compared with results from the Fourier decomposition element with Cartesian displacements developed in the next chapter. Those results show that the benefits of cylindrical displacement components are



outweighed by the problems produced by inaccurate rigid body motions. This does not mean, however, that the cylindrical formulation should be abandoned, only that more work is required to develop an element displacement field in cylindrical components that can model rigid body motions.

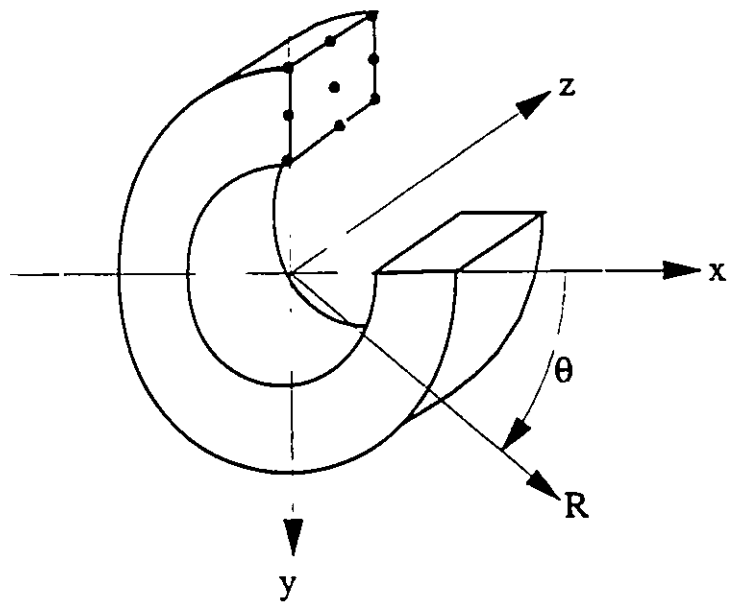


Figure 3.1 Axisymmetric three dimensional solid element

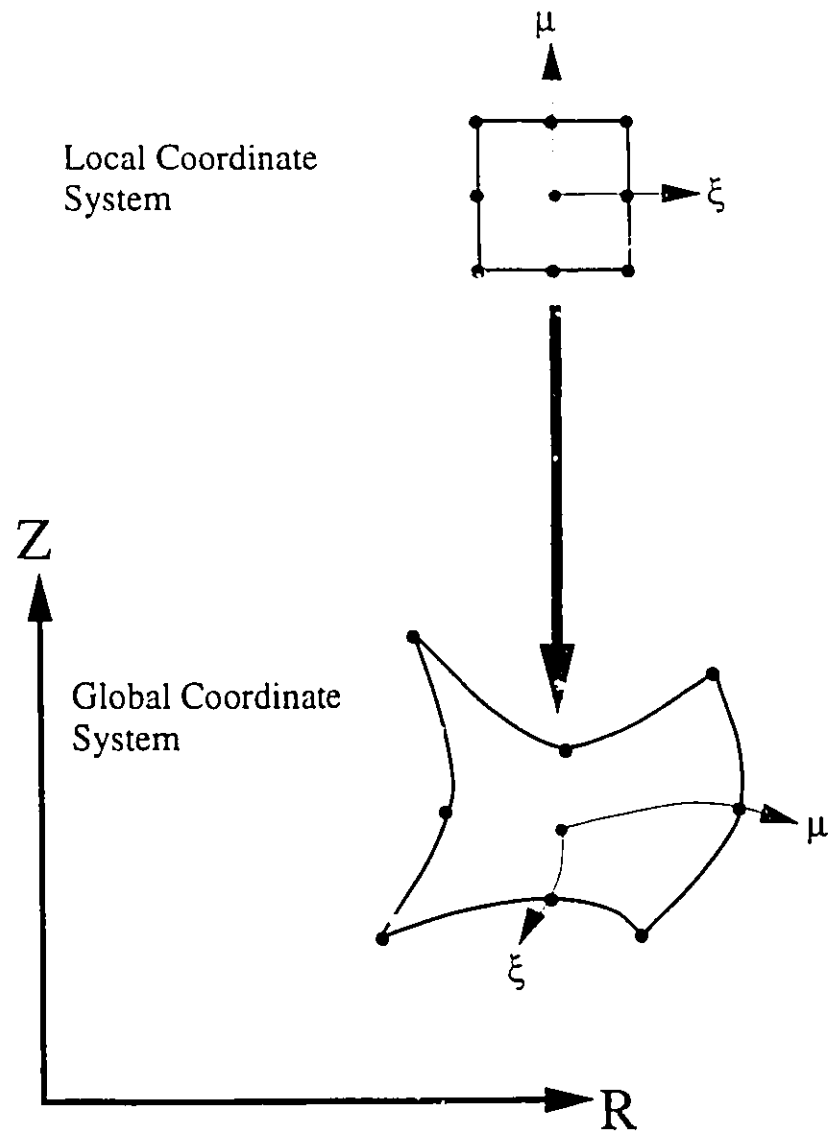


Figure 3.2 Isoparametric geometry transformation

## **4. Cartesian Formulation**

### **4.1. Overview**

The use of cylindrical displacement components is very useful for linear problems because the harmonic stiffnesses are uncoupled, and the stiffness matrix can be integrated analytically, thereby simplifying generation of the system of equations for three dimensional problems. However, these benefits are lost when nonlinear problems are considered. Furthermore, the interpolation functions used in cylindrical formulations can only approximate rigid body motion when large deflections are considered. Increasing the number of Fourier overlays improves the range over which rigid body motion is reasonably approximated. However results presented later (Chapter 6) show that many harmonics are required to model even modest amounts of lateral motion, rendering the cylindrical displacement field inadequate for modelling large displacement problems.

Conventional brick elements are formulated in Cartesian coordinates using Cartesian displacement components. These elements are well proven for modelling large displacement problems. Cylindrical coordinates can be transformed to a Cartesian system, thus it is possible to use Cartesian displacement components in a cylindrical element. This provides the benefits of both systems: a cylindrical system is used to simplify geometrical properties of the element, and a Cartesian system is used to reference the displacements. The element formulation is, in fact, simpler than the cylindrical displacement formulation, yet models rigid body displacements and rotations exactly.

This chapter details development of the axisymmetric element for non-axisymmetric behaviour using Cartesian displacements, referred to henceforth as the Cartesian element, and makes frequent comparisons to the cylindrical element developed in the previous chapter. Many of the fundamental concepts are carried over from the previous chapter, and the reader is advised to refer to that chapter for a more detailed explanation of concepts which are not discussed here in full detail.

### **4.2. Displacement Field**

#### **4.2.1. Displacement Components**

The geometry of the element is still expressed in terms of the cylindrical coordinate system, defined by  $R$ ,  $\Theta$ , and  $Z$ . A Cartesian coordinate system is defined

with a coincident origin and Z axis. The transformation functions between R,  $\Theta$ , and X, Y are as follows:

$$X = R \cos(\Theta) , \quad (4.1a)$$

$$Y = R \sin(\Theta) , \quad (4.1b)$$

$$R = \sqrt{X^2 + Y^2} , \text{ and} \quad (4.2a)$$

$$\Theta = \tan^{-1} \left( \frac{Y}{X} \right) \quad (4.2b)$$

The scale functions for displacements in Cartesian systems are unity for all three displacement components. Consequently, there is no need to distinguish between physical and coordinate displacements, and the displacements are defined simply as

$$u_x = x - X , \quad (4.3a)$$

$$u_y = y - Y , \text{ and} \quad (4.3b)$$

$$u_z = z - Z . \quad (4.3c)$$

#### 4.2.2. Fourier Decomposition of Circumferential (Out-of-Plane) Displacement

The three dimensional displacement field is decomposed into a Fourier series of two dimensional functions using the same procedures as the cylindrical formulation. However, Cartesian displacements are used rather than cylindrical displacements. Although this approach has not previously been applied to finite element analyses of axisymmetric structures, solutions do exist in classical mechanics which use Fourier techniques. For example, Sokolnikoff(1956) shows the solution for a cylindrical bar subject to bending loads using Cartesian displacement components. The exact linear solution for the displacement field is given as two or three Fourier terms depending on the particular problem. This solution demonstrates that effective, simple solutions exist for problems using Cartesian displacements and Fourier decomposition.

Using indicial notation the displacement field is expressed as the Fourier series

$$u_i = \sum_{f=1}^{\infty} u_{ic}^f(R,Z) \cos(f\Theta) + \sum_{f=1}^{\infty} u_{is}^f(R,Z) \sin(f\Theta) , \quad i = x, y, z \quad (4.4),$$

where  $u_{ic}^f$  and  $u_{is}^f$  are respectively the two dimensional amplitude functions for the cosine and sine Fourier terms.

It is important to distinguish between the two coordinate systems which are employed. The displacement components,  $u_i$ , are Cartesian displacements,  $u_x$ ,  $u_y$ , and  $u_z$ . These are expressed as functions of the cylindrical coordinates which define the element geometry.

The harmonic amplitude functions,  $u_{ic}^f$  and  $u_{is}^f$ , are independent of  $\Theta$ , thus differentiating term by term with respect to  $\Theta$ , the derivative becomes

$$\frac{\partial u_i}{\partial \Theta} = \sum_{f=0}^{\infty} -f u_{ic}^f(R,Z) \sin(f\Theta) + \sum_{f=1}^{\infty} f u_{is}^f(R,Z) \cos(f\Theta) . \quad (4.5)$$

#### 4.2.3. Polynomial In-Plane Interpolation with Parametric Transformation

Polynomial interpolation of the harmonic displacement amplitudes is the same as that used for the cylindrical element. As with other elements described in two dimensions, the axisymmetric section of the element is transformed to a local coordinate space to simplify the interpolation functions and integration:

$$u_{ic}^f(\xi, \mu) = \sum_{p=1}^{NP} P_p(\xi, \mu) u_{ic}^{pf} , \text{ and} \quad (4.6a)$$

$$u_{is}^f(\xi, \mu) = \sum_{p=1}^{NP} P_p(\xi, \mu) u_{is}^{pf} . \quad (4.6b)$$

The variables  $u_{ic}^{pf}$  and  $u_{is}^{pf}$  are the nodal values of displacement field amplitudes for cosine and sine harmonics respectively. These are in fact the degrees of freedom of the element.

#### 4.2.4. Combined Interpolation

To summarize, the subscript  $i$  represents the displacement component in the X, Y, or Z directions; subscripts  $c$  and  $s$  respectively denote cosine and sine terms of the Fourier series; superscript  $p$  represents polynomial interpolation number, or node number; and superscript  $f$  denotes the harmonic number. The element matrices have the

same size as the cylindrical element, since it requires the same number of degrees of freedom.

Combining interpolation functions from Eq. (4.4) and Eq. (4.6) provides the displacement field for the element in terms of combined interpolation functions and nodal harmonic displacements:

$$u_i = \sum_{p=1}^{NP} \sum_{f=0}^{NF} (N_c^{pf} u_{ic}^{pf} + N_s^{pf} u_{is}^{pf}) , \quad (4.7)$$

where

$$N_c^{pf} = P_p(\xi, \mu) \cos(f\Theta) , \text{ and} \quad (4.8a)$$

$$N_s^{pf} = P_p(\xi, \mu) \sin(f\Theta) . \quad (4.8b)$$

#### 4.2.5. Displacement Gradients

Conventional solid elements use the Jacobian matrix to transform spatial gradients from the local coordinate system to the global coordinate system. The Fourier element local domain is defined in two dimensions by the  $\xi, \mu$  coordinates, and in the third dimension by the  $\Theta$  coordinate. The Jacobian transformation between these coordinate spaces is

$$\begin{Bmatrix} \frac{\partial}{\partial \xi} \\ \frac{\partial}{\partial \mu} \\ \frac{\partial}{\partial \Theta} \end{Bmatrix} = \begin{bmatrix} \frac{\partial X}{\partial \xi} & \frac{\partial Y}{\partial \xi} & \frac{\partial Z}{\partial \xi} \\ \frac{\partial X}{\partial \mu} & \frac{\partial Y}{\partial \mu} & \frac{\partial Z}{\partial \mu} \\ \frac{\partial X}{\partial \Theta} & \frac{\partial Y}{\partial \Theta} & \frac{\partial Z}{\partial \Theta} \end{bmatrix} \begin{Bmatrix} \frac{\partial}{\partial X} \\ \frac{\partial}{\partial Y} \\ \frac{\partial}{\partial Z} \end{Bmatrix} . \quad (4.9)$$

In this formulation, then, the Jacobian matrix is a function of  $\Theta$ . The amount of information which must be stored at each integration point can be reduced by using the  $R$  coordinate as an intermediate value. Noting that  $Z$  is not a function of  $\Theta$ , the transformation becomes

$$\begin{Bmatrix} \frac{\partial}{\partial \xi} \\ \frac{\partial}{\partial \mu} \\ \frac{\partial}{\partial \Theta} \end{Bmatrix} = \begin{bmatrix} \frac{\partial R}{\partial \xi} \cos(\Theta) & \frac{\partial R}{\partial \xi} \sin(\Theta) & \frac{\partial Z}{\partial \xi} \\ \frac{\partial R}{\partial \mu} \cos(\Theta) & \frac{\partial R}{\partial \mu} \sin(\Theta) & \frac{\partial Z}{\partial \mu} \\ -R \sin(\Theta) & R \cos(\Theta) & 0 \end{bmatrix} \begin{Bmatrix} \frac{\partial}{\partial X} \\ \frac{\partial}{\partial Y} \\ \frac{\partial}{\partial Z} \end{Bmatrix}. \quad (4.10)$$

It is interesting to note that the determinant of the matrix above, known as the Jacobian, is the same as the two dimensional Jacobian in conventional axisymmetric formulations. Since from physical considerations the determinant must have a non-zero value, the inverse of this Jacobian matrix exists. Indeed, the inverse relationship may be expressed directly as

$$\begin{Bmatrix} \frac{\partial}{\partial X} \\ \frac{\partial}{\partial Y} \\ \frac{\partial}{\partial Z} \end{Bmatrix} = \begin{bmatrix} \frac{\partial \xi}{\partial X} & \frac{\partial \mu}{\partial X} & \frac{\partial \Theta}{\partial X} \\ \frac{\partial \xi}{\partial Y} & \frac{\partial \mu}{\partial Y} & \frac{\partial \Theta}{\partial Y} \\ \frac{\partial \xi}{\partial Z} & \frac{\partial \mu}{\partial Z} & \frac{\partial \Theta}{\partial Z} \end{bmatrix} \begin{Bmatrix} \frac{\partial}{\partial \xi} \\ \frac{\partial}{\partial \mu} \\ \frac{\partial}{\partial \Theta} \end{Bmatrix}. \quad (4.11)$$

The partial derivative of  $\Theta$  with respect to  $Z$  is trivial, since these two coordinates are independent. The derivatives of  $\Theta$  with respect to the other Cartesian coordinates are easily obtained using the transformation functions between the two systems:

$$\Theta = \tan^{-1}(X, Y), \quad R = \sqrt{X^2 + Y^2}. \quad (4.12)$$

Differentiating these relationships gives

$$\frac{\partial \Theta}{\partial X} = \frac{-\sin(\Theta)}{R}, \quad \frac{\partial \Theta}{\partial Y} = \frac{\cos(\Theta)}{R}, \quad (4.13a)$$

$$\frac{\partial R}{\partial X} = \cos(\Theta), \text{ and } \frac{\partial R}{\partial Y} = \sin(\Theta). \quad (4.13b)$$

Derivatives of the local coordinates ( $\xi, \mu$ ) with respect to Cartesian coordinates cannot be expressed directly, however, they can be expressed using the two dimensional Jacobian inverse components:



$$\frac{\partial \xi}{\partial X} = \frac{\partial R}{\partial X} \frac{\partial \xi}{\partial R}, \quad \frac{\partial \mu}{\partial X} = \frac{\partial R}{\partial X} \frac{\partial \mu}{\partial R}, \quad (4.14a)$$

$$\frac{\partial \xi}{\partial Y} = \frac{\partial R}{\partial Y} \frac{\partial \xi}{\partial R}, \text{ and } \frac{\partial \mu}{\partial Y} = \frac{\partial R}{\partial Y} \frac{\partial \mu}{\partial R}. \quad (4.14b)$$

Again, using the transformation functions,

$$\frac{\partial \xi}{\partial X} = \cos(\Theta) \frac{\partial \xi}{\partial R}, \quad \frac{\partial \mu}{\partial X} = \cos(\Theta) \frac{\partial \mu}{\partial R}. \quad (4.15a)$$

$$\frac{\partial R}{\partial Y} = \sin(\Theta) \frac{\partial \xi}{\partial R}, \text{ and } \frac{\partial \mu}{\partial Y} = \sin(\Theta) \frac{\partial \mu}{\partial R}. \quad (4.15b)$$

Substituting these transformation functions into the inverse three dimensional Jacobian matrix in Eq. (4.11) gives

$$\begin{Bmatrix} \frac{\partial}{\partial X} \\ \frac{\partial}{\partial Y} \\ \frac{\partial}{\partial Z} \end{Bmatrix} = \begin{bmatrix} \cos(\Theta) \frac{\partial \xi}{\partial R} & \cos(\Theta) \frac{\partial \mu}{\partial R} & \frac{-\sin(\Theta)}{R} \\ \sin(\Theta) \frac{\partial \xi}{\partial R} & \sin(\Theta) \frac{\partial \mu}{\partial R} & \frac{\cos(\Theta)}{R} \\ \frac{\partial \xi}{\partial Z} & \frac{\partial \mu}{\partial Z} & 0 \end{bmatrix} \begin{Bmatrix} \frac{\partial}{\partial \xi} \\ \frac{\partial}{\partial \mu} \\ \frac{\partial}{\partial \Theta} \end{Bmatrix} \quad (4.16)$$

Thus, the two dimensional Jacobian matrix inverse,  $[J]^{-1}$ , can be stored for each element and used to form the three dimensional Jacobian matrix inverse during integration of the element stiffness matrix. The two dimensional matrix is identical to that used in the cylindrical element or, for that matter, conventional axisymmetric or plane stress/strain elements.

It is important to note that the three dimensional Jacobian transformation is dependent upon  $\Theta$ . Consequently, the polynomial and Fourier interpolation functions cannot be completely separated in the complete interpolation function gradients as they were in the cylindrical formulation. Symbolically, the interpolation function gradient expressions are more complex. However, computationally, there is little difference in the implementation. Much of the same code can be used, and the gradients of the polynomial interpolation functions with respect to the R - Z coordinate system can still be used:

$$\frac{\partial N_c^{pf}}{\partial X} = \left[ \frac{\partial P_p}{\partial R} \cos(f\Theta) \cos(\Theta) + \frac{f}{R} P_p \sin(f\Theta) \sin(\Theta) \right] , \quad (4.17a)$$

$$\frac{\partial N_s^{pf}}{\partial X} = \left[ \frac{\partial P_p}{\partial R} \sin(f\Theta) \cos(\Theta) - \frac{f}{R} P_p \cos(f\Theta) \sin(\Theta) \right] , \quad (4.17b)$$

$$\frac{\partial N_c^{pf}}{\partial Y} = \left[ \frac{\partial P_p}{\partial R} \cos(f\Theta) \sin(\Theta) - \frac{f}{R} P_p \sin(f\Theta) \cos(\Theta) \right] , \quad (4.17c)$$

$$\frac{\partial N_s^{pf}}{\partial Y} = \left[ \frac{\partial P_p}{\partial R} \sin(f\Theta) \sin(\Theta) + \frac{f}{R} P_p \cos(f\Theta) \cos(\Theta) \right] , \quad (4.17d)$$

$$\frac{\partial N_c^{pf}}{\partial Z} = \frac{\partial P_p}{\partial Z} \cos(f\Theta) , \text{ and} \quad (4.17e)$$

$$\frac{\partial N_s^{pf}}{\partial Z} = \frac{\partial P_p}{\partial Z} \sin(f\Theta) . \quad (4.17f)$$

Thus, the displacement gradients are expressed in terms of the interpolation function derivatives:

$$\frac{\partial u_i}{\partial X_j} = \sum_{p=1}^{NP} \sum_{f=0}^{NF} \left[ \frac{\partial N_c^{pf}}{\partial X} u_c^{pf} + \frac{\partial N_s^{pf}}{\partial X} u_s^{pf} \right] . \quad (4.18)$$

#### 4.2.6. Vector Notation for Interpolation Functions

As with the cylindrical formulation, the convention used to arrange the nodal degrees of freedom is grouped first by harmonics, then within each harmonic by node, for each node into symmetric and antisymmetric parts, and finally within each part by x, y and z degrees of freedom. Clearly, with the degrees of freedom coupled by additional cosine and sine functions, even linear problems will not have decoupled harmonic stiffnesses, thus this arrangement provides no real advantage except that the program structure remains very similar to the cylindrical formulation,

$$\{u_i(\xi, \mu, \Theta)\} = [N(r, s, \Theta)] \{U\} . \quad (4.19)$$

The interpolation matrix is partitioned into harmonic parts,

$$[N(R,\Theta,Z)] = \left[ [N^0] [N^2] \dots [N^f] \dots [N^{NF}] \right] , \quad (4.20a)$$

and the harmonic parts into nodal harmonic parts,

$$[N^f] = \left[ [N^{1f}] [N^{2f}] \dots [N^{pf}] \dots [N^{Npf}] \right] , \quad (4.20b)$$

in which

$$[N^{pf}] = \begin{bmatrix} N_c^{pf} & 0 & 0 & N_s^{pf} & 0 & 0 \\ 0 & N_s^{pf} & 0 & 0 & N_c^{pf} & 0 \\ 0 & 0 & N_c^{pf} & 0 & 0 & N_s^{pf} \end{bmatrix} . \quad (4.20c)$$

Since the scale functions are unity in the Cartesian reference system, the unscaled spatial derivatives,  $[N'_u]$ , and the scaled derivatives,  $[N']$ , are the same. The displacement gradient tensor,  $\{D\}$ , can therefore be written in terms of nodal displacement amplitudes and interpolation function derivatives as indicated by Eq. (4.18) as

$$\{D_u\} = [N'] \{u\} \quad (4.21)$$

in which

$$\{D\} = \left\{ \begin{array}{c} \frac{\partial u_x}{\partial X} \\ \frac{\partial u_x}{\partial Y} \\ \frac{\partial u_x}{\partial Z} \\ \frac{\partial u_y}{\partial X} \\ \frac{\partial u_y}{\partial Y} \\ \frac{\partial u_y}{\partial Z} \\ \frac{\partial u_z}{\partial X} \\ \frac{\partial u_z}{\partial Y} \\ \frac{\partial u_z}{\partial Z} \end{array} \right\}. \quad (4.22)$$

The interpolation function derivative matrix is also partitioned into harmonic parts,

$$[N'_u(R,\Theta,Z)] = [ [N'_u{}^0] [N'_u{}^2] \dots [N'_u{}^f] \dots [N'_u{}^{NF}] ], \quad (4.23)$$

and each harmonic part into nodal harmonic parts,

$$[N'_u{}^f] = [ [N'_u{}^{1f}] [N'_u{}^{2f}] \dots [N'_u{}^{2pf}] \dots [N'_u{}^{Npf}] ], \quad (4.24)$$

where

$$[N'{}^p{}_u] = \begin{bmatrix} \frac{\partial N_c^{pf}}{\partial X} & 0 & 0 & \frac{\partial N_s^{pf}}{\partial X} & 0 & 0 \\ \frac{\partial N_c^{pf}}{\partial Y} & 0 & 0 & \frac{\partial N_s^{pf}}{\partial Y} & 0 & 0 \\ \frac{\partial N_c^{pf}}{\partial Z} & 0 & 0 & \frac{\partial N_s^{pf}}{\partial Z} & 0 & 0 \\ 0 & \frac{\partial N_s^{pf}}{\partial X} & 0 & 0 & \frac{\partial N_c^{pf}}{\partial X} & 0 \\ 0 & \frac{\partial N_s^{pf}}{\partial Y} & 0 & 0 & \frac{\partial N_c^{pf}}{\partial Y} & 0 \\ 0 & \frac{\partial N_s^{pf}}{\partial Z} & 0 & 0 & \frac{\partial N_c^{pf}}{\partial Z} & 0 \\ 0 & 0 & \frac{\partial N_c^{pf}}{\partial X} & 0 & 0 & \frac{\partial N_s^{pf}}{\partial X} \\ 0 & 0 & \frac{\partial N_c^{pf}}{\partial Y} & 0 & 0 & \frac{\partial N_s^{pf}}{\partial Y} \\ 0 & 0 & \frac{\partial N_c^{pf}}{\partial Z} & 0 & 0 & \frac{\partial N_s^{pf}}{\partial Z} \end{bmatrix} \quad (4.25)$$

In the symbolic representation of the nodal harmonic parts,  $[N'{}^p{}_u]$ , the superscript  $f$  refers to the  $f$ th harmonic component of the displacement vector. However, this does not mean that it contains only cosine ( $f\Theta$ ) and sine ( $f\Theta$ ) terms, because the derivative transformation to the Cartesian generate harmonic functions of  $(f-1)\Theta$  and  $(f+1)\Theta$  in  $[N'{}^p{}_u]$ .

The displacements and displacement gradients have now been expressed in terms of the interpolation functions and nodal displacement amplitudes. These are used in the following sections to develop matrix forms of the virtual work equation.

### 4.3. The Strain Representation

In Chapter 2 the finite element form of the virtual work equation was developed in general terms. Differential operator matrices were defined symbolically in Eqs. (2.36) and (2.39) which, combined with the interpolation matrix  $[N]$ , form the basic components of the stiffness matrix. In this section, the symbolic components of Eq. (2.43) are developed for the Cartesian coordinate system into matrix form suitable for computer implementation. The equations were developed in Chapter 2 for orthogonal

curvilinear coordinate systems. However, many of the additional terms are not required here, because there are no incremental scale function terms in the Cartesian formulation. This element is not new in terms of its variational formulation (which is the same as any conventional brick element), but is novel in terms of the mapping of the displacement field to the cylindrical geometry, and the Fourier decomposition of the displacement field in the circumferential direction, both of which were discussed in the previous section.

Because the coordinate transformations were developed to maintain as much similarity between cylindrical and Cartesian formulation, the finite element equations maintain a high degree of similarity. Some significant differences do exist however, and these are highlighted in this section.

#### 4.3.1. Small Strain Increment - Matrix Representation

The small strain increments defined in Eq. (2.22a), are written in matrix form as

$$\{\Delta \epsilon\} = [b]\{\Delta u\} = [[d] + [h]]\{\Delta u\} ,$$

where  $[d]$  is a differential operator matrix for the displacement gradient component of  $\{\epsilon\}$ , and  $[h]$  is the scale factor component. The complete matrix form of the small strain increment in Cartesian coordinates is:

$$\begin{Bmatrix} \Delta \epsilon_x \\ \Delta \epsilon_y \\ \Delta \epsilon_z \\ 2\Delta \epsilon_{xy} \\ 2\Delta \epsilon_{yz} \\ 2\Delta \epsilon_{xz} \end{Bmatrix} = \begin{bmatrix} \frac{\partial}{\partial X} & 0 & 0 \\ 0 & \frac{\partial}{\partial Y} & 0 \\ 0 & 0 & \frac{\partial}{\partial Z} \\ \frac{\partial}{\partial Y} & \frac{\partial}{\partial X} & 0 \\ 0 & \frac{\partial}{\partial Z} & \frac{\partial}{\partial Y} \\ \frac{\partial}{\partial Z} & 0 & \frac{\partial}{\partial X} \end{bmatrix} \begin{Bmatrix} \Delta u_x \\ \Delta u_y \\ \Delta u_z \end{Bmatrix} \quad (4.26)$$

There is no scale function increment component in this form, leaving only the displacement increment part, and only six strain terms need be considered, since the strain tensor is symmetric.

Eq. (4.19) gives the displacement field in terms of the nodal degrees of freedom using the interpolation matrix. Substituting this into the equation above, and combining the differential operator matrix and the interpolation matrix, the small strain vector is expressed in terms of a strain-displacement matrix,  $[B]$ , and the element displacement vector,  $\{\Delta U\}$ ,

$$\{\Delta \epsilon\} = [B]\{\Delta U\} , \text{ in which} \quad (4.27)$$

$$[B] = [b][N] .$$

Following the same conventions for partitioning the interpolation function matrix in Eqs. (4.20) for the interpolation function derivative matrix, the strain - displacement matrix is partitioned into harmonic parts,

$$[B] = \left[ [B^0] [B^1] \dots [B^f] \dots [B^{NF}] \right] , \quad (4.28a)$$

and each harmonic part into nodal harmonic parts,

$$[B^f] = \left[ [B^{0f}] [B^{1f}] \dots [B^{pf}] \dots [B^{Npf}] \right] , \quad (4.28b)$$

where  $[B^{pf}]$  is the strain-displacement matrix associated with node  $p$  and harmonic  $f$ . Each nodal harmonic submatrix has six columns, the first three columns associated with symmetric degrees of freedom, the last three with the antisymmetric degrees of freedom. Thus each nodal harmonic part can be subdivided into these two parts,

$$[B^{pf}] = \left[ [B_s^{pf}] [B_a^{pf}] \right] , \quad (4.28c)$$

where the symmetric part,  $[B_s^{pf}]$ , is given as

$$[B_s^{pf}] = \begin{bmatrix} \frac{\partial N_c^{pf}}{\partial X} & 0 & 0 \\ 0 & \frac{\partial N_s^{pf}}{\partial Y} & 0 \\ 0 & 0 & \frac{\partial N_c^{pf}}{\partial Z} \\ \frac{\partial N_c^{pf}}{\partial Y} & \frac{\partial N_s^{pf}}{\partial X} & 0 \\ 0 & \frac{\partial N_s^{pf}}{\partial Z} & \frac{\partial N_c^{pf}}{\partial Y} \\ \frac{\partial N_c^{pf}}{\partial Z} & 0 & \frac{\partial N_c^{pf}}{\partial X} \end{bmatrix}, \quad (4.29)$$

and the antisymmetric part,  $[B_s^{pf}]$ , is the same, except that  $N_c^{pf}$  is replaced by  $N_s^{pf}$ , and vice versa. Thus, the infinitesimal strain increments are essentially expressed as a sum of nodal harmonic components,

$$\{\Delta \epsilon\} = \sum_{f=1}^{NF} \sum_{p=1}^{NP} \{\Delta \epsilon^{pf}\}, \quad (4.30a)$$

where the nodal harmonic strain increments,  $\{\Delta \epsilon^{pf}\}$ , are given by

$$\{\Delta \epsilon^{pf}\} = [B^{pf}]\{u^{pf}\}. \quad (4.30b)$$

The strain increment vector,  $\{\Delta \epsilon^{pf}\}$ , is the component of the strain vector associated with the  $f$ th harmonic displacement amplitude at node  $p$  and  $\{u^{pf}\}$  is the nodal harmonic displacement vector.

#### 4.3.2. Nonlinear Strain Increment Component

The component of the strain increment tensor which depends on the displacement gradient tensor was defined as  $\Delta \epsilon'_{ij}$  in Eq. (2.22b). It includes components of the displacement gradient tensor,  $D_{ij}$ , or in vector form  $\{D\}$  which was defined in Cartesian coordinates by Eq. (4.22).

The procedure to develop the small strain - displacement matrix,  $[B]$  also applies to the nonlinear strain-displacement matrix,  $[B']$ . The nodal harmonic part of  $[B]$  was shown to be similar in form to the small strain differential operator matrix, and the same



is true for  $[B']$ . Therefore, the intermediate steps to arriving at the nodal harmonic part are not shown, and the symmetric part of  $[B_s^{pf}]$  is presented directly:

$$[B_s^{pf}] = \begin{bmatrix} D_{11} \frac{\partial N_c^{pf}}{\partial X} & D_{21} \frac{\partial N_s^{pf}}{\partial X} & D_{31} \frac{\partial N_c^{pf}}{\partial X} \\ D_{12} \frac{\partial N_c^{pf}}{\partial Y} & D_{22} \frac{\partial N_s^{pf}}{\partial Y} & D_{32} \frac{\partial N_c^{pf}}{\partial Y} \\ D_{13} \frac{\partial N_c^{pf}}{\partial Z} & D_{23} \frac{\partial N_s^{pf}}{\partial Z} & D_{33} \frac{\partial N_c^{pf}}{\partial Z} \\ \left( D_{12} \frac{\partial N_c^{pf}}{\partial X} + D_{11} \frac{\partial N_c^{pf}}{\partial Y} \right) & \left( D_{22} \frac{\partial N_s^{pf}}{\partial X} + D_{21} \frac{\partial N_s^{pf}}{\partial Y} \right) & \left( D_{32} \frac{\partial N_c^{pf}}{\partial X} + D_{31} \frac{\partial N_c^{pf}}{\partial Y} \right) \\ \left( D_{13} \frac{\partial N_c^{pf}}{\partial Y} + D_{12} \frac{\partial N_c^{pf}}{\partial Z} \right) & \left( D_{23} \frac{\partial N_s^{pf}}{\partial Y} + D_{22} \frac{\partial N_s^{pf}}{\partial Z} \right) & \left( D_{33} \frac{\partial N_c^{pf}}{\partial Y} + D_{32} \frac{\partial N_c^{pf}}{\partial Z} \right) \\ \left( D_{11} \frac{\partial N_c^{pf}}{\partial Z} + D_{13} \frac{\partial N_c^{pf}}{\partial X} \right) & \left( D_{21} \frac{\partial N_s^{pf}}{\partial Z} + D_{23} \frac{\partial N_s^{pf}}{\partial X} \right) & \left( D_{31} \frac{\partial N_c^{pf}}{\partial Z} + D_{33} \frac{\partial N_c^{pf}}{\partial X} \right) \end{bmatrix} \quad (4 - 31)$$

With the infinitesimal and deformation gradient strains defined in terms of element nodal degrees of freedom, the element linear stiffness matrix can be evaluated and integrated using an appropriate numerical integration technique.

#### 4.3.3. Linear Stiffness Matrix

The linear stiffness matrix is the integral over the element volume of the matrix expression  $[B_L]^T [C] [B_L]$ . The matrix  $[B_L]$  is the sum of  $[B]$  and  $[B']$  which were developed above. The linear stiffness matrix can be integrated using the same numerical techniques discussed in chapter 3. The geometric stiffness matrix can also be integrated simultaneously, and its development follows in the next section.

#### 4.3.4. Geometric or Nonlinear Stiffness Matrix

In Chapter 2 the geometric stiffness matrix was shown to be composed of three parts corresponding to the three different parts of the second order strain increment variation in Eq. (2.23). Only the first part is required in the Cartesian system, because there are no scale function increments. The same stress matrix is used again to form the geometric stiffness matrix:

$$[S] = \begin{bmatrix} [s] & [0] & [0] \\ [0] & [s] & [0] \\ [0] & [0] & [s] \end{bmatrix}, \quad [s] = \begin{bmatrix} S_{xx} & S_{xy} & S_{xz} \\ S_{yx} & S_{yy} & S_{yz} \\ S_{zx} & S_{zy} & S_{zz} \end{bmatrix}. \quad (4.32)$$

The displacement operator matrix which forms the basis of the geometric stiffness matrix is also formulated in terms of the interpolation functions, just as the small strain differential operator matrix was, and the intermediate steps to arrive at the nonlinear strain-displacement matrix are again omitted. The nodal harmonic parts of this matrix are presented directly:

$$[B_G^{pf}] = \begin{bmatrix} \frac{\partial N_c^{pf}}{\partial X} & 0 & 0 & \frac{\partial N_s^{pf}}{\partial X} & 0 & 0 \\ \frac{\partial N_c^{pf}}{\partial Y} & 0 & 0 & \frac{\partial N_s^{pf}}{\partial Y} & 0 & 0 \\ \frac{\partial N_c^{pf}}{\partial Z} & 0 & 0 & \frac{\partial N_s^{pf}}{\partial Z} & 0 & 0 \\ 0 & \frac{\partial N_s^{pf}}{\partial X} & 0 & 0 & \frac{\partial N_c^{pf}}{\partial X} & 0 \\ 0 & \frac{\partial N_s^{pf}}{\partial Y} & 0 & 0 & \frac{\partial N_c^{pf}}{\partial Y} & 0 \\ 0 & \frac{\partial N_s^{pf}}{\partial Z} & 0 & 0 & \frac{\partial N_c^{pf}}{\partial Z} & 0 \\ 0 & 0 & \frac{\partial N_c^{pf}}{\partial X} & 0 & 0 & \frac{\partial N_s^{pf}}{\partial X} \\ 0 & 0 & \frac{\partial N_c^{pf}}{\partial Y} & 0 & 0 & \frac{\partial N_s^{pf}}{\partial Y} \\ 0 & 0 & \frac{\partial N_c^{pf}}{\partial Z} & 0 & 0 & \frac{\partial N_s^{pf}}{\partial Z} \end{bmatrix}. \quad (4.33)$$

There are no scale function and mixed parts for the geometric stiffness matrix because the scale function increments are zero. The complete matrix is assembled from these nodal harmonic parts just as the linear strain-displacement matrix was assembled in Eq. (3.26). This displacement gradient matrix has the same general form as the geometric stiffness matrix for Bathe's, 1982 three dimensional solid element . The main

difference lies in the Fourier interpolation functions and the number of degrees of freedom.

#### 4.4. Integration

Integration of the stiffness matrix functions in this chapter uses essentially the same procedures as those developed in the previous chapter for the cylindrical formulation element. Integration in the axisymmetric plane is performed using Gauss quadrature, and trapezoidal integration is applied in the circumferential direction. The general form of the Cartesian stiffness functions have a slightly different form, however, requiring some modifications to the rules regarding the number of trapezoidal integration points. The interpolation functions presented in Eq. (4.8) have the same form as that used in the cylindrical formulation. However, when the interpolation function gradients are transformed from the local  $(\xi, \mu, \Theta)$  system to global  $(X, Y, Z)$  coordinates by Eq. (4.17), additional sine and cosine functions are included.

The harmonic parts of the linear strain displacement matrix could thus be separated, not into just sine and cosine parts as it was in the cylindrical formulation, but instead into four parts to accommodate the additional sine and cosine terms;

$$[B] = [B^0] [B^1] \dots [B^f] \dots [B^{NF}] ,$$

where the harmonic part  $[B^f]$  is given in terms of the components associated with each Fourier product,

$$[B^f] = [B_{cc}^f] \cos(f\Theta) \cos(\Theta) + [B_{cs}^f] \cos(f\Theta) \sin(\Theta) \\ + [B_{sc}^f] \sin(f\Theta) \cos(\Theta) + [B_{ss}^f] \sin(f\Theta) \sin(\Theta).$$

Applying the trigonometric identity used to develop the integration rules in Chapter 3, the harmonic parts of the linear strain displacement matrix are expressed in an alternate four part form;

$$[B^f] = [B_{c+}^f] \cos((f+1)\Theta) + [B_{c-}^f] \cos((f-1)\Theta) \\ + [B_{s+}^f] \sin((f+1)\Theta) + [B_{s-}^f] \sin((f-1)\Theta) .$$

When the linear stiffness matrix is integrated, the harmonic coupling stiffnesses are nonzero only in the case where

$$[K_{nm}] \neq 0, \quad n \pm 1 = m \pm 1 .$$

The stiffness matrix form is therefore

$$[K] = \begin{bmatrix} [K_{01}] & [K_{01}] & 0 & & \dots & 0 \\ [K_{10}] & [K_{11}] & [K_{12}] & 0 & \dots & 0 \\ 0 & [K_{10}] & [K_{11}] & [K_{12}] & 0 & \dots & 0 \\ \vdots & & & \ddots & & \vdots \\ 0 & \dots & 0 & [K_{ff(f-1)}] & [K_{ff}] \end{bmatrix}.$$

While some degree of decoupling is achieved, the storage required for the linear stiffness matrix is triple that of the linear cylindrical formulation stiffness matrix in terms of the harmonic coupling. However, in real models, nodal coupling must also be taken into consideration, making the savings in the structure stiffness matrix bandwidth and solution time negligible compared with the fully coupled stiffness matrix. The only real savings result from the ability to analytically integrate the element in the circumferential direction and from the reduction in the number of element submatrices which must be evaluated. Compared with the small displacement, linear elastic cylindrical formulation, this formulation has increased computational requirements, but no modelling advantages, and therefore is not considered further.

#### 4.4.1. Nonlinear Non-Axisymmetric Integration

With nonlinear problems, much of the integration advantage is lost in the cylindrical formulation because the harmonic stiffnesses are coupled, and numerical integration is required as a consequence. The additional coupling of the Cartesian formulation demonstrated in the linear case above, should impose little, if any, additional overhead in such cases, and it would seem that the simplified finite element equations would be less difficult to evaluate in the numerical integration process.

Recalling from Chapter 3, the number of trapezoidal integration points required to exactly integrate the finite element equations in the circumferential direction was  $\gamma_{\max} + 1$ , where  $\gamma_{\max}$  is the maximum value of the sum of Fourier numbers in the stiffness equation  $[B+B']^T[C][B+B']$ . For example, a full nonlinear problem modelled using the cylindrical formulation with  $F$  harmonics for the displacement field and material properties gives a maximum value for  $\gamma$  of  $5F$ : each  $[B+B']$  has a maximum Fourier number of  $2F$ , and the constitutive matrix would use  $F$  harmonics. The  $[B]$  matrix actually has a maximum Fourier number of  $F$ , but it is added to  $[B']$  (containing  $2F$

harmonics) before the matrix product with  $[C]$  is formed. The  $[B']$  matrix has a maximum Fourier number of  $2F$  because it includes products of the displacement gradients interpolation function derivatives, each of which has a harmonic number of  $F$ .

The number of integration points in the circumferential direction increases slightly in the Cartesian formulation. The additional cosine and sine functions introduced to the interpolation gradient functions of Eq. (4.17) by the three dimensional transformation from the local coordinate system effectively adds an additional Fourier function to the strain-displacement matrix,  $[B]$ , and to the deformation gradient part,  $[B']$ . Therefore, for an equivalent full nonlinear problem,  $\gamma_{\max}$  increases to  $5F + 4$ .

The circumferential integration rules may then be summarized as follows:

**Linear, small displacement analysis:** Product of two Fourier functions may be integrated analytically, or numerically using  $2*NF+3$  circumferential integration points, where  $NF$  is the number of harmonics to be modelled. The cylindrical formulation should be utilized for these problems because of the greater degree of harmonic decoupling it provides.

**Small displacement, material nonlinear analysis:** Product of three Fourier functions is integrated.  $3*NF+3$  integration points will model a material variation of the same order as the displacement variation. More circumferential points will improve the circumferential representation of the material by increasing the effective number of Fourier terms in the material model.

**Large displacement, linear material analysis:** Deformation gradient strain-displacement matrix includes products of two Fourier functions, each with a maximum Fourier number of  $NF+1$ , thus the stiffness matrix must integrate four Fourier functions. Therefore,  $4*NF+5$  integration points will exactly integrate the stiffness matrix in the circumferential direction.

**Large displacement, material nonlinear analysis:** Two Fourier functions from the strain - displacement matrix and one from the constitutive matrix produce a total of five Fourier functions which must be integrated. This requires  $5*NF+5$  integration points to model material variation equivalent to displacement variation in the circumferential direction.

The element uses the usual polynomial serendipity functions in the axisymmetric plane, for which Gauss quadrature provides the most effective integration. Thus, the integration formula is expressed as

$$[K_{el}] = \int_{V_{el}} [K] dV = w_T R \sum_{i=1}^{NG_r} \sum_{j=1}^{NG_s} w_i w_j |J| \sum_{k=1}^{NT} [K_{ijk}] , \quad (4.34)$$

where  $NG_r$  and  $NG_s$  are the number of Gauss points in the  $r$  and  $s$  directions of the element in local coordinate space,  $NT$  is the number of circumferential sampling points,  $w_i$  and  $w_j$  are the usual Gauss quadrature weighting factors, and  $w_T$  is the weighting factor for trapezoidal integration, which is simply  $2\pi/NT$ . The matrix  $[K_{ijk}]$  is the stiffness matrix function evaluated at the integration point:

$$[K_{ijk}] = [B_L(r_i, s_j, \Theta_k)]^T [C] [B_L(r_i, s_j, \Theta_k)] + [B_G(r_i, s_j, \Theta_k)]^T [S] [B_G(r_i, s_j, \Theta_k)] . \quad (4.35)$$

The coordinate values of  $r_i$  and  $s_j$  are the Gauss integration point coordinates, and  $\Theta_k$  are the circumferential integration locations,  $(k-1)(2\pi/NT)$ .

This completes the formulation of the Fourier decomposition element in Cartesian coordinates. The matrix equations required to generate the element stiffness matrix are less complex than the equations developed for the cylindrical formulation. This advantage is offset by increased integration demands, and imposes equivalent computation demands. However, the displacement field in Cartesian coordinates models exactly rigid body motion in the zero'th and first harmonics, making it much more powerful for modelling large displacement problems, and more efficient than conventional finite element formulations.

#### 4.5. Boundary Conditions

Boundary condition considerations are, for the most part, the same for the Cartesian formulation as they were for the cylindrical formulation. Often, however, the loading applied to the axisymmetric finite element model, will be given in terms of the cylindrical coordinate system, and these loads must be transformed to a Cartesian equivalent form. The  $z$  dimension is the same in Cartesian and cylindrical coordinates, but the transformations between  $r$  and  $\theta$  dimensions are performed by the harmonic functions, cosine and sine. Consequently, loads of the  $F$ 'th harmonic in the  $r$  and  $\theta$

directions will be transformed to loads in the (F-1) and (F+1) harmonic in the x and y directions.

For example, consider a total pressure distribution on the surface of an element. Assume, in the general case, that the variation in the circumferential direction has been decomposed into harmonic components:

$$p(\Theta) = \sum_{f=0}^{NF} p_c^f \cos(f\Theta) + p_s^f \sin(f\Theta) . \quad (4.36)$$

At any point on the circumference, the normal pressure applied to the surface can be expressed in terms of its Cartesian components (Figure 4.1):

$$T_x = R p(\Theta) \cos(\Theta) dRdZ ,$$

$$T_y = R p(\Theta) \sin(\Theta) dRdZ , \text{ and}$$

$$T_z = R p(\Theta) dRdZ .$$

The finite element expression for the load vector integrates the product of the traction functions and the interpolation function matrix. Integrating with respect to  $\Theta$ ,

$$\{F\} = \int_{-\pi}^{\pi} [N]^T \{T\} d\Theta .$$

The interpolation matrix was shown partitioned into harmonic parts. Similarly, partitioning the load vector into harmonic parts and expanding  $\{T\}$  into a Fourier series, the element load vector can be separated into harmonic parts. The part associated with the  $f$ th harmonic is expressed as

$$\{F^f\} = \sum_{g=0}^{NF} \int_{-\pi}^{\pi} [N^g]^T \{T^f\} d\Theta .$$

Separating  $[N]$  and  $\{T\}$  into sine and cosine components, and moving the Fourier functions outside the matrices:

$$\{F_{cc}^f\} = \sum_{g=0}^{NF} \int_{-\pi}^{\pi} \left[ [N_c^g]^T \begin{Bmatrix} T_{xc}^f \cos(\Theta) \\ T_{yc}^f \sin(\Theta) \\ T_{zc}^f \end{Bmatrix} \cos(g\Theta) \cos(f\Theta) \right] d\Theta ,$$

where  $\{F_{cc}^f\}$  is the component of  $\{F^f\}$  from the cosine parts of  $[N]$  and  $p(\Theta)$ . Three more components,  $\{F_{cs}^f\}$ ,  $\{F_{sc}^f\}$ , and  $\{F_{ss}^f\}$ , have the same form with sine replacing cosine in the integral when  $s$  replaces  $c$  in the subscripts of  $\{F\}$ . The rules used by Chan and Trbojevic, 1975, and extended in the previous chapter are then applied here:

$$\int_{-\pi}^{\pi} \cos(a\Theta) \cos(g\Theta) \cos(f\Theta) d\Theta = \begin{cases} 0 & \text{for } a = g = f = 0 \\ \pi & \text{for } a = 0, g = f \\ \pi/2 & \text{for } \pm(f - g) = 1 \text{ and } a=1 \end{cases} , \quad (4.37a)$$

$$\int_{-\pi}^{\pi} \cos(a\Theta) \sin(g\Theta) \sin(f\Theta) d\Theta = \begin{cases} \pi & \text{for } a = 0 \text{ and } g = f \\ \pi/2 & \text{for } a = 1 \text{ and } \pm(f - g) = 1 \end{cases} , \quad (4.37b)$$

$$\int_{-\pi}^{\pi} \sin(a\Theta) \sin(g\Theta) \cos(f\Theta) d\Theta = \begin{cases} \pi/2 & \text{for } a = 1 \text{ and } g - 1 = f \\ -\pi/2 & \text{for } a = 1 \text{ and } g + 1 = f \end{cases} , \quad (4.37c)$$

$$\int_{-\pi}^{\pi} \sin(a\Theta) \cos(g\Theta) \sin(f\Theta) d\Theta = \begin{cases} \pi/2 & \text{for } a = 1 \text{ and } f - 1 = g \\ -\pi/2 & \text{for } a = 1 \text{ and } f + 1 = g \end{cases} , \text{ and} \quad (4.37d)$$

$$\int (\text{other combinations of sin and cos}) = 0 . \quad (4.37e)$$

Thus a harmonic variation in axial tractions will appear as nodal harmonic equivalent loads in the corresponding harmonic of the load vector,  $\{F\}$ , as one might intuitively expect. Radial traction components, however, have no nodal harmonic equivalent loads in corresponding harmonic parts of the load vector. Equivalent forces appear instead in the harmonics immediately before and after that which corresponds to the harmonic variation. The results chapter also illustrates this transformation phenomenon in the displacement pattern. An elastic wave in the circumferential direction with an angular wavelength of  $2\pi/N$  requires  $N + 1$  harmonics to model such behaviour.



These results demonstrate that the Cartesian formulation imposes more overhead, relative to the cylindrical formulation, than just increasing the number of circumferential integration points. It also demands an additional harmonic be included for a given harmonic response, and this additional harmonic also implies even more trapezoidal integration points should be added.

#### 4.6. Transformation to Cylindrical Degrees of Freedom

The formulation in this chapter has been based on a cylindrical geometrical description, but used Cartesian displacement, stress and strain components to simplify the development of the nonlinear finite element equations. Given the stresses at integration points, the procedure for transforming the stress components to a cylindrical reference system is straight forward. Also, given the Cartesian displacements at a point, the transformation to cylindrical displacements is also a simple task. These results transformations may be useful in interpreting the behaviour of the structure, but obviously have no impact on the implementation of the formulation.

Often the mechanical behaviour can be expressed more efficiently in terms of a cylindrical system. For example, thin shells of revolution will buckle into axial and circumferential waves. The circumferential waves in particular, are best expressed in terms of cylindrical components. In contrast, using Cartesian components requires the X and Y degrees of freedom in the harmonics above and below the equivalent radial harmonic degree of freedom.

Consider the displacement transformation shown in **Figure 4.2**. The displacement vector is shown in terms of the Cartesian components, and in terms of displacement components which are coincident with the cylindrical coordinate system at the point considered. The latter components are equivalent to the physical displacements used in the small displacement cylindrical formulation. However, when used in a large displacement formulation, these components should not be referred to as physical cylindrical displacements. A preferred description is to refer to them as transformed displacements. In the following, only the symmetric parts of the displacement field will be considered, though certainly the same development can be applied to the antisymmetric part as well.

The relationship between Cartesian and transformed displacements is

$$u_x = u_r \cos(\theta) - u_\theta \sin(\theta) , \quad (4.38a)$$

$$u_y = u_r \sin(\theta) + u_\theta \cos(\theta) , \quad (4.38b)$$

$$u_r = u_x \cos(\theta) + u_y \sin(\theta) , \text{ and} \quad (4.39a)$$

$$u_\theta = -u_x \sin(\theta) + u_y \cos(\theta) . \quad (4.39b)$$

The symmetric parts of the X and Y components of the circumferential displacement field are interpolated using Eq. (4.4);

$$u_x = \sum_{f=0}^{\infty} u_{xc}^f(R,Z) \cos(f\Theta) \quad \text{and} \quad (4.40a)$$

$$u_y = \sum_{f=1}^{\infty} u_{ys}^f(R,Z) \sin(f\Theta) . \quad (4.40b)$$

Substituting these into the displacement transformations in Eq. (4.39) gives the interpolated transformed displacement field;

$$u_r = \sum_{f=0}^{\infty} u_{xc}^f \cos(f\Theta) \cos(\Theta) + \sum_{f=1}^{\infty} u_{ys}^f \sin(f\Theta) \sin(\Theta) \text{ and} \quad (4.41a)$$

$$u_\theta = \sum_{f=0}^{\infty} u_{xc}^f \cos(f\Theta) \sin(\Theta) + \sum_{f=1}^{\infty} u_{ys}^f \sin(f\Theta) \cos(\Theta) \quad (4.41b)$$

Applying the trigonometric identities, the transformed displacement field is given as

$$2u_r = \sum_{f=0}^{\infty} u_{xc}^f \left( \cos((f+1)\Theta) + \cos((f-1)\Theta) \right) - \sum_{f=1}^{\infty} u_{ys}^f \left( \cos((f+1)\Theta) - \cos((f-1)\Theta) \right) \quad (4.42a)$$

$$2u_\theta = \sum_{f=0}^{\infty} u_{xc}^f \left( -\sin((f+1)\Theta) + \sin((f-1)\Theta) \right) + \sum_{f=1}^{\infty} u_{ys}^f \left( \sin((f+1)\Theta) - \sin((f-1)\Theta) \right) \quad (4.42b)$$

The transformed displacements can also be expressed in terms of a Fourier series. The symmetric part of the transformed displacement field is

$$u_r = \sum_{f=0}^{\infty} u_{rc}^f(R,Z) \cos(f\Theta) \quad \text{and} \quad (4.43a)$$

$$u_{\theta} = \sum_{f=1}^{\infty} u_{\theta s}^f(R,Z) \sin(f\Theta) . \quad (4.43b)$$

Thus a relationship between the Cartesian nodal harmonic component degrees of freedom and the transformed nodal harmonic component degrees of freedom can be seen to be

$$u_{rc}^f = \frac{1}{2} ( u_{xc}^{f-1} - u_{ys}^{f-1} + u_{xc}^{f+1} + u_{ys}^{f+1} ), \quad f=2, 3, \dots, \infty , \text{ and} \quad (4.44a)$$

$$u_{\theta c}^f = \frac{1}{2} ( -u_{xc}^{f-1} + u_{ys}^{f-1} + u_{xc}^{f+1} + u_{ys}^{f+1} ), \quad f=2, 3, \dots, \infty . \quad (4.44b)$$

Note that these relationships are given for the second harmonic and above. If the expressions produced by the trigonometric identities are considered carefully, it will be seen that they may be applied correctly to the zero'th and first harmonic. However, the relationship between nodal harmonic degrees of freedom must be given explicitly. The first harmonic relationships are therefore

$$u_{rc}^0 = ( u_{xc}^1 + u_{ys}^1 ), \quad (4.45a)$$

$$u_{rc}^1 = u_{xc}^0 + \frac{1}{2} ( u_{xc}^2 + u_{ys}^2 ), \text{ and} \quad (4.46b)$$

$$u_{\theta c}^1 = -u_{xc}^0 + \frac{1}{2} ( u_{xc}^1 + u_{ys}^1 ) . \quad (4.47c)$$

The reader is reminded that the superscripts refer to Fourier number, rather than an exponent.

These simple transformations are easily expressed in matrix form,

$$\{u_n\} = [T] \{u_{xy}\} , \quad (4.48)$$

where  $\{u_{xy}\}$  are the Cartesian nodal harmonic degrees of freedom,  $[T]$  is the transformation matrix and  $\{u_n\}$  are the transformed degrees of freedom. This matrix equation can be used directly with the Cartesian formulation to easily provide equivalent cylindrical displacement components. The transformation can also be used to transform the load vector to equivalent cylindrical components.

The transformation equation can also be inverted. By doing so, the Cartesian displacement gradient, stress, strains, and so forth may be evaluated in terms of transformed cylindrical displacements. Consider for example the strains. The matrix equation,

$$\{\epsilon\} = [B]\{u_{xy}\} , \quad (4.49)$$

is used to give the strains in terms of the nodal harmonic degrees of freedom. Using the inverse transformation equation, the strains may also be expressed in terms of the transformed nodal harmonic degrees of freedom;

$$\{\epsilon\} = [B][T]^{-1}\{u_n\} , \text{ or} \quad (4.50)$$

$$\{\epsilon\} = [B_n]\{u_n\} , \quad (4.51)$$

where  $[B_n]$  is the strain-displacement matrix transformed in terms of the cylindrical displacement components. The strains,  $\{\epsilon\}$ , however, remain Cartesian.

It is possible to evaluate the finite element equations, either on a global or element level, and then transform the system in terms of cylindrical displacements and loads. Consider for example the global system of equations,

$$[K_{xy}]\{u_{xy}\} = \{F_{xy}\} . \quad (4.52)$$

Using the inverse transformation to replace the Cartesian displacements with cylindrical components, and premultiplying both sides of the equation by the transpose, inverse transformation matrix, and noting that the transpose of the transformation matrix is equal to the inverse of the transformation matrix, the global system becomes

$$([T]^T)^{-1}[K_{xy}][T]^{-1}\{u_n\} = [T]\{F_{xy}\} , \text{ or} \quad (4.53)$$

$$[K_n]\{u_n\} = \{F_n\} , \quad (4.54)$$

where  $[K_n]$  is the stiffness matrix transformed in terms of the cylindrical displacements.

There is no economy, in performing this transformation unless the behaviour is adequately described by a few harmonic components in the cylindrical reference system. In such cases, however, it hardly makes any sense to develop the complete system of equations (or a complete element for that matter) using all harmonics, perform the transformation, and then discard the unnecessary degrees of freedom. Instead, the logical approach to take would be to evaluate the transformed strain-displacement with the required harmonics, and use this to directly evaluate the transformed linear stiffness matrix. Likewise, a transformed geometric stiffness matrix could be evaluated directly with only the required harmonics.

Of course, these additional transformations do not alter the underlying Cartesian formulation, only the degrees of freedom which are used to describe the behaviour. These transformed degrees of freedom exist in a cylindrical reference system. However, although they represent a physical displacement in a cylindrical reference system, they are not physical, cylindrical displacement components. It was shown in Chapter 3 that physical, cylindrical displacements could not be properly defined because of complications arising from the scale functions.

#### **4.7. Cartesian Formulation Summary**

The Fourier decomposition element in a Cartesian reference system is complete. The formulation is similar to the cylindrical element developed in the previous chapter, but the finite element equations are considerably less complex since the scale functions do not introduce any incremental terms. It was also shown that the transformation to Cartesian displacements makes loading functions and boundary conditions somewhat more difficult for this element. The same integration procedures can be applied, but additional circumferential integration points must be used for the Cartesian formulation, because of the Fourier functions used to transform gradients from the local coordinate system to the global Cartesian system. It was noted that an additional harmonic must be added to the system of equations to model a given degree of circumferential variation in response because of this transformation.

It was also shown that the Cartesian form of the finite element equations could be transformed back in terms of physical displacements and forces in a cylindrical reference system. Although the transformed displacements are in a cylindrical reference system they are not cylindrical physical displacements. The transformation is useful for problems, such as thin shell problems, where the behaviour is adequately described by a

few transformed harmonics, requiring fewer degrees of freedom relative to an untransformed system of equations. In most problems, however, all of the harmonics below a certain number will be required for an acceptable solution. In such cases, the coordinate transformation imposes additional overhead, with providing any improvement in the solution. In these situations, a simple transformation of the output displacements may be all the cylindrical response information that is required.

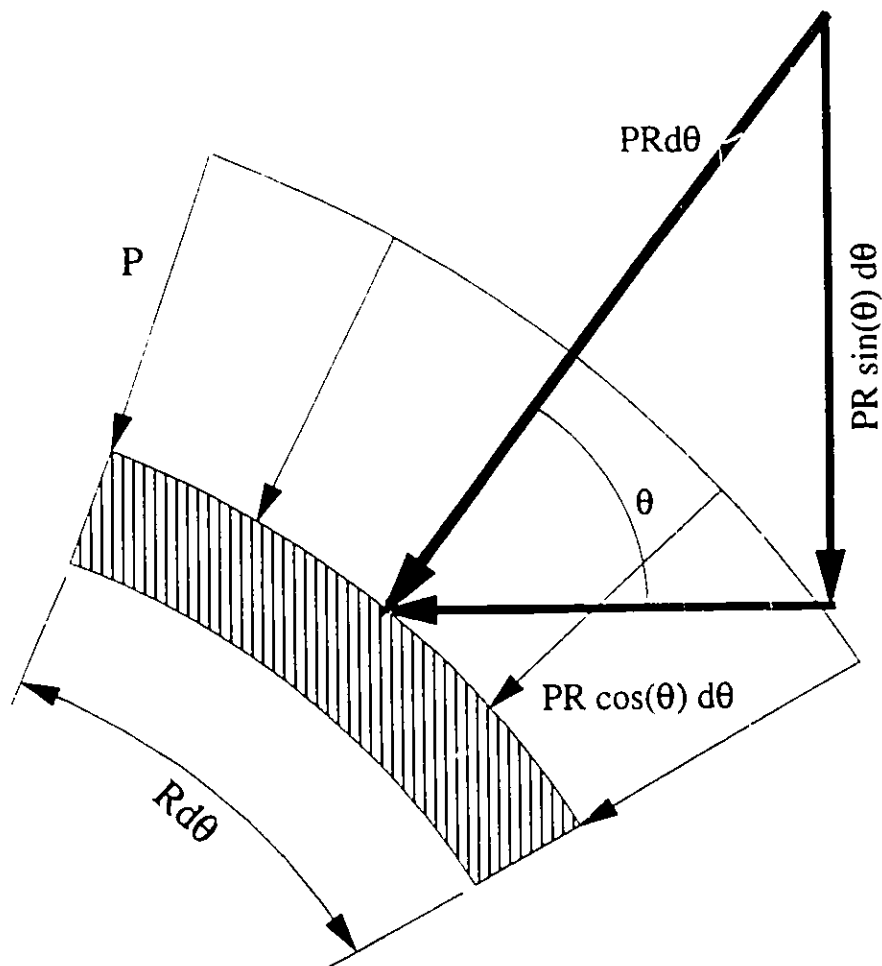
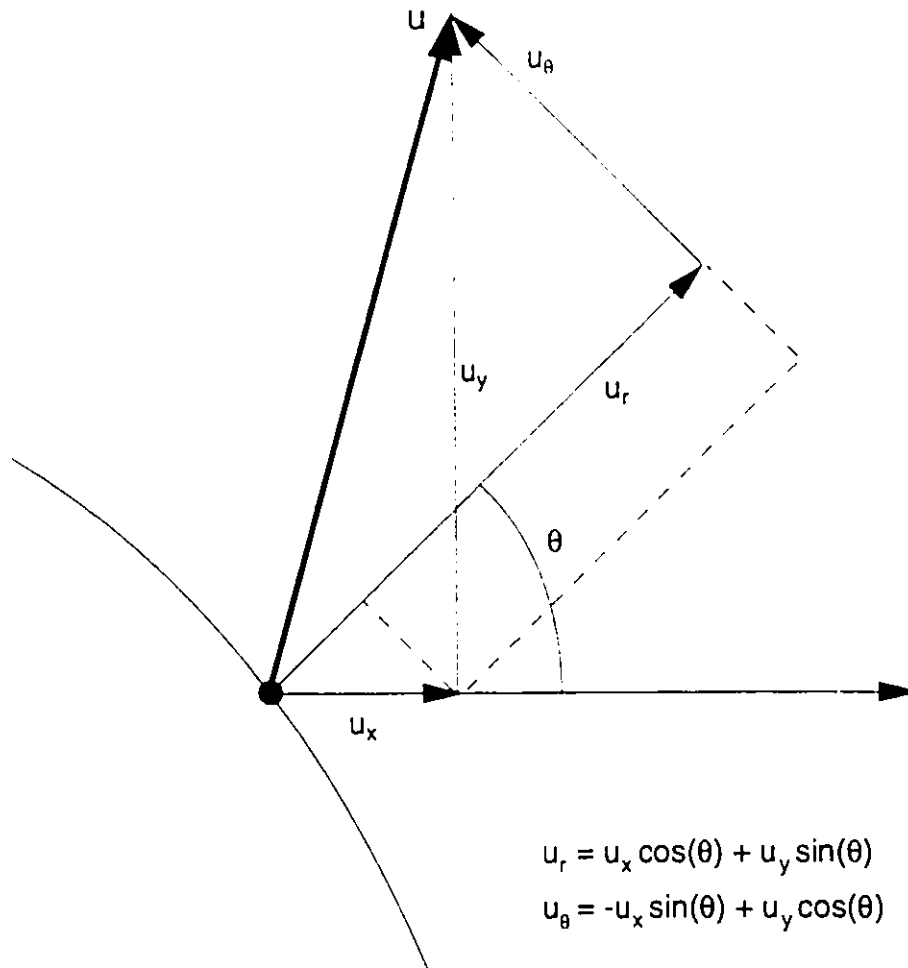


Figure 4.1      Decomposition of radial pressure into Cartesian components



**Figure 4.2** Transformation between Cartesian and cylindrical displacements



## **5. Program "Static Lagrangian Analysis of Tubular Structures (SLATS)"**

A finite element program was written to evaluate the performance of the Harmonic Lagrangian Tubular (HLT) element developed in the Chapters 2, 3 and 4 for modelling large displacement behaviour of axisymmetric structures. The program is essentially a vehicle for assembling and solving the nonlinear finite element equations generated by the element for the structure. It was written in the Fortran 77 programming language, developed primarily on a DOS based personal computer, and later ported to OS/2, Unix and Macintosh operating systems. No extensions to the Fortran standard were utilized so that the code would remain portable. However, some matrix subroutines were replaced with hardware specific vector calls in the Apollo version to improve performance.

This chapter discusses the organization and capabilities of the finite element program used to test the formulation. A basic description of the program organization is provided by the flow charts at the end of this chapter.

### **5.1. The Harmonic Lagrangian Tubular (HLT) Finite Element**

#### **5.1.1. General Description**

The element geometry is identical to the shape of conventional axisymmetric finite elements used for assembling axisymmetric models. Although solid elements are evaluated in this study, the same Fourier decomposition techniques could be applied to shell elements. Both Cartesian and cylindrical formulations were implemented, sharing most of the same program code, with the exception of the subroutines which evaluate the strain-displacement matrices, and the geometric stiffness matrix. The intent of this study is to evaluate the effectiveness of the harmonic decomposition formulation for modelling geometric nonlinearities. Hence, nonlinear material capabilities have not been incorporated into this implementation. However, adding nonlinear material models can be accomplished with relative ease. Currently, the code limits the displacement field to symmetric behaviour about one plane but this limitation will be removed in the future.

#### **5.1.2. Geometric Properties**

The element volume is formed by rotating a two dimensional surface about an axis of symmetry. Axisymmetric elements are formed from a variety of surfaces in the

R-Z plane - triangular or quadrilateral surfaces described by linear or higher order boundaries. Harmonic decomposition was tested using quadratic elements, formulated to utilize either linear or quadratic element boundaries. Figure 3-1 shows the geometry of the quadratic version of the element, with nodes on the midside of the element.

### 5.1.3. Nodal Degrees of Freedom

Chapters 3 and 4 discussed the decomposition of the three dimensional displacement field into a Fourier series of two dimensional fields of harmonic displacement amplitudes. Thus the formulation is essentially an extension of common two dimensional analysis techniques, since any of the common two dimensional interpolation techniques can be used for each of the harmonics.

The displacement harmonics include two parts; one part is symmetric about the plane  $\Theta = 0$ , the other antisymmetric about  $\Theta = 0^7$ . Each part requires three degrees of freedom for the three displacement components at each node. Thus, an eight node element requires 24 degrees of freedom for the symmetric part of each harmonic and another 24 degrees of freedom for the antisymmetric part of each harmonic. There is an exception for the zero'th harmonic, because the sine terms reduce to zero, eliminating one degree of freedom in the symmetric part and two degrees of freedom in the antisymmetric part. The number of degrees of freedom for the element is then

$$NDOF = (NFOU+1)*NFND*6 - 3, \quad (5.1)$$

where NDOF is the number of degrees of freedom for the element, NFOU is the maximum Fourier number used in the decomposition, and NFND is the number of nodes used to describe the element.

Often, the coordinate reference system can be chosen so that the load description and response will be symmetric or antisymmetric about one plane, and only one part of each harmonic is required, reducing the number of degrees of freedom by one half.

The nonlinear terms of the stiffness matrix couple the harmonics, making evaluation of the entire element stiffness matrix necessary, rather than the diagonal submatrices required by linear and some nonlinear formulations. Consequently, the size

---

<sup>7</sup> See Chapter 3 for a discussion of the symmetric and antisymmetric parts of the harmonics.

of the stiffness matrix produced by this formulation increases with the square of the harmonics used in the formulation, and the time required to evaluate the stiffness terms increases accordingly.

#### 5.1.4. Integration Requirements

Integration of the element properties is performed using two dimensional Gauss quadrature in the axisymmetric plane, while the trapezoidal rule is used for integration in the circumferential direction at each Gauss point. The order of Gauss integration is user selectable, but must be the same in the  $\xi$  and  $\mu$  directions. Integration of the Fourier functions was discussed in detail in Chapter 3, where it was shown that the number of integration points required in the circumferential direction depends linearly on the number of harmonics modelled by the element. The total number of integration points,  $N$ , required to integrate the stiffness matrix is thus

$$N = N_{GAUSS} * N_{GAUSS} * N_{TRAP}, \quad (5.2)$$

where  $N_{GAUSS}$  is the number of Gauss points in each local element direction and  $N_{TRAP}$  is the number of trapezoidal integration points in the circumferential direction at each Gauss point.

Integration point data is maintained in a file that is created during the input phase. As the solution proceeds, this file is read during each iteration. When convergence is achieved, the information in the file is updated to reflect the state of the model at the new converged configuration, and solution results are sent to the output files. To reduce the amount of integration point data required, all elements use the same number of nodes, so that the interpolation functions do not need to be stored with each integration point. The polynomial and Fourier interpolation functions are stored in core memory instead.

For each Gauss point, a record of geometric data is stored which includes the initial radius of the point, the inverse of the Jacobian matrix, and a multiplier for the point. This multiplier is the product of combining the Gauss weighting factor, trapezoidal weighting factor and Jacobian. Following this are records for each trapezoidal integration point, each of which contains stress and strain tensors and material history data for the integration point. The stresses and strains are maintained to simplify evaluation of the strain increments and internal nodal stress-equivalent forces. The space for material history information is for implementing nonlinear material models in the future.

## 5.2. Element Generation

Chapters 3 and 4 showed the element stiffness partitioned into harmonic parts (for example Eq. 3.46). The stiffness matrix can also be partitioned into smaller nodal harmonic parts:

$$[K_{pqg}] = \int_{V_{el}} [B^{pf}]^T [C] [B^{qg}] R I J d\mathbf{r} d\mathbf{s} d\Theta, \quad f, g = 0, 1, \dots, NF, \quad (5.3)$$

$$p, q = 1, 2, \dots, NFND,$$

where  $[K_{pqg}]$  is a nodal harmonic part of  $[K]$  and  $[B^{pf}]$  is a nodal harmonic part of the element strain - displacement matrix.

During initial program development, the element stiffnesses were evaluated one part at a time and assembled into the global stiffness matrix. This approach was used to reduce storage requirements for the strain-displacement and element stiffness matrices, reserving as much main storage as possible for the global system of equations. A slight improvement in performance was achieved when the stiffness was evaluated by harmonic parts, rather than nodal harmonic parts, because of a reduction in program control overhead. Regardless of which type of submatrix is used, evaluating the stiffness matrix part by part requires that the stiffness terms be assembled into the global stiffness as they are evaluated at each integration point. Thus, generating the element part by part trades off element generation speed for increased maximum model size.

The size of this trade-off was not fully appreciated until the program was ported to Unix, where memory restrictions were effectively removed. The element generation routines were modified to generate the entire element matrix at each integration point. The stiffness terms could therefore be assembled into the global system once, after integration is complete, rather than at each integration point. The vector calls were also utilized to perform the matrix multiplication  $[B]^T [C] [B]$ , which reduced matrix operation time by more than fifty percent relative to that required by equivalent Fortran routines. Generating the full element matrix reduced the stiffness matrix time by an additional 35 percent on the Apollo workstation.

Evaluating the stiffness matrix in full requires significantly increased storage for the element matrices, particularly if many harmonics are modelled. The size of the strain-displacement matrix is linearly dependent on the number of harmonics, and the

required stiffness matrix storage increases with the square of the number of harmonics. For example, an eight node element modelling harmonics zero through ten requires nearly two megabytes for a complete double precision stiffness matrix, compared with 18 kilobytes for one harmonic part of the element matrix or two kilobytes for an eight node axisymmetric element.

Furthermore, this large element matrix must be evaluated at each integration point. The number of circumferential integration locations also varies linearly with the number of harmonics modelled, thus the computational time required to evaluate an element stiffness matrix increases with the cube of the number of harmonics modelled.

The process for evaluating the stiffness matrix is described by the flow charts in **Figures 5.1 to 5.3**. In both cases, integration point data is read in sequence and used to form the strain-displacement matrix. Data stored with each Gauss point is used at every associated trapezoidal integration point, which provides significant savings in storage requirements for integration point data. The most significant difference between the two approaches is that the element is assembled once after it is integrated in its entirety with the full matrix approach, as opposed to the submatrix approach, where each submatrix must be assembled into the global system at each integration point.

Once the linear stiffness matrix (or matrix part) is evaluated for an integration point, the geometric stiffness matrix components are evaluated and added. Each element of the geometric stiffness matrix is evaluated directly, rather than by the matrix operations which are shown in previous chapters (for example, the last three terms of Eq. 3.62) because of the number of zero operations involved in the matrix form. As a result, evaluating the geometric stiffness matrix in the system of equations requires only 15 to 20 percent of the time required for the linear stiffness matrix.

### **5.3. Stiffness Matrix Storage**

The program uses the skyline storage technique to contain the stiffness matrix (discussed in Bathe, 1982). This format minimizes both the storage and arithmetical operations requirements for Gaussian elimination solution algorithms for linear systems. This format stores the matrix values in an array in column order, and uses a second array of integer pointers to locate the diagonal values. The stiffness matrix is symmetric, so only the upper diagonal part of the global matrix is stored in this program. However, the approach can be extended to non-symmetric systems which are produced by some techniques such as contact algorithms and some nonlinear material properties.

Currently, the program arranges the equation numbers in the order of the nodal number sequence. The program is structured so that inclusion of a bandwidth optimization routine can be accomplished quite easily. Two methods of assigning nodal degrees of freedom to equation numbers by harmonics are employed. For linear systems using the cylindrical formulation, the harmonics are uncoupled, so the degrees of freedom for each harmonic are grouped together for the entire structure to minimize storage requirements and numerical operations. For example, the two degrees of freedom for node 1, harmonic zero are assigned equation number 1 and 2; for node 2, equations 3 and 4; for node N equations  $2N - 1$  and  $2N$ , and so on until the last node, NNODE. Equations are then assigned for the next harmonic, harmonic one, with the three degrees of freedom for node 1 assigned to equations  $2NNODE + i$ ,  $i=1, 2, 3$ ; for node 2, equations  $2NNODE + i$ ,  $i = 4, 5, 6$ ; for node N equations  $2NNODE + 3(N-1) + i$ ,  $i = 1, 2, 3$ ; and so on. This sequence is repeated for each harmonic to be modelled. The column height for a degree of freedom using this assignment pattern is the maximum difference between node numbers for all elements which use the degree of freedom times  $h$ , where  $h$  is 2 for the zero'th harmonic and 3 for other harmonics, plus the other degrees of freedom for that node and harmonic which were previously assigned.

The other pattern is used to assign degrees of freedom when the harmonics are coupled. In this case, degrees of freedom for all harmonics are grouped together for each node, rather than be grouped by harmonic as discussed in the previous paragraph. This grouping is used in the nonlinear formulations which require the entire coupled stiffness matrix, and is currently employed in the small displacement Cartesian formulation. The equation number sequence for the coupled stiffness matrix assigns all degrees of freedom for node 1 first, to equations 1, 2, 3, . . . ,  $3NF + 2$ , where  $NF$  is the number of harmonics. Node 2 is assigned equations numbered  $3NF + 3, 3NF + 4, \dots, 2(3NF + 2)$ . The sequence is repeated for each node in the structure. The column height for each degree of freedom is therefore the maximum difference between node numbers for all elements which use that degree of freedom multiplied by  $(3NF + 2)$ , plus the other degrees of freedom assigned previously for the same node.

#### **5.4. Load Vector Calculation**

The incremental load vector and out of balance load vector are formed using the same technique. The total load vector is calculated, and the nodal equivalent internal stress vector is subtracted, leaving the incremental or out of balance loads. This method ensures that the solution satisfies equilibrium, and provides a better basis for including

deformation dependent loading. Deformation dependent loading has not yet been included. Formulating a generalized deformation dependent load description is relatively complex, because the loads must be transformed to the axisymmetric geometry of the undeformed structure. This transformation would produce load and stiffness terms in every harmonic modelled.

The nodal equivalent internal stress vector for an element,  $\{F_i^e\}$ , is formed by the matrix product integral

$$\langle F_i^e \rangle = \int_{V_o} \langle S \rangle [B] dV_o, \quad (5.4)$$

where  $\langle S \rangle$  is a row vector containing the second Piola-Kirchoff stress tensor and  $[B]$  is the strain-displacement matrix, composed of the linear and nonlinear parts,  $[B] = [B_L] + [B_{NL}]$ . The process for evaluating the nodal equivalent internal stress vector for the structure is very similar to that used to generate the stiffness matrix. All of the steps shown in **Figures 5.2 and 5.3** are the same, except that the matrix product  $[B^T][C][B]$  is replaced by  $\langle S \rangle [B]$ , and the result is assembled into  $\{F\}$  rather than  $[K_L]$ . The same subroutine is therefore used to assemble the stiffness matrix and nodal equivalent internal stress vector. A parameter is passed to the assembly routine to determine which matrix product and assembly is to be performed.

## 5.5. Boundary Conditions

Only the most basic boundary conditions are provided in this version of SLATS. Input of total loads is limited to point loads applied to individual degrees of freedom, and to pressure loads on an axisymmetric line which can have a harmonic variation. The integration of such pressure loads is discussed in sections 3.8 and 4.5. This is sufficient for the majority of load conditions which are encountered. More complex load types can be modelled by writing a preprocessor to generate nodal harmonic point loads for individual degrees of freedom.

Boundary restraints are limited to removing particular degrees of freedom. In the harmonic decomposition technique, this usually provides sufficient capability for modelling restraints which would be very difficult in other formulations. An example is the shear restraint boundary condition, where lateral motion is removed by constraining the zero'th harmonic in the Cartesian formulation. The cross section remains free to

deform, but total lateral motion of the cross section is fixed. Such a boundary condition would be most difficult to model with conventional formulations.

Some program hooks have been included in the code for future enhancements to the boundary modelling capabilities. These include imposed displacements and linear multipoint constraints. Once these are included, SLATS will provide boundary conditions capabilities for most problems suited to solution by Fourier decomposition.

## **5.6. Solution Strategies**

Two nonlinear solution strategies have been implemented in SLATS; a Newton - Raphson (Bathe, 1985), and the Constant Arc Length technique (Ramm, 1981). The strategy first implemented was the Newton-Raphson iterative technique. This provides a basic load control approach to solving a nonlinear system of equations by fixing the load vector and iteratively solving for the displacement vector until equilibrium is satisfied, within a specified tolerance. Input parameters specify whether full Newton iteration is used, in which case the stiffness matrix is formed for each iteration, or if a modified iteration is used. In the modified Newton solution strategy, the stiffness matrix is not reformed for every iteration. Instead the stiffness is reformed after a given number of iterations, at the beginning of each solution increment, after a specified number of increments, or only at the start of the solution. Full Newton iteration can model severe nonlinearities, and usually requires fewer iterations, however, each iteration takes longer because of the time required to reform the stiffness matrix. This is particularly so for the HLT element, because of the relatively large amount of time required to form the stiffness matrix, and the small number of degrees of freedom required for a given model. Modified Newton iterations can model less severe nonlinearities, and require more iterations to achieve equilibrium. However, since the stiffness matrix is not reformed for each iterate, the total solution time can be considerably less than that required by a Full Newton approach.

The nonlinear capabilities of the HLT element were initially verified with the Newton - Raphson solution strategy, but because it uses load control, post peak behaviour, and the large displacements associated with it, could not be modelled. Therefore, the Constant Arc Length Method (Ramm, 1981) has been implemented in SLATS code and used in all verification problems in subsequent work. This solution strategy controls both the load and displacement vector during the equilibrium iterations. The load vector is defined by a reference vector scaled by a load factor. Thus, the load is



controlled by the load factor. The square of the length of the increment is defined by the sum of the Euclidean norm of the incremental displacement vector and the square of the load factor increment. During equilibrium iterations, the orthogonality condition

$$\sum_{d=1}^{NS} \Delta u_0^d \Delta u_i^d + \Delta \lambda_0 \Delta \lambda_i = 0 \quad (5.5)$$

is applied, in which  $d$  is a degree of freedom number,  $NS$  is the total number of degrees of freedom in the system,  $i$  is the equilibrium iteration number,  $\Delta u_0$  and  $\Delta \lambda_0$  are the initial incremental values of the displacements and load factor (which define the arc length), and  $\Delta u_i$  and  $\Delta \lambda_i$  are the iterate increments of the displacement vector and load vector. This condition defines a solution path during equilibrium iterations which is orthogonal (or normal) to the initial increment (or zero'th iterate). Thus, the load is controlled during the equilibrium iterations, and response beyond critical loads can be modelled.

If the determinant of the stiffness matrix is positive, the load is increasing, so the load factor increment is positive. If the determinant is negative, the solution is proceeding on a descending branch of the solution path. The matrix reduction routine was modified to count the number of negative pivots encountered during triangulation of the stiffness matrix to indicate whether the determinant is positive or negative. Thus, the Constant Arc Length solution strategy is able to follow descending solution branches beyond the peak load for the structure.

Modifications similar to those available in the Newton-Raphson solution strategy are also provided for the Constant Arc Length approach. Input parameters are used to specify the frequency with which the stiffness matrix is reformed during an increment, and for which increments the stiffness is reformed. In addition, the length of the arc is modified dynamically, according to the convergence rate during the increments. Input parameters specify a maximum and minimum allowable arc length, the number of iterations beyond which the arc length is reduced, the number of iterations below which the arc length is increased, and the maximum number of iterations allowed before the solution is restarted with a smaller arc length. This approach allows the solution to proceed rapidly in regions far from critical points, yet enables the solution path to be traced near critical points.

## 5.7. Summary

Program SLATS is a basic finite element program developed to test the effectiveness of the Harmonic Lagrangian Tubular element. A complete program was written, because the structure of the HLT element equations makes it difficult to incorporate this element into common finite element packages. The program currently supports only elastic material properties, but because of its nonlinear capabilities, SLATS can be used as a platform for continued development and incorporation of other nonlinearities into the Fourier decomposition formulation.

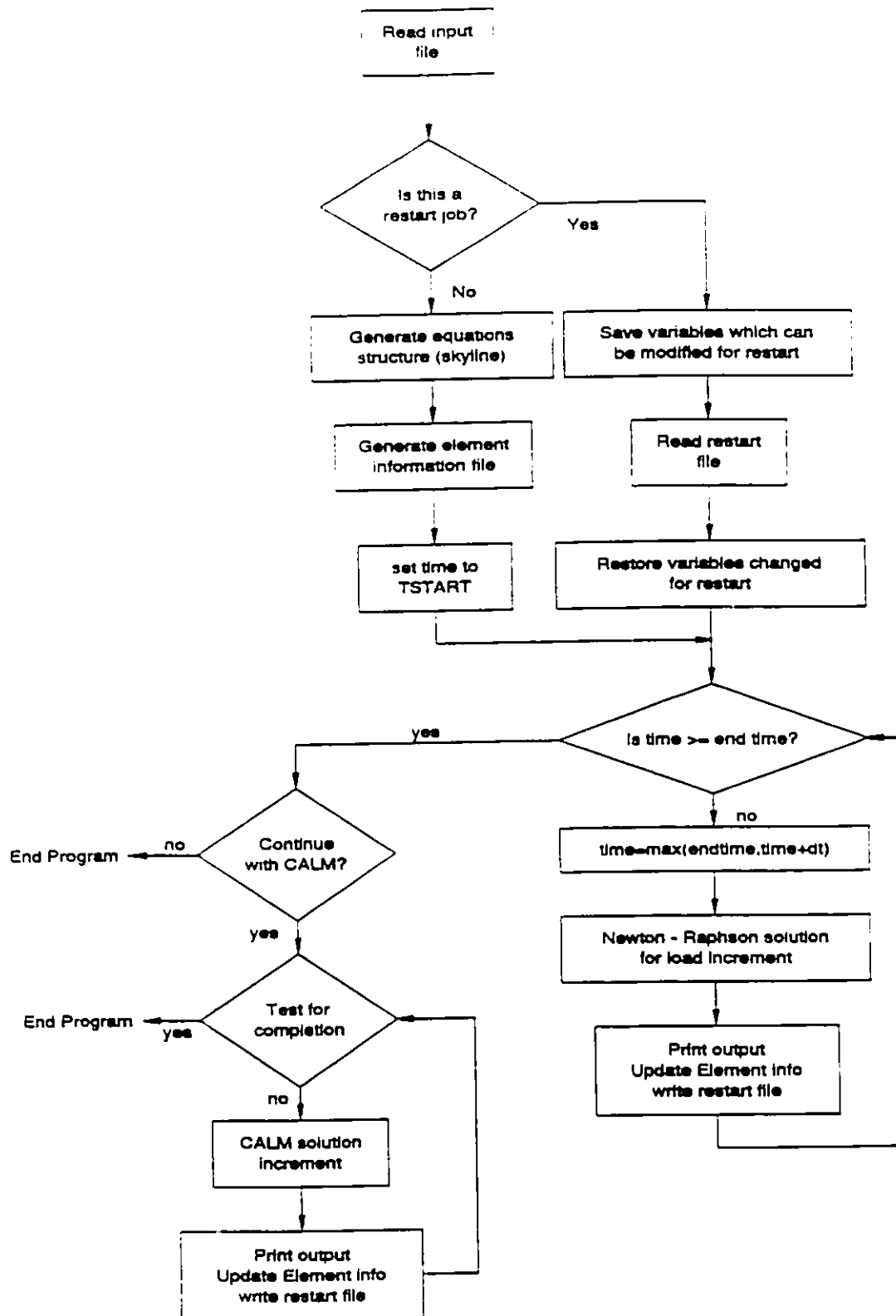


Figure 5.1 Main program flow chart

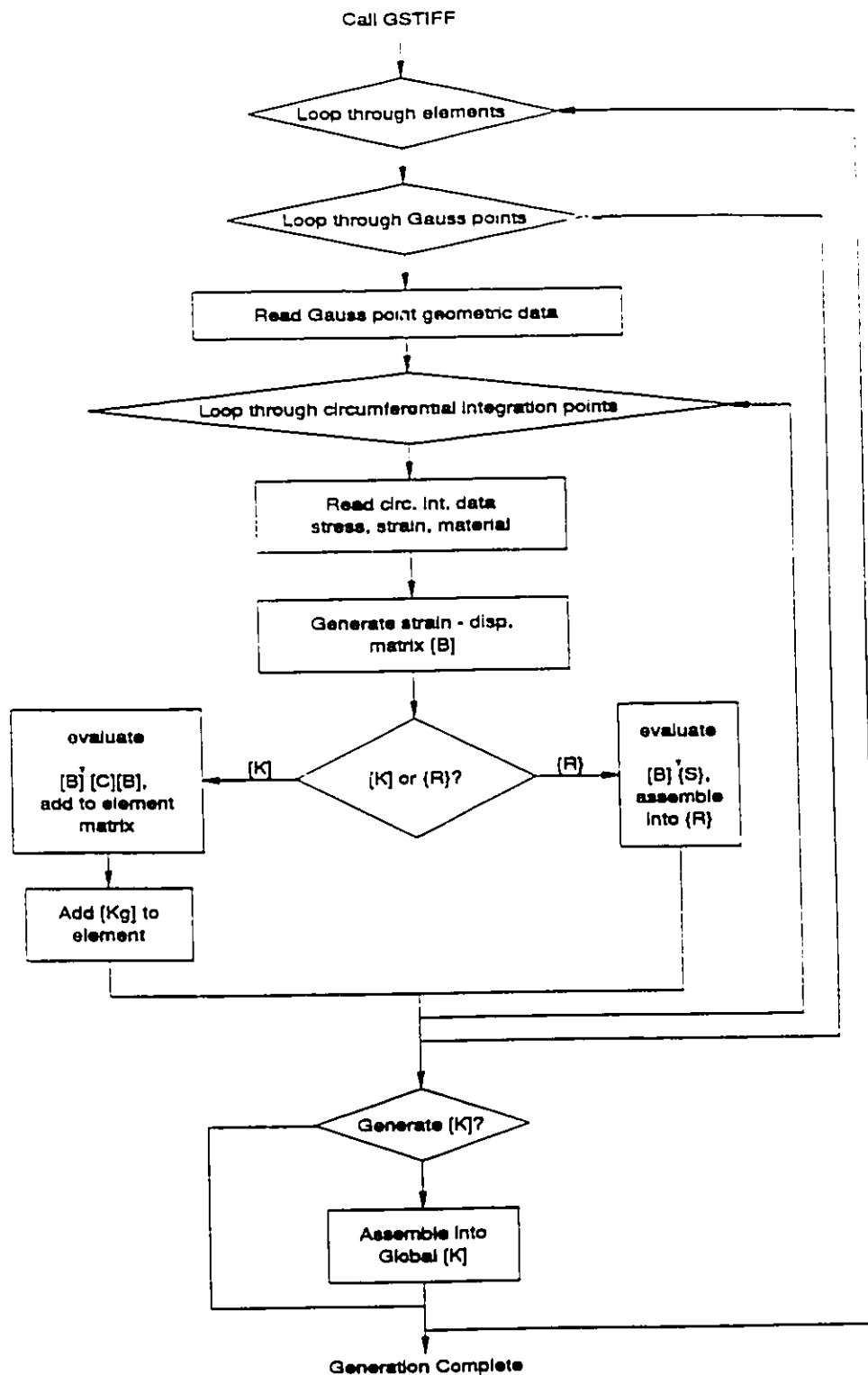


Figure 5.2 Flow chart for stiffness matrix or equilibrating force vector generation - full element matrix form.

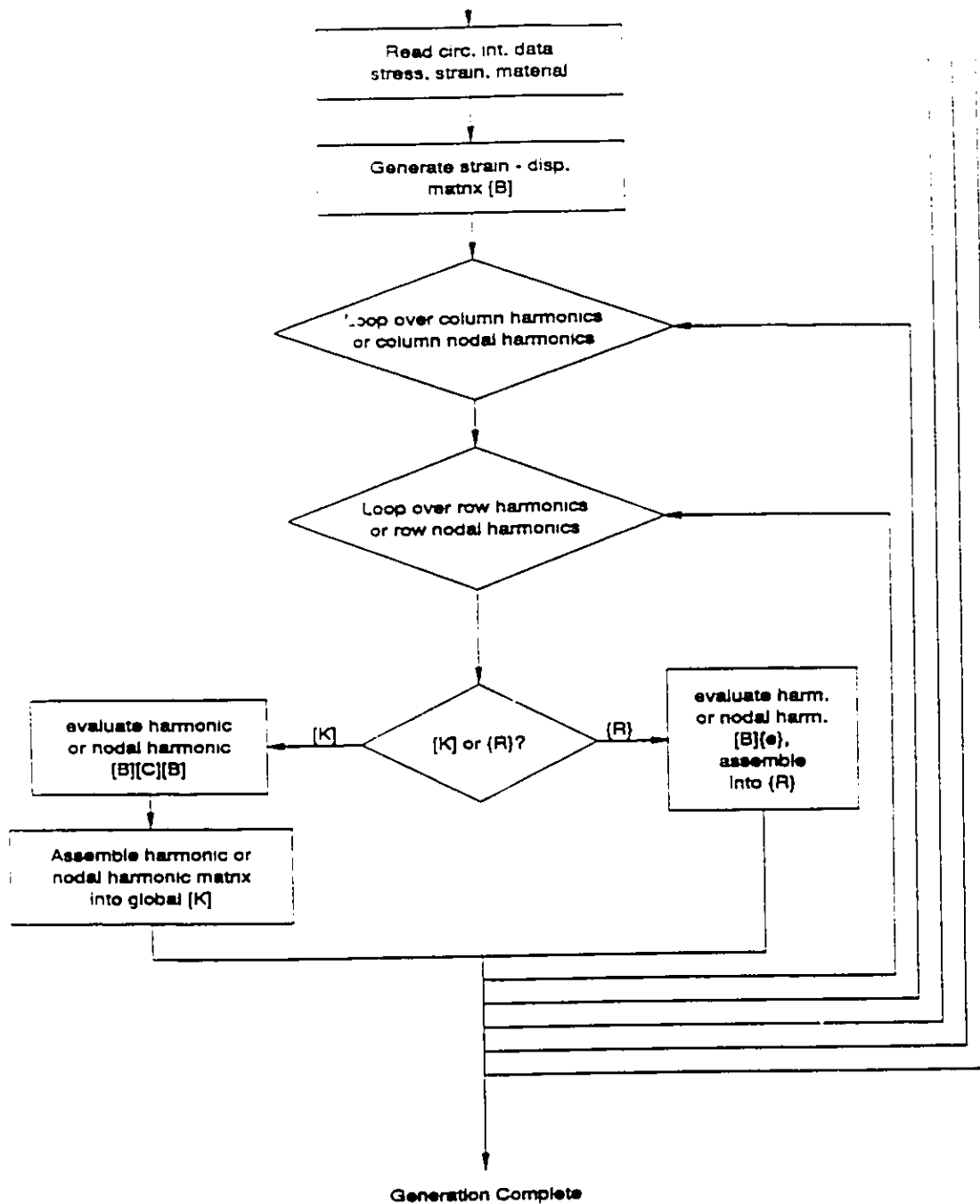


Figure 5.3

Flow chart for stiffness matrix or equilibrating force vector generation - partial element matrix form., inside loops (see Figure 5.2 for outside loops)

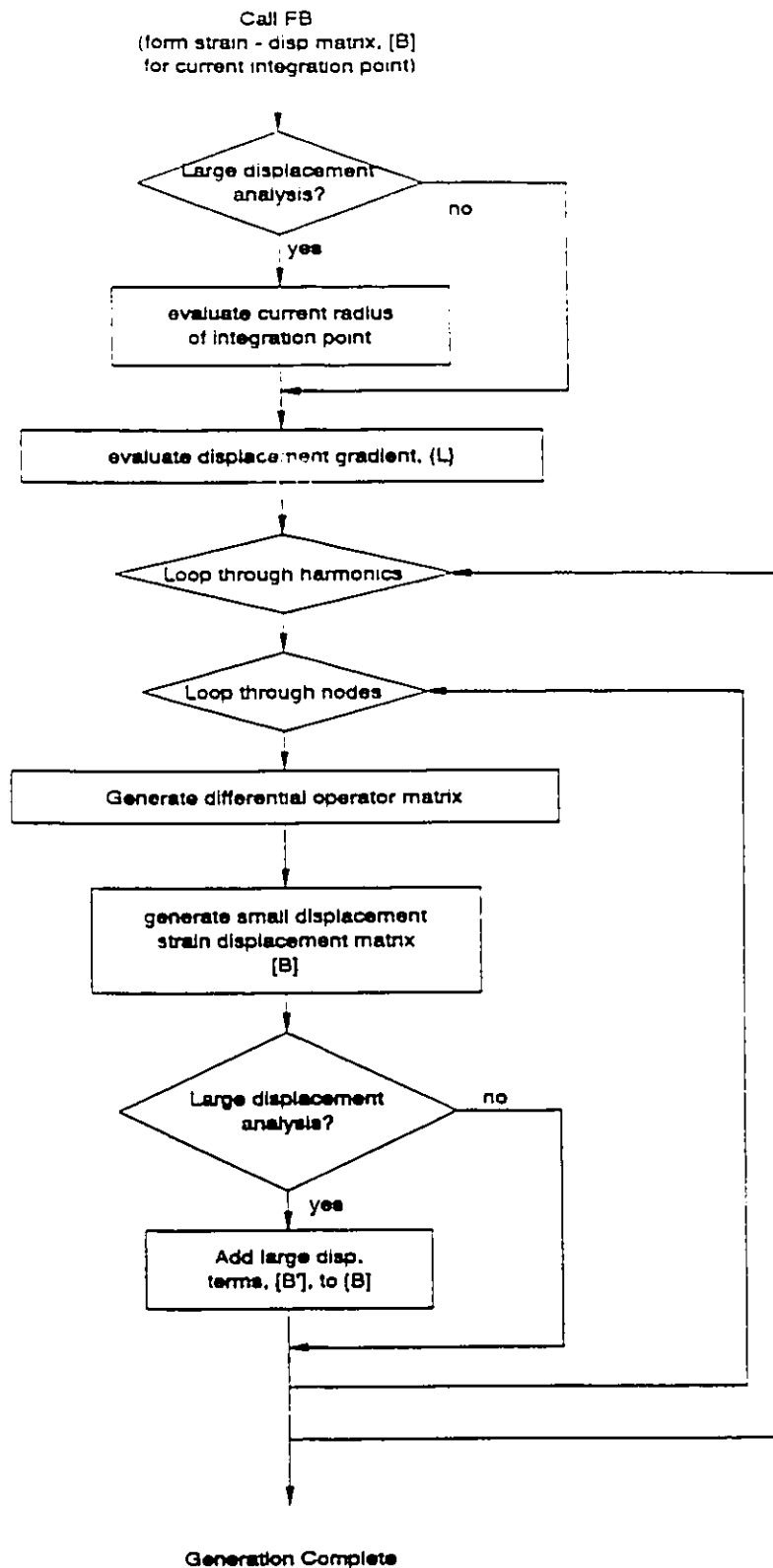


Figure 5.4 Strain - displacement matrix generation flow chart

## **6. Discussion and Verification of Formulation**

### **6.1. Introduction**

This chapter presents results of the non-axisymmetric formulation for axisymmetric elements, applied to several sample analysis cases. Analysis types include linear cases, geometrically nonlinear, thin shell cases with relatively small displacements (in the order of the shell thickness), and very large displacement thick shell problems (displacements in the order of the dimensions of the structure). The Cartesian and cylindrical formulations are compared with other Fourier decomposition techniques from the literature which use physical displacements, and with each other.

The discussion of linear problems is limited to a small displacement bending problem. This simple problem provides an exact linear analytical solution for comparison, and demonstrates the non-axisymmetric capabilities of the Fourier decomposition technique. The nonlinear examples start with several axisymmetric cases, including the torus and spherical cap problems. Nonlinear effects are demonstrated through comparison with linear results, and numerous comparison are made with results in the literature.

Nonlinear, non-axisymmetric capabilities are the objectives of this work. These capabilities are demonstrated first in shell analyses. Comparisons are made with published shell results, including results of other Fourier decomposition shell elements. Although the element developed here was not intended to be utilized for thin shell problems, the efficiency of the formulation is shown to be potentially high relative to conventional shell formulations, and the results demonstrate that the formulation is both accurate and robust.

The major evaluation analysis is performed on a thick tube - column, subjected to a slightly offset axial load. The response of the tube to this load includes two critical points: the first at the load where Euler buckling occurs; the second at the point where bending at the centre produces ovalization and Brazier collapse of the tube. Because of the highly nonlinear relationship between the applied axial load and Brazier collapse, and the obvious non-axisymmetric behaviour, this model serves as a good test for the formulation, and is used as the basis for studying the various element parameters.

Finally, the performance of the program is compared with conventional formulations. The equation structure imposed by the formulation causes the solution time to increase dramatically as the number of harmonics employed increases. However, mesh refinement has the same impact on conventional polynomial formulations. The performance results show that for a wide range of problems, the Fourier decomposition formulation provides better computational efficiency than general purpose three dimensional elements.

## 6.2. Linear Formulation in Pure Bending

Clearly, the results of a large displacement formulation must converge to a small displacement solution as the displacements and strains approach infinitesimal values. Therefore, the non-axisymmetric formulations are evaluated in their small displacement form. In addition to the Cartesian and cylindrical formulations which were developed in the previous chapters, the cylindrical formulation based on physical displacements (Wilson, 1965) is also compared. In their axisymmetric forms, both formulations are exactly equivalent to conventional axisymmetric formulations and will not be considered. Furthermore, nonlinear axisymmetric analysis cases are discussed in later sections, so small displacement axisymmetric cases are not considered here. Simple three dimensional load cases are considered, and the elements' capabilities for modelling the correct behaviour are compared.

The problem considered is a tube subject to pure bending (Figure 6.1), which is a three dimensional load case. The exact solution to the linear elastic displacement field for this case is easily determined (Sokolnikoff, 1956) to be

$$u_x = \frac{\sigma_{\max}}{2ER_o} (Z^2 + \nu X^2 - \nu Y^2) , \quad (6.1a)$$

$$u_y = \frac{\sigma_{\max}}{ER_o} \nu XY , \text{ and} \quad (6.1b)$$

$$u_z = - \frac{\sigma_{\max}}{ER_o} \nu XZ , \quad (6.1c)$$

where  $\sigma_{\max}$  is the maximum bending stress on the beam cross section.



The displacement field of the harmonic element is interpolated in terms of the cylindrical (R,  $\Theta$ , Z) coordinate system. Expressing the displacement field of the beam in terms of these coordinates produces

$$u_x = \frac{\sigma_{\max}}{2ER_o} (Z^2 + vR^2 \cos(2\Theta)) , \quad (6.2a)$$

$$u_y = \frac{\sigma_{\max}}{ER_o} vR^2 \sin(2\Theta) , \text{ and} \quad (6.2b)$$

$$u_z = - \frac{\sigma_{\max}}{ER_o} vRZ \cos(\Theta) . \quad (6.2c)$$

The physical displacements in the R- $\Theta$  plane in cylindrical coordinates (Wilson, 1965) are found using the coordinate transformation functions:

$$u_r = u_x \cos(\Theta) + u_y \sin(\Theta) , \text{ and} \quad (6.3a)$$

$$u_\theta = u_y \cos(\Theta) - u_x \sin(\Theta) . \quad (6.3b)$$

Thus, the physical displacements of the tube are

$$u_r = \frac{\sigma_{\max}}{2ER_o} (Z^2 + vR^2) \cos(\Theta) \quad (6.4a)$$

$$u_\theta = \frac{\sigma_{\max}}{2ER_o} (vR^2 - Z^2) \sin(\Theta) \quad (6.4b)$$

$$u_z = \frac{\sigma_{\max}}{ER_o} vZR \cos(\Theta) \quad (6.4c)$$

Coordinate displacements in a small displacement formulation are the same as physical cylindrical displacements, except that the  $\Theta$  displacement is divided by the radius to give the change in the  $\Theta$  coordinate. The two  $\Theta$  displacements are therefore distinguished by a superscript "p" and "c" for physical and coordinate displacements respectively:

$$u_\theta^p = \frac{\sigma_{\max}}{2ER_o} (vR^2 - Z^2) \sin(\Theta) \quad (6.5a)$$

$$u_\theta^c = \frac{\sigma_{\max}}{2ER_o} \left[ vR - \frac{Z^2}{R} \right] \sin(\Theta) \quad (6.5b)$$

All of the displacement components in Eqs. (6.2) to (6.5), with the exception of the  $\Theta$  coordinate displacement, can be modelled exactly with a second order polynomial and the first harmonic<sup>8</sup>. The  $\Theta$  component of the coordinate displacements includes a term with  $\frac{1}{R}$  which can only be approximated by the polynomial interpolation functions. This clearly puts this formulation at a disadvantage. In fact, rigid body translation also includes  $R$  in the denominator of the  $\Theta$  coordinate displacement. Thus the small displacement form using cylindrical coordinate displacements cannot exactly model rigid body translation normal to the axis of radial symmetry.

Figure 6.2 shows the model that was used to test and verify the small displacement formulations for bending problems. The tube - beam is 200 inches long with an outside diameter of 10 inches. An elastic modulus of  $30 \times 10^6$  psi. and Poisson's ratio of 0.3 were used. The inside diameter was varied from 9.998 inches down to zero to evaluate the elements' capabilities for modeling a wide range of diameter ratios, though the very thin shell cases are obviously of pure academic interest. The mesh consisted of nine node elements so that the polynomial components of the displacement field would be modelled exactly. Models constructed of quadratic elements used 20 element rows in the axial direction. Those using linear elements consisted of 20 and 40 elements in the axial direction. The number of rows through the wall thickness was varied between one and three. The integration order was also investigated by varying the number of Gauss points in the R-Z plane between two and four.

Boundary conditions were applied to approximate those used by Sokolnikoff in his solution of the elasticity equations. A bending moment was applied to the end of the tube using axial tractions in the first harmonic. A linear variation through the wall thickness was used to ensure that the exact axial stress distribution was applied. Symmetric boundary conditions were applied at one end of the tube model, and one additional degree of freedom was constrained at the plane of symmetry to remove rigid body modes. In the Cartesian formulation, the  $x$  degree of freedom in the zero'th harmonic was removed from one node. The cylindrical formulations used the  $\Theta$  degree of freedom in the first harmonic to remove the rigid body displacement mode.

---

<sup>8</sup> The reader is reminded that the first harmonic refers to Fourier number one. The zero'th harmonic, with Fourier number zero, refers to the axisymmetric part of the displacement field.

The base case considers one element row through the wall thickness, nine node elements providing a quadratic Lagrangian displacement field, and three point Gauss quadrature in both R and Z directions. The base geometry uses an outside diameter of ten inches and an inside diameter of nine inches.

The first parameter considered is the inside diameter of the tube. This can also be interpreted as a study of the ratio of the element thickness to radius. Figure 6.3 shows the error in the maximum displacement at the centre of the pipe relative to the exact value for each of the three formulations as a function of the inside radius of the tube. The Cartesian formulation produces exact results, as does the cylindrical formulation with physical displacements for all inside diameter values. On the other hand, the cylindrical formulation with coordinate displacements produces relatively accurate results only where the element size in the radial direction is small relative to the diameter of the element. This is because the  $1/R$  displacement terms are represented somewhat accurately when the element thickness is small relative to element radius.

Analyses using variations on the quadratic element all show similar behaviour to that shown in Figure 6.3. The variations studied included reduced (two point) Gauss quadrature and an incomplete quadratic meridional displacement field (eight node elements). In every case, the Cartesian and cylindrical formulation with physical displacements produced exact results within output precision, with one exception, that being two point Gauss quadrature with nine node regular rectangular elements. In that case, spurious deformation modes resulted a singular stiffness matrix.

The cylindrical formulation with coordinate displacements produced accurate results only for large  $R/t_{el}$  values, where  $t_{el}$  is the element thickness as shown in Figure 6.4. Interestingly, the reduced integration provided an improved solution for small  $R/t$  values. Clearly, the error in the displacement field produced by coordinate displacements and polynomial interpolation functions is large over a wide range of  $R/t$  values, even in the small displacement form. In all cases, the degree of element locking in bending problems is significant in the range  $R/t < 10$ .

The element diameter to thickness ratio can be increased for a given tube by increasing the number of rows through the wall thickness. Figure 6.5 shows the improvement in solution accuracy by plotting cylindrical formulation results with various mesh densities through the wall thickness. Note that models with similar element radius to thickness ( $R/t_{el}$ ) ratios produce similar errors, regardless of the tube  $R/t$  ratio. Upon

consideration of the poor performance of the cylindrical formulation with coordinate displacements, it was realized that the formulation could be cast into a form which retains the coordinate displacement concept, but scales the circumferential displacements in the finite element form to be equivalent to the physical displacements. Finite element degrees of freedom could be defined in terms of the coordinate nodal displacements as

$$u_{\theta}^F = \frac{u_{\theta}}{R}, \quad (6.6)$$

and the spatial derivatives would be expressed as

$$\frac{\partial u_{\theta}}{\partial R} = R \frac{\partial u_{\theta}^F}{\partial R} + u_{\theta}, \quad (6.7a)$$

$$\frac{\partial u_{\theta}}{\partial \Theta} = R \frac{\partial u_{\theta}^F}{\partial \Theta}, \text{ and} \quad (6.7b)$$

$$\frac{\partial u_{\theta}}{\partial Z} = R \frac{\partial u_{\theta}^F}{\partial Z}. \quad (6.7b)$$

Substituting these into the linear form of the cylindrical formulation produces equations identical to the small displacement formulation using physical displacements. The same substitutions could be made into the large displacement formulation. However, it is important to note the resulting equations would not be formulated in terms of **physical displacements**, since the  $\Theta$  component is scaled by the original (undeformed) radial coordinate. Such  $\Theta$  degrees of freedom instead are correctly referred to as **scaled coordinate displacements**.

Although such a modification to the circumferential displacement degrees of freedom would produce a large displacement formulation which reduces to a proven linear formulation in the limit as the displacements vanish, the modified formulation would still not model rigid body motion with a finite number of harmonics when large displacement terms are included. Thus, this modification has not been explored, in favour of pursuing the Cartesian formulation instead.

Four point quadrature was not investigated, since three point quadrature integrates the element matrices exactly for rectangular elements.

The Cartesian formulation was also studied using a four node implementation of the harmonic elements in the bending model. A first order displacement field significantly impacts the results, because the displacement field must be approximated by a piece wise linear representation. Figure 6.6 plots the error in displacement at the end of the tube for the Cartesian formulation as a function of the inside diameter. Results are shown for two mesh densities in the axial direction and three in the radial directions. Comparing results from the radial refinement, one observes that the solution is markedly improved for  $R/t_e$  ratios less than about 10. Axial mesh refinement is clearly more significant for higher  $R/t_e$  ratios. In other words, the first harmonic of the element performs like a linear beam element, providing a linear displacement field in the axial direction and in the direction normal to the neutral axis. It models simple beam theory, but since quadratic displacement terms are not included, the exact displacement field through the thickness is not represented.

### 6.3. Nonlinear Analyses

The behaviour of a structure undergoing collapse is a nonlinear process. Although the response of a structure near collapse depends strongly on the displacement field, the displacements at collapse are often relatively small, and the geometry of the structure remains essentially unchanged. This is frequently true for thin shell structures. Several finite element formulations using Fourier decomposition techniques have been developed for thin shells. Examples include the displacement based SABA5 element presented by Chan and Firmin, 1970, 1970a, and the mixed formulation of Chan and Trbojevic, 1976 and 1977. These formulations are limited, however, to displacements which are small relative to the radius of the structure.

The Fourier decomposition formulations discussed in this dissertation were developed to model nonlinear behaviour arising out of arbitrarily large displacements. The importance of accurately determining structural responses near collapse is one of the most important aspects of large displacement formulations. This section will focus on geometrically nonlinear problems involving displacements which are small relative to the dimensions of the structure, so that comparisons can be made with results available in the literature. In addition to verifying the capability for modelling large displacement nonlinearities, the results prove the element to be applicable to thin axisymmetric shells

undergoing asymmetric deformations. Some of the results also illustrate the errors which are introduced by fundamental shell theory assumptions.

### 6.3.1. Torus

The torus under external pressure serves as a useful problem for verifying the nonlinear capabilities of axisymmetric formulations. Nonlinear terms in a large displacement analysis produce results which are much different than those from a linear analysis. A large displacement analysis of the torus is provided by Kalnins, 1967, and comparisons to Kalnins' solution are made by Chan and Firmin, 1970a, and Chan and Trbojevic, 1977.

A model of the torus analysed is shown in Figure 6.7. Utilizing the symmetry of the problem, half of the shell was modelled, using 20 elements for one model, and 40 elements for a second model to approximate the higher bending gradients of the nonlinear solution. The elements are assembled around half of the minor diameter of the shell, from the inside major diameter to the outside major diameter. The axisymmetric element geometry is thus generated around the major diameter of the torus. Quadratic elements with a full Lagrangian description of the meridional displacement field were utilized. Linear and nonlinear analyses were performed, using both cylindrical and Cartesian formulation elements. The cylindrical formulation used only the zero'th harmonic. Since axisymmetric Cartesian displacements include displacement amplitudes in the zero'th and first harmonics, both of these harmonics were included in the Cartesian model.

The results of the Cartesian and cylindrical formulations were identical, verifying that both formulations resolve to the usual axisymmetric formulation. Axisymmetric displacement results for the torus are shown in Figure 6.8 along with the results from Kalnins, 1967. The linear solution is adequately modelled using 20 elements. Kalnins shows that higher bending gradients are produced in a nonlinear analysis, and Figure 6.8 shows that 20 quadratic elements are insufficient to accurately model such gradients. The 40 element model, however, clearly provides sufficient degrees of freedom to accommodate the nonlinear displacement field for this shell. Figure 6.9 plots the hoop stress in the shell, and Figure 6.10 gives the bending force in the shell calculated by the nonlinear formulation. These figures show clearly the large stress gradients in the shell which require additional mesh refinement for accurate representation. Results from Chan and Trbojevic, 1977 are also given in Figures 6.9 and 6.10 for comparison. The

difference between the HLT results and those from Kalnins is slight. Kalnins' technique is based on shell theory, and therefore does not account for shear deformation in the shell. On the other hand the HLT element is a continuum formulation with a quadratic meridional element displacement field models shear deformations.

Compared with Kalnins' ten segment model, and the six element models of Chan and Firmin, 1970 and Chan and Trbojevic, 1977, the number of HLT elements required for an accurate solution may seem large. However, the HLT element is formulated with a quadratic field, whereas the SABA5 element uses a quintic displacement field, and Kalnins' technique was developed specifically for solving the nonlinear shell equations for shells of revolution. The HLT formulation could also be optimized for thin shell problems by increasing the order of the displacement field in the meridional plane of the shell to reduce the number of elements required for such problems. However, this avenue is not pursued here. Although the quadratic element is not particularly efficient when applied to this problem, the results prove that the formulation accurately models axisymmetrical nonlinear behaviour.

### **6.3.2. Spherical Cap**

#### **Axisymmetric Analyses**

Three spherical caps were modelled for comparison with results from Chan and Firmin, 1970, and Chan and Trbojevic, 1977. The first two shells were modelled under axisymmetric loads (uniform external pressure) with axisymmetric behaviour, while the third was subjected to asymmetric loading, using four complete harmonics to model the asymmetric behaviour. Analyses were performed with the Cartesian and cylindrical formulations.

The torus analysis demonstrated that both formulations are equivalent to a conventional axisymmetric formulation when only axisymmetric terms are included. The axisymmetric analyses of the spherical caps provides further proof of this. The geometry of the first cap was chosen by Chan and Firmin to demonstrate a softening behaviour as pressure is applied. The second cap was selected to demonstrate stiffening behaviour at the centre of the cap.

Figure 6.11 shows the caps that were analysed. The first cap is thicker, relative to the cap radius and curvature, and therefore has a higher membrane bending stiffness. Consequently, when pressure is initially applied, the maximum displacement occurs at

the centre of the cap. On the other hand, the second cap, being thinner, initially develops an axisymmetric wave about half way between the centre and the edge of the cap as pressure is applied. Thus, in this case, the maximum displacement is not at the centre of the cap.

Figure 6.12 gives the load - displacement results from the analysis of cap 1 using the nine node HLT element. Results from Chan and Firmin, 1970, are also shown for comparison. The softening behaviour exhibited at the centre of the cap in this problem is well suited to the displacement control solution strategy used by Chan and Firmin, enabling a solution to be determined beyond the peak load. The range of their solution, however, remains in the relatively small displacement regime. The maximum displacement they model is only in the order of the shell thickness, and only one third of the cap height. The HLT element is able to model the cap as it is pressured through inversion. The curve shows a single load maximum, then a drop in pressure as the cap snaps through. The results should be qualified by noting that the pressure loading as modelled does not include any follower force effects. Since the cap is quite shallow, though, follower force effects would have little significance.

Results for cap 2 are shown in Figure 6.13 in the range modelled by Chan and Firmin. Because they used a displacement controlled solution strategy, the range of their solution was limited in this case to the first displacement maximum. Although the cap stiffens at the centre as pressure is applied, the discussion later will show softening at other locations as the pressure is applied. Had Chan and Firmin chosen a location midway between the centre and edge of the cap as the point for displacement control, they could have determined the cap response significantly beyond the peak displacement that they achieved. However, as the loading sequence progresses, the deformation pattern changes completely. Thus, no single point displacement control solution strategy could model the complete response of this cap during snap through.

The Constant Arc Length Method solution strategy implemented in SLATS is able to trace the equilibrium path past load and displacement critical points, regardless of where the maximum displacement increment is, providing much greater solution flexibility. Figure 6.14 shows the equilibrium path for the centre location of cap 2 over a greater range. This cap clearly exhibits far more complex behaviour than the first, because of the initial deformation mode which develops. The labels on the curve for the crown denote points where displacement distributions are plotted in the present discussion. In general, critical points were chosen, that is, local load and displacement



maxima and minima. The solution points closest to the point where the equilibrium path crosses are also chosen. Figure 6.15 shows the initial stages of equilibrium paths for two additional points in the second cap; one half way between the edge and crown, the other three quarters of the distance towards the crown from the edge. These curves clearly demonstrate that the initial hardening characteristic exhibited at the centre is not evident everywhere in the cap.

The curves include several unstable equilibrium branches and demonstrate occurrences of snap-through and snap back. It must be remembered that the equilibrium curve is a mathematical construct, and by no means represents the physical behaviour of the cap. Only when dynamic effects are included in the analysis can it be said that the results are physically meaningful.

Figures 6.16 and 6.17 show the bending stress distribution for caps 1 and 2. The bending stress plotted is the difference between the meridional membrane stress at the inside and outside Gauss integration points. Positive bending indicates compressive bending stress on the inside, tensile bending stress on the outside of the cap. In the first cap, the bending distribution is almost linear across the cap, and changes in magnitude as pressure is applied, but the distribution remains essentially the same. The second cap, on the other hand, exhibits a bending distribution which changes as loading progresses. Comparing the bending distributions for the first three critical points, one observes that initially there is one complete wave in the bending distribution, but at the first load maximum, there are almost one and a half waves in the bending distribution. Also, the bending stresses increase most in the midsection of the cap meridian, rather than at the centre or edge of the cap.

The displacement distribution shows most clearly the cause of the unusual behaviour of cap 2. Figure 6.18 gives the displacement distributions at three locations on cap 2 at the first four critical points of the equilibrium curve. In particular, compare the displacements at the centre of the cap (element 40) with the mid-section (specifically, element 19) as loading progresses. The centre of the cap moves very little, even rebounding slightly, as loading progresses - hence the apparent stiffening. The displacements at the midsection, however, are greatest and increase more rapidly as loading proceeds. Essentially, an axisymmetric buckle half way between the edge and the centre of the cap forms, and a minor snap-through of the mid-section of the meridian occurs as the pressure drops to the value at point d. The cap stabilize at this point and begins to carry more load.

The displacement at point d is quite different from that when the cap is fully inverted. Ultimately, the point of maximum displacement must move to the centre of the cap for the snap-through to be complete. For example, comparing the displacement distributions in Figure 6.19 for two nearly adjacent points on the equilibrium curve, d and h, it is obvious that the redistribution of displacements is quite significant. As the load increases to the maximum near point e, the buckled form changes from one to one and a half waves, and the point of maximum displacement moves to the centre of the cap (Figure 6.20). This axisymmetric buckle remains a dominant feature of the deformed shape and increases in size up to point f on the curve. At this point, the final snap-through process of the cap begins. The buckled shape is reduced as the cap snaps back towards point g. From this point, the cap undergoes its final snap-through (Figure 6.21), with the axisymmetric buckle disappearing and the displacement at the centre increasing as the pressure drops. After passing through the last pressure minimum, point i, membrane action takes over, and the cap stiffens in its inverted form.

The cylindrical and Cartesian formulations produce identical results, as demonstrated by the single HLT line in Figures 6.12 through 6.14. The slight differences are in the order of the machine accuracy, which indicates that the formulations are identical in their axisymmetric forms.

Although the initial slope of the load displacement curves (Figure 6.12) matches results from shell analyses reported in the literature, the peak load given by the HLT element is lower in both cases, and the local displacement maximum in the second cap is also lower than the result given by Chan and Trbojevic, 1977. The difference in loading discussed in the torus analysis is partially responsible for this discrepancy. However, another significant source of the disparity could be due to differences in the stress distribution through the shell modelled by the two techniques. The shell theory on which the earlier formulations are based assumes a linear displacement and stress distribution through the shell. More recent research has considered higher order deformation theories through the shell thickness. For example, Dennis and Palazotto, 1989, and Tsai and Palazotto, 1990, discuss shell formulations which incorporate higher order shear deformation theory, and show significant differences between their solutions and linear shear deformation theory results. The quadratic HLT element provides a higher order representation of shear, membrane and bending deformations through the wall. Consequently, the system of equations is less stiff (more accurate), and a lower peak load is predicted.

To test this theory, the second cap was modelled using four node elements. The shell was modelled using one element row through the wall, and 200 elements in the axisymmetric length of the shell. This mesh provides a good representation of the displacement field along the shell, and the through-thickness behaviour modelled by the linear displacement field elements is equivalent to that in linear deformation shell models like those employed by Chan and Firmin, 1970a. The results of this analysis, which are also included in Figure 6.13, show better comparison with those of Chan and Firmin. It should be noted that the integration error in the SABA5 formulation of Chan and Firmin is a consideration only in asymmetric analyses, and thus is not a factor in this axisymmetric comparison.

This is an interesting result, because it highlights a limitation of shell formulations which is often neglected; the assumption of a linear variation in behaviour through the wall thickness. Although the through thickness behaviour is almost linear, the sensitivity of the critical load to inaccuracies in the stress and strain field is great enough that the predicted critical load can be significantly affected. It is true that many problems are imperfection sensitive, and this is the usual explanation for the discrepancy between experimental and analytical results. But the improvement in results produced with more accurate modelling of through thickness behaviour suggests that a significant portion of the error stems from the fundamental assumptions made in shell theory. In the first cap example, the collapse pressure predicted by the nine node HLT is about 35% higher than the 60.5 psi experimental result quoted by Chan and Firmin, 1970, compared with an error of over 60% calculated by their shell model, and that of Budianski, 1960. Thus, while imperfections play a significant role in these collapse problems, limitations of the finite element models are also a contributor to the discrepancies.

### **Asymmetric Analysis**

The third cap was modelled under asymmetric pressure loading. Chan and Firmin, 1970a applied the displacement based SABA5 element to the same problem, and Chan and Trbojevic, 1977 used the mixed formulation harmonic shell element to study this problem as well. They also pointed out the error made by Chan and Firmin in integrating the harmonic function products, thus producing an artificially low buckling load.

Figure 6.22 shows the asymmetric analysis results of the third cap at the two most significant locations; at the centre of the cap, and at the location of maximum

displacement. Included with the figure is an illustration of the loading which is applied to approximate a pressure load over one half of the shell. Chan and Firmin's results are included for comparison. Results from Chan and Trbojevic are not shown because their results were different by a factor of two at the centre. Since good agreement is achieved at the centre location, with the harmonic displacement amplitudes, and with Chan and Firmin's solution, it is assumed that a scaling error occurred in the preparation of the figure in Chan and Trbojevic's paper.

Figure 6.23 shows the harmonic displacement amplitudes at the location of maximum displacement for the Cartesian formulation, along with comparison with Chan and Trbojevic's results. Aside from the discrepancy with Chan and Trbojevic centre location results, the asymmetric analysis also shows good agreement with published results. Of particular note is the harmonic coupling in the nonlinear problem. Although there is no loading component in the  $2\Theta$  harmonic, there is a  $2\Theta$  displacement component. As the displacements increase, the nonlinear terms become large, and the coupled displacement becomes particularly pronounced as the buckling load is approached.

Figure 6.24 contains a series of plots comparing harmonic displacement results from the Cartesian and cylindrical formulations. It is clear that the cylindrical formulation is stiffer and gives a slightly higher maximum load. The difference is quite small, however, and the shape of each harmonic displacement is similar for both formulations, even into the post critical regime.

The linear bending study in Section 6.2 showed that the major source of error in the cylindrical formulation was its inability to model lateral motion. This is not a major component of the deformation of the asymmetrically loaded cap. Thus the cylindrical formulation does a reasonable job of modelling its behaviour. However, the lower buckling load produced by the Cartesian formulation suggests a more accurate representation of the deformation and stress field. As with the axisymmetric caps, the maximum stress is lower than that given by the shell analysis of Chan and Trbojevic, 1977, perhaps because of the higher order representation of deformations and stresses through the shell thickness. It is also interesting to note that, although it is inferior to the Cartesian formulation, the cylindrical formulation still gives a more accurate result than do the shell models.

### 6.3.3. Cylinder Collapse

Cylinders subject to external pressure collapse in a variety of deformation patterns, depending on the geometry of the shell. Short cylinders buckle circumferentially into several harmonic waves. If the length of tube considered is increased, the number of circumferential waves in the buckling pattern decreases until the buckled form is elliptical, described by the second cylindrical displacement harmonic. Figure 6.25 shows the deformation modes for various cylinder lengths evaluated for this discussion.

Flügge, 1960, and Von Mises et al, 1961, provide analytical predictions of the buckling pressure and pattern. Experimental studies by Gerrard, 1962, and numerical results from Chan and Firmin, 1970a, compare favourably with these predictions. Chan and Firmin also explored the impact of deformation dependent loads on the cylinder's response to external pressure. Additionally, Chan and Trbojevic, 1977 reported results produced for a similar model using their harmonic mixed formulation. They also pointed out that a minor error integrating multiple harmonics by Chan and Firmin, 1970a, produced buckling loads which are artificially low.

A model geometrically identical to Chan and Firmin's (Figure 6.26) was constructed out of the Harmonic Lagrangian Tubular element for comparison. A second model was also prepared using the general purpose nonlinear finite element code ADINA (1986) to compare results with a conventional formulation. The harmonic model consisted of 20 quadratic elements with a complete Lagrangian displacement field in the meridional plane (9 node elements). The ADINA model was constructed using the MIT4 shell element using various mesh densities. Variations of the model used combinations of 20 and 40 element rows in both axial and circumferential directions. Both the ADINA and harmonic models utilized the symmetry at the axial midplane, and the ADINA model utilized the plane of symmetry along the longitudinal axis. Radial displacement and meridional rotations were restrained at the end of the model.

Like SLATS, ADINA provides a constant arc-length solution technique which permits evaluation of the equilibrium state of the structure beyond the peak load. However, this capability cannot be utilized with deformation dependent loads. Furthermore, ADINA's implementation of the constant arc-length algorithm usually caused the solution strategy to jump from the primary equilibrium path to a secondary or

complimentary solution. Consequently, ADINA's linearized buckling algorithm was employed to determine the approximate buckling load.

Chan and Firmin, 1970a demonstrated the influence of deformation dependent loading on the collapse load with their harmonic shell element. Their results showed that inclusion of this effect can have a significant impact on the solution of a buckling problem. However, it is not clear how the integration error in their paper contributed to this conclusion. In any case, a deformation dependent load capability has not been developed for the solid harmonic element presented here. Thus, a comparison with the deformation independent load results is appropriate to evaluate the accuracy of the formulation.

Table 6.1 shows the buckling pressures determined by the various techniques for a variety of cylinder lengths. Results from SLATS and ADINA in this table were produced using the basic mesh densities. The Cartesian formulation results compare well with the harmonic shell model. The ADINA models generated higher collapse pressures because both the circumferential geometry and displacement field is approximated by a piecewise linear function, and the linearized buckling solution does not include the nonlinearities introduced by the deformation as loading commences. On the other hand, the Cartesian and harmonic shell formulations can model the circumferential geometry and displacement field exactly, thus producing a better solution with fewer degrees of freedom.

Tables 6.2 and 6.3 show the improvement in solution achieved by increasing the mesh refinement for the various techniques at the minimum and maximum cylinder length considered. Also shown is the increase in solution time required. The solution clearly improves with increased mesh refinement. The improvement is greatest for the short cylinder because the number of circumferential waves is higher, resulting in a greater variation in the circumferential displacement field. The ADINA model shows the largest improvement, but remains the most inaccurate predictor of the buckling pressure because of the linearized buckling evaluation. Furthermore, the timing results show that the size of the model and solution time increase rapidly as the mesh is refined.

The harmonic Lagrangian tubular element produced the correct collapse mode for the various cylinder lengths modelled. There is also excellent agreement between the collapse pressures predicted by the element and the results from Chan and Firmin which do not include deformation dependent loading. This demonstrates the formulation is

valid for modelling the geometrically nonlinear, asymmetric behaviour of cylinder collapse under pressure.

#### **6.3.4. Hyperbolic Cooling Tower**

The cooling tower analyses were performed exclusively with the Cartesian formulation of the HLT element because of its superior large displacement capability. The tower is basically a thin shell problem, and the dominant displacements are in the radial direction, rather than the X or Y direction. In Chapter 4, it was pointed out that the transformation between Cartesian and cylindrical reference systems requires an additional Cartesian harmonic to model a given Fourier decomposition of the radial and circumferential displacement components. Because of this, some elaboration of the Fourier numbering in the following examples is in order to clarify the comparisons between the present study and the harmonic numbering used in the literature.

Chan and Firmin, 1970a, and Chan and Trbojevic, 1977 use the term "harmonic" to describe the total number of Fourier overlays employed in their models, including the zero'th, or axisymmetric, harmonic. Thus, when they refer to ten harmonics, for example, they mean specifically Fourier overlays zero through nine. To model an equivalent displacement field with the Cartesian HLT element, a total of eleven harmonics are required, numbered zero through ten. To remain consistent with the conventions from the literature, we will refer to the number of harmonics by the highest number employed - in this case ten. In so doing, the displacement field for a given number of harmonics is consistent between SLATS and models reported in the literature.

#### **External Pressure Load Case**

Chan and Trbojevic, 1977 present an analysis of a cooling tower under external pressure. Their paper also includes an analysis of a scale model for comparison with experimental results from Ewing, 1971. Analyses were performed using the displacement based SABA5 element and the mixed formulation element developed in the paper.

A model of the full size tower was prepared using the HLT element. Details of the model are given in Figure 6.27. Clamped boundary conditions are applied to the base of the model. Two load cases were considered. In the first, external pressure is applied incrementally to the model along with a perturbation load of  $10^{-6}$  times the external pressure in each harmonic to initiate buckling. All harmonics are perturbed

simultaneously. The second load case duplicates the asymmetric wind loading given by Chan and Trbojevic, 1977. The tower was modelled in both cases beyond the collapse load and the results are compared with those given in the literature.

Figure 6.28 shows the results from the uniform external pressure load case. Chan and Trbojevic modelled the tower with a total of ten harmonics. However, they indicated that the higher harmonics, 2 through 9, were "tested one at a time." It is not clear if this meant that a perturbation load was introduced in only one harmonic in each analysis, or that one harmonic was modelled in addition to the axisymmetric harmonic to determine the coupling between the load and each collapse mode. In any case, the modelling parameters are different from the simultaneous perturbations used to produce the results presented here. Consequently, no direct comparisons can be made between load - harmonic displacement relationships determined in this study, and those given in the literature. Collapse pressures, however, can be compared.

Their conclusion was that the lowest collapse mode occurred in the seventh harmonic. The HLT results, however, show that the collapse mode is in the ninth harmonic, at a pressure of 209 psf. The seventh harmonic is the next most significant displacement mode. This collapse pressure is at a lower pressure than those given by Chan and Trbojevic, which range from 260 psf. to 275 psf., depending on the harmonic. This is not surprising though, given the discussion in the previous section regarding the behaviour modelled through the shell thickness. Furthermore, Chan and Firmin, 1970a, note the large discrepancies between experimental results and shell theory predictions, both numerical and theoretical.

The fact that the tower buckles in the highest harmonic modelled suggests that the true buckling mode may be in an even higher harmonic. Program SLATS has not yet been equipped to efficiently model select higher order harmonics, therefore tests with more harmonics were not practical. These results do, however, indicate that the cooling tower problem has not been definitively answered in the literature surveyed here.

### **Wind Loading Case**

Chan and Trbojevic, 1977 also modelled the cooling tower under wind loads. The number of harmonics used in their wind load study was reduced from ten to eight, presumably because of the computation demands of the coupled nonlinear problem. Chan and Firmin, 1970, evaluated the Fourier coefficients for the pressure distribution



around a cylinder subject to lateral wind loading, which Chan and Trbojevic also used for their analysis. These pressure coefficients employed in the present analysis as well. In all analyses, the pressure distribution in the vertical direction was assumed to be constant.

Results from the Cartesian formulation are given in Figures 6.29 and 6.30, along with Chan and Trbojevic's results. Deformed shapes are shown in Figure 6.31 for the initial and large displacement deformation modes. Figure 6.29 gives the radial harmonic displacement amplitudes at the top of the shell for the fourth and fifth harmonics. Figure 6.30 plots the total radial displacement at the stagnation point at two vertical locations. Initial solutions using eight harmonics with the HLT element showed poor correlation with Chan and Trbojevic's results, so a additional runs were executed, using ten harmonics. Despite the additional harmonic refinement, the HLT solution is significantly different from Chan and Trobojevic's as the collapse load is approached. Initially, the slope of the load - displacement curves compare well between the formulations, but as the deformations increase, so does the deviation between the two solutions.

Several measures were taken to verify that comparable evaluations were being performed. Loading was changed from total (or normal) pressure loads to lateral pressure alone. The effect on the solution was minimal. Clearly, some fundamental differences between the two formulations exist.

Reviewing Chan and Trbojevic's formulation, it must be noted that all of the geometric nonlinear terms are not included. Their formulation is valid only where the displacements are small, that is, in the order of the shell thickness, meaning that the axisymmetric nature of the structure is not affected by the displacements. This characteristic of their formulation limits it to modelling the linearized buckling response of the shell, rather than the nonlinear buckling analysis which is provided by true Lagrangian formulations such as that employed in the HLT element.

### **6.3.5. Cylindrical Shell under Wind Load**

The above conclusion was tested by comparison with a similar analysis, performed using large displacement shell elements with a cubic displacement field. The analysis is presented by Schweizerhof and Ramm, 1986, in their paper on follower force effects on shell stability. Their paper includes a discussion of a cantilever cylinder subject to wind loading. The pressure distribution is similar to that given by Chan and Firmin, 1970a, thus allowing the same pressure coefficients to be used in a comparative

analysis. A model of the same cylinder was prepared with HLT elements (Figure 6.32), using three axial mesh densities and two levels of harmonic refinement - eight and ten harmonics.

Results of the wind loaded cylinder are presented in Figure 6.32 along with the solution from Schweizerhof and Ramm which does not consider follower type loading. The displacement shown is the radial displacement of the stagnation point at the free end of the cylinder. The correlation between these two formulations is obviously much better than that seen earlier. An interesting feature of the results is the limit point in the ten harmonic solution, where the load drops slightly before picking up more load as the displacement increases. An explanation for this behaviour will be presented in the following discussion of the harmonic displacements. But first, we should note the influence of the axial mesh refinement on the solution. Schweizerhof and Ramm used four cubic element rows in the axial direction of their model. Initially, eight quadratic HLT elements were used to provide an approximately equivalent displacement field in the axial direction. As Figure 6.32 demonstrates, this problem is relatively insensitive to the degree of axial mesh refinement. It appears that the harmonic refinement is far more important in this model. Although the model with ten harmonics is initially stiffer, after the initial peak, the response of the ten harmonic model is closer to that given by Schweizerhof and Ramm.

Figure 6.33 shows the load-harmonic displacement relationship for the first five radial displacement amplitudes at the free end of the shell. These are the largest displacement amplitudes, because the lower harmonic components of the loading function are most significant. When the cylinder undergoes collapse, however, these displacement components do not grow rapidly. In many cases, in fact, the harmonic displacement amplitudes decrease after passing the critical point.

The higher harmonic displacements are given in Figure 6.34. The amplitudes of these displacements are smaller than the lower harmonics. But, when the critical load is reached, it is these higher order harmonics which increase rapidly. Clearly, the higher order harmonics dominate the nonlinear buckling behaviour of the shell. Several additional harmonics would have to be added to approach the displacement field provided by Schweizerhof and Ramm's model, which employed 16 cubic elements around half of the circumference. Since the cubic displacement field can closely approximate a complete sine wave, 32 harmonic would be required to be comparable.

Given the rate at which the computational time increases with additional harmonics, this degree of harmonic refinement is impractical.

The higher order displacement field provided by Schweizerhof and Ramm's model permits a greater degree of deformation localization to be modelled. Figure 6.35 shows the deformation at the top of the cylinder during initial loading, and after the initial collapse. A sketch of the deformed shape given by Schweizerhof and Ramm is also shown for qualitative comparison. One can see that the lobes of deformation move from the sides of the tower towards the stagnation point as the wind load is increased. The lobes on Schweizerhof and Ramm's results are more localized. The finite number of harmonics limits the degree to which the deformation localization can be modelled. By the same token, however, a finite number of polynomial based shell elements also limits the degree of localization which can be modelled by the usual shell formulations. For example, Schweizerhof and Ramm's results show displacement lobes closer to the stagnation point because of the higher order circumferential displacement field provided by 16 rows of cubic elements. Very high degrees of mesh or harmonic refinement would be required to model the sharp bends or kinks which develop in the physical shell under wind load. However, comparing the two results, it does appear that a less refined mesh than that used by Schweizerhof and Ramm would suffice.

#### **6.4. Large Displacement Analysis: Beam Bending**

One of the major motives for developing the harmonic Lagrangian tubular element was to model the response of heavy walled tubular goods to bending. The curvature of a bent beam produces an accumulated lateral displacement which may be small relative to the wall thickness, or many times larger than the pipe diameter. Other harmonic elements which model geometric nonlinearities are restricted to thin shell structures and are limited to displacements in the order of the shell thickness. Given the target problem type for which the element was developed it is appropriate to evaluate its effectiveness for modelling a simple problem.

The cylindrical beam modelled is shown in Figure 6.36. The outside diameter of the beam is 100 mm, the wall thickness 10 mm, and the length 20 meters. The elastic modulus is specified as 200,000 MPa, and Poisson's ratio is 0.3. The bending stiffness,  $EI$ , is thus  $5.796 \times 10^{11}$ . A vertical plane of symmetry is utilized at the centre of the beam, and bending loads are applied to the end. Displacements are referenced relative to the plane of symmetry.

Since SLATS admits only nodal forces and deformation dependent tractions are not yet available, the bending forces do not rotate with the end of the tube as bending increases. The moment arm for the loads becomes smaller, the loads develop an in-plane component, and the end of the pipe is "pinched" (Figure 6.37) as loading progresses. Thus, the bending moment experienced by the beam does not vary linearly with the load increment. This must be taken into consideration when comparing with analytical evaluations of the large displacement bending response of the beam. However, the pinching phenomenon is also reduced by partially restraining the radial displacement of the pipe at the point where load is applied.

Timoshenko, 1961 and Sokolnikoff, 1956 both provide elastic solutions for beams subject to pure bending. This solution is easily extended to large displacement, as the curvature of the beam,  $\kappa$ , and its inverse, the radius of curvature,  $\rho$ , are constant along the beam length (Figure 6.38). The curvature is given by

$$\frac{1}{\rho} = \frac{M}{EI} . \quad (6.8)$$

The included angle,  $\beta$ , formed at any point  $x$  on the undeformed neutral axis is  $x/\rho$ , therefore

$$\beta = \frac{Mx}{EI} . \quad (6.9)$$

The angle included by the arc of the deformed neutral axis also corresponds to the section rotation of the beam where the load is applied. Because the tractions of the model in Figure 6.36 are not deformation dependent as mentioned above, the bending moment varies with the bending stress and the projected area of the beam section where the moment is applied (Figure 6.39). The bending moment is expressed in terms of the axial tractions on the end of the pipe, and the rotation of the pipe,

$$M = \frac{\lambda I \sigma_0}{r_0} \cos(\beta_L) , \quad (6.10)$$

where  $\lambda$  is the loading scale factor,  $\sigma_0$  is the reference bending stress, and  $r_0$  is the outside radius of the pipe. Substituting into the curvature expression yields a nonlinear relationship between  $\lambda$  and  $\beta_L$ ;

$$\frac{\beta_L}{\cos(\beta_L)} = \lambda \left[ \frac{\sigma_0 L}{ER} \right]. \quad (6.11)$$

Once  $\beta$  is determined, the applied bending moment and beam curvature can be calculated, and the displacement field along the neutral axis evaluated using

$$u_x = x - \rho \sin(\beta) \quad (6.12a)$$

$$u_z = \rho (1 - \cos(\beta)) \quad (6.12b)$$

Figure 6.40 shows the load factor - displacement relationships for the beam and the results of analyses using the Cartesian formulation. The Cartesian formulation matches the analytical description above almost exactly over a wide range of displacements using only three Cartesian harmonics (0, 1, and 2). Since the bending loads do not rotate with the end of the beam, the theoretical limit to the rotation at the end of the tube is 90 degrees. The Cartesian formulation remains accurate to within a few percent of this theoretical limit. The cylindrical formulation, however, would stiffen immediately, and would not produce meaningful results for such a long slender beam, even when several more harmonics are included. This is a consequence of the large lateral translation at the end of the beam, which the cylindrical displacement field is unable to model. The Cartesian formulation element provides much greater capability for modelling such problems and better solution economy because it requires a minimal number of harmonics to model lateral motion.

This conclusion also suggests a possible application to modelling tubular components in structural assemblies such as flexible space frames. The element could be implemented as a structural member with appropriate transformations. Using the first one or two harmonics, the element would behave like a conventional large displacement beam or truss element. By utilizing more harmonics, however, more complex behaviour could be modelled in the structural component by this formulation. This could be valuable in analyses where predictions of post failure response are required.

## 6.5. Large Displacement Analysis: Beam-Column Collapse

### 6.5.1. Problem Overview

A tube was modelled under compressive axial loading (Figure 6.41) to test the effectiveness of the formulation for modelling nonlinear collapse problems with very large displacements. A small bending moment applied to the end of the beam produced

the effect of a slight eccentricity in the load relative to the beam axis. Model parameters were selected to produce Euler buckling at loads approaching the yield of common steel materials. Local post collapse stresses are large compared to typical yield stresses, but since nonlinear material properties have not yet been integrated into the program, comparisons with post collapse results of physical tests are not possible. Instead numerical results from conventional codes are used to verify the results.

### **6.5.2. Model Descriptions**

The model is shown in Figure 6.41. The half length is 100 inches long, ten inches in diameter, and one half inch through the wall thickness. Symmetric boundary conditions are applied at one end, and other end has one lateral degree of freedom fixed to remove the rigid body mode. In addition to the axial load applied to the free end, a small perturbing moment corresponding to a load eccentricity of 0.14 inches was included to initiate lateral motion of the neutral axis. The nodal harmonic loads calculated from these boundary conditions were maintained in the same ratio throughout the analysis.

Several SLATS models were used to model the problem with varying parameters. Most used 15 nine node elements with three point Gauss quadrature and full integration of the Fourier products. Results were first verified by comparison with analytical solutions and numerical solutions from the commercial finite element program, ADINA. Additional models were then used to test the influence of the various parameters, including integration order in and out of the axisymmetric plane, displacement field (eight, or nine node elements), and mesh density and distribution.

The ADINA models used 27 node quadratic brick elements, since the displacement field provided by these elements most closely approximates that in the quadratic HLT element. The computational demands of this model limited the number of cases that could be modelled. The mesh included one element row through the wall thickness, 20 elements along the length of the meridional plane, and circumferential mesh densities of eight and twelve elements around half of the circumference.

### **6.5.3. General Behaviour**

The first comparison is with the linear buckling analysis of the column. Popov, 1978 gives the linear buckling solution for a column subjected to a combination of

bending and axial compression. His solution for the fourth order differential equation for elastic buckling of columns with an eccentric load<sup>9</sup> is:

$$v = A \sin (\lambda x) + e (\cos (\lambda x) - 1) , \quad (6.13)$$

where  $v$  is the lateral displacement of the beam,  $A$  is a constant, determined from boundary conditions,  $\lambda^2 = P/EI$ , and  $e$  is the eccentricity of the load. The constant  $A$  is determined to be:

$$A = e \frac{\sin (\lambda L/2)}{\cos (\lambda L/2)} . \quad (6.14)$$

The equation for the displacement at the centre of the column is the familiar secant formula:

$$v(L/2) = e (\sec (\lambda L/2) - 1) \quad (6.15)$$

Figure 6.42 shows the initial load - displacement behaviour at the end of the column, compared with the secant formula Eq. (6.15). The numerical solution is in close agreement with the linear analytical solution, particularly in the early stages of loading. The finite element model includes nonlinear terms, thus giving a buckling load that is lower than the linear buckling solution. The difference is small, however, with the linear analytical result only 4% higher than the nonlinear solution.

The linear beam-column analysis does not consider nonlinearity arising out of deformations in the beam cross-section. This has minor significance in determining the limit load of the column, as evidenced by the agreement cited above. But, as the column buckles, the lateral displacement of the centre of the beam, combined with the axial load produces an increasing bending moment at the centre of the beam. As bending increases, the circumferential distribution of axial stress produces ovalization of the tube. As the ovalization increases, the moment of inertia is reduced, thus reducing the resistance to

---

<sup>9</sup> Although Popov, 1978 does not make it clear, his solution is for the deformed shape of the beam relative to the eccentric load point, rather than the neutral axis of the beam. Equation (1.13) includes a correction to Popov's equation, giving the displacement field relative to the unloaded neutral axis of the column.

bending. The bending resistance decreases with bending, until a maximum bending stress is reached, at which point collapse by ovalization will occur.

The reduction in bending resistance with bending was first studied by Brazier, 1926, and is known as the Brazier effect. Collapse by Brazier buckling is a nonlinear effect, because the reduction in bending stiffness is produced by the change in the geometry of the cylinder. Brazier showed the critical bending load for a thin walled cylinder to be

$$M_{cr} = \frac{2\sqrt{2}}{9} \frac{E\pi R t^2}{\sqrt{1-\nu^2}}, \quad (6.16)$$

where  $R$  is the radius at the centre of the cylinder wall and  $t$  is the wall thickness. The critical bending moment for the cylinder under consideration is  $36.87 \times 10^6$  lb-in., assuming a shell radius of 4.75 inches. The bending stress for this bending moment is well beyond the elastic limit of tubular goods made of steel. The nonlinear analysis, however, is valuable for verifying the formulation. This sample is therefore pursued numerically.

Figure 6.43 gives the load - displacement relationship for the axial and lateral deflections at the end of the beam. This problem is interesting because it exhibits two types of collapse in the course of the solution. The first is Euler buckling at the classically defined limit load. The second is Brazier collapse at the symmetry plane due to bending produced by the lateral deflection of the loaded end as the column buckles. Although the load - displacement relationship appears quite complex, the Brazier collapse is perhaps easier to understand when the results are expressed in terms of the bending moment on the collapsing sections, rather than the axial load, Figure 6.44. Comparing the critical points on the load - displacement and bending - displacement curves one sees clearly that the first limit point is only a limit relating to the magnitude of the axial load, while the second limit point is related to the bending moment on the critical cross section and is a consequence of the nonlinear ovalization behaviour of the section (Brazier, 1926, and Brush and Almroth, 1975).

Figure 6.45 shows the shape of the tube at three stages of loading; immediately prior to Brazier buckling on the equilibrium curve (point a, Figure 6.43); at the minimum displacement point after collapse of the section (point b); and at a point far beyond the critical bending point on the curve (point c). The deformations shown are



actual deformed shapes, not exaggerated. Figure 6.46 shows an enlarged perspective view of the outside surface of the tube at the last point of the analysis. It illustrates clearly the large asymmetric deformations that the formulation is able to model. At the end of this analysis, the inside diameter has not closed to the point of touching at the centre. In other cases, the analysis was continued beyond the point where contact occurs. However, no procedures to handle contact have been developed, so the two surfaces would penetrate each other, making any solution beyond the point of contact invalid.

Figure 6.44 shows the bending moment - displacement relationship for the tube - column calculated using SLATS. The bending moment at the column centre is calculated by multiplying the axial load by the lateral displacement at the centre. The load eccentricity moment (about 0.14 lb-in.) is insignificant in comparison. The maximum bending calculated is  $34.83 \times 10^6$  lb-in., which is about 6% less than Brazier's solution. This agreement is considered excellent, given that Brazier's analysis assumes a long thin wall cylinder, and does not consider the influence of axial load on the solution.

#### **6.5.4. Numerical Verification**

The analytical comparisons described above clearly provide high confidence in the large displacement Fourier decomposition technique. Further verification is achieved by numerical solution of the same problem using a general purpose finite element program with a conventional polynomial based solid element. The nonlinear finite element code ADINA was used to model the same problem. The same number of elements in the axial direction (20) and also in the radial direction (1) were used. A three dimensional quadratic Lagrangian element which uses 27 nodes was selected from ADINA's element library. This provides a meridional displacement field equivalent to that used in the SLATS model. Two mesh densities were employed in the circumferential direction, the first using eight elements around the circumference, and the second using 12 elements to provide additional refinement to the cylinder geometry and element displacement field. A third model using 16 elements around the half circumference was attempted, but the solution time was unacceptably high.

The load - displacement curves from ADINA and SLATS are compared in Figure 6.47. The models show good agreement up to the point of Brazier buckling. The ADINA models calculate larger lateral displacements, and therefore bending moments, before the ovalization collapse occurs, but comparing results from the two

circumferential mesh densities, it is clear that the solution approaches the SLATS results as the circumferential geometry and displacement field are refined.

The ADINA solution has problems evaluating the post Brazier collapse response of the tube, presumably because of the manner in which it adjusts the size of the arc length in the incremental solution strategy. In the ADINA model with eight circumferential elements, the arc length became too large, and the solution strategy found a different equilibrium path, which was traced for a time before execution was terminated. The twelve element model reversed direction more accurately, but the post collapse solution proceeded slowly, and it was necessary to stop the solution before much of the post collapse response could be determined. The point of collapse is close to the HLT result, and the slope of the post collapse curve is much closer in the higher resolution ADINA model.

### **Cylindrical Formulation Results**

The tube - column was also analysed using the large displacement cylindrical formulation. Previously in this chapter, it was shown that this formulation stiffens with lateral displacements making it unsuitable for global bending type problems. The tube - column obviously falls into this category, particularly near the collapse load. Even with the load eccentricity used in the previous problem, the lateral displacements early in the loading process produced problems.

Figure 6.48 shows the load - displacement relationship produced with the cylindrical problem for a column with a much smaller load eccentricity - 0.0004 inches. These results show the cylindrical formulation to provide a reasonable solution over the initial portion of the curve. But, as the lateral displacements increase, the solution breaks down because rigid body translation is not modelled exactly. Increasing the number of harmonics also increases the range over which the solution is reasonably accurate, but eventually, the strain energy developed by the inaccurate displacement field causes the structure to stiffen artificially, and the solution to deviate from the correct behaviour.

The results show that even with six harmonics, the range of motion is only 0.4 inches, which is less than the wall thickness of the tube. Furthermore, this magnitude of displacement can be reached at load levels much lower than the collapse load if, for example, the eccentricity of the load were higher. In such cases, the solution would be inaccurate over most of the range of the response, and no valid conclusions could be

drawn from the results. In contrast, the Cartesian model will accurately model beam behaviour including arbitrarily large displacements with only two harmonics, or one harmonic if the degrees of freedom are transformed into cylindrical components.

As discussed in previous sections, the deficiencies in the cylindrical formulation stem entirely from the difficulty in providing an element displacement field which can model rigid body modes with large displacements, not from an inherent flaw in the formulation. The cylindrical formulation could be as accurate and more efficient than the Cartesian formulation if this problem were resolved.

## **6.6. Element Parameters**

Several parameters affect the performance of the HLT element in modelling structural behaviour. The element displacement field is currently selectable through the use of four, eight, and nine node elements, and by the number of displacement harmonics included in the analysis. Other configurations are also possible with higher order meridional displacement fields in one or two directions. Integration parameters are also significant factors in the performance of the element. Meridional integration is influenced by the Gaussian integration order; circumferential integration is affected by the trapezoidal integration order. The following subsections discuss the manner in which these various parameters influence the element behaviour.

### **6.6.1. Polynomial Displacement Field**

The behaviour of a beam under pure bending was shown to be modelled exactly by elements with a quadratic displacement field. Both eight and nine node elements include quadratic terms, but the nine node version has the quadratic cross-terms,  $R^2Z^2$ , whereas the eight node version does not. These higher order cross terms are not a component of the linear pure bending displacement field, so the eight and nine node element models produce identical results.

Section 6.2.2 showed that the linear displacement field of the four node version of the element produced significant errors in the displacement field under pure bending, but the eight and nine node elements produced identical exact results. In the current subject model, the lateral displacement field is a trigonometric function which can be approximated reasonably well with a quadratic polynomial function, but not with the linear displacement field of the four node element. It was therefore understood that the four node element would produce results significantly different from the eight and nine

node elements. There was some question, though, regarding any differences between the eight and nine node element results. A test model was run to determine the difference in solutions produced by eight and nine node elements.

Figure 6.49 shows the load - displacement results produced by identical eight and nine node element models. Both models used eight harmonics to model the circumferential displacement field, 20 elements in the axial direction, three point Gauss quadrature in the plane R - Z, and full integration in the circumferential direction. The results show virtually no difference up to and beyond the Brazier collapse point. Only slight differences appear when the asymmetric deformations at the centre become large. Consequently, it may be concluded that the displacement field does not have any significant  $R^2 Z^2$  terms in the displacement field while the deformations in the cross section of the tube are small. Only when the cross section is subject to large deformations are any differences noticeable, but even so, the differences are slight.

This conclusion should not automatically be assumed valid for all problems. In some situations, the highest order displacement terms can be significant. It must be remembered, though, that in this element, these higher order terms would be significant **through the element thickness**, not the entire element cross section, since the overall cross sectional displacement field is modelled by the Fourier functions. This explains why the difference between the eight and nine node solutions is slight and noticeable only when the cross sectional deformations become large.

#### 6.6.2. Harmonic Displacement Field

As the complexity of the circumferential displacement field increases, the number of harmonics required to model the displacement field increases as well. The simple beam behaviour, for examples, requires only the zero'th, first, and second Cartesian displacement harmonics. If the displacement degrees of freedom are transformed to the cylindrical components, only the zero'th and first harmonics would be necessary. The results referred to in the following discussion were calculated with the Cartesian formulation, using Cartesian degrees of freedom, but since the model is a shell, albeit a thick one, the displacements have been transformed to cylindrical components for discussion.

Figures 6.50 shows the lateral displacement (first radial cylindrical harmonic) for the beam column calculated using the Cartesian formulation with a variety of harmonic

refinements. As the previous paragraph stated, simple beam behaviour producing Euler buckling is modelled well with two harmonics. The model stiffens as the displacements become very large, but this is a consequence of nonlinear terms becoming significant, not a limitation of the formulation. When higher harmonics are included, the structure shows a more significant softening behaviour produced by the reduced bending resistance as the cross section ovalizes. Ovalization is modelled by the second cylindrical harmonic, which is plotted with load in Figure 6.51. Note that models using three or more Cartesian harmonics model a similar limit point behaviour because of the ovalization capability. The model with two Cartesian harmonics cannot model ovalization, because the second cylindrical displacement harmonic is reproduced in the first, second, and third Cartesian displacement harmonics.

As the bending moment at the centre approaches the critical value, where Brazier buckling occurs, the circumferential displacement begins to localize. The first occurs in the third cylindrical harmonic, Figure 6.52. Although the axial load begins to increase, the bending moment decreases because the lateral displacement decreases. Four Cartesian harmonics are required to complete the third cylindrical harmonic. However, the four harmonic model would not produce a large displacement in the third harmonic mode. This must be due to significant coupling terms between the third and fourth harmonics cylindrical harmonics.

Figure 6.53 shows the fourth radial cylindrical harmonic at the centre of the tube. The fourth harmonic first decreases in magnitude as the section begins to collapse, while the third harmonic increases rapidly. When the load reaches a maximum, the fourth harmonic reverses direction and increases rapidly as the load drops off.

The plots of harmonic displacements may not clarify the role each plays in the deformation of the cross section. Figure 6.54 shows the deformed shape of the outside diameter of the pipe at several points in the load deflection curve. The first shape is for the undeformed shape of the tube outside diameter. The second shape is near the point where Brazier buckling is imminent, point (a) on the equilibrium curve (Figure 6.43). The cross section exhibits a strong ovalization pattern at this point. The next shape is at the snap back, point (b), where the third harmonic is at a maximum. Note that the side of the pipe on the inside of the radius of curvature has moved slightly outward, giving the cross section something of a kidney shape. The final form given is for point (c) of the analysis. The deformed shape shows that the ovalization suggested by the displacement

graphs translates into a shape similar to an hourglass, with some asymmetry about the neutral plane produced by the third and fourth harmonics.

Using more than five Cartesian harmonics for the displacement field has an insignificant effect on the response of the model up to the point of Brazier collapse. Initially, the post collapse behaviour is the same in all cases, but as the deformation at the point of symmetry increases, differences between results arise. Figure 6.55 demonstrates how additional harmonics affect the solution. Obviously more than five harmonics are not required to determine the collapse point, or the immediate post buckling behaviour. It is interesting that the post collapse displacement curves are grouped into pairs. This suggests the higher order harmonic deformations are in modes which are multiples of the basic ovalization mode. This simply means that higher localization of the deformations in the lobes of the ovalization mode can be modelled when more harmonics are included.

### 6.6.3. Gaussian Integration Order

As in the linear analysis case, reduced integration in the meridional plane of the quadratic element using a Lagrangian element displacement field (nine node element) produced an indefinite stiffness matrix, because of spurious modes. It was shown that reduced integration worked fine for the eight node element, and in some cases yielded better results than full integration using three point Gauss quadrature. It was also shown that for uniform rectangular elements, three point quadrature integrates the elements exactly.

In nonlinear analyses, the strain - displacement matrix,  $[B_L]$ , includes higher order polynomial terms which require more integration points for an accurate evaluation of the element stiffness matrix and equilibrium condition. In the unloaded configuration, the nonlinear strain displacement matrix reduces to the linear version. Therefore, the nonlinear analysis can be started using the same integration parameters used in the linear analysis case. As loading progresses, the higher order terms in the strain - displacement matrix, and the geometric stiffness matrix, become significant, requiring higher order integration procedures.

An effort was made to model the tube - column with eight node elements using reduced (2 x 2) Gauss quadrature in the meridional plane and full integration of the Fourier terms in the circumferential direction. The first increment produced a correct

answer, but because of the relatively large lateral displacements, the stiffness matrix in subsequent increments produced negative pivots, and the solution was unable to proceed.

When the Gauss integration order was increased to four point quadrature, the solution was identical to the three point quadrature solution. Therefore, it must be concluded that, since the Jacobian is constant throughout the regular rectangular element, the order of displacement terms in the stiffness matrix must be no higher than  $R^5$  and  $Z^5$ , since quadrature using  $n$  points will exactly integrate a polynomial of order  $2n - 1$ . If distorted elements are used, the influence of Gauss integration order will be noticeable, since the variation in the Jacobian will not generally be a polynomial distribution. Usually, though, unless element distortions are very large, it will not dramatically affect the solution.

#### **6.6.4. Fourier Integration Order**

Gaussian integration of the polynomial meridional interpolation functions has been commonly addressed in the literature, and is discussed in virtually all finite element texts because of the prevalence of polynomial interpolation functions in finite elements. Utilization of the Fourier functions, on the other hand, is relatively uncommon. In those cases where Fourier decomposition is employed, the formulations are primarily linear, permitting analytical integration of the element in the circumferential direction. In the rare instances where the decomposition technique is used in nonlinear formulations, such as Chan and Firmin, 1970a, and Chan and Trbojevic, 1977, the formulation is limited to relatively small displacements because analytical integration was determined for a product of three Fourier functions at most.

The HLT formulation was developed to model general three dimensional behaviour. To achieve this, it was shown in Chapters 3 and 4 that the product of as many as five harmonic functions must be integrated. Rather than try to perform this analytically, numerical procedures were developed to integrate all of the Fourier products simultaneously. The validity of the integration procedures was investigated by analysing the tube - column, using a range of circumferential integration orders. Figure 6.56 shows the load displacement results for the column with a number of circumferential integration orders. All models used nine node Cartesian formulation elements, five Cartesian displacement harmonics, and three point Gauss quadrature in the meridional plane. The number of harmonics specified in the legend give the number of integration points employed about the entire circumference of the tube. The analysis assumed, however,

that the displacement field would be symmetric about the meridional plane, so only half the total number of harmonics actually were needed to integrate the stiffness matrix. Consequently, only even numbers of circumferential sample points could be used for the Fourier product integration.

A model with only ten circumferential integration points was attempted. The stiffness matrix evaluated at the initial, unloaded state was indefinite and could produce no meaningful results. When the number of integration points was increased to 12, a reasonable solution could be achieved up to and beyond the point of Brazier buckling at the centre of the tube. Even in the region well beyond Brazier buckling, the 12 point integration scheme gives results that are surprisingly close to the full integration case. This level of integration would be adequate to exactly integrate the linear form of the finite element equations for four harmonics. Why, then, would this number of integration points produce such good results over such a large region of the column's response? The reason is that until Brazier collapse occurs, the deformation of the beam section is relatively small, and the dominant displacements are in harmonics numbered zero, one and two. The nonlinear stiffness terms associated with these harmonics only are also integrated exactly with 12 integration points. The model is initially governed by these lower harmonics. Since the nonlinear terms for the lower harmonics, and the linear terms for the higher harmonics are integrated exactly, the solution is very accurate.

It is only in the post - Brazier collapse regime where the difference between integration orders become significant. Figure 6.56 shows that the 12 integration point model exhibits minor deviations from the full integration base case soon after Brazier buckling occurs, snapping back further than the higher order integration cases. The 18 point model follows the base case around the curve after Brazier buckling, deviating noticeably only after relatively large deformations in the tube section are produced.

The most interesting result is from the 22 point integration model, which matches the "full" 26 point model exactly over the entire analysis range. Higher integration orders also produced solutions which were identical. The close match between these models indicates that only 22 integration points are required for exact integration of the Fourier products. This number of circumferential sampling points would exactly integrate the stiffness matrix in the cylindrical formulation, but since trigonometric functions must be used in the strain - displacement matrix for the geometrical transformations, it was expected that additional integration points would be required. This result suggests that not all of the harmonic components are cross - multiplied in



evaluating the stiffness matrix or equilibrium state. Thus, the same circumferential integration rules used in the cylindrical formulation can also be applied to the Cartesian formulation to determine the number of circumferential points required for exact integration of the Fourier products.

#### 6.6.5. Element Geometry

To determine the effect of element geometry on the solution of the test problem, the tube - column was evaluated with a variety of mesh densities for comparison purposes. The first evaluation considered the axial mesh density used to model the tube. The base model used a higher mesh density near the plane of symmetry to more accurately model the axial harmonic displacement gradients of the kink in the tube. Two more models were executed which used the same number of elements, but distributed them more uniformly along the length. The length of the elements at the centre of the tube were extended from 1.2 inches in the base case to 2 inches and 5 inches in the other two cases. Two more models were also run with fewer elements, and the mesh in these cases was uniform along the length of the tube: one model with 10 elements used an element length of 10 inches, and the other used five element each 20 inches long.

Figure 6.57 shows the lateral displacement at the tube centre for each axial refinement model. Clearly Euler collapse is not significantly affected by the mesh density. Every model gives a peak load within 0.02% of the mean 1196.75 kip average. The cross sectional deformations are small at the peak load, and the axial distribution of the harmonic displacement distributions is closely approximated by the quadratic displacement field. Even halving the number of elements from ten to five produced no significant change in the limit load of the column.

Brazier buckling, on the other hand, is strongly influenced by the mesh density because of the accompanying high axial gradients of the harmonic displacements. Figure 6.58 shows the axial distribution of the second, third and fourth radial displacement harmonics for point (b) on the equilibrium curve (Figure 6.43). The curves are referenced to the harmonic displacement at the centre of the tube. It shows the length of the asymmetric deformation region to be prevalent over an 18 inch region. Obviously, the 20 inch element in the five element model cannot model the localized deformations which occur in this region. consequently there is no bifurcation in the load - displacement curve for this model. The ten element model has elements more closely matched to the asymmetric deformation region, and therefore shows some tendency to

collapse at the centre. However, the displacement field of the smaller element provides only a crude approximation of the axial displacement field, and does not accurately represent the behaviour of the tube. The ten element model predicts collapse significantly beyond that produced by the higher resolution models, and rather than a bifurcation in the load - displacement curve, it produces a less significant change in the slope of the curve.

The element size in all of the 15 element models is smaller than the length of the asymmetric deformation pattern. In these cases, a more accurate representation of the harmonic displacement field can be modelled by the elements. Consequently, the collapse behaviour is modelled more completely. All of the 15 element models give a similar collapse load and lateral displacement, and thus displacement. The 15 element model least refined at the centre calculates a critical bending moment on the cross section only 1.4% below that given by the most refined model, which utilizes a localized mesh density more than four times higher. The initial post buckling response is also similar amongst these three models. However, once significant axisymmetric deformations develop, the models begin to produce different solutions because of the higher gradients which develop. The model with 5 inch elements is significantly different from the two higher resolution models. The 2 inch and 1.2 inch elements are very similar, indicating mesh density convergence has been achieved for this collapse mode.

The mesh density in the radial direction was also investigated by testing a model which used the highest resolution axial mesh near the centre, along with two elements through the wall thickness. The results from the two element row model are compared with the base case single row model in Figure 6.59. The analysis proves that the displacement field through the wall thickness modelled with sufficient accuracy up to the point of Brazier collapse. The difference between results in terms of collapse loads (bending and axial) and lateral displacement is negligible. The higher resolution model through the thickness give a significantly different post Brazier collapse response, because of the high displacement gradients through the wall thickness which result from large asymmetric deformations at the centre of the tube.

## **6.7. Solution Efficiency**

Others have demonstrated the solution efficiency achieved by the Fourier decomposition technique in linear analysis, and in a few nonlinear cases where the large displacement formulation is not completely general. In linear formulations the solution

efficiency is high because the harmonics are uncoupled. In mildly nonlinear problems, the harmonic coupling may be ignored in the stiffness matrix. A correct solution can still be obtained by using equilibrium iterations. But, as the nonlinearities and harmonic coupling increase, the number of iterations required for convergence also increase. At some point, the stiffness properties become such that a solution will not be found without the coupling terms in the stiffness matrix.

Of course, the Cartesian formulation presented here, by necessity has coupled harmonic stiffnesses because of the trigonometric geometric transformation which is used. There was some discussion of transforming the finite element degrees of freedom from Cartesian displacement components to cylindrical type components which would decouple the stiffness matrix for the unloaded structure. However, this exercise will be left for another time. Comparisons of solution efficiency are therefore made between the coupled harmonic analyses and solutions using the general purpose program ADINA.

Figure 6.60 compares the solution times for the thin shell cylinder using SLATS and ADINA. All times for one iterate in the nonlinear solution strategy. The ADINA model used the four node shell element, which models a linear element displacement field. Two mesh densities - 20 and 40 element rows - were used in each of the axial and circumferential directions, for a total of three models. The SLATS model consisted of 10 elements with a quadratic harmonic displacement field. Three runs are compared, with three, five and eight harmonics. The graph shows the two models to be roughly comparable in terms of total execution time, but the distribution of distribution of solution times is quite different. While the simple ADINA shell element can be evaluated quite quickly, the system of equations is much larger, so most of the execution time is consumed solving the equations. The HLT element requires more time to evaluate, but the system of equations is more compact, requiring only a fraction of the solution time. The time required to evaluate the elements could be reduced by a factor of four if a linear meridional displacement field were used in the HLT model which would make the meridional displacement field equivalent to the ADINA model. Although the HLT element was not designed for modelling thin shell problems, it proved to be quite capable for modelling several thin shell problems accurately and with relative efficiency.

Where the HLT formulation truly excels in terms of performance is in axisymmetric structures which require a solid element formulation. Figure 6.61 shows a comparison of solution times from SLATS and ADINA for comparable solid models. The HLT elements in SLATS used a Lagrangian biquadratic element displacement field,

while the 27 node polynomial based solid element was chosen from the ADINA element library, because it most closely resembles the behaviour of the element used in the harmonic formulation. Both models consisted of 20 elements in the axial direction. In both models, solution times are given for a variety of circumferential displacement fields radial mesh refinements.

The analysis results demonstrated superior accuracy from the HLT formulation, while the solution times are significantly less than those from ADINA. As with the timing comparison for the shell models, the HLT element requires significantly more time to generate the system of equations, but because the number of degrees of freedom is so much smaller, the stiffness matrix can be solved much more quickly. The significance of this is illustrated by comparing the solution times for the one and two row models. Since matrix generation dominates the total calculation time in these simple SLATS models, total solution time approximately doubles when the mesh is doubled in the radial dimension. With ADINA, the total time nearly quadruples: matrix generation increases by more than a factor of two, because the stiffness matrix is too large to be contained in main memory, and solution of the equations takes more than five times as long because the bandwidth and number of equations has doubled.

In both the shell and solid models, the number of elements is relatively small. The advantage of the Fourier decomposition formulation will increase even more dramatically in models where the number of elements, and the number of rows, are higher. As more elements are required to represent practical structures, the size of the system of equations will increase, and the associated increase in solution time for the stiffness matrix will cause the major processing task to shift from matrix generation to matrix solution. The computing requirements will be large, but three dimensional analysis will be possible for problems which were previously out of reach.

## **6.8. Chapter Summary**

This chapter focussed on investigation and verification of the Total Lagrangian formulation of the axisymmetric finite element using Fourier decomposition for the circumferential variation in the displacement field. Comparisons with analytical and numerical studies in the literature verified that the Cartesian form of the element provides accurate evaluations of asymmetric behaviour in axisymmetric structures. The cylindrical form produced poor results in general because of inaccurate rigid body

modelling. Problems which did not include rigid body translation were, however, modelled reasonably well.

While not intended for thin shell structures, the program works well in modelling these structures, provided the deformations do not become too localized, in which case the number of harmonics required for adequate displacement field representation becomes unmanageable.

The main analysis suite focussed on a tube subjected to an eccentric axial load. The analysis was limited to elastic material properties, so comparisons were made to analytical solutions and numerical solutions produced by the commercial finite element program, ADINA. The results from the Fourier decomposition formulation corresponded very well with analytical and numerical solutions.

The element exhibited modest variations in behaviour with changes in element evaluation parameters. Parameters in the meridional plane, such as Gauss quadrature order and number of nodes (displacement field order) influence element behaviour in the same way conventional polynomial based elements are influenced. Circumferential integration parameters produced relatively small changes in the solution, provided the number of integration points was sufficient to integrate the linear stiffness matrix. It appears that the trigonometric geometry transformation functions have no influence on the number of circumferential integration points that are required to exactly integrate the Fourier products in the formulation. It also seems that refinement of the circumferential integration techniques holds the most promise for increasing the solution efficiency even further.

Table 6.1 - Cylinder Critical Pressures  
Basic Mesh<sup>1</sup> Results

Cylinder Length	FLUGGE <sup>2</sup> -	SABA5 <sup>3</sup> 1 element 5 harmonics	SLATS <sup>4</sup> 10 elements 5 harmonics	ADINA <sup>5</sup> 20 x 20 elements
30	30.5	31.4	32.1	39.17
100	8.9	9.6	9.96	11.39
200	4	4.9	5.32	5.60
600	2.7	3.5	3.65	3.77

Notes:

- 1 Mesh refinement of model,  $a \times b$ , where  $a$  refers to number of element rows in axial direction, and  $b$  refers to the number of element rows or the number of harmonics in the circumferential direction.
- 2 Reference - Flugge, 1960
- 3 Reference - Chan and Firmin, 1970a, Pressure independent loading.
- 4 Present Study
- 5 ADINA, 1987

Table 6.2 - Cylinder Critical Pressures  
30 inch Cylinder

Source	Mesh <sup>1</sup>	Pcr
FLUGGE <sup>2</sup>	-	30.5
SABA5 <sup>3</sup>	1 x 5	31.4
SLATS <sup>4</sup>	10 x 5	32.1
SLATS	20 x 5	30.1
ADINA <sup>5</sup>	20 x 20	39.17
ADINA	20 x 40	36.21
ADINA	40 x 40	35.96

See Table 6.1 for complete references

Table 6.3 - Cylinder Critical Pressures  
600 inch Cylinder, Basic Mesh

Source	Mesh <sup>1</sup>	P <sub>cr</sub>
FLUGGE <sup>2</sup>	-	2.7
SABA5 <sup>3</sup>	1 x 5	3.5
SLATS <sup>4</sup>	10 x 5	3.65
SLATS	20 x 5	3.40
ADINA <sup>5</sup>	20 x 20	3.77
ADINA	20 x 40	3.72
ADINA	40 x 40	3.71

See Table 6.1 for complete references



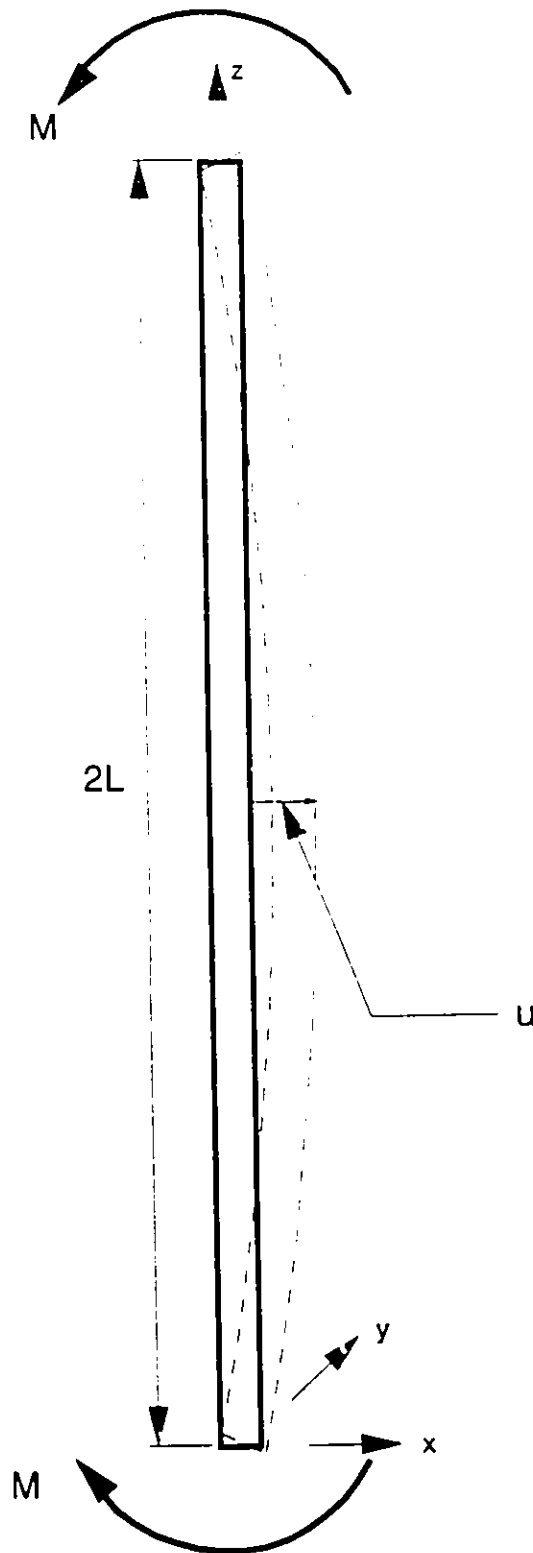


Figure 6.1 Tube - beam bending problem

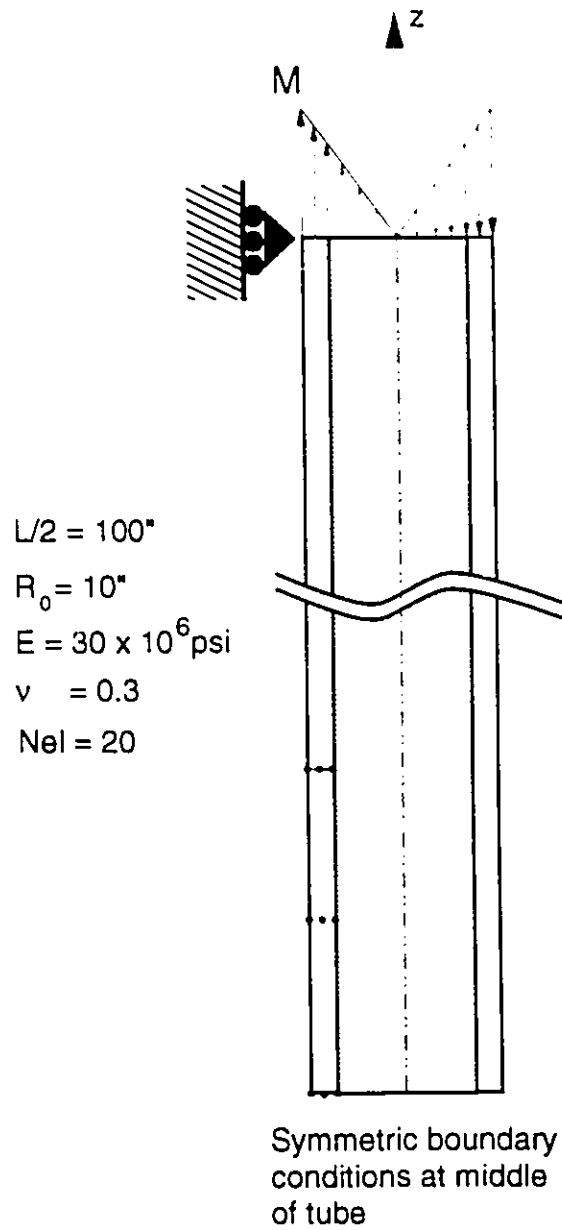


Figure 6.2 Tube - beam bending model

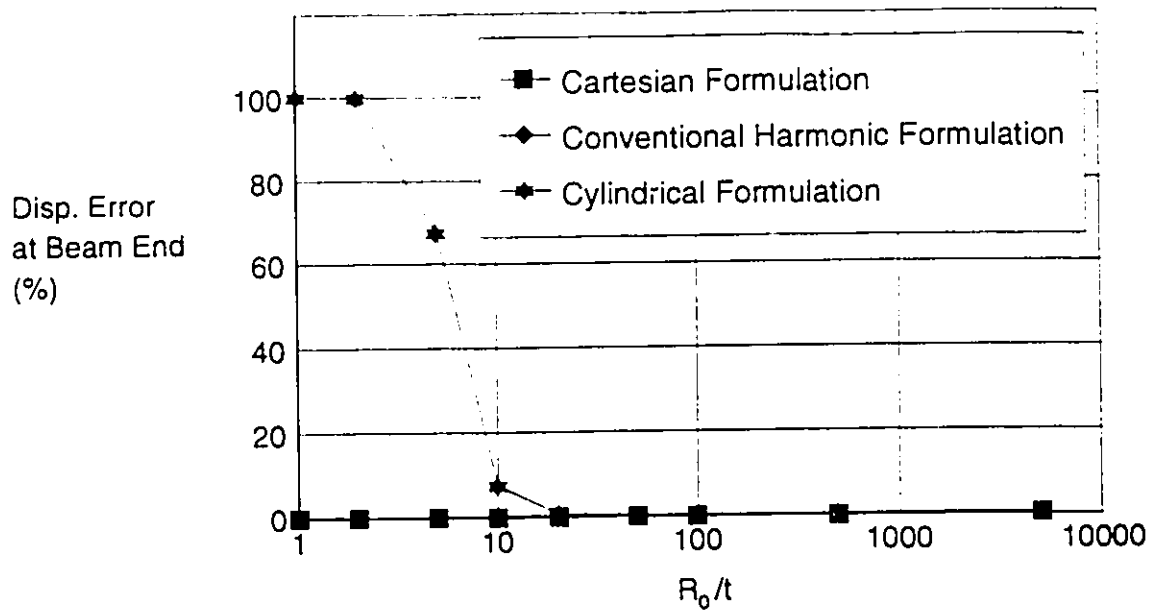


Figure 6.3 Formulation comparison in pure bending, small displacement and quadratic element displacement field

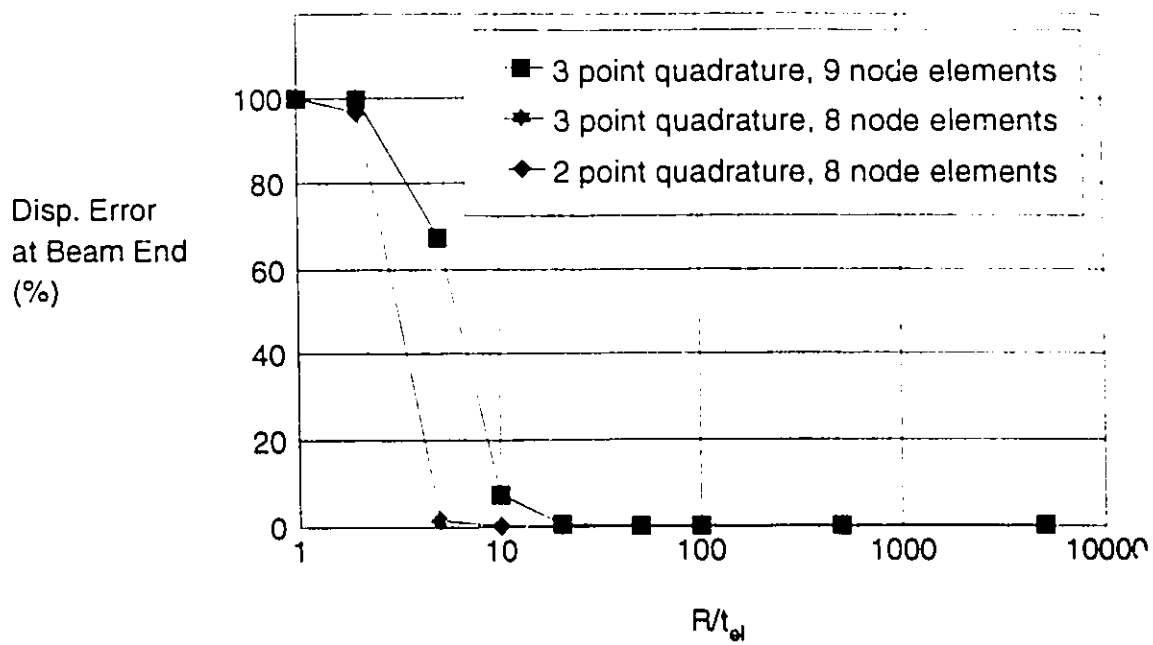


Figure 6.4 Cylindrical formulation with coordinate displacements:  
Pure bending, small displacement, quadratic element  
displacement field

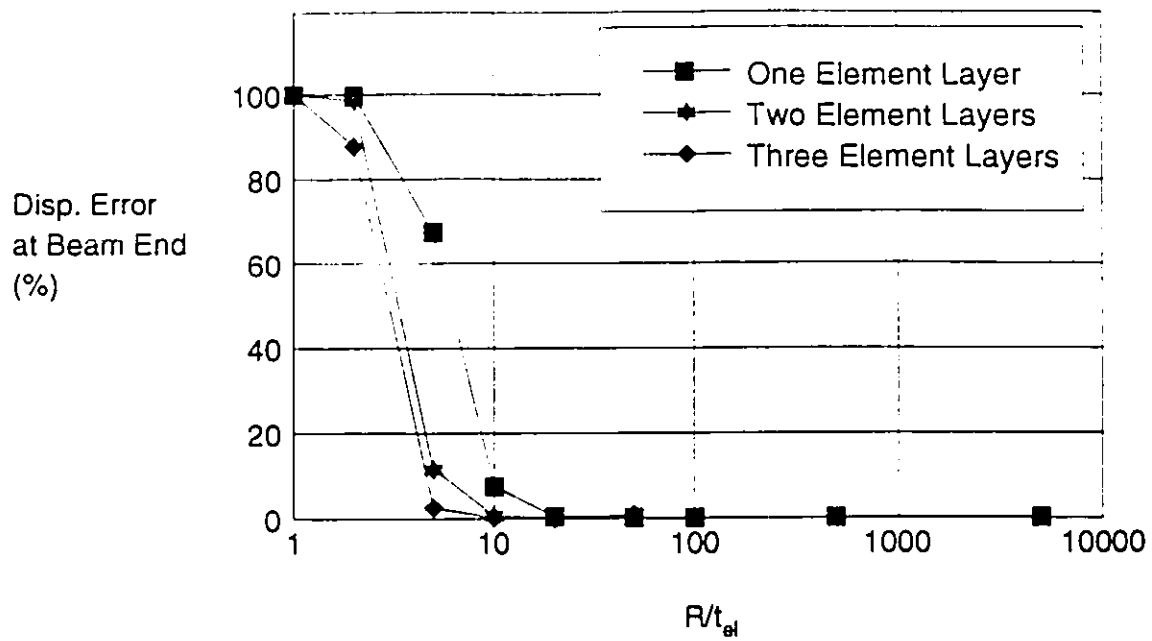


Figure 6.5 Radial mesh refinement performance of the cylindrical formulation with coordinate displacements

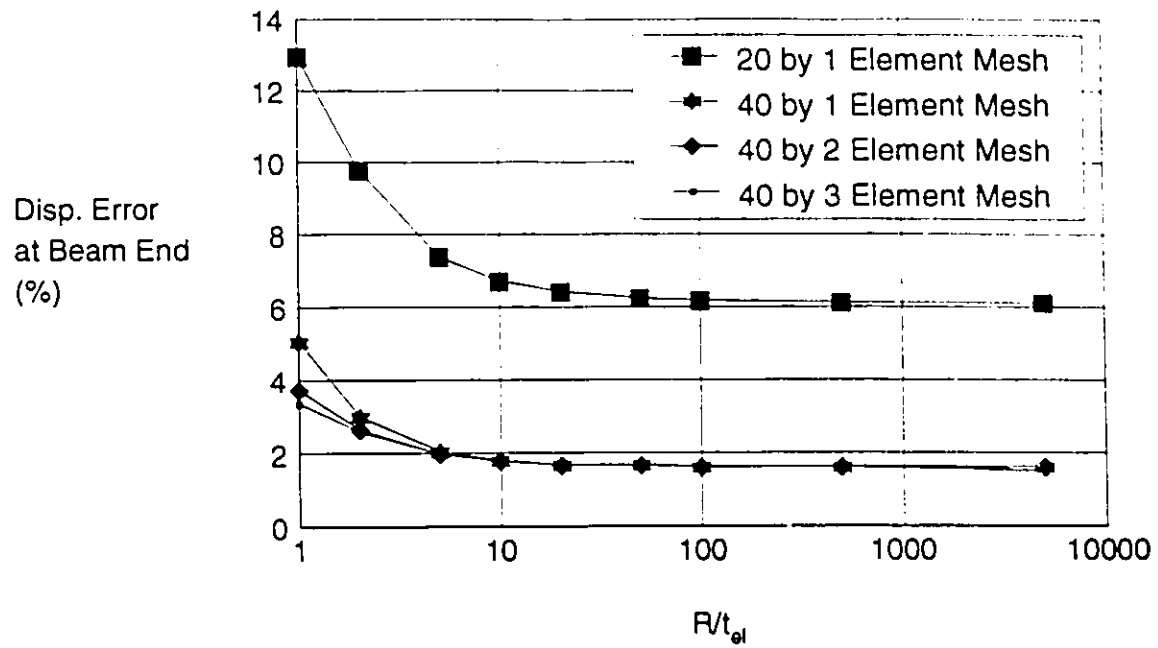
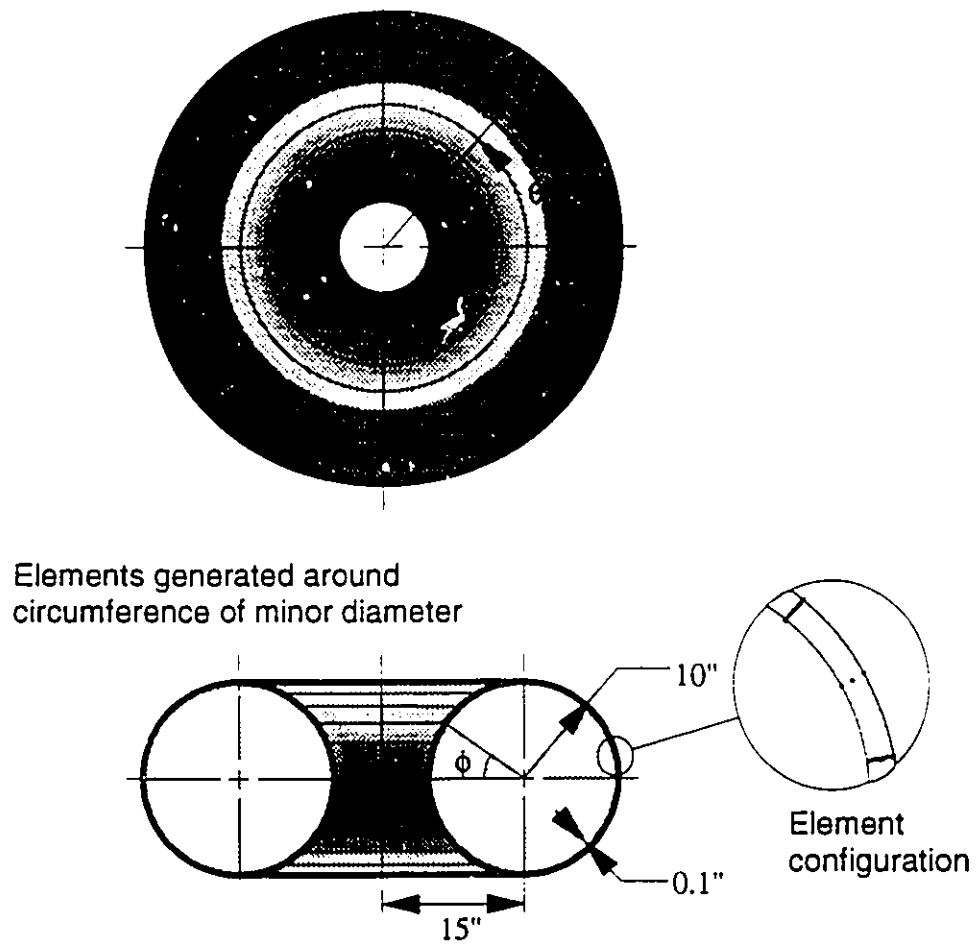


Figure 6.6 Radial mesh refinement performance of the Cartesian formulation, four node element, three point quadrature, pure bending, small displacement



Young's Modulus =  $10^7$  psi  
 Poisson's Ratio = 0.3  
 Applied Pressure = -100 psi

Figure 6.7      Torus model

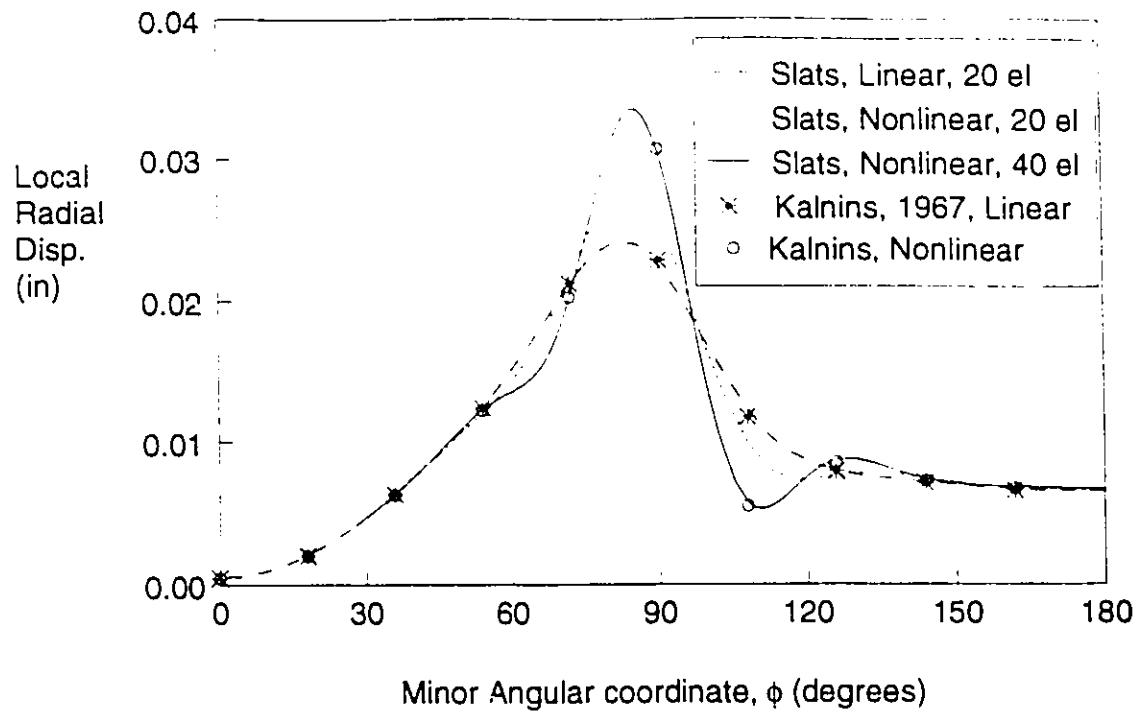


Figure 6.8 Normal displacement distribution in a toroidal shell under external pressure



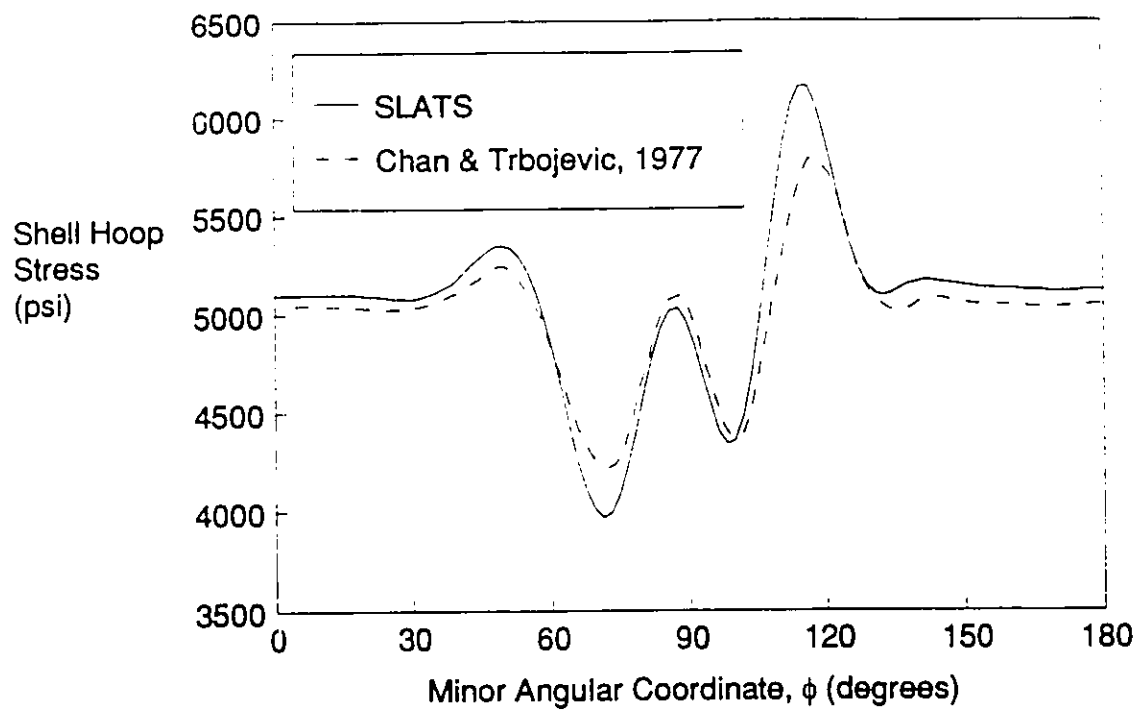
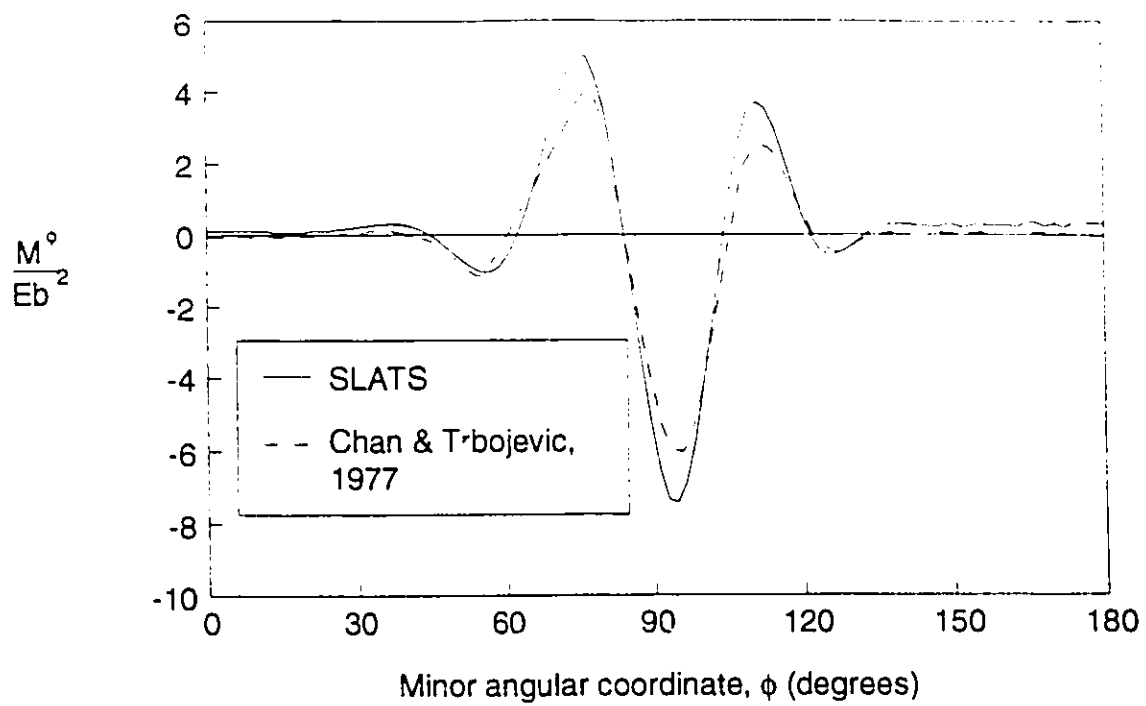


Figure 6.9 Hoop stress distribution in toroidal shell under external pressure - nonlinear results - 40 quadratic elements



**Figure 6.10**      **Bending moment distribution in toroidal shell under external pressure - nonlinear results**

Specimen	$R/t$	$\theta$	$h$	$r$	Young's Modulus	Poisson's Ratio
1 *	228	0.176	0.3536	4	6.5e6	0.32
2 &	362	0.206	0.4134	4	6.5e6	0.32
3 #	1000	0.105	5.515	104.88	23.8e6	0.30

\* Reference Kaplan and Fung, NACA TN 3212, Specimen 4  
 & Reference Kaplan and Fung, NACA TN 3212, Specimen 21  
 # Reference Ball, 1968

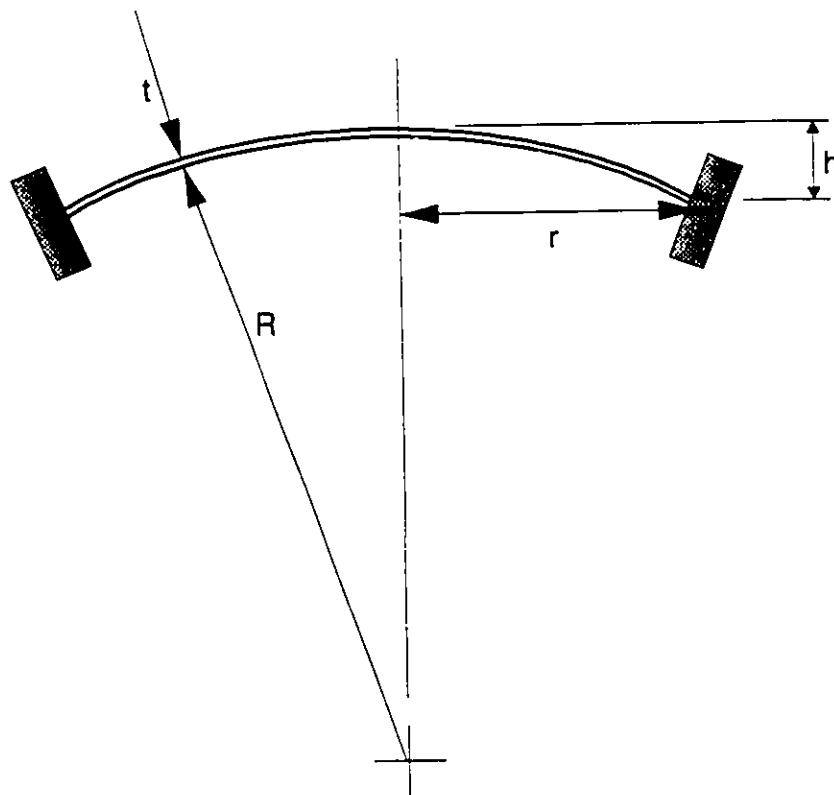


Figure 6.11 Spherical cap models

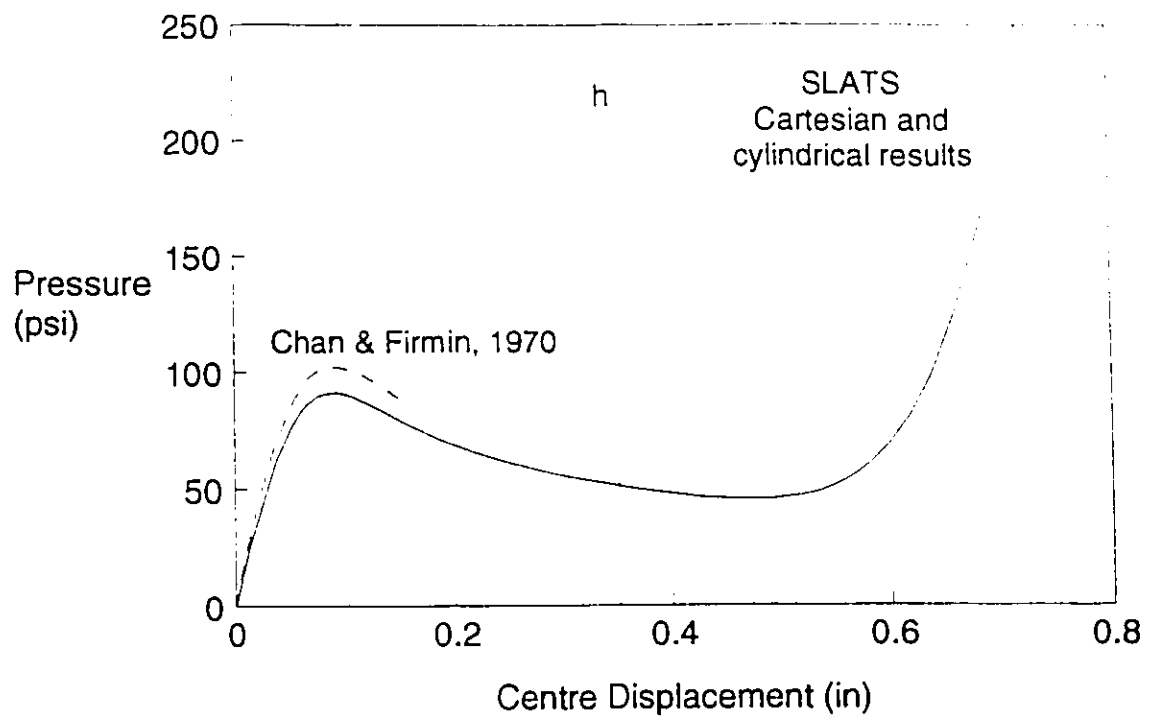


Figure 6.12 Pressure - displacement relationship for Cap 1  
Full displacement range

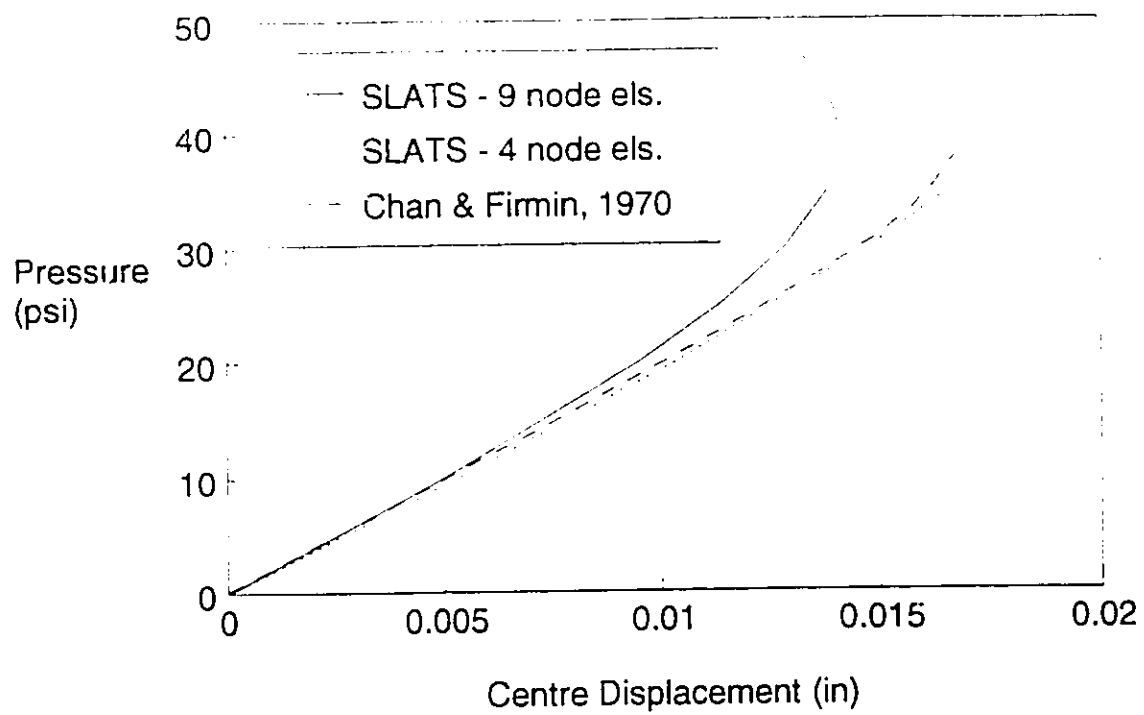


Figure 6.13 Pressure - displacement relationship for Cap 2

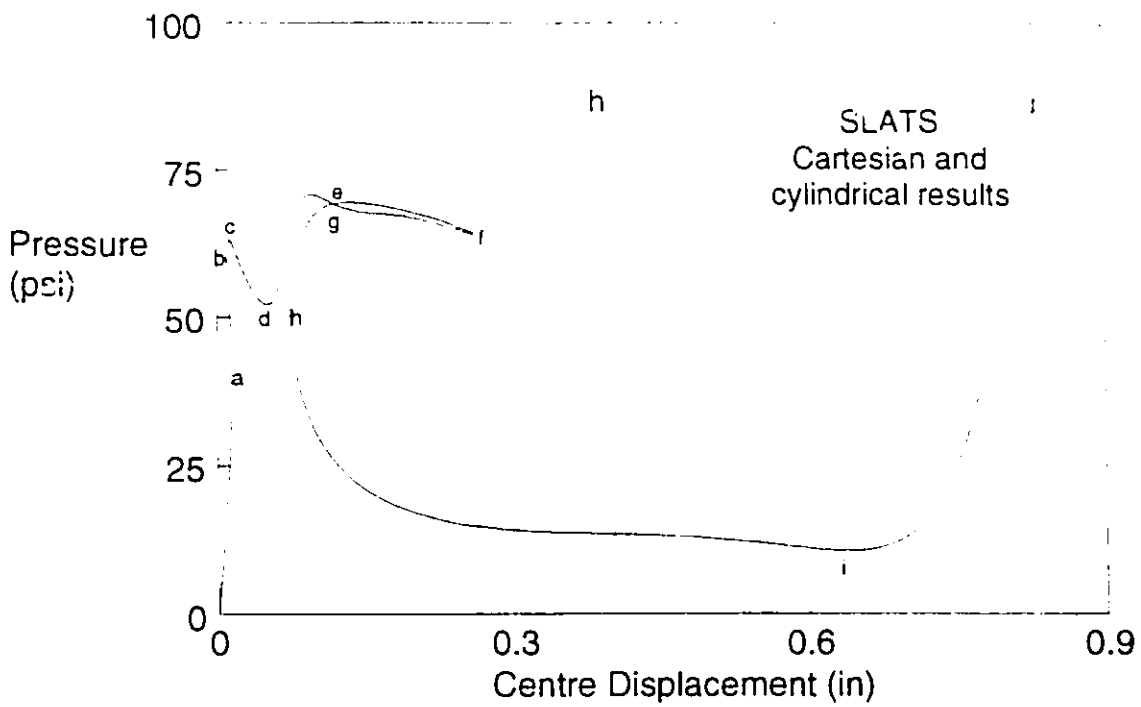


Figure 6.14 Pressure - displacement relationship for Cap 2  
Full displacement range

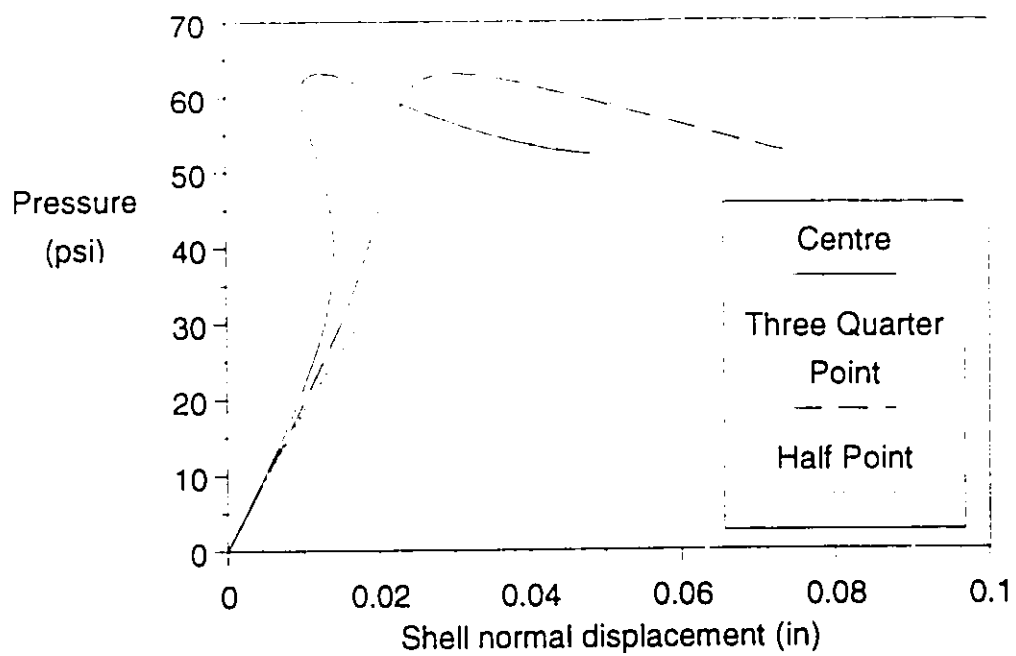
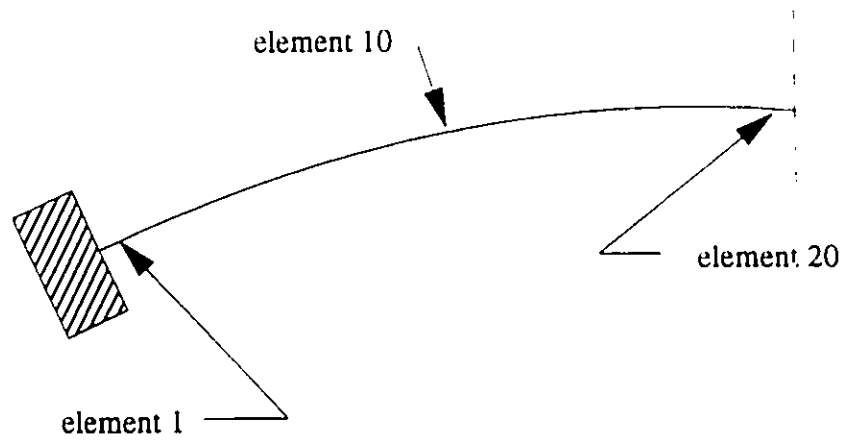
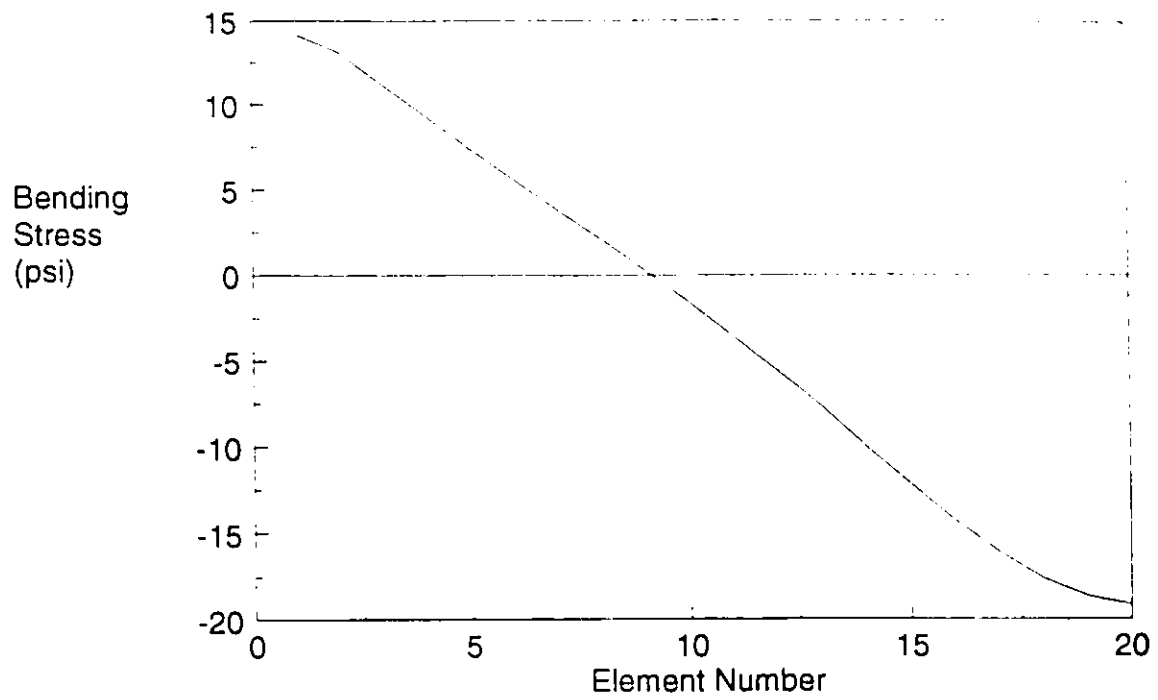


Figure 6.15 Equilibrium curves at secondary points on Cap 2



**Figure 6.16** Bending stress distribution in Cap 1 during pressure loading sequence



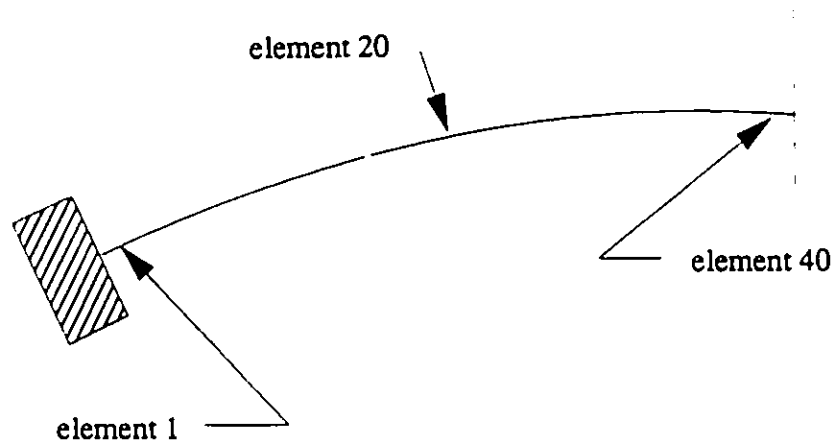
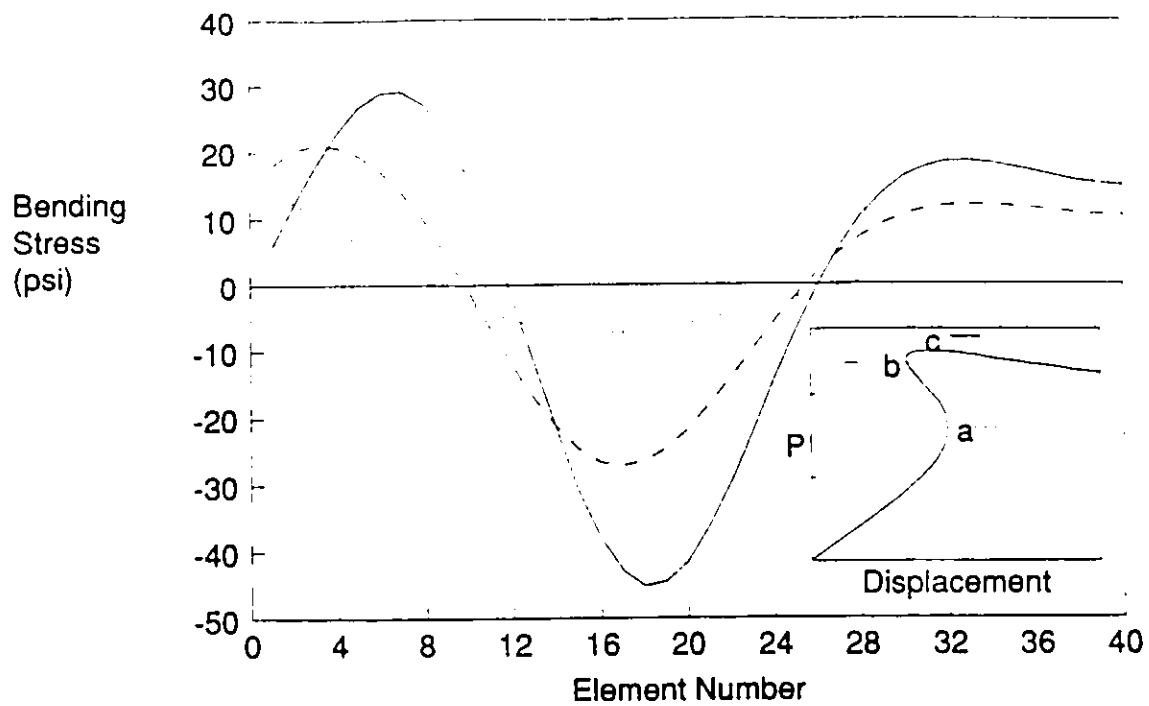


Figure 6.17 Bending stress distribution in Cap 2 during pressure loading sequence

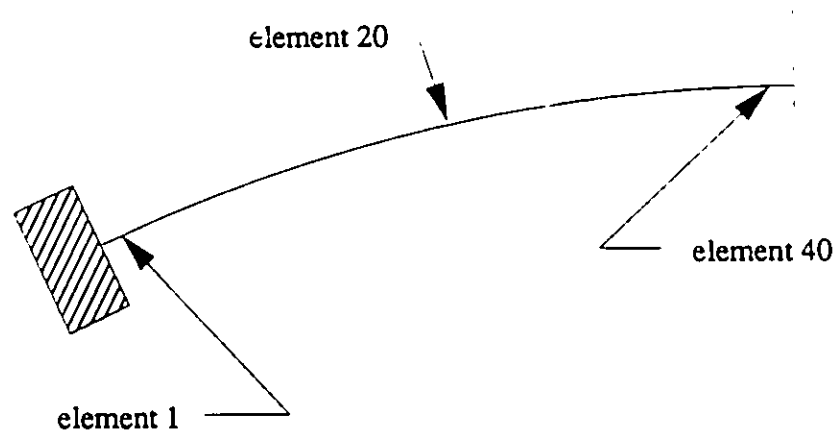
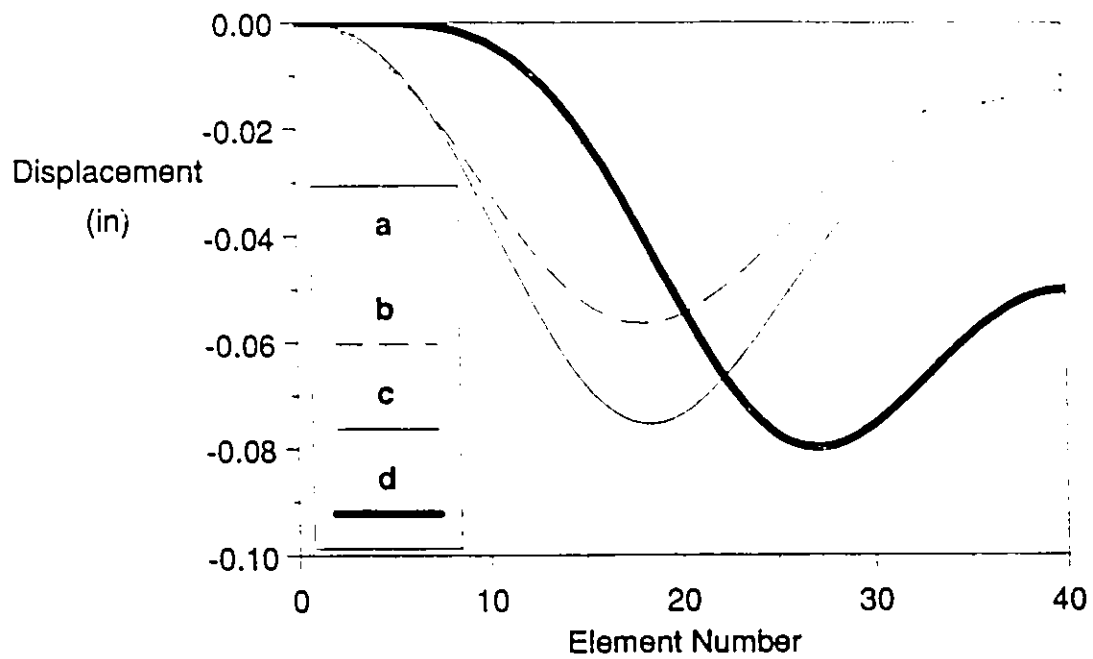


Figure 6.18 Cap 2 displacement distribution at first four critical points, a, b, c and d in Figure 6.14

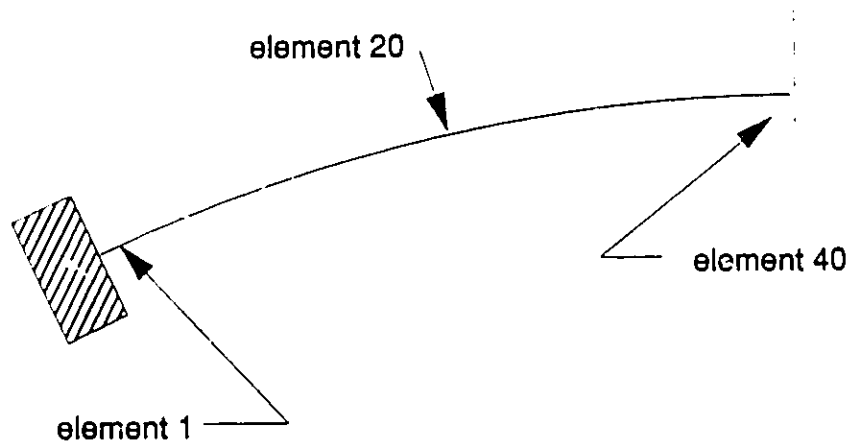
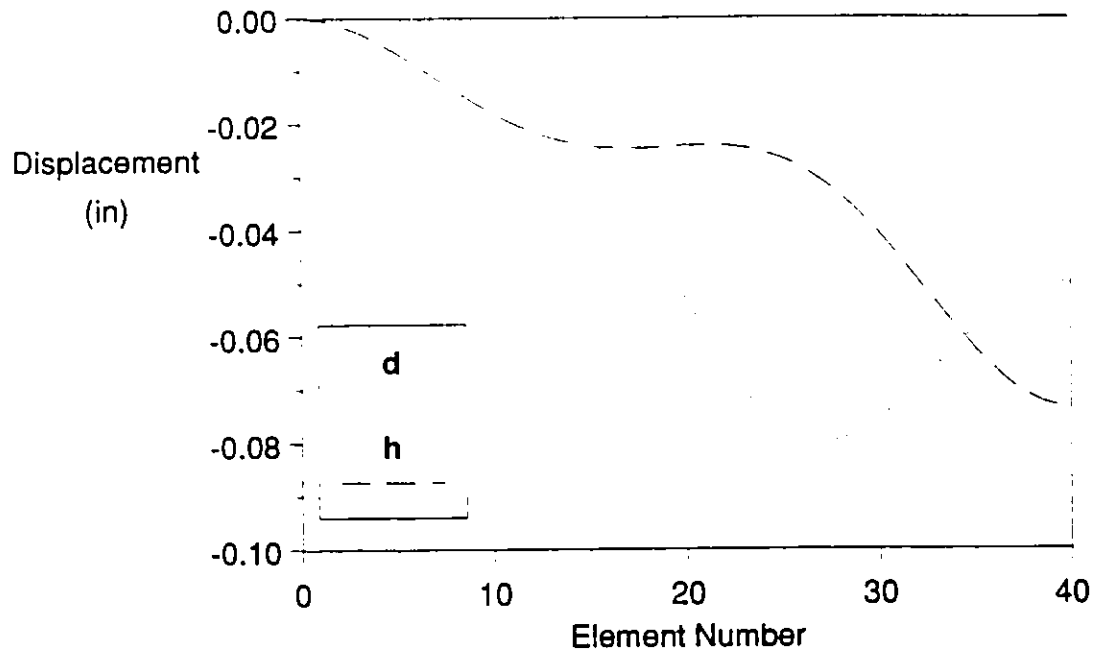


Figure 6.19 Cap 2 displacement distribution comparison for critical points **d** and **h** in load displacement curve (refer to Figure 6.14)

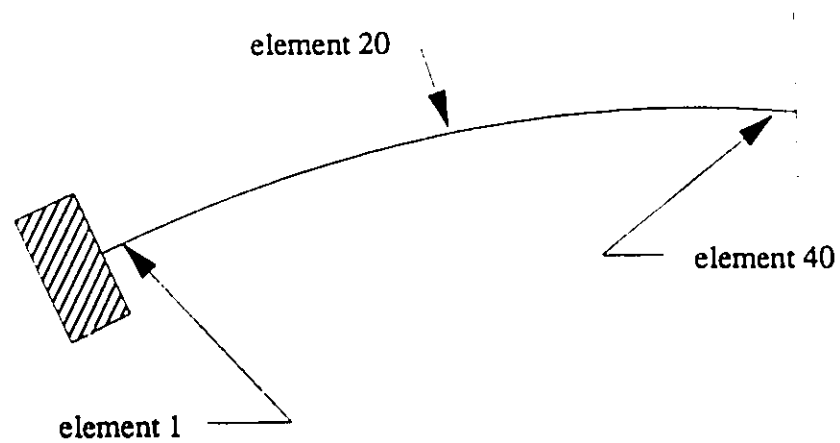
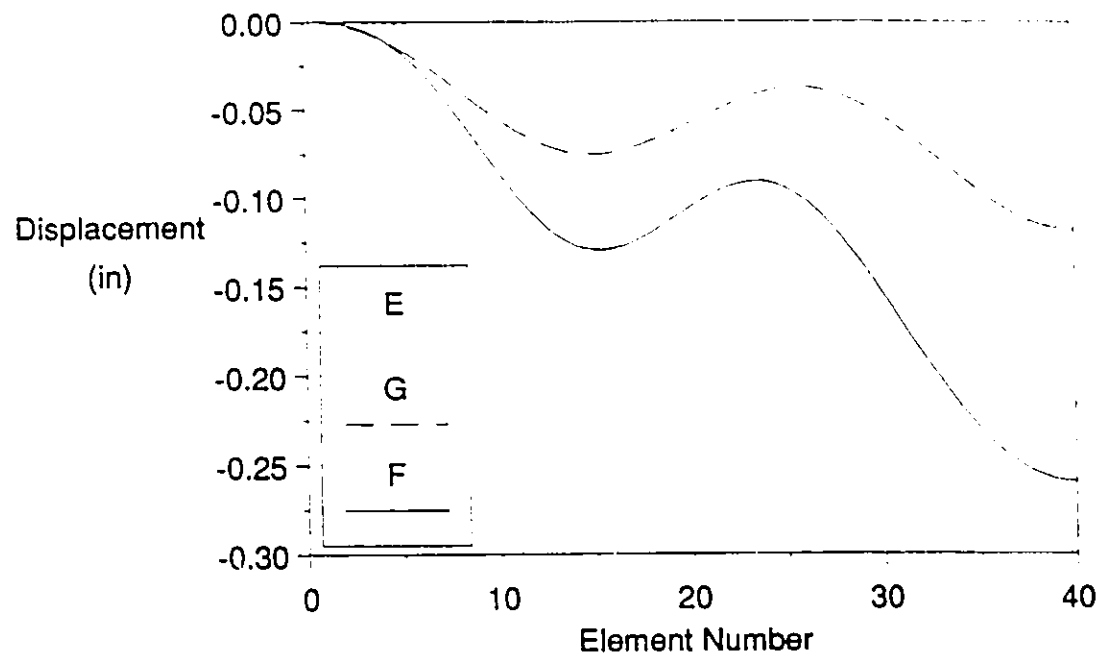


Figure 6.20 Radial displacement distribution during snap back of Cap 2

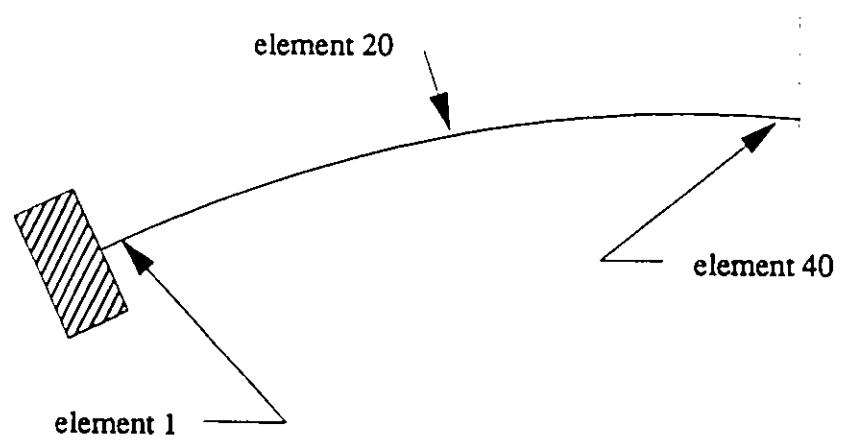
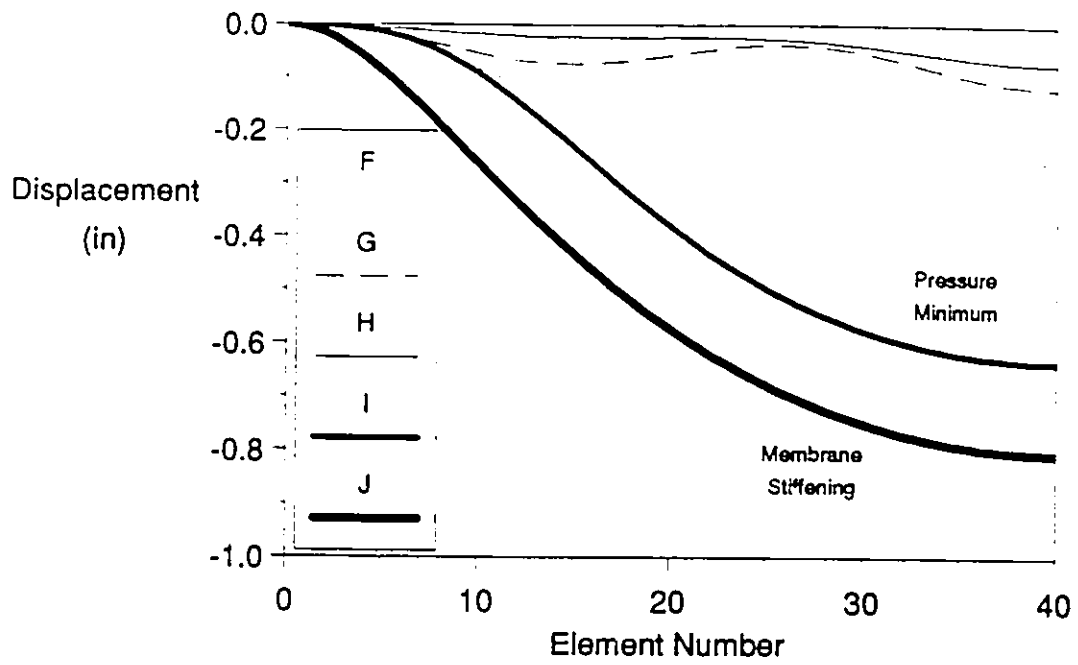


Figure 6.21 Displacement distribution for Cap 2 from snap back to snap through

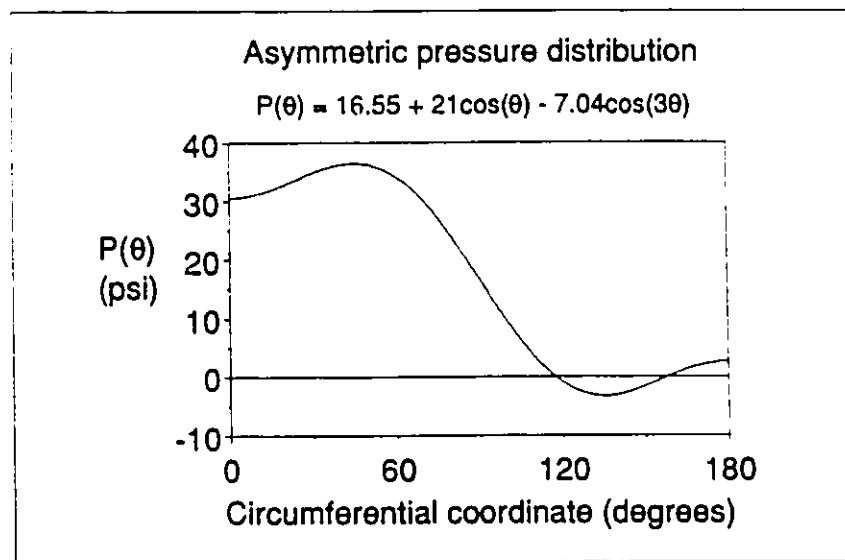
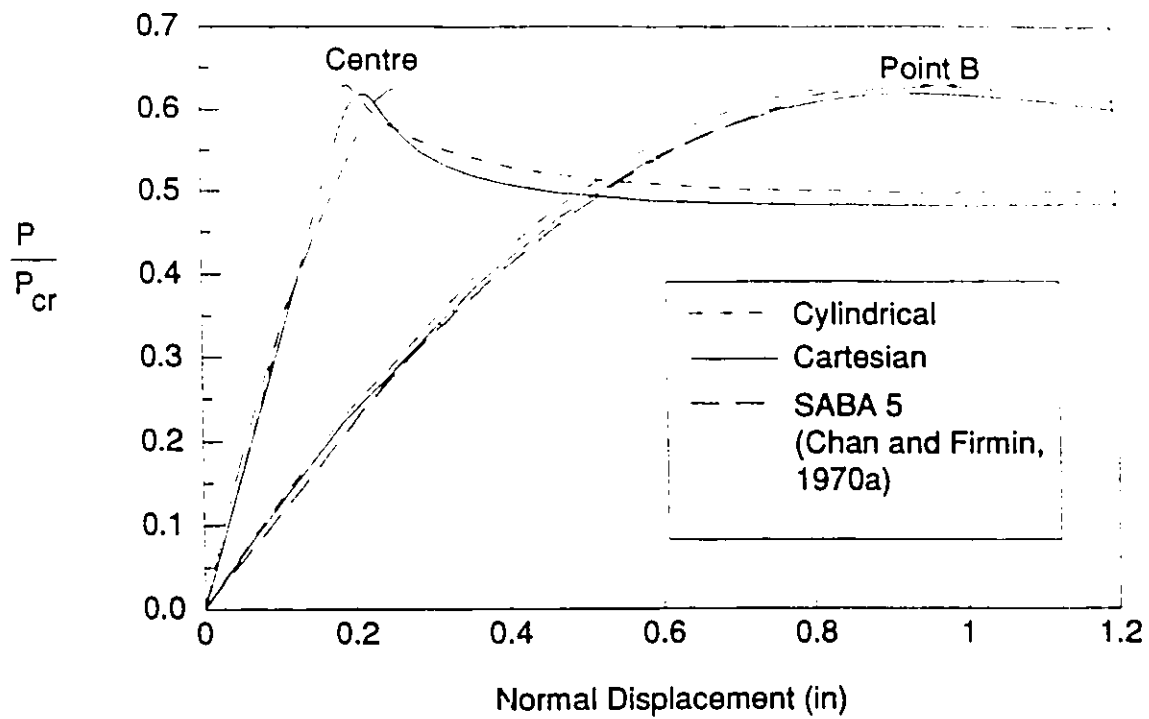


Figure 6.22 Load - displacement relationship for asymmetrically loaded spherical cap (Cap 3)

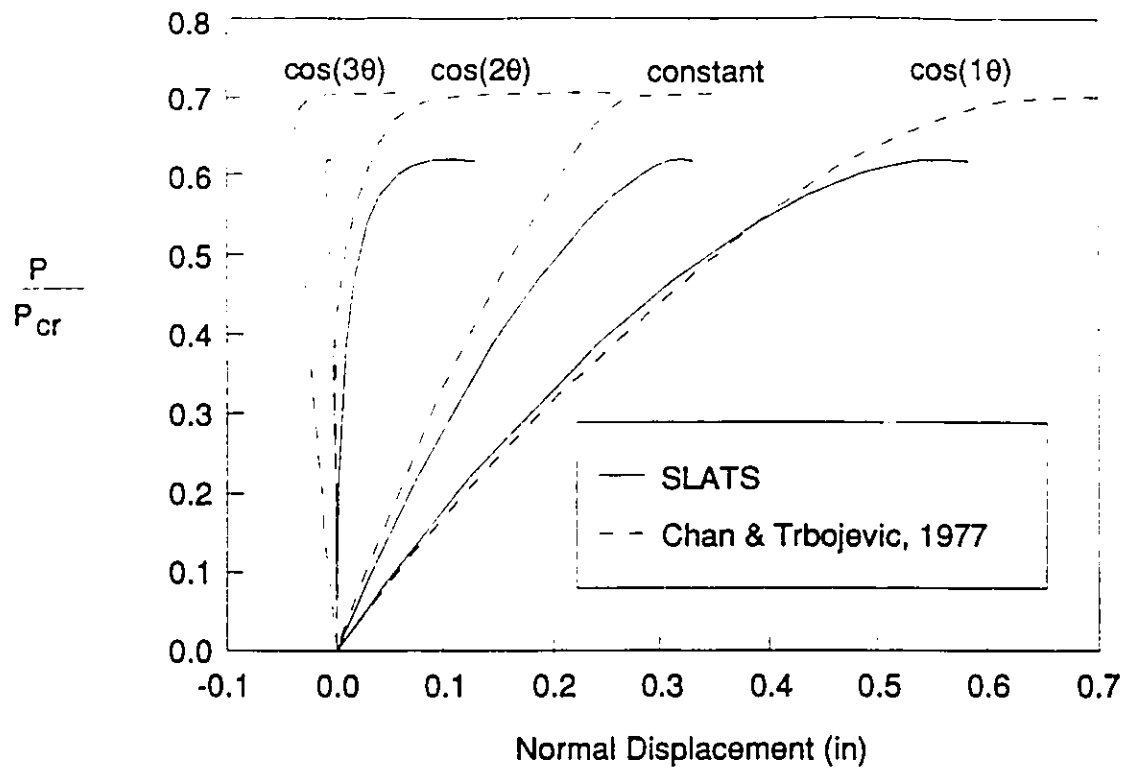


Figure 6.23 Load - displacement for asymmetrically loaded cap.  
Harmonic displacement components, Cartesian formulation

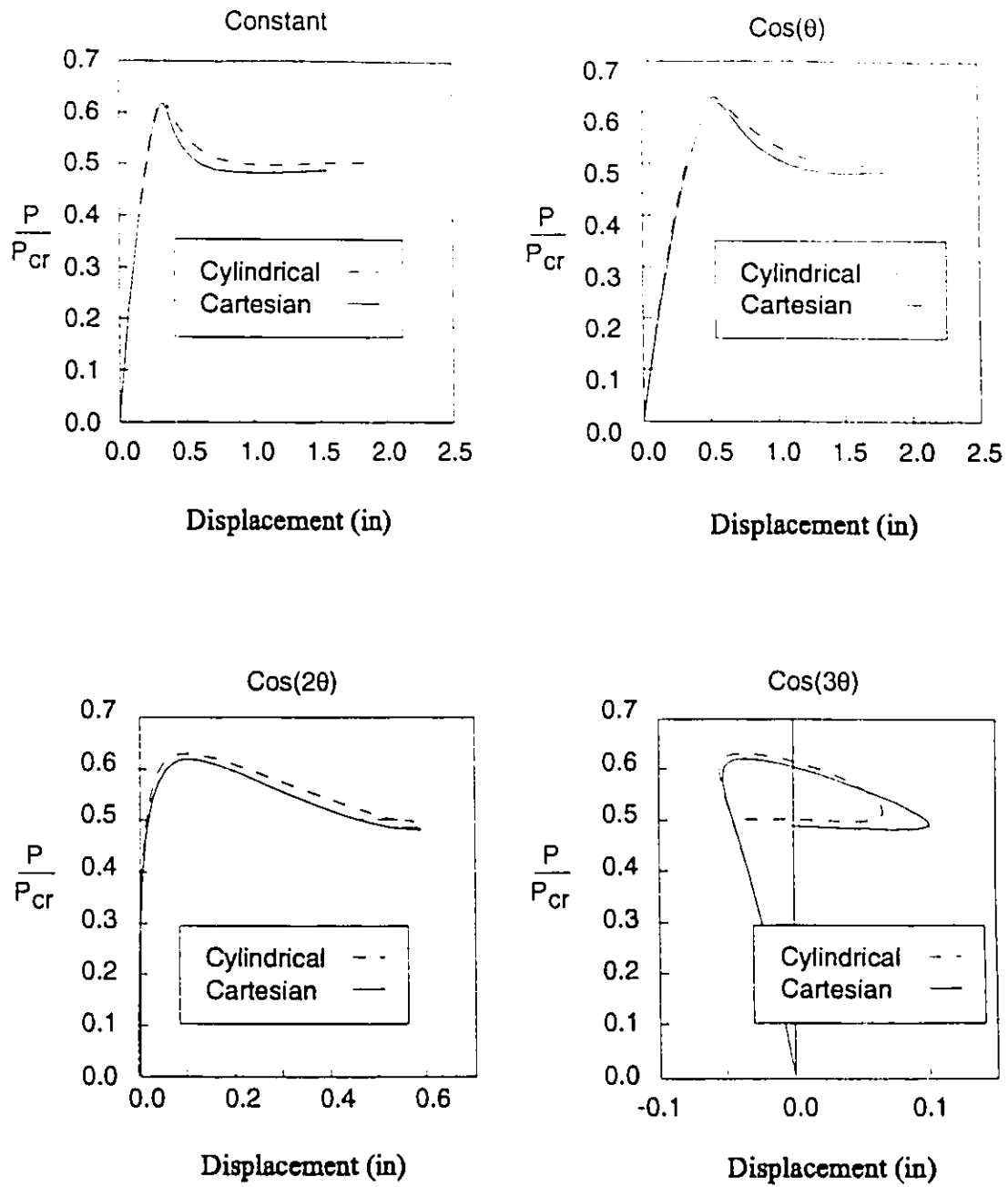
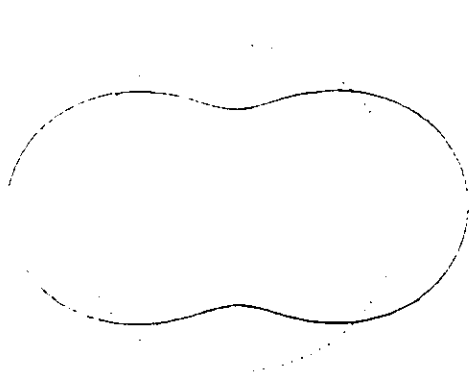
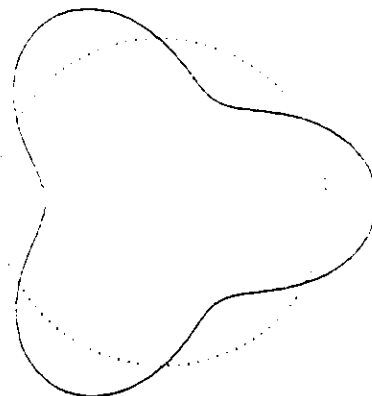


Figure 6.24 Harmonic displacement components at maximum displacement location for asymmetrically loaded cap.

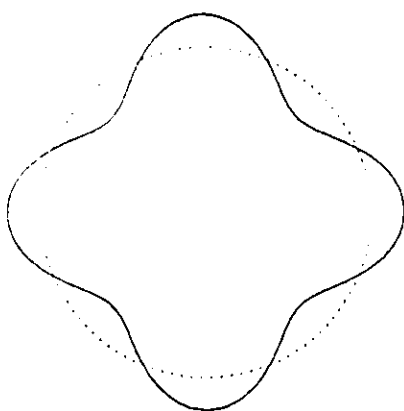




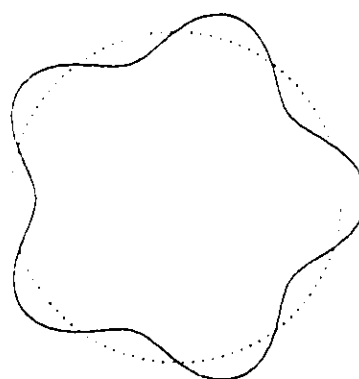
Waveform:  $\cos(2\theta)$   
Length = 200"



Waveform:  $\cos(3\theta)$   
Length = 100"

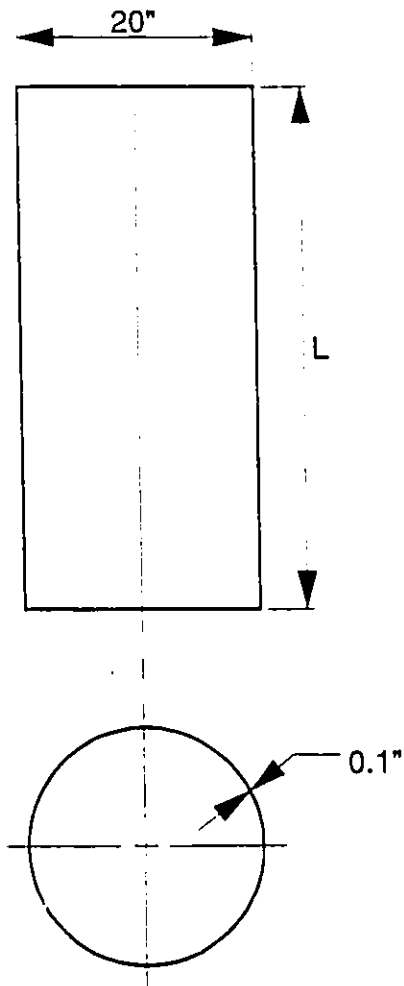


Waveform:  $\cos(4\theta)$



Waveform:  $\cos(5\theta)$   
Length = 30"

Figure 6.25 Buckling modes for various length cylinders under external pressure

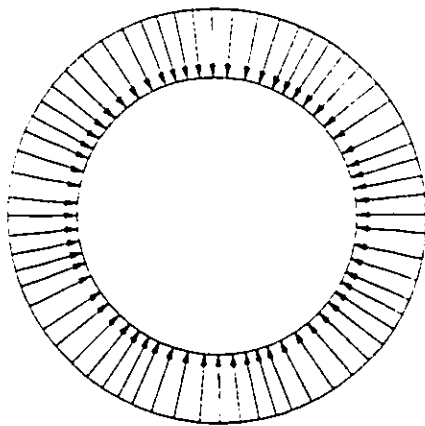


Youngs Modulus:  $10^6$  psi  
 Poison's Ratio: 0.3

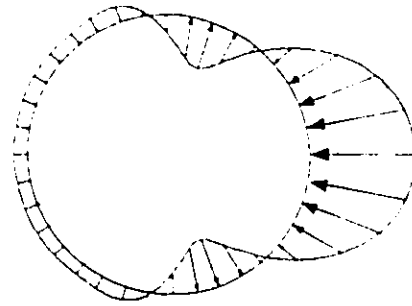
Symmetric boundary  
 conditions at centre

Fixed in radial direction  
 at each end

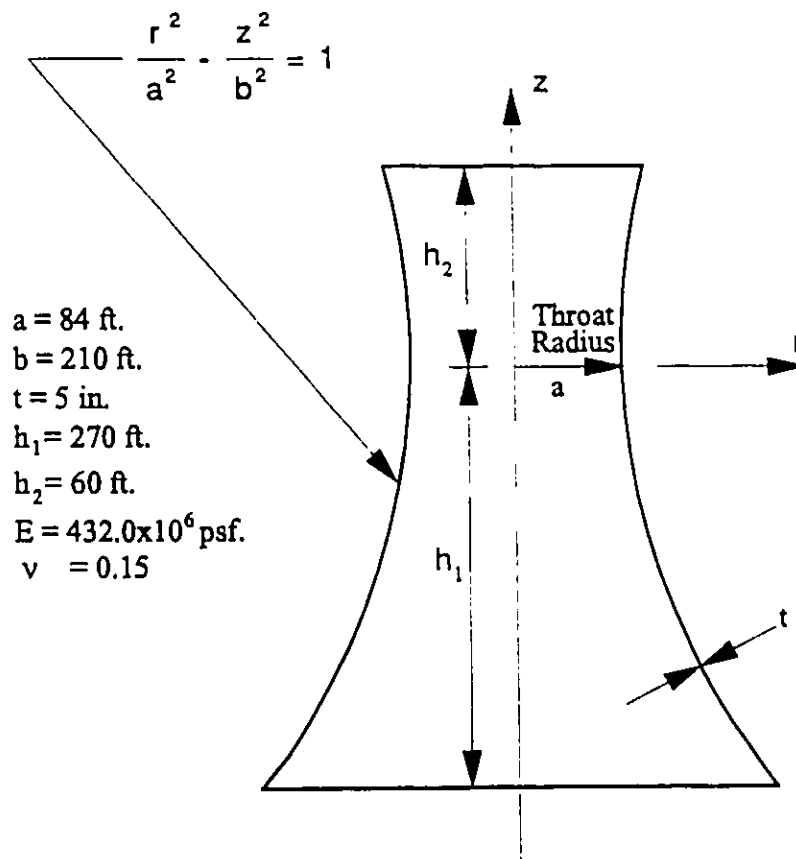
Figure 6.26 Cylindrical shell model under uniform external pressure



Uniform External  
Pressure



Wind Loading  
Pressure Distribution



Built in at base.

Figure 6.27 Full size cooling tower model, two load cases

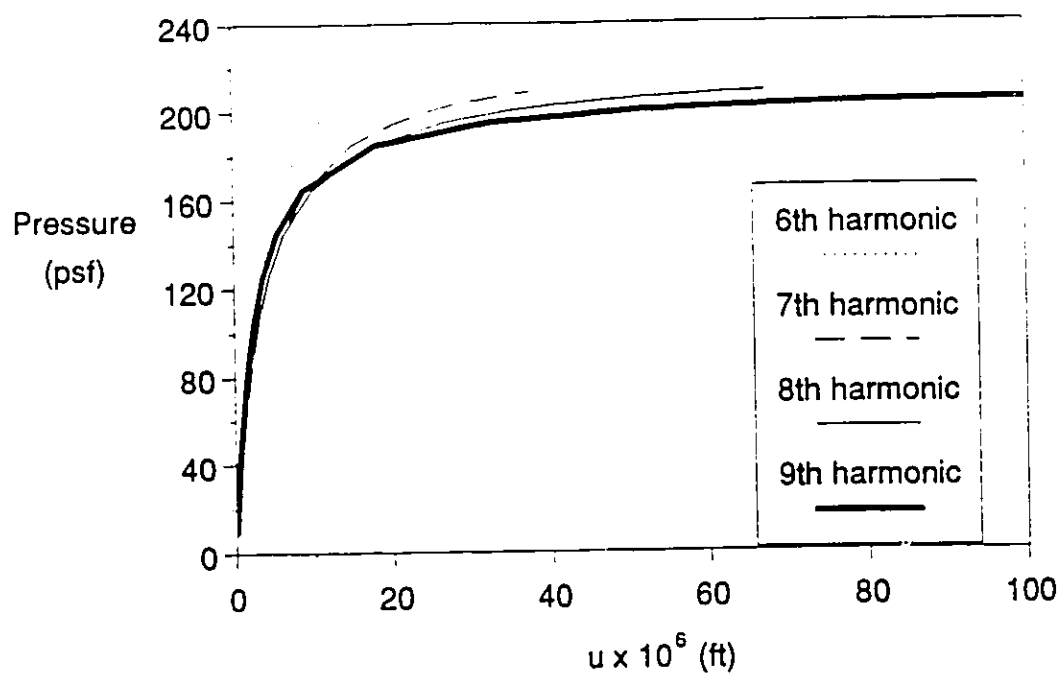


Figure 6.28 Load - radial displacement amplitude response for the cooling tower under external pressure measured 150 ft below throat

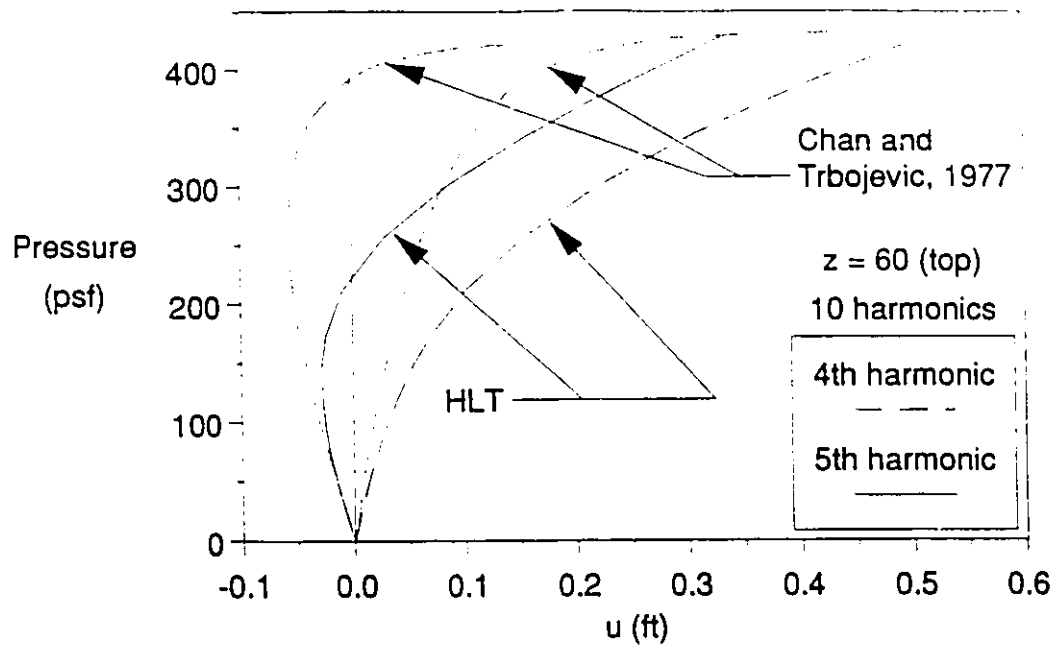


Figure 6.29 Load - radial displacement amplitude at top of hyperbolic tower under wind loading using 10 harmonics

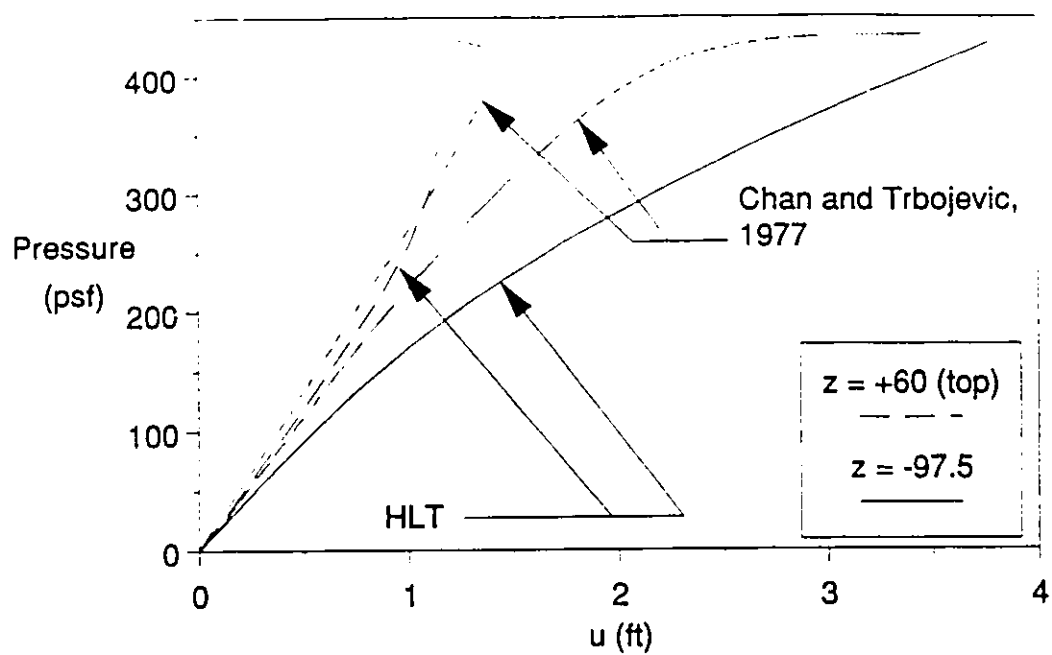


Figure 6.30 Total radial displacements at two vertical locations at the stagnation point of the cooling tower using 10 harmonics

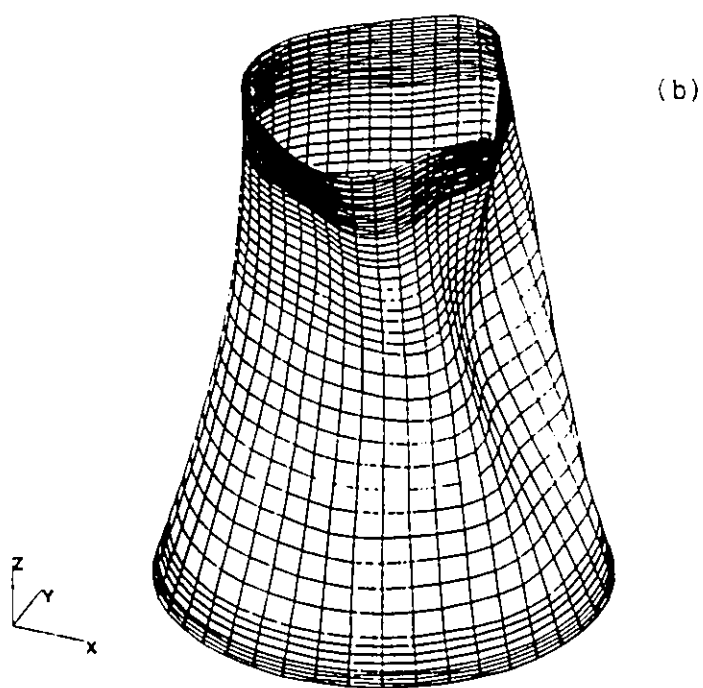
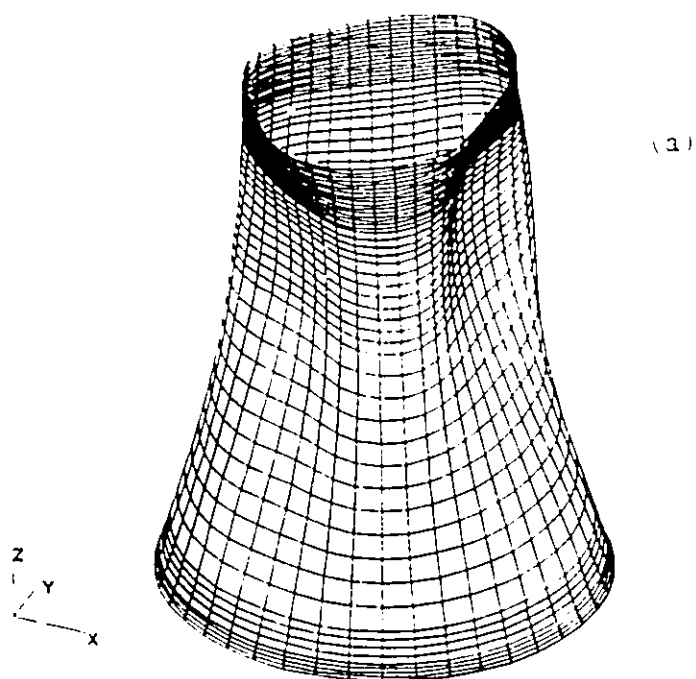


Figure 6.31 Deformed shapes for cooling tower: a) initial deformation magnified 500x; b) advanced deformation mode magnified 6x

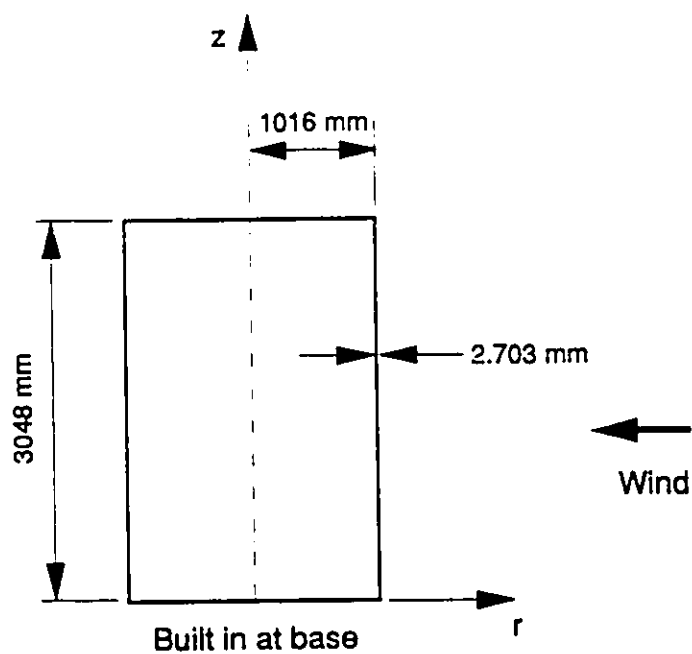
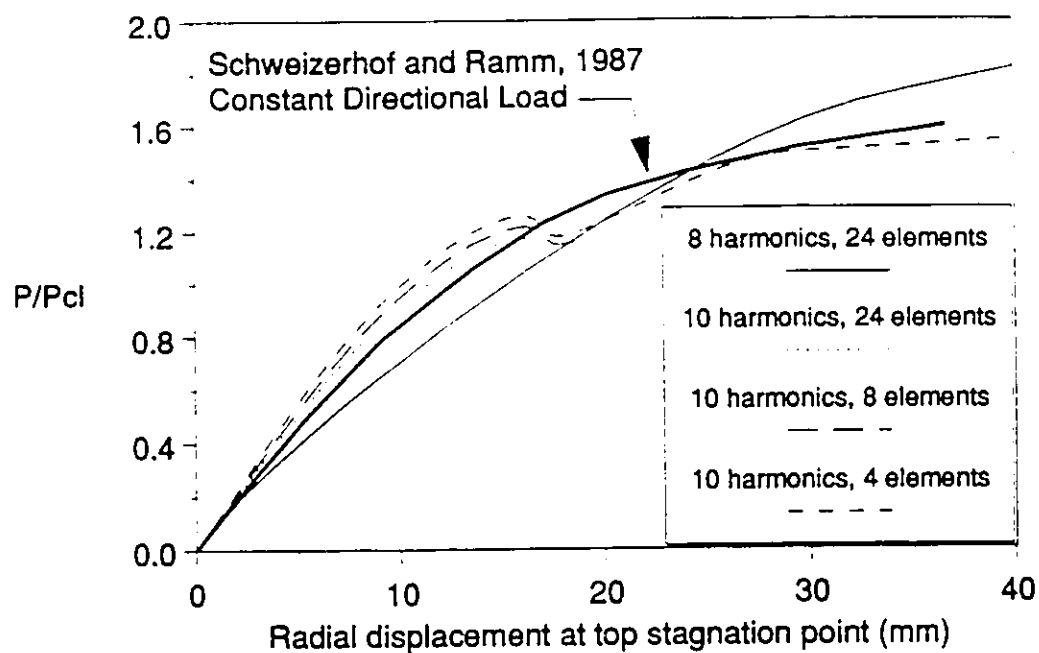


Figure 6.32 Radial displacement at top of cylindrical shell subject to wind load



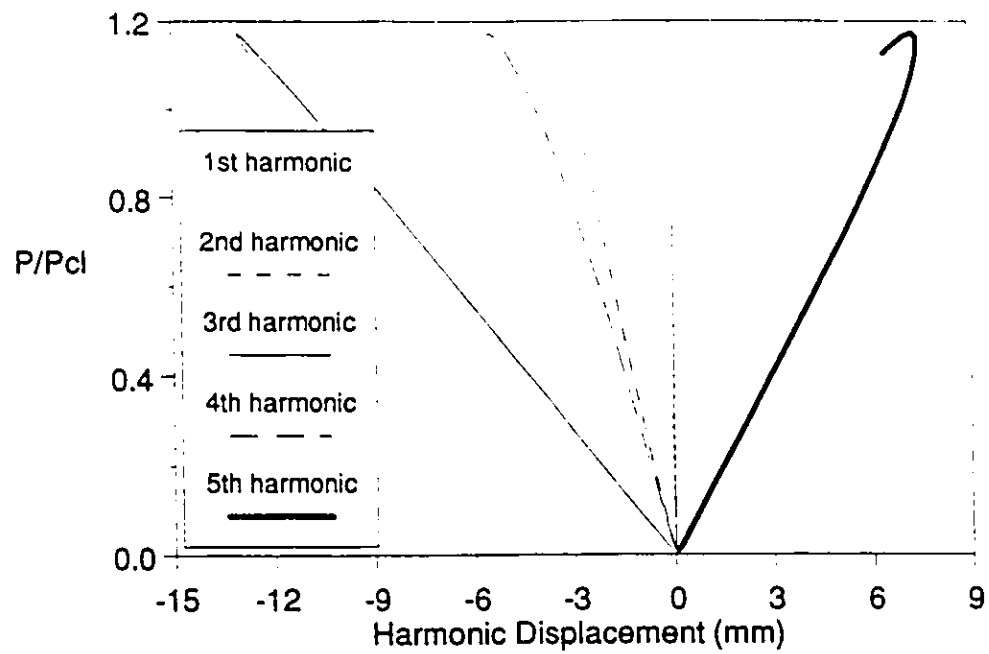


Figure 6.33 Load - Harmonic displacement relationship for cylinder under wind loading - lower Fourier numbers

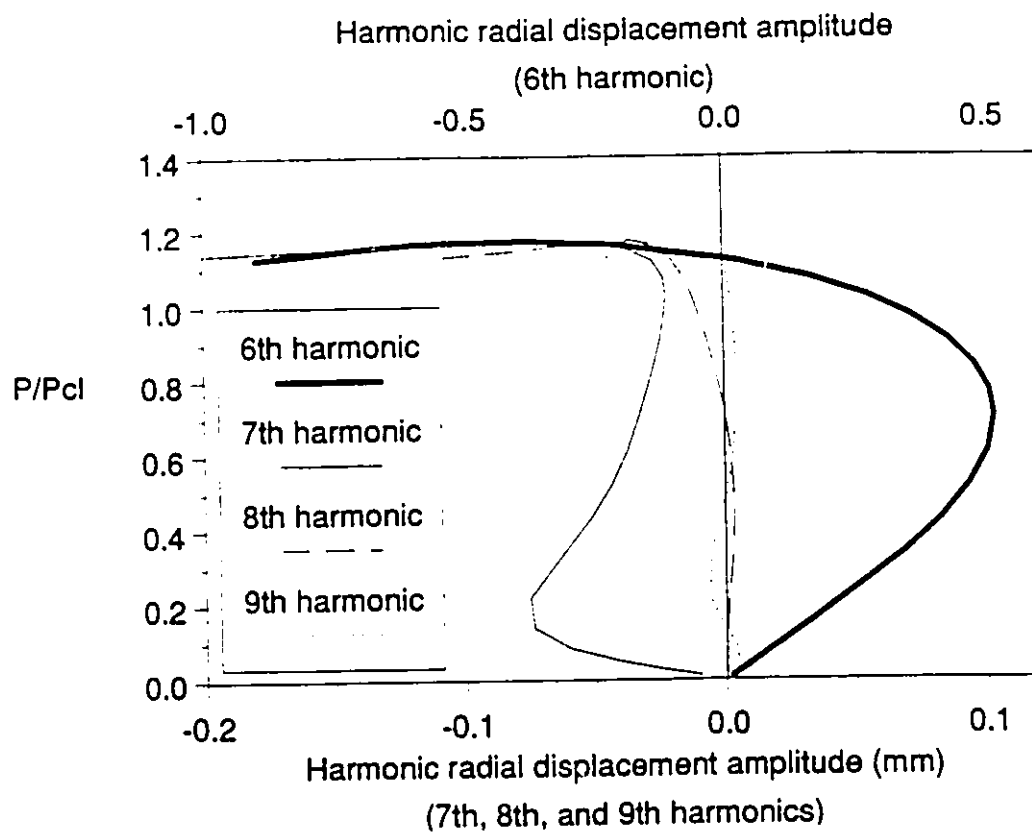


Figure 6.34 Higher order harmonic displacement amplitudes at top of cylinder under wind loads.

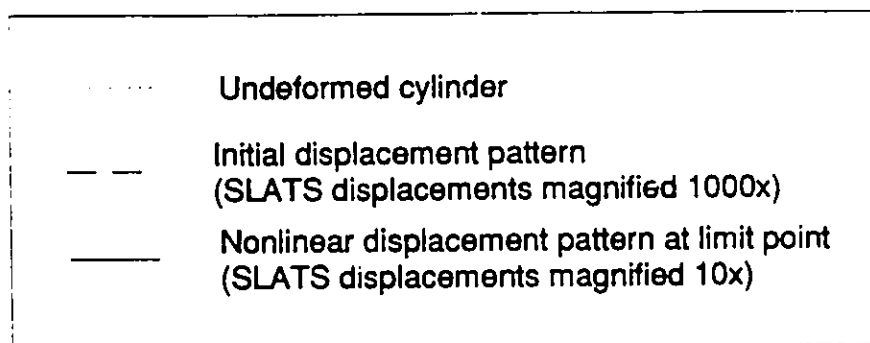
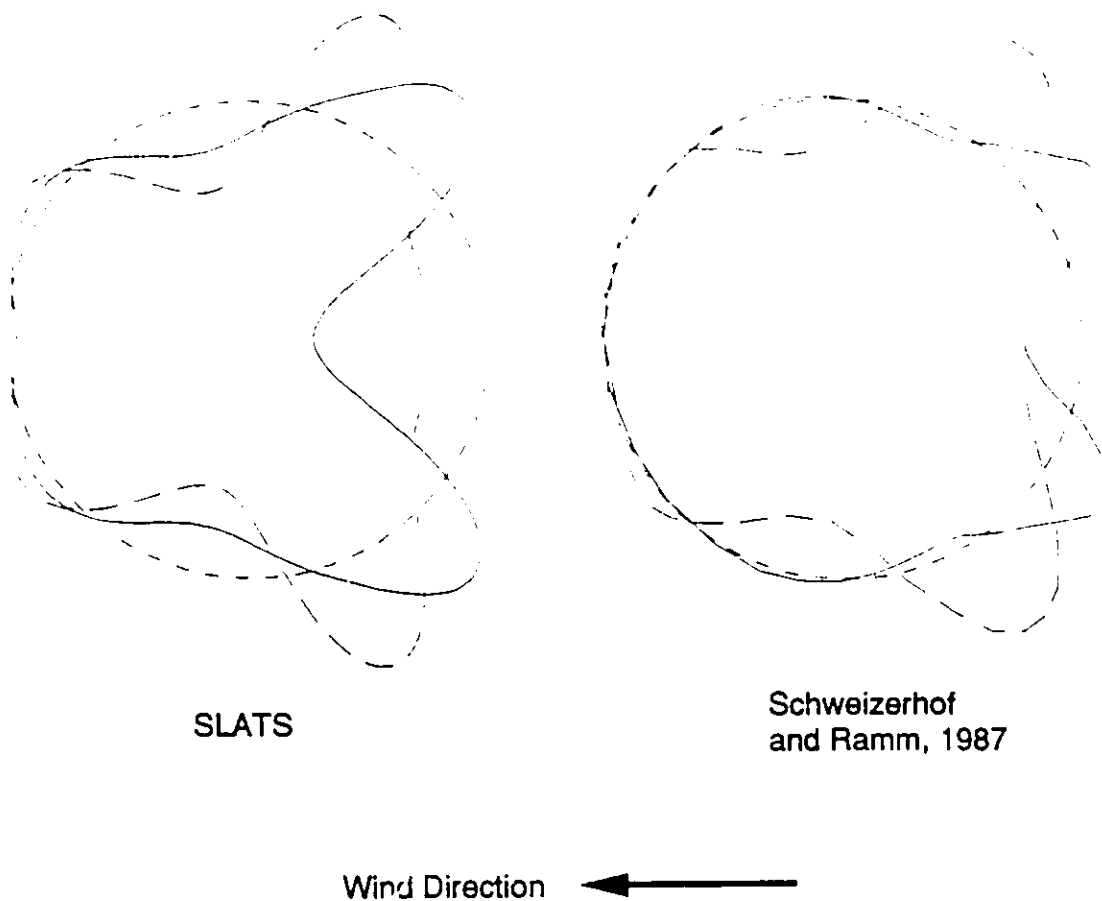
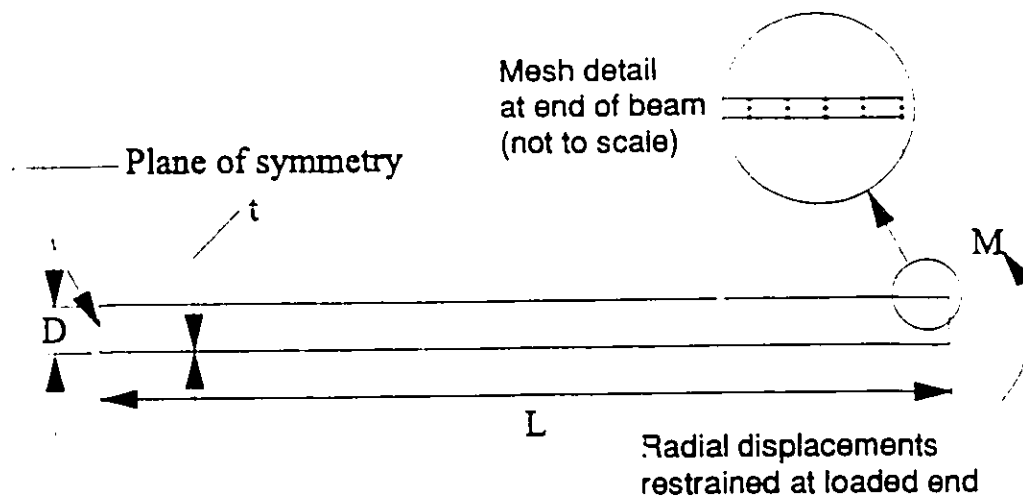


Figure 6.35 Displacement patterns at top of cylinder subjected to wind load. (10 harmonics, 4 elements)



#### Model Parameters

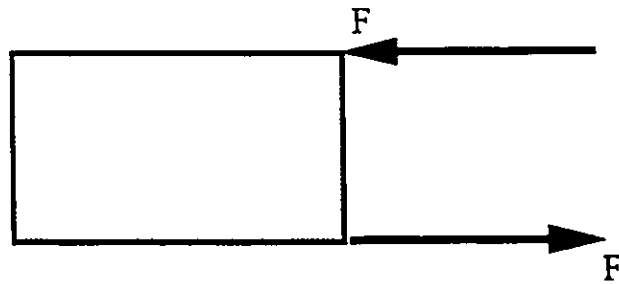
$L = 10000 \text{ mm}$   
 $D = 100 \text{ mm}$   
 $t = 10 \text{ mm}$   
 $d = D - 2t$   
 $E = 200,000 \text{ Mpa}$   
 $\nu = 0.3$

#### Model Description

Element Layers = 1  
 Nel = 10 quadratic elements  
 Nodes = 123  
 Harmonics: 0, 1, 2  
 Cartesian Formulation

Figure 6.36 Large displacement bending model (not shown to scale)

Undeformed bending load increment



Deformed bending load increment

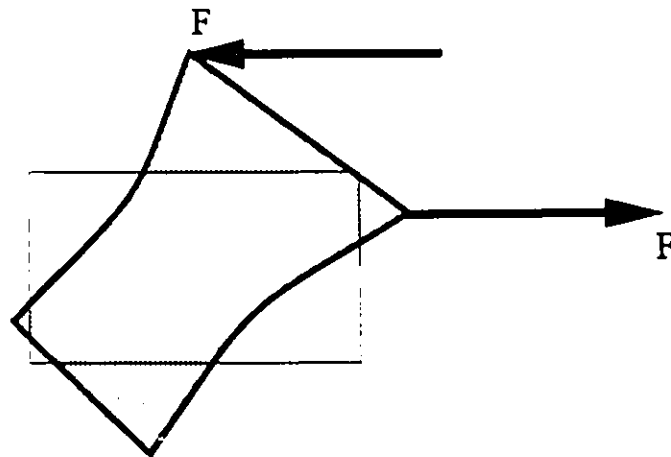


Figure 6.37 Pinching effect of deformation independent nodal harmonic loads

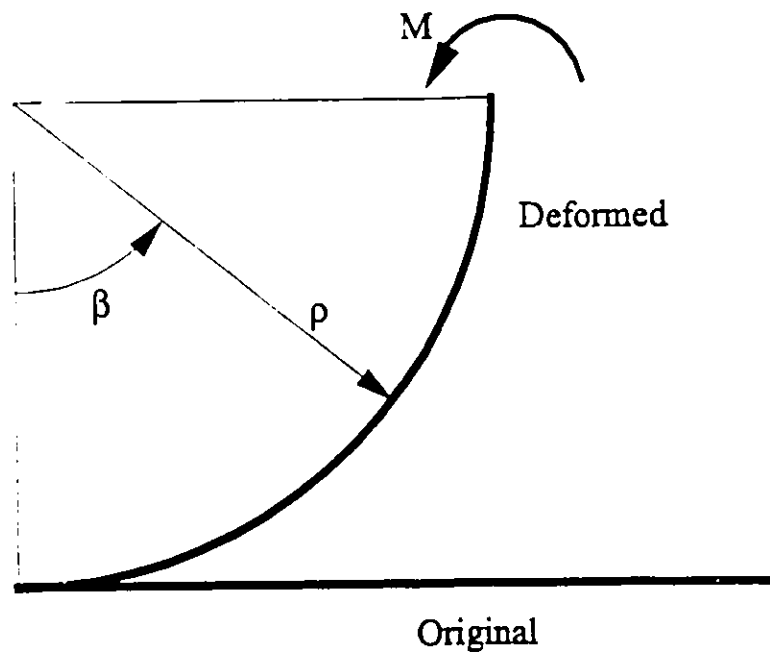


Figure 6.38 Deformed beam geometry, pure bending

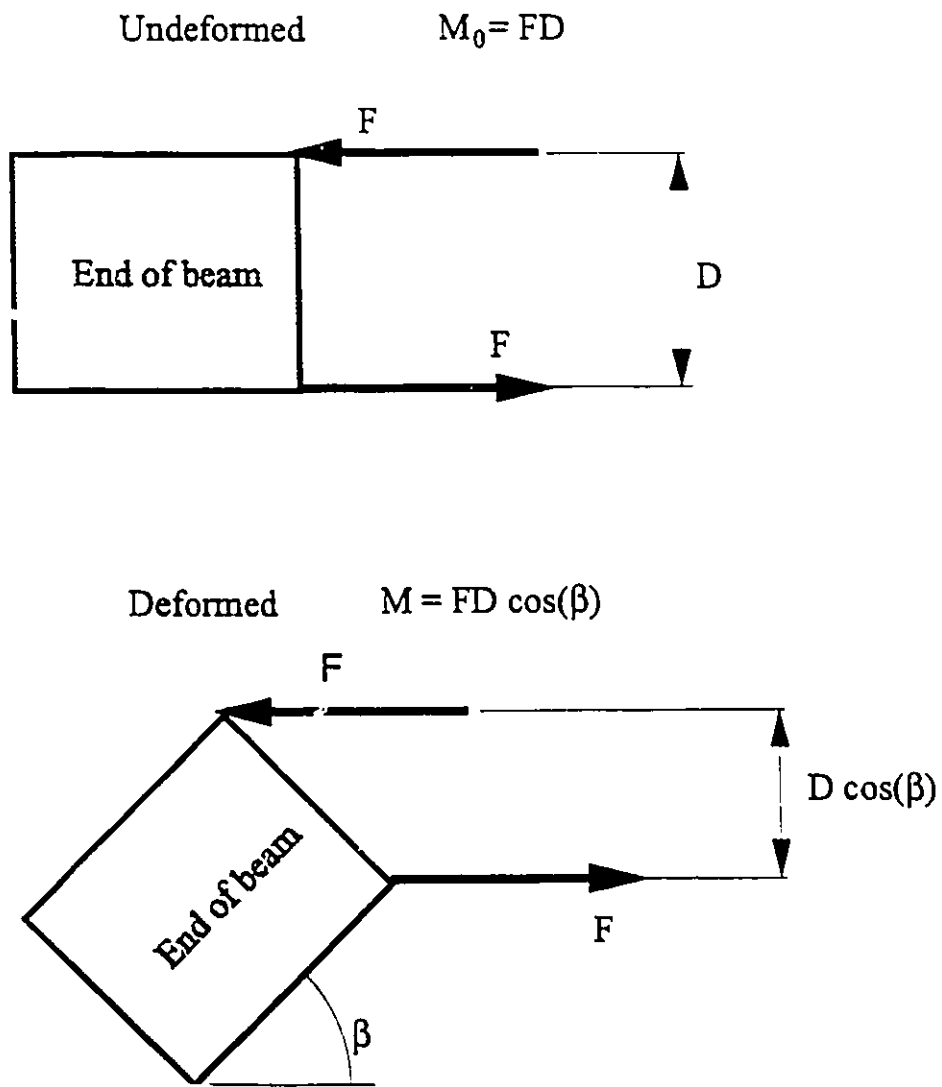


Figure 6.39 Deformation dependence of bending load with deformation independent nodal harmonic forces

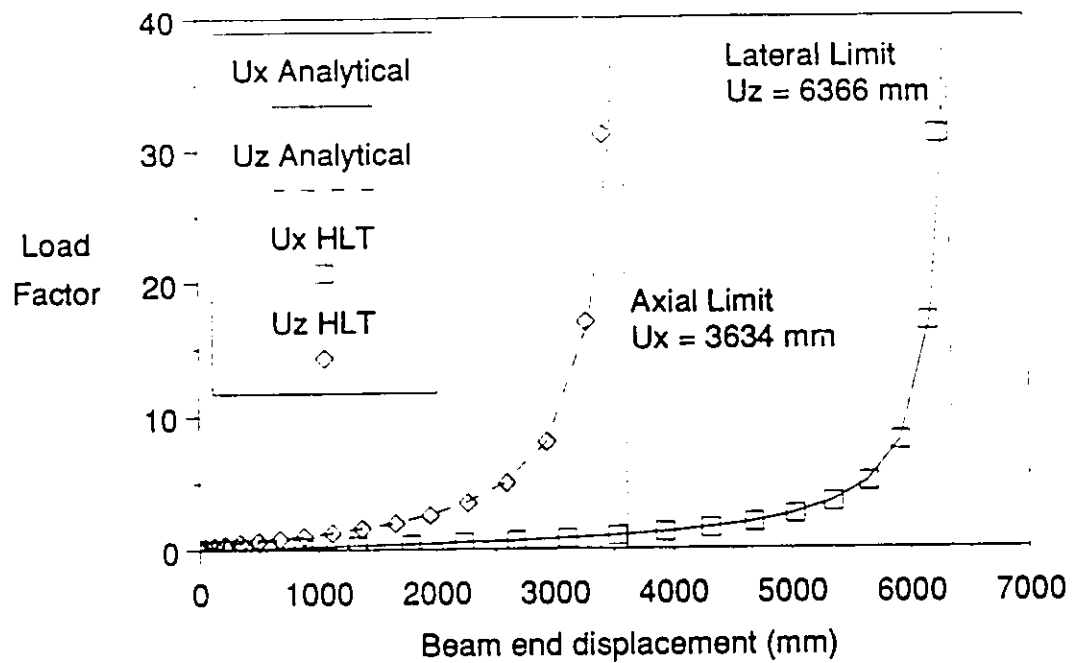


Figure 6.40 Load vs. displacement at the neutral axis for the slender beam



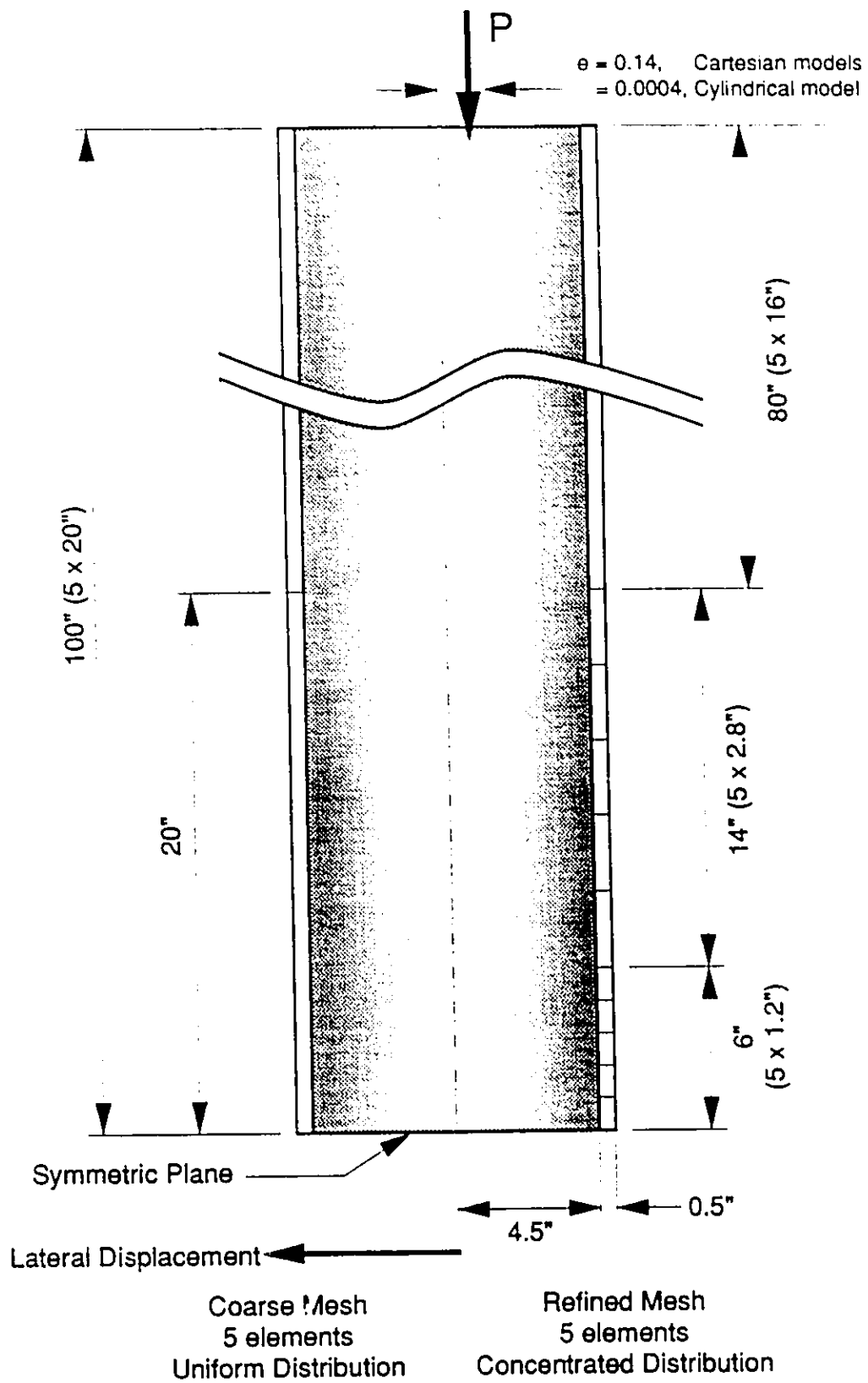


Figure 6.41 Large displacement tube - column models

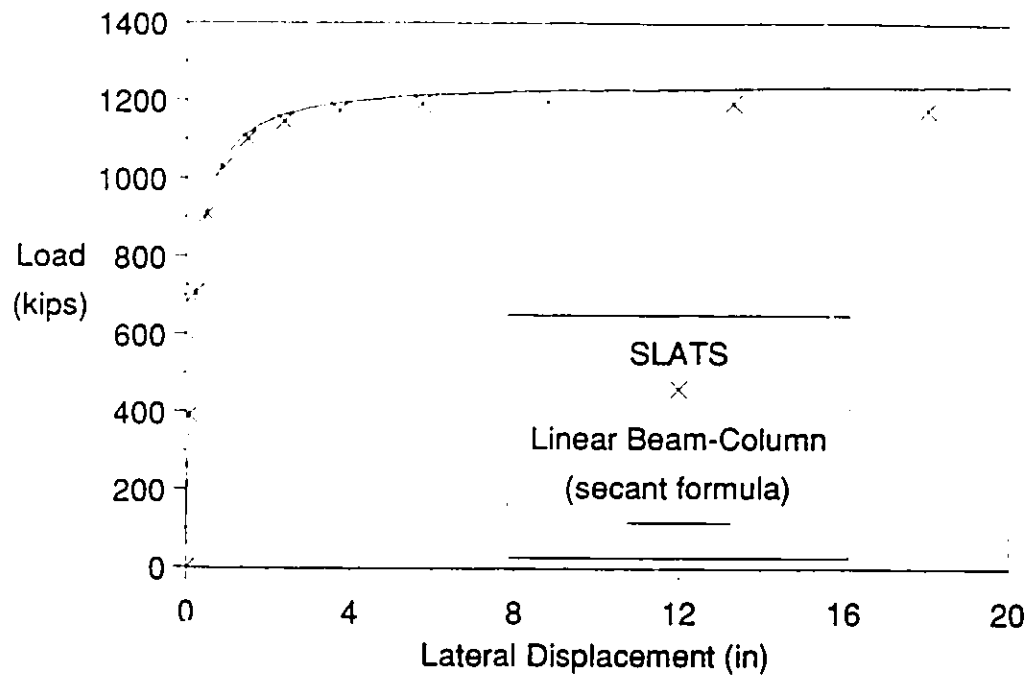


Figure 6.42 Initial load - displacement comparison between SLATS and secant formula for column

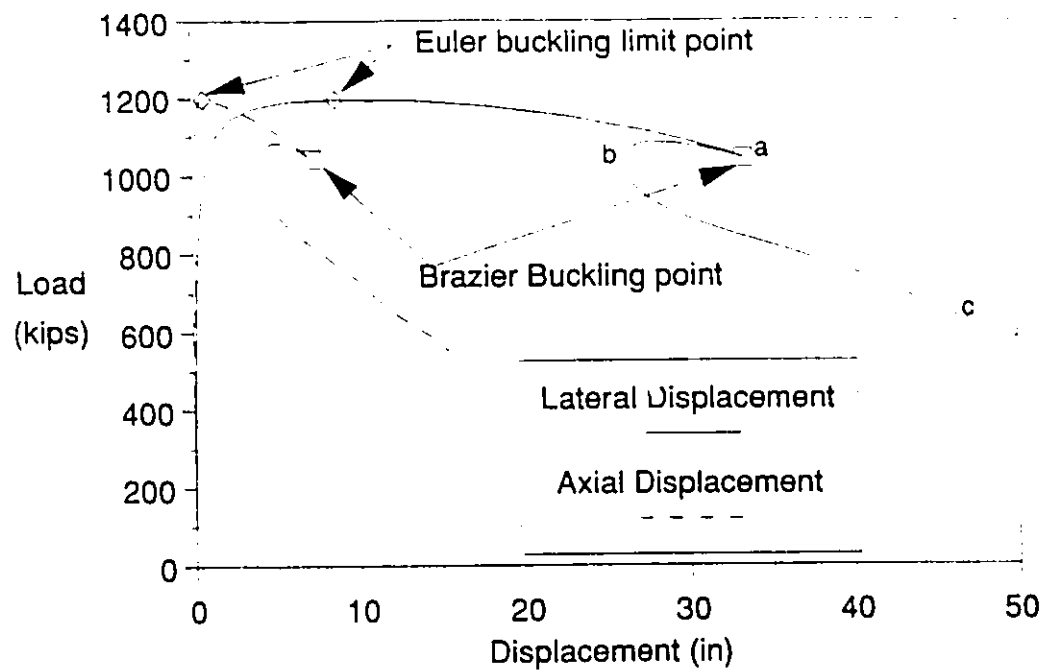


Figure 6.43 Load vs. displacement at end of tube for the tube - column problem

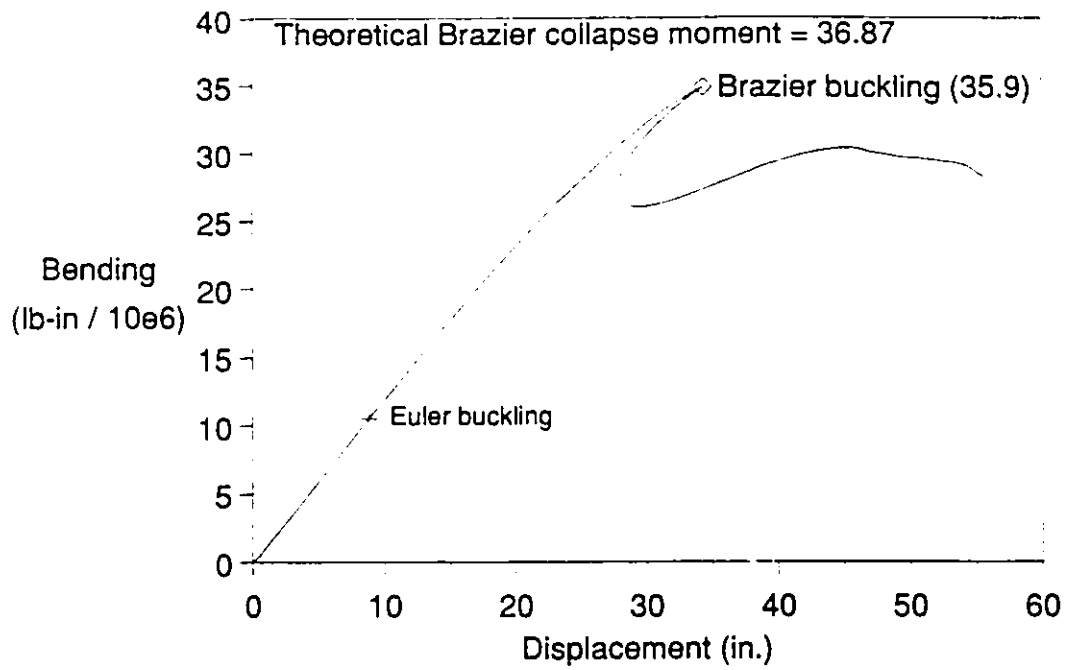


Figure 6.44 Bending moment at plane of symmetry vs. displacement at middle for the tube - column problem

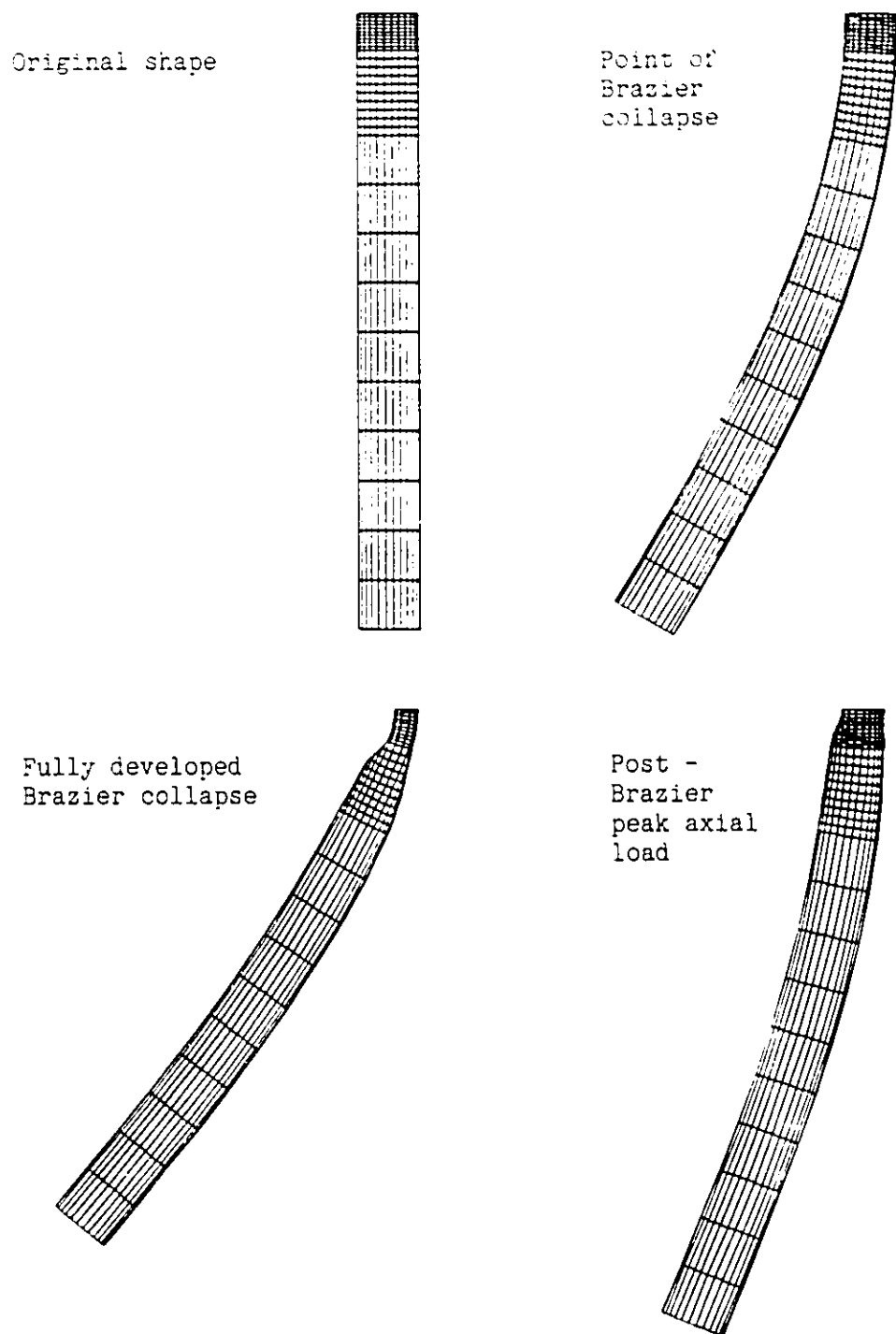


Figure 6.45 Overall tube shape at various stages of buckling

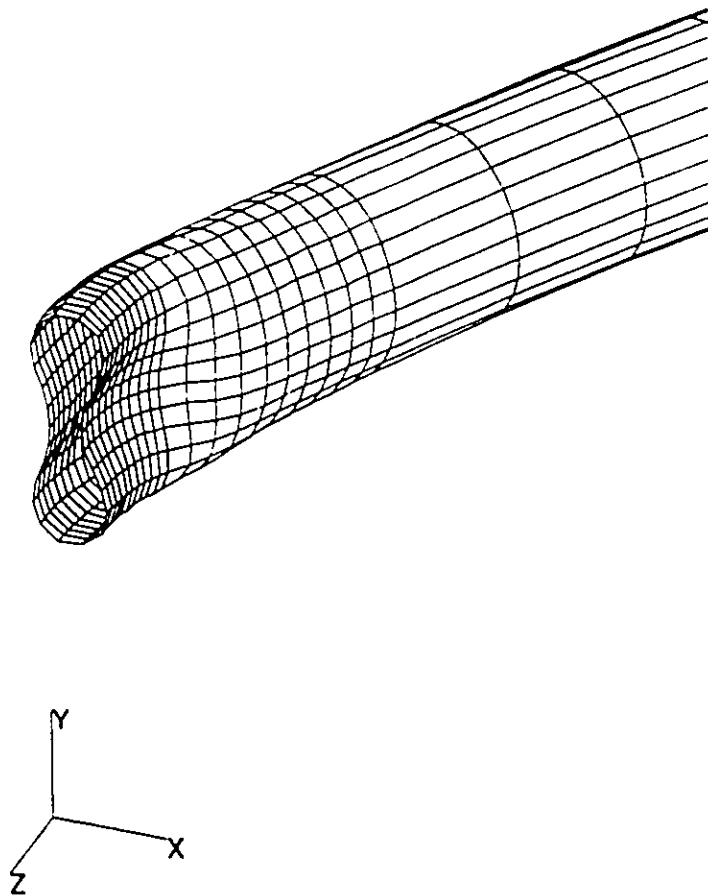


Figure 6.46      Enlarged view of collapsed cross section at middle of tube

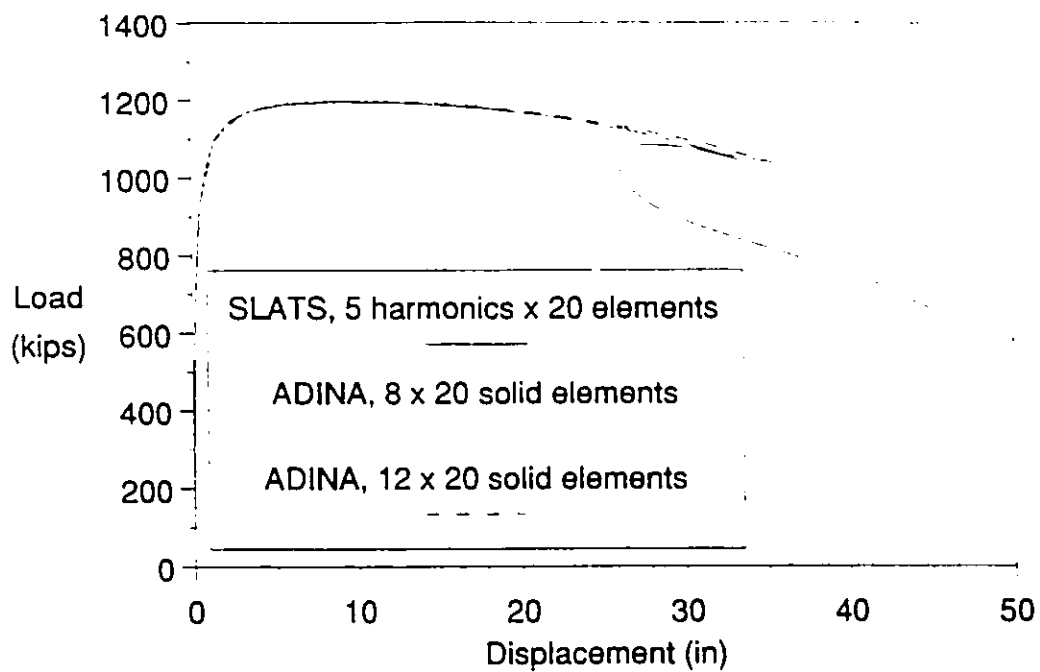


Figure 6.47 Load - displacement comparison between SLATS and ADINA

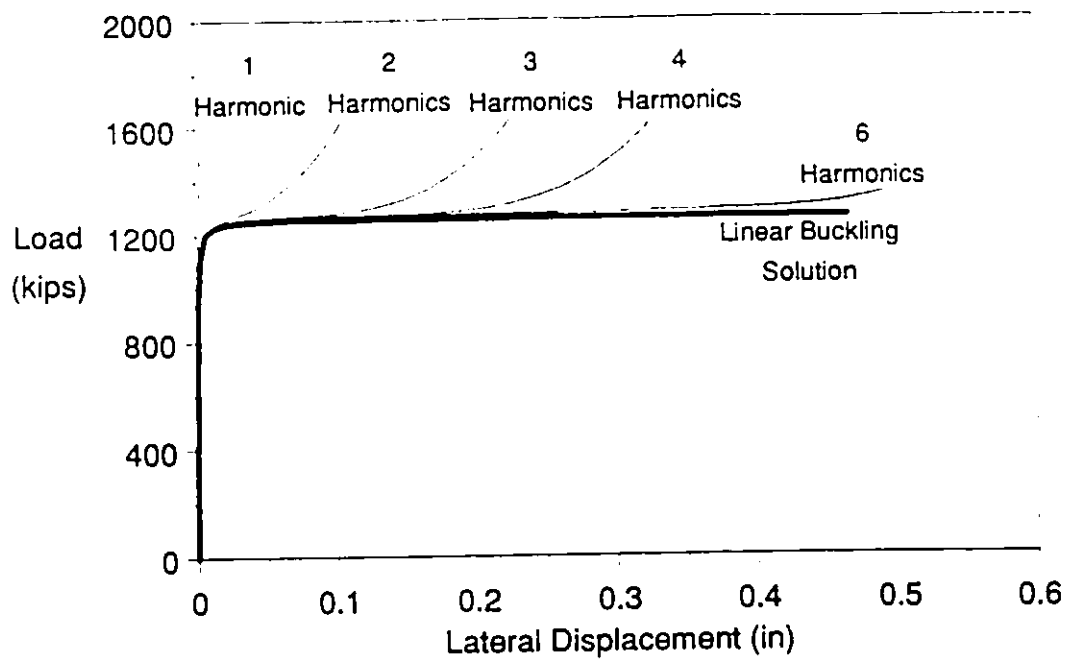


Figure 6.48 Cylindrical formulation results  
(load eccentricity = 0.0004 inches)



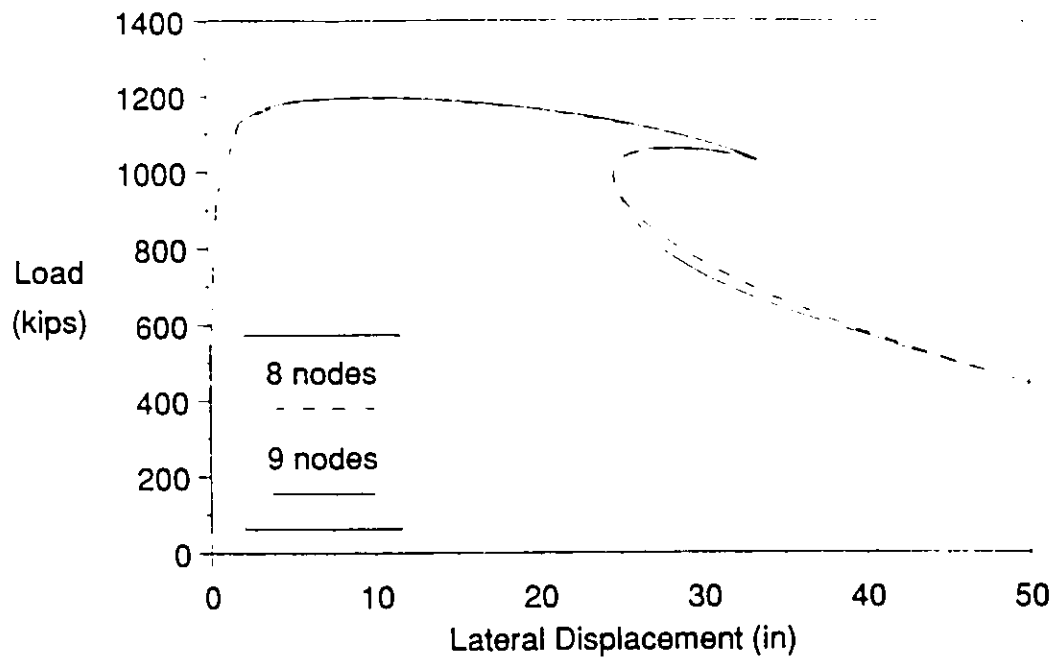


Figure 6.49 Polynomial displacement field comparison  
Eight node vs. nine node elements, 8 harmonics

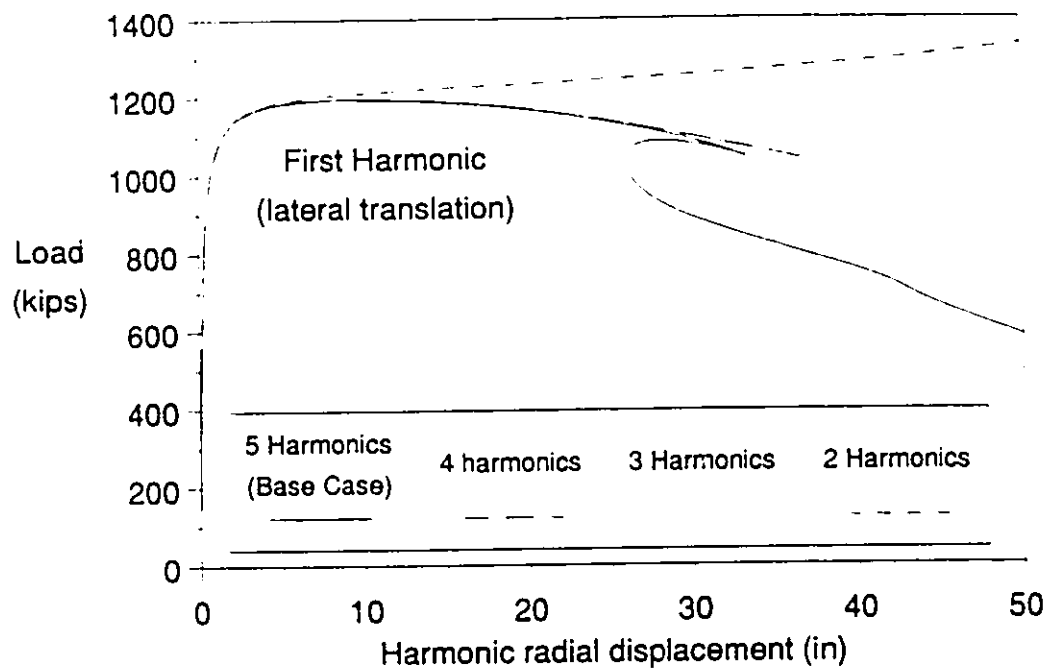


Figure 6.50 Load - displacement variation with harmonic refinement

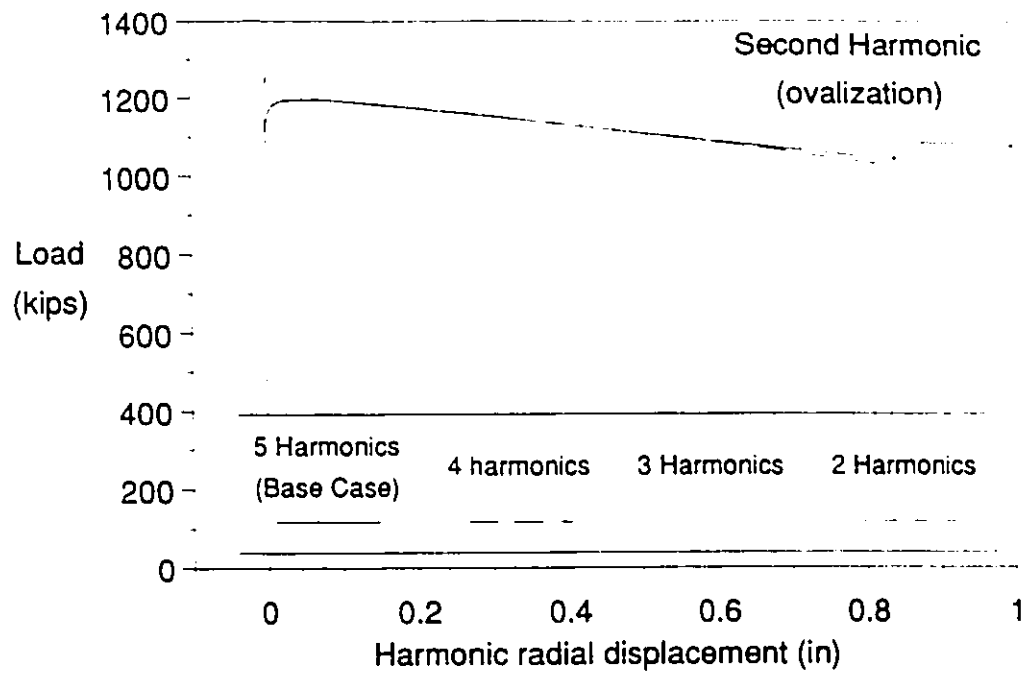


Figure 6.51 Load - ovalization relationship at middle of tube

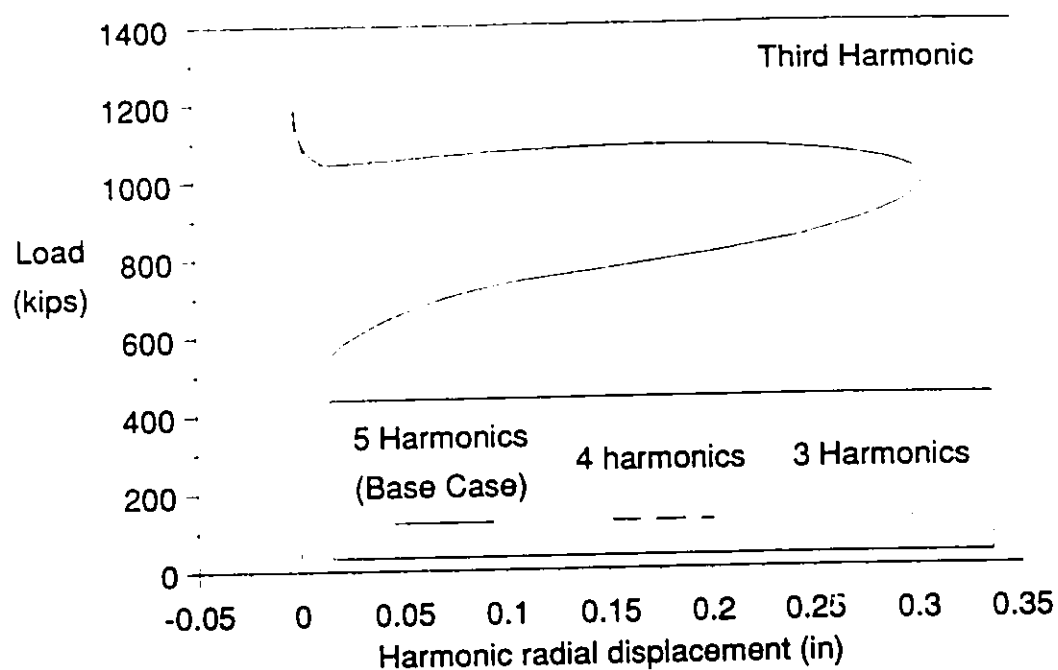


Figure 6.52 Load - third harmonic displacement at middle of tube

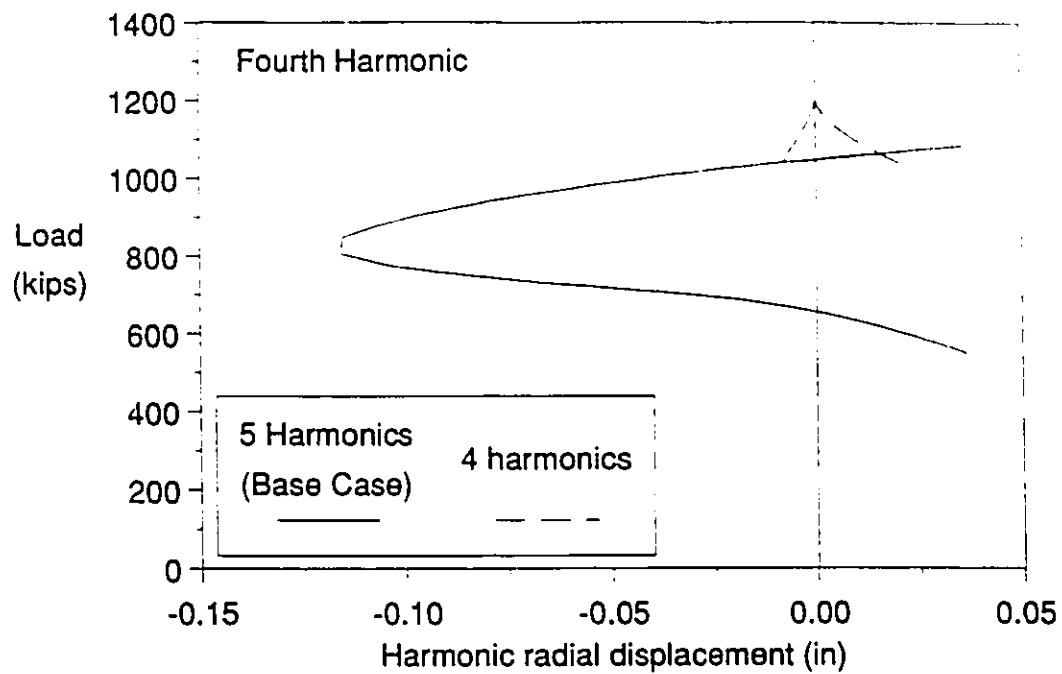
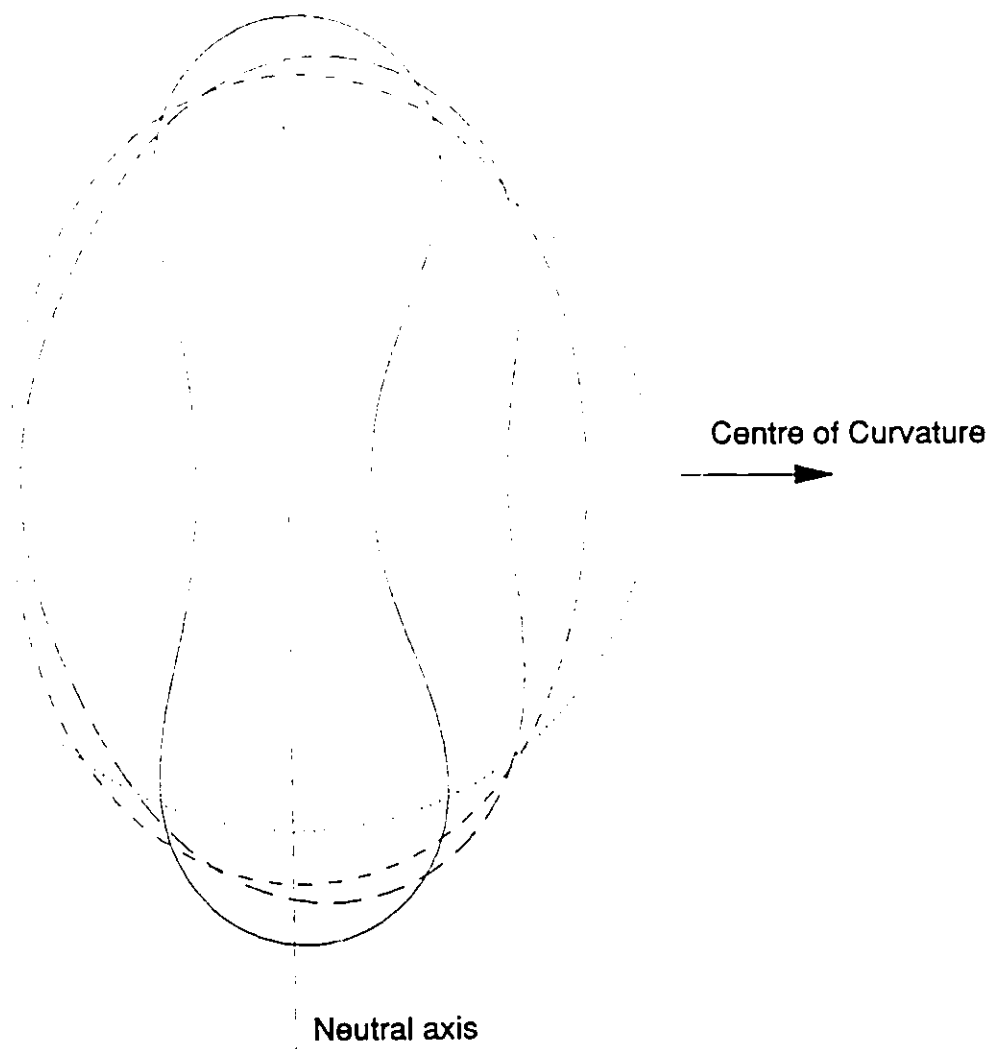
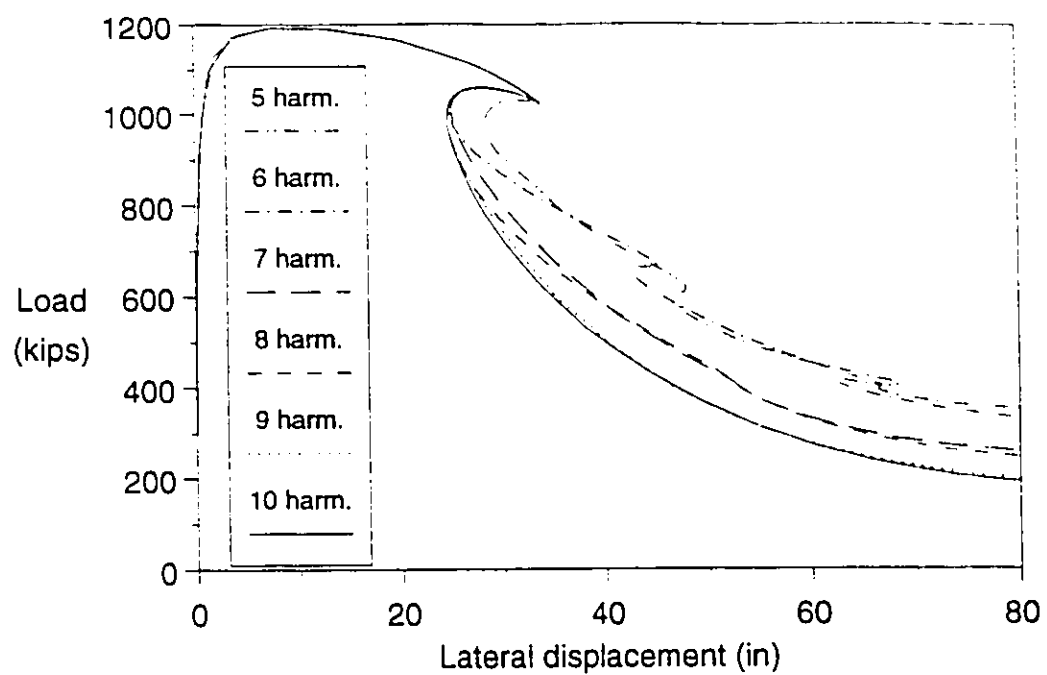


Figure 6.53 Load - fourth harmonic displacement at middle of tube



- |                                       |           |
|---------------------------------------|-----------|
| Original shape - outside diamer       | .....     |
| Point a - Impending Brazier buckling  | - - - - - |
| Point b - Snap - back deformed shaped | — — —     |
| Point c - Buckled shape               | —————     |

**Figure 6.54** Deformed shape of tube cross section at middle



**Figure 6.55** Load vs. lateral displacement with additional harmonic refinement.

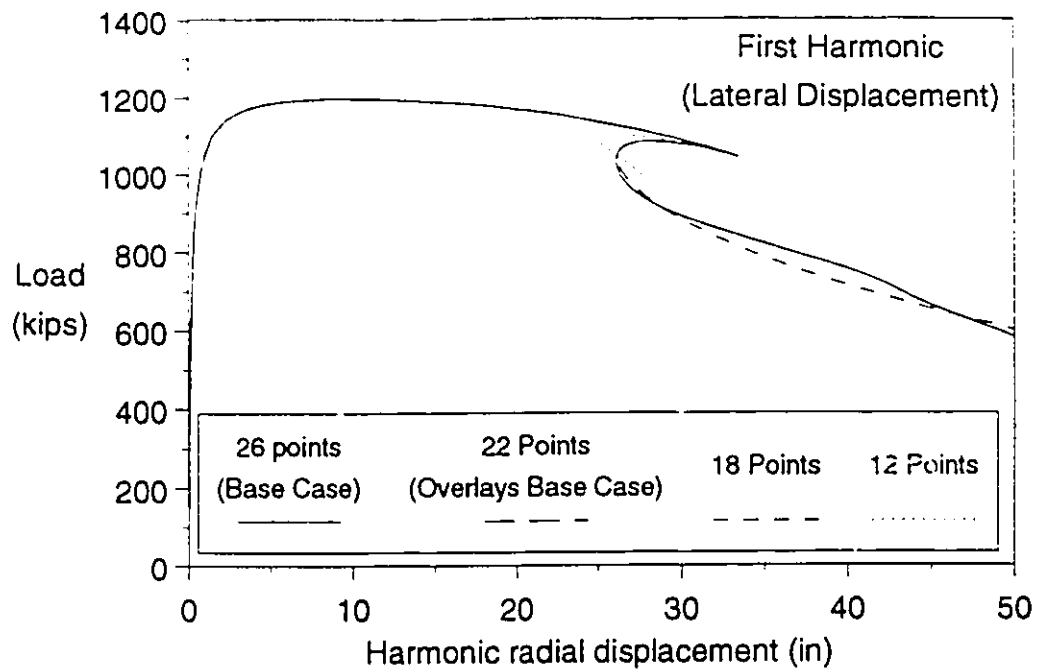


Figure 6.56 Influence of circumferential integration order on results



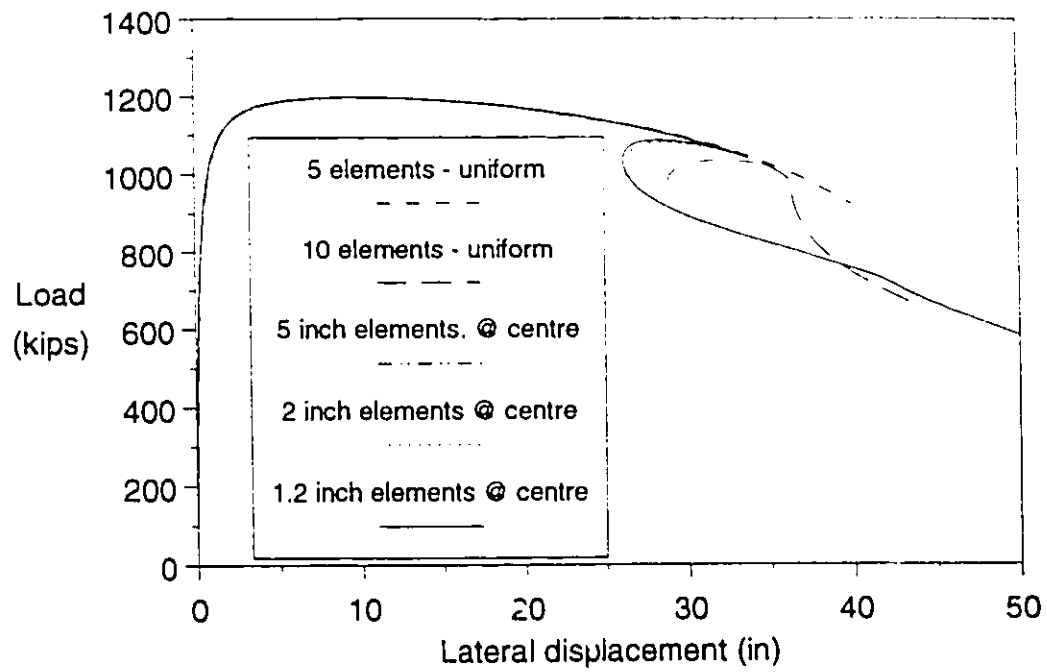


Figure 6.57 Effect of axial mesh refinement on on nonlinear solution

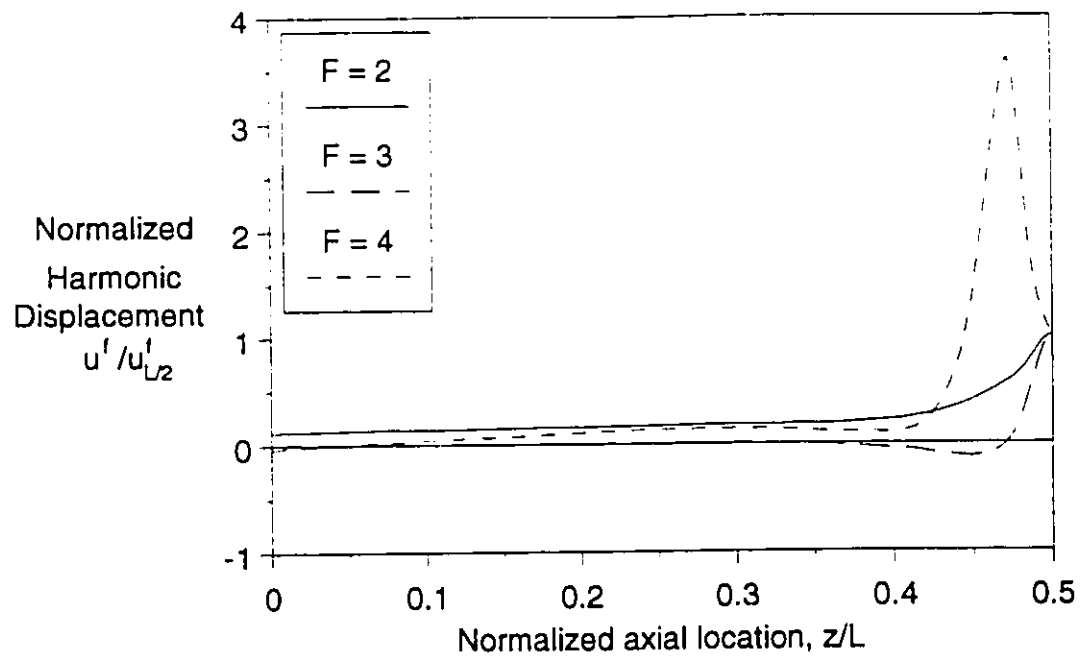


Figure 6.58 Normalized axial distribution of harmonic radial displacement at point b on equilibrium curve (Figure 6.43)

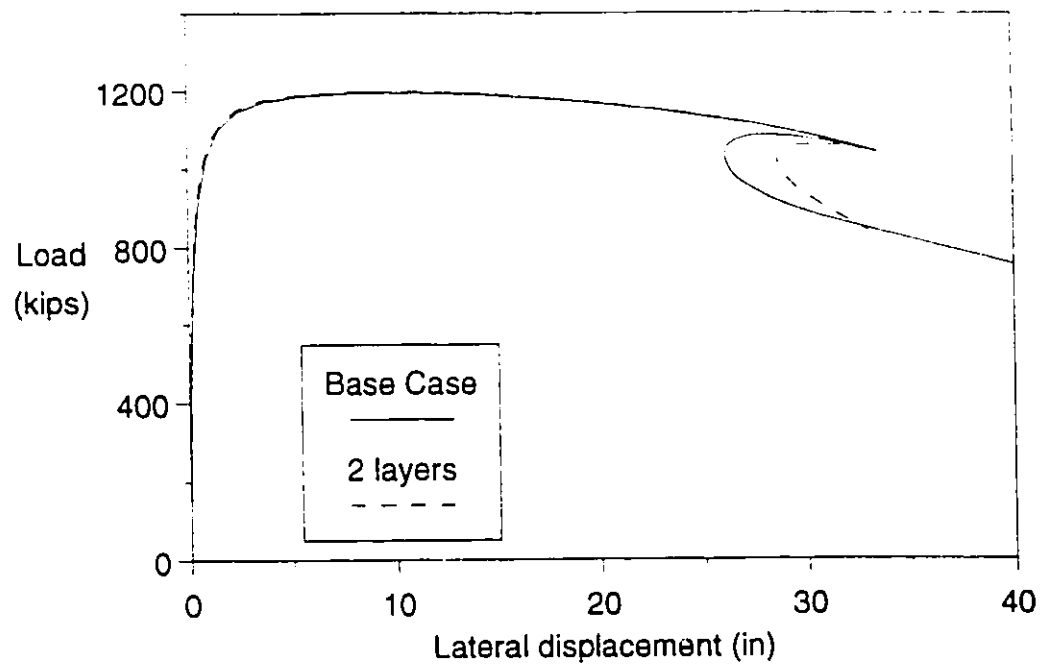


Figure 6.59 Effect of radial mesh refinement on nonlinear solution

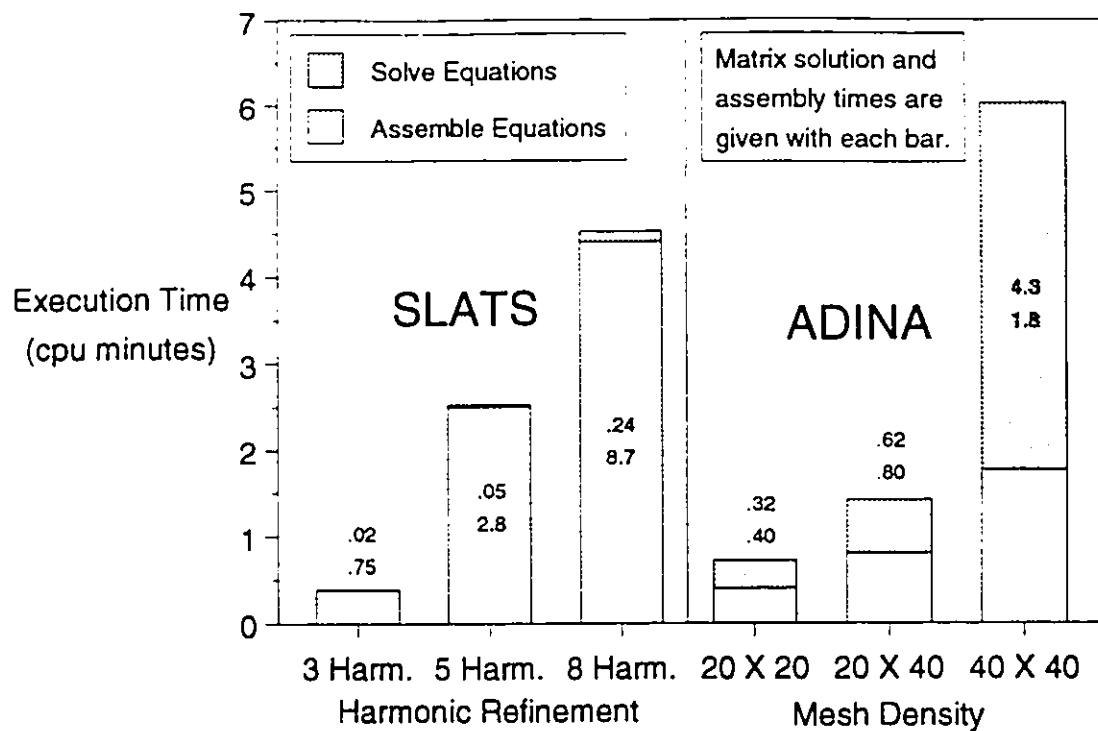


Figure 6.60 Solution time comparison for thin shell type problems

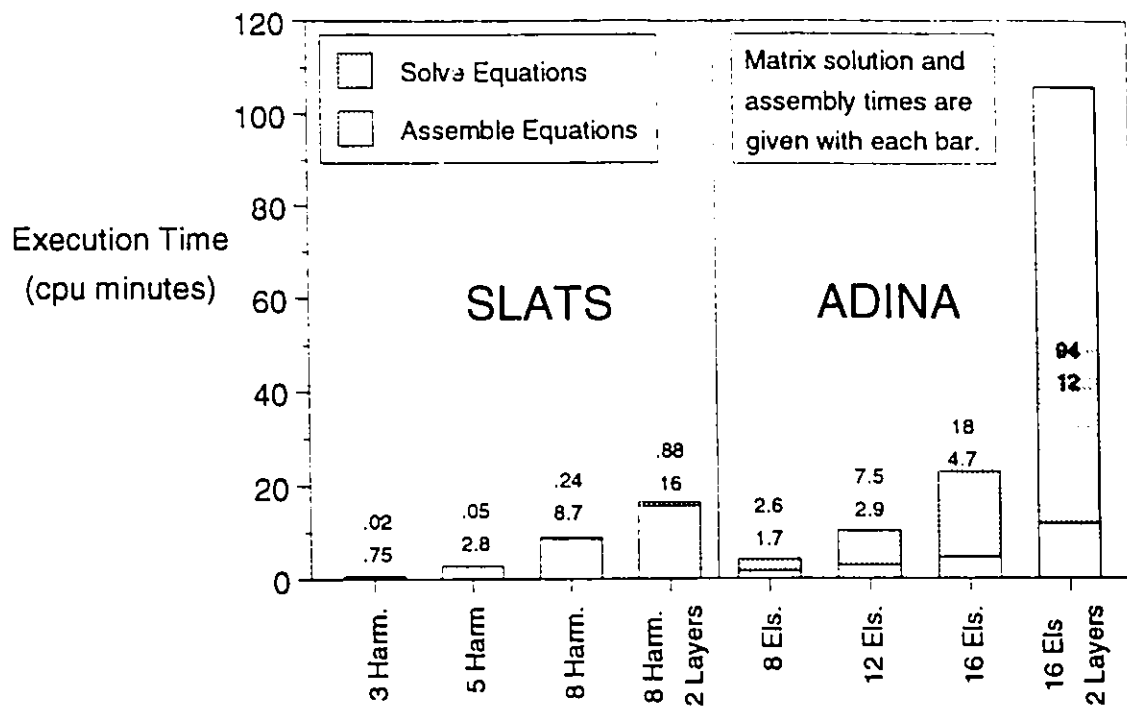


Figure 6.61 Solution time comparison for solids type problems

## 7. Summary and Conclusions

### 7.1. Overview of Formulation

In this thesis, the technique of Fourier decomposition was applied to the Total Lagrangian formulation of the virtual work equation to produce the finite element equations for an axisymmetric solid element. Additional degrees of freedom are used at the element nodes to model a non-axisymmetric displacement field, allowing more general behaviour to be modelled while utilizing the geometric simplicity afforded by the circumferential symmetry. All of the nonlinear stiffness terms on the left hand side of the virtual work equation are retained. Consequently, the Fourier components are coupled, which increases the computational effort significantly, relative to linear formulations, but permits a solution to be determined when the deformations become very large.

The Fourier decomposition form of the virtual work equations was first developed by extending earlier published works, using cylindrical displacement components. During early verification runs, it was discovered that the coordinate displacements utilized would not adequately model large displacement problems. Though it was not investigated, a partial solution was found to correct the element displacement field so that small displacement problems could be accurately modelled over the entire range of element thickness to radius ratios. However, this would not solve the large displacement problem of modelling rigid body motion.

In previous linear formulations, the Fourier stiffnesses were decoupled when cylindrical displacements were used. This desirable characteristic is lost, however, when nonlinear problems are considered. It was realized that cylindrical displacements possessed no inherent advantage over Cartesian displacement coordinates in nonlinear problems. Therefore, the same Total Lagrangian formulation was developed using the simple geometrical description of the cylindrical coordinate system, but employing Cartesian displacement components to describe the deformations. Using appropriate transformation functions, expressions were developed for the strains in terms of these two reference systems. The formulation which results includes slightly more overhead in evaluating the stiffness and equilibrium equations, but this is well worth the improvement in modelling capability.

Because Cartesian displacement components are used as nodal harmonic degrees of freedom, this form is referred to as the Cartesian formulation. The Cartesian displacement components are interpolated using the polynomial functions in the meridional plane, and Fourier decomposition is used in the circumferential direction. As a result, the problem of modelling rigid body motion is eliminated, in both small and arbitrarily large displacement problems. The results show this formulation to be very capable of modelling complex, non-axisymmetric, arbitrarily large displacement problems.

## **7.2. Solution Efficiency**

For problems where the deformation does not become too localized, only the first few Fourier harmonics are required for an accurate solution. The results demonstrate that for such problems, the Fourier decomposition approach is significantly more efficient than general purpose polynomial solid or shell elements, both in terms of solution accuracy and efficiency. The HLT element demonstrated faster execution times and more reliable predictions of the post collapse behaviour in the test problems. There are many opportunities for improving the efficiency of evaluating the stiffness matrix, particularly in the realm of circumferential integration of the system of equations. The nature of the Fourier functions could provide far more efficient numerical integration techniques than those developed thus far.

## **7.3. Future Directions**

The formulation developed in this thesis provides the basic framework for developing a complete analysis system for axisymmetric structures. Following are descriptions of additional capabilities which are under consideration for development.

### **7.3.1. Nonlinear Material Models**

The most significant enhancement to be added to SLATS is nonlinear material modelling capabilities. The formulation was developed for modelling tubular goods, particularly threaded connections. Material properties for steel will therefore be implemented first. There is also great potential for application to well analysis. With the addition of formation material models, the program will be able to model the mechanical behaviour of, and interaction between tubular goods and formation.

### **7.3.2. Contact Model**

One of the most significant factors in threaded connection behaviour is the interface between the mating components in the threads, and the sealing region if one is present. Extending the axisymmetric model to include asymmetric contact conditions presents some challenging problems, if it is to have the same generality as the solid element formulation. This may be undertaken in stages, with the first efforts focussing on asymmetric, small deformation contact modelling. This will probably be sufficient for connection modelling, since the connection is usually stiffer than tubular body, and the displacements are relatively small.

### **7.3.3. Antisymmetric Capability**

Although the formulation was developed in a general mathematical form, implementation of the finite element program included only the symmetric part of the Fourier series. Since torsional behaviour and antisymmetric buckling modes are included in the antisymmetric part of the Fourier series, it will be important to include the antisymmetric terms in the program to address such problems.

### **7.3.4. Curved Axis of Symmetry**

The oil industry is demonstrating a great deal of interest in advancing deviated well technology as a means of making oil recovery more cost effective. The asymmetric loading and behaviour in well systems and formations are ideally suited to analysis by Fourier decomposition. The geometry of these wells is not truly axisymmetric because of the curvature in the well. However, it may be possible to develop transformation functions which would permit the element to include the effects of well curvature.

### **7.3.5. Additional Symmetric and Selective Harmonic Capabilities.**

Many analyses utilize partial circumferential symmetry to reduce the size of model required to model a particular deformation mode. In fact, the current form of SLATS utilizes such symmetry, that is the restriction to symmetric terms in the Fourier series, to reduce the number of integration point required in the circumferential direction. In analyses where higher harmonic deformation modes are to be modelled, the lower order Fourier terms could be neglected, and integration would only have to occur over one wave of the lowest order harmonic which is to be modelled. It might also be desirable to include selective higher order harmonics to model specific deformation localization. For



example, the post collapse behaviour of the cylinders under external pressure, modelled in Chapter 6, could be improved significantly if higher order harmonics could be included to allow the deformations to become localized.

### **7.3.6. Improved Integration Techniques**

The circumferential integration requirements, combined with the large number of element degrees of freedom, makes the effort of element stiffness matrix generation grow rapidly with increasing numbers of Fourier terms. There is no way to decouple the harmonic stiffnesses, but there may be potential in reducing the circumferential integration requirements. The work so far has shown, for example, that the cylindrical formulation stiffness matrix requires  $4*NF+1$  circumferential integration points to exactly integrate the Fourier products. In the Cartesian formulation, it appeared that  $4*NF+5$  would be required, the additional four points added by the geometrical transformations which are incorporated into the strain - displacement matrix and the displacement gradient tensor. However, test case analyses showed that the Cartesian formulation also required only  $4*NF+1$  integration points.

It may be possible to utilize some of the characteristics of the Fourier functions to provide exact circumferential integration of the stiffness matrix much more efficiently. If, for example, the number of integration points could be fixed at a specific number, the increase in cpu time to generate an element would vary with the square of the maximum harmonic number, rather than the cube as it does currently. This would make feasible analysis with higher harmonic numbers, thus permitting greater capabilities for modelling localized behaviour, and extending the range of application for the program significantly.

### **7.3.7. Resolve Cylindrical Formulation Rigid Body Motion**

There are several advantages to formulating the Fourier decomposition element in terms of cylindrical coordinates. Boundary conditions are usually more naturally applied in cylindrical coordinates, and the harmonic displacement modes often are decomposed into separate Fourier displacement components, particularly with relatively thin shell models. This is in contrast to the Cartesian formulation, where the geometrical transformation functions distribute a harmonic displacement mode across three Cartesian displacement harmonics. These are the primary reasons for pursuing the cylindrical formulation further.

Several avenues could be explored to correct the problems with the cylindrical formulation. The most elegant solution would be to define the displacement field in terms of some physical displacement definition in the cylindrical reference system to eliminate the nonlinear influence of the metric tensor.

Another approach could be to transform all of the variables in the Cartesian formulation into cylindrical counterparts. This was partially accomplished in Chapter 4 where transformations from Cartesian to cylindrical nodal harmonic degrees of freedom were developed to simplify results comparisons with published solutions. It was shown that the transformations could be extended to produce a global system of equations in terms of the cylindrical system. The exercise could be carried further, transforming stresses and strains to complete the description in terms of cylindrical coordinates.

A third approach would retain the coordinate displacement based formulation presented in Chapter 2, and use a refined element displacement field to develop the Cylindrical formulation, along the lines of development in Chapter 3. One way to refine the displacement field to accommodate the rigid body modes might be to define additional degrees of freedom to model the lateral motion of the nodal rings, and superimpose circumferential deformations in the rings, using the remaining nodal harmonic displacements.

It is presumed that the first two models would resolve to the same formulation, given the correct physical displacement definition in the cylindrical form. All three models should resolve to the small displacement Fourier decomposition of Wilson, 1965 when reduced to the small displacement case.

#### 7.4. Closure

This thesis has presented a large displacement finite element formulation for modelling general three dimensional behaviour of axisymmetric structures. Analyses prove the formulation to be accurate and efficient relative to three dimensional models using conventional polynomial based elements. However, the formulation does maintain many similarities to common polynomial based formulations, so incorporation of the most important enhancements discussed above should be a relatively straight forward process. In particular, addition of nonlinear material properties will make the program applicable to a wide range of problems which cannot be dealt with by current analysis techniques.

## References

- "ADINA, A Finite Element Program for Automatic Dynamic Incremental Nonlinear Analysis", Report ARD 87-1, ADINA R & D Inc, Waterton, MA., 1987.
- Brazier, L. G., "On the Flexure of Thin Cylindrical Shells and other 'Thin' Sections", Proc. Roy. Soc., ser. A, vol. 116, pp. 104-114, 1926.
- Brush, D. O., and Almroth, B. O., Buckling of Bars, Plates, and Shells, McGraw-Hill Inc., 1975.
- Ball, R. E., "A Geometrically Nonlinear Analysis of Arbitrarily loaded Shells of Revolution", NASA CR 909, January 1968.
- Bathe, K.J., Ramm, E. and Wilson, E.L., "Finite Element Formulations for Large Deformation Dynamic Analysis", Int. J. Num. Meth. Eng., v. 9, pp. 353-386, 1975.
- Bathe, K.J., Finite Element Procedures in Engineering Analysis, Prentice-Hall Inc., 1982.
- Chan, A.S.L. and Firmin, A., "The Analysis of Cooling Towers by Matrix Finite element Method - Small Displacements", Aeron. J. Roy. Aeron. Soc., v. 74, pp. 826-835, 1970.
- Chan, A.S.L. and Firmin, A., "The Analysis of Cooling Towers by Matrix Finite element Method - Large Displacements", Aeron. J. Roy. Aeron. Soc., v. 74, pp. 971-982, 1970a.
- Chan, A.S.L., and Trbojevic, V.M., "Thin Shell Finite Element by the Mixed Method Formulation", Comp. Meth. in App. Mech. and Eng., v. 9, pp 337-367, 1976.
- Chan, A.S.L., and Trbojevic, V.M., "Thin Shell Finite Element by the Mixed Method Formulation - Parts 2 and 3", Comp. Meth. in App. Mech. and Eng., v. 10, pp. 75-103, 1977.
- Chan, A.S.L., and Wolf, J.P., "Cooling Tower Supporting Columns and Reinforcing Rings in Small and Large Displacement Analyses", Comp. Meth. in App. Mech. and Eng., v. 13, pp. 1-26, 1978.
- Crisfield, M. A., "A Fast Incremental/Iterative Solution Procedure that handles 'Snap-Through'", Symp. on Comp.. Meth. in Nonlinear Struct. and Solid Mech., Washington, 1980.
- Dennis, S. T., and Palazotto, A. N., "Transverse Shear Deformation in Orthotropic Cylindrical Pressure Vessels Using Higher Order Shear Theory", AIAA, v.27, pp1441-1447.
- Ewing, D. J. F., "The buckling and vibration of cooling tower shells", Part I and II CERL, RD/L/R 1763, Nov. 1971.

Flügge, W., Stresses in Shells, Springer-Verlag, 1960.

Fung, Y.C., Foundations of Solid Mechanics, Prentice-Hall Inc., 1965.

Gallagher, R. H., Gellatly, R. A., Padlog, J., and Mallet, R. H., "A Discrete Element Procedure for Thin Shell Instability Analysis, AIAA Journal, v. 5, no. 1, pp. 138-145, 1967.

Gerrard, G., Introduction to Structural Stability Theory, McGraw-Hill, 1962.

Kalnins, A., and Lestingi, J. F., "On Nonlinear Analysis of Elastic Shells of Revolution.", J. App. Mechs, March 1967, pp 59-64.

Kaplan, A., and Fung, Y. C., "A Nonlinear Theory of Bending and Buckling of Thin Elastic Spherical Shells.", NACA TN3212.

Kleiber, M., and Hien, T.D., "Nonlinear Dynamics of Complex Axisymmetric Structures under Arbitrary Loads", Comp. Meth. in Applied Mech. and Eng., v. 37, pp. 93-107, 1983.

Malvern, L.E., Introduction to the Mechanics of a Continuous Medium, Prentice-Hall Inc, 1969.

Popov, E.P., Mechanics of Materials, SI Version, Second Edition, Prentice-Hall Inc., 1978.

Ramm, E., "Strategies for Tracing the Nonlinear Response Near Limit Points", Non-linear Finite Element Analysis in Structural Mechanics, (Eds. W. Wunderlich, E. Stein and K.J. Bathe), Springer-Verlag, New York Inc., pp. 68, 1981.

Schweizerhof, K., and Ramm, E., "Follower Force Effects on Stability of Shells under Hydrostatic Loads", Journal of Engineering Mechanics, v.113, No. 1, pp. 72-88.

Singh, S.P., and Spilker, R.L., "Elasto-Plastic Analysis of Axisymmetric Structures Subject to Arbitrary Loads by Hybrid-Stress Finite Elements", Computers and Structures, v. 19, No. 3, pp. 447-465, 1984.

Sokolnikoff, I.S., Mathematical Theory of Elasticity, Second Edition, pp. 213-229, McGraw-Hill Inc., 1956.

Spilker, R.L., and Daugirda, D.M., "Analysis of Axisymmetric Structures under Arbitrary Loading using the Hybrid-Stress Model", Int. J. Num. Meth. Eng., v. 17, pp. 801-828, 1981.

Timoshenko, S. P., and Gere, J. M., Theory of Elastic Stability, McGraw-Hill, 1961.

Truesdell, C., and Toupin, R.A., "The Classical Field Theories", Encyclopedia of Physics, Principles of Classical Mechanics and Field Theory, Vol. III/1, pp. 226-325, Springer-Verlag New York Inc., 1960.

Tsai, C. T., and Palazotto, A. N., "A Modified Riks Approach to Composite Shell Snapping Using a High-Order Shear Deformation Theory", *Computers and Structures*, v. 35, pp.221-226.

Wilson, E.L., "Structural Analysis of Axisymmetric Solids," *AIAA Journal*, v. 12, pp. 2269-2274, 1965.

Winnicki, L.A., and Zienkiewicz, O.C., "Plastic (or Visco-Plastic) Behaviour of Axisymmetric Bodies Subjected to Non-symmetric Loading - Semi-analytical Finite Element Solution," *Int. J. Num. Meth. Eng.*, v. 14, pp. 1399-1412, 1979.

Wunderlich, W., Cramer, H., and Obrecht, H., "Application of Ring Elements in the Nonlinear Analysis of Shells of Revolution under Nonaxisymmetric Loading, *Comp. Meth. in Applied Mech. and Eng.*, v. 51, pp. 259-275. 1985.

Wunderlich, W. and Obrecht, H., Springer, H., and Lu, Z., "Semi-analytical Approach to the Nonlinear Analysis of Shells of Revolution.", *Anal. Comput. Model Shell*, Winter Annual Meeting ASME, pp. 509-536, 1989.

Zienkiewicz, O.C., The Finite Element Method, 3rd Ed., McGraw-Hill, 1977.

Zienkiewicz, O.C., and Cheung, Y.K., "Stress in Shafts", *The Engineer*, 24 Nov., 1967.